HYPERSPECTRAL IMAGING AND DATA ANALYSIS

OF

SKIN ERYTHEMA

POST RADIATION THERAPY TREATMENT

HYPERSPECTRAL IMAGING AND DATA ANALYSIS
OF
SKIN ERYTHEMA
POST RADIATION THERAPY TREATMENT

By

RAMY ABDLATY, M.Eng. B.Eng.

A Thesis
Submitted to the School of graduate Studies
In Partial Fulfilment of the Requirements for the Degree
Doctor of Philosophy

McMaster University

Doctor of Philosophy (2016)	McMaster University
School of Biomedical Engineering	Hamilton, Ontario

TITLE:	HYPERSPECTRAL IMAGING AND DATA ANALYSIS OF SKIN ERYTHEMA POST RADIATION THERAPY TREATMENT
Author	Ramy Abdlaty, M.Eng., B.Eng., Military Technical College, Cairo, Egypt
Supervisor	Assoc. Prof. Qiyin Fang
Number of pages	xxi, 182

Abstract

Recent cancer statistics show that 40% of Canadians might contract cancer during their life and 25% of Canadians might die due to cancer. In skin, head and neck cancers, surgery and radiation therapies are the most prevalent treatment options, while radiation therapy is the most commonly used approach. A common problem in radiation therapy is tumors behave differently against ionizing radiation. For instance, with the same dose, some tumors are fully damaged or shrunk, while others are less affected. The difference in individual tumor response to therapy is transformed into a research question: how to quantitatively assess tumor response to radiation and how to tune radiation therapy to achieve full destruction for tumor cells? Few past studies addressed the question, although no definite answer was realized.

This work is a part of a project that investigates the hypothesis that radiation response of skin is correlated to individual tumor response. In the case of high correlation, the skin's faster response to ionizing radiation can be used to modify the irradiation dose to achieve the maximum destruction of individual's tumor. To examine the project hypothesis, radiation-induced skin redness or erythema was selected as an acute skin reaction to being objectively quantified. Hence, the overall goal of the research thesis work is to objectively assess and precisely quantify radiation-induced erythema or radiation dermatitis. Skin erythema was assessed formerly by multiple optical and non-optical modalities. The current gold standard is the visual assessment (VA). Unfortunately, VA lacks objectiveness, precise communication, and quantification. To push the limitations of VA and past techniques, hyperspectral imaging (HSI) was proposed to be used for erythema assessment. The work detailed in this thesis aims to create more confidence in HSI to be utilized toward objectively quantify skin erythema. To reach this goal, **initially**, a new high-throughput dual channel acousto-optic tunable filter (AOTF)-based-HSI instrument was developed for monitoring radiation dermatitis. AOTF-HSI instrument design, implementation, and full characterization are presented. **Second**, the developed AOTF-HSI instrument is evaluated against a liquid crystal tunable filter (LCTF) instrument. **Third**, to be prepared for clinical operation, the AOTF-HSI equipment was used to classify an artificially-induced erythema on healthy volunteers in an exploratory study. A robust linear discriminant analysis (LDA)-based classification method was developed for the purpose of image classification. **Finally**, HSI instrument and LDA classification method were utilized in a preliminary clinical study to properly monitor and precisely quantify radiation dermatitis for skin cancer patients. In the clinical study, erythema indices were computed using Dawson's method. Least square fitting was used to fit the acquired absorbance data, and thus quantify the hemoglobin concentration change along the study duration. Moreover, LDA was used to contrast spectral and digital imaging for erythema classification. In sum, the work documented in this thesis was willfully directed to achieve an efficient, portable, user-friendly hyperspectral imaging system which has the opportunity to be a benchtop in the clinical daily procedure in the near future.

Acknowledgments

Primarily, I am extremely grateful to ***my lord God*** *who guided and provided me the chance to reach this interesting point in my life. Upon that, I would like to deeply thank* ***my parents especially my angel mother*** *who always asks for me all the chance and goodness during all my life. I cannot ignore as well* ***my awesome wife*** *who did a great job supporting, loving, and compensating my absence with the kids.*

I would like to report, testify, and confirm my intact gratitude for my supervisor, ***Dr. Qiyin Fang****, for his continuous support, infinite patience, extensive knowledge, and far vision during my Ph.D. program years. He always acts as the bank of golden advice that provided me with the way to shortcut the long time needed to complete my research work. Moreover, he is always very generous, caring, and supporting to me in my social life issues as well.*

Besides my advisor, I would like to record here my great thanks to my supervising committee ***Dr. Joseph E. Hayward, and Dr. Thomas Farrell****. They always inspired me to reach genuine ideas to resolve hard work troubles and frustrating research obstacles. Moreover, a special recognition should be mentioned here for their effort and time on improving my writing skills through editing the thesis. In addition, I couldn't neglect the role of Dr. John Oreopoulos, Dr. Peter Sinclair, and Dr. Richard Berman in assisting me with their optics and manufacturing experience. Furthermore, I would like to document a distinguishable gratitude for* ***Dr. Josiane Zerubia, and Ali Madooei*** *for their sincere efforts during our collaborated work.*

Furthermore, I would like to mention a testimonial to my clinical work partner ***Lilian Doerwald*** *that she was the best work partner I ever had in my education life. I believe that I need to thank all Dr. Fang research current and previous group members including but not limited to Dr. Samir Sahli, Dr. Veronika, Dr. Allison, Anthony Tsikouras, Nehad Hirmiz, Eric Mahoney, Ian Philips, Fahad Aljekhedab, Du Le, Fiona Du, and Sharon Goh for providing me with a friendly and supportive environment.*

Table of Contents

Contents

List of Figures

List of Tables

List of Abbreviations

ACD	Allergic contact dermatitis
AO	Acousto-optics
AOTF	Acousto-optic tunable filter
BCC	Basal cell carcinoma
CCD	Charge coupled-device
CMOS	Complementary metal-oxide semiconductor
CTF	Contrast transfer function
CW	Continuous wave
DEI/c	Dawson’s erythema index/corrected
DF	Dermatofibroma
DMI	Dawson’s melanin index
DOF	Depth of focus
DRS	Diffuse reflectance spectroscopy
EI	Erythema index
EMCCD	Electron multiplying charge coupled-device
Er	Erythematous region
Er1	Very faint erythema
Er2	Faint erythema
Er3	Bright erythema
Er4	Very bright erythema
FD	Frequency domain
FFT	Fast Fourier transforms
FOV	Field of view
FPA	Focal plane array
FSD	Full-scale deflection
FT	Fourier transforms
FTIR	Fourier transforms infrared
FWHM	Full-width half maximum
Gy	Grey/ irradiation unit
HSI	Hyperspectral imaging
Hb	Hemoglobin deoxygenated part
HbO_2	Hemoglobin oxygenated part
ICA	Individual component analysis
ICCD	Intensified charge coupled-device
IHB	Index of hemoglobin content
IMRT	Intensity modulated radiation therapy
IS	Integrating sphere
K	Absorption coefficient
KM	Kubelka-Munk
LCTF	Liquid crystal tunable filter
LDA	Linear discriminant analysis

LDF	Laser Doppler flowmeter
LDI	Laser Doppler imager
LED	Light emitting diode
LP	Linear polarizer
LRR	Logarithm of reflectance reciprocal
M	Mean
MC	Monte Carlo Simulation
MCP	Micro channel plate
MDI	Minimum detectable increase
MED	Minimal erythema dose
MI	Melanin index
MLRR	Matrix low-rank representation
MMSE	Minimum mean square error
MRI	Magnetic resonance imaging
MSC	Melanoma skin cancer
MSI	Multispectral imaging
MTF	Modulation transfer function
n	Refractive index
NIR	Near infrared
NMSC	Non-melanoma skin cancer
NOS	Neoplasms of the skin
OCT	Optical coherence tomography
OPD	Optical path difference
PBS	Polarizing beam splitter
PCA	Principal Component Analysis
PGP	Prism-grating-prism
PIH	Post inflammatory hyperpigmentation
R	Retardance
RF	radio frequency
RGB	Red-green -blue
ROI	Region of interest
RP	Random polarized
RTE	Radiation transport equation
S	Scattering coefficient
SC	Skin cancer
SCC	Squamous cell carcinoma
SFDR	Spurious-free dynamic range
SI	Spectral imaging
SNR	Signal to noise ratio
TBWP	Time bandwidth product
TD	Time domain
TeO_2	Tellurium dioxide
TF	Tunable filter
USAF	United States air force resolution target

USI	Ultraspectral imaging
UV	Ultra-violet
V	Light speed reduction in the tissue medium / variance
VA	Visual assessment
VC	Visual colorimeter
VIS	Visible spectra
VIS-NIR	Visible-near infrared spectra
VS	Variable selection

Chapter 1: Introduction

1.1 Motivation

Radiation therapy/ radiotherapy is a common treatment option for cancer, be it alone or combined with surgery, chemotherapy, or both [1]. Recent cancer statistics show that, ~50% of cancer patients use radiotherapy either for curative or palliative treatment [1]. The extended use of radiotherapy is due to few reasons such as the less possible comorbidity in old-aged patients and the more accepted cosmetic result in comparison with the surgical alternative. Radiotherapy uses a prescribed dose of ionizing radiation with different types such as X-rays or Gamma rays. The ionizing radiation aims to damage the tumor cells' Deoxyribonucleic acid (DNA) to reach the no repair extent. As such, it stops the replication and growth. However, the ionizing radiation mission is not successfully completed all the time. Since equivalent tumors which are receiving the same dose could respond differently. Therefore an interesting question was raised; how to precisely evaluate the tumor's response due to the ionizing radiation and how to adapt radiotherapy to realize definite destruction for the malignant cells? This question was addressed by few studies [1]–[3], but no definite answer was realized. Thus, a new approach to address the raised question was needed.

Our approach for optimizing radiation therapy, for individuals, is based on a hypothesis. The proposed hypothesis assumes that the tumor and skin of an individual patient have a correlated behavior towards radiation therapy. In order to verify the proposed hypothesis, induced skin reaction to radiotherapy needs to be detected and quantified objectively. Following that, the correlation between the induced skin reaction and the tumor response, for individuals, due to radiotherapy needs to be computed. If the correlation value is proved to be significantly high, early estimation of patients' tumor response becomes possible. As a result, the patient's entire treatment plan can be modified and improved results could be achieved. For that purpose, a single skin reaction needs to be designated to be properly monitored and precisely quantified.

In spite of radiotherapy great advance in instrumentation, it is still far from the precision of solely attacking the malignant cancer cells. As a result, an extension surrounding the tumor cross section is included in the targeted region in radiotherapy. Two reasons for the extension, the first is to compensate for the unintentional movement of the patient, such as breathing, during radiotherapy. The second reason is to destroy the possible microscopic spreading of the tumor cells in the surrounding tissue. The irradiated tissue damage is a cumbersome sequential process. Since it is dependent on intersected factors including, but not limited to, the skin type, human age, gender, and more or less on the received radiation dose [4]. The tissue damage ranges from mild to severe. Mild tissue damage becomes detectable and disappears before severe tissue damage is evident. Radiation dermatitis or skin erythema is a mild radiotherapy induced skin reaction that precedes skin severe damage.

Skin erythema is the abnormal redness of the skin or mucous membranes caused by blood accumulation in dilated capillaries [5]. Erythema is different from hemorrhages, in which blood escapes the vasculature. However, like hemorrhage, erythema may occur in response to infection, irritation and/or injury in response to various physical [6], chemical [7] or biological stimuli [8]. As a result, skin erythema is often the first indicator of healthy skin perturbation [9]. This is particularly the case in radiotherapy, where the ionizing radiation trigger erythema of various grades of severity (severe cases involve moist desquamation- open wounds- and ulcerations) [10]–[17]. In fact, approximately 90% of patients who undergo radiotherapy is expected to develop skin erythema [14], [18]. As such, skin erythema can be used to assess individuals’ response to radiotherapy.

At present, qualitative visual assessment (VA) is still the most common method for evaluating erythema. VA involves a daily evaluation of the skin, using a predefined qualitative scale, based on radiotherapist observation. Since most of the qualitative scales have few divisions, it often provides non-precise information on the progression of erythema. Moreover, the evaluation in itself is subjective which depends on both experience time and vision acuity. Consequently, there is a pressing need to objectively monitor and properly quantify the rate of erythema development.

To-date, some studies put an effort to objectively quantify skin erythema that is induced due to distinct causes based on the way skin interacts with light. A common light-tissue interaction used for skin erythema quantification is to compute the optical absorbance. Optical absorbance can be computed via the natural logarithm of the reciprocal (inverse) of the tissue’s reflectance. In general, the inverted natural logarithm of the measured skin reflectance correlates to the existing local hemoglobin concentration. Thus, in the case of erythema, hemoglobin concentration could be used to quantify erythema severity (redness).

In practice, the detection of the tissue’s color change is primarily dependent on 1) the illumination conditions (angle of incidence, spectral profile, and spatial distribution), 2) the tissue optical properties (refractive index, scattering, and absorption), and 3) the detector spectral sensitivity attributes. Diffuse reflectance spectroscopy (DRS) measurement and digital photography are two widely utilized modalities for objectively quantifying skin erythema. Unfortunately, skin erythema quantification using DRS measurement is limited to a small region. Over and above, DRS measurement needs direct contact with the skin which may not be applicable in some cases like burned skin. Digital photography, although it overcomes DRS measurement limitations, is poor in physiologically interpreting skin color changes due to radiotherapy. Since Digital photography is dependent on measuring the back-reflected light within three wide bands: red, green, and blue. As such, digital photography is incapable of resolving tiny spectral differences within any of the bands. Accordingly, there is a room for technical improvement to overcome the limitations regarding both DRS measurement and digital photography. One candidate technique for this challenge is hyperspectral imaging (HSI).

HSI is a highly attractive optical imaging technique. Since HSI is favored by the simultaneous acquisition of spectral and spatial wealth of data regarding an imaged object. Advanced technologies in both sensor fabrication and optics production have promoted HSI to acquire data with high levels of spectral and spatial resolution [19] while contracting both the equipment size and cost [20]. The high-resolution spectral and spatial data, acquired by HSI, facilitates remote sensing of the tissue's contained molecules including chromophores. HSI, unlike DRS, enables the opportunity to investigate a sizable region of interest (ROI) in one scan while being contact-free [17], [21]–[26]. In contrast with digital photography, HSI provides profound spectral information for the investigated tissue's ROI. Thereby, HSI offers a chance to properly quantify the tissue's color changes due to sensing the apparent concentration of the local skin pigments [8], [27]–[32]. For verification purposes, a comprehensive study is conducted to examine the feasibility of HSI and data analysis for objectively quantifying radiation induced skin erythema. Based on the success of the current study, HSI can be used to address skin response in a step toward establishing a correlation with the individual relevant tumor. Hence, a chance is possible to early predict the tumor response, once the correlation is proved to be significant.

The novelty of this study is mainly and primarily, developing a new high throughput dual channel acousto-optic tunable filter (AOTF)-HSI configuration. The new configuration beats the current configurations with at least 1.5 times higher throughput. In a second place, the new HSI configuration was used to classify distinct erythema intensities induced artificially in an exploratory study. The classification technique, used in this study, is based on a newly adapted linear discriminant analysis (LDA) algorithm. Regarding erythema classification, HSI achieved higher performance in contrast with digital photography. In a third place, both the developed HSI equipment and the adapted LDA algorithm were used in a preliminary study to properly monitor and precisely quantify the temporal evolution of skin dermatitis in a real clinical environment. By this work done, the thesis added a novel supplementary technique, to objectively quantify skin erythema and also map its distribution within the ROI. The new standard aimed to have erythema; objectively quantified by remotely sensing the apparent hemoglobin concentration, and spatially mapped by image pixels classification. The success of the current study is supposed to be the trigger for the second phase of the project to be launched. As such, individuals' skin erythema data is ready to be correlated to their tumors response. To date, this work is the first one to use HSI to objectively quantify radiation dermatitis induced on cancer patients on daily basis. Since the skin is the targeted tissue in the work related to this thesis, it is briefly overviewed in the next section.

1.2 Human Skin

The skin is an imperative part of the human body. For a typical human weighing 70 kg, skin accounts for 3% of the total weight (~2100 gram) while covers an approximate area of 20,000 cm^2 [33]. The skin acts as an interface between the human body and the outside environment. This body interface permits controlled in and out transfers of minute particles, such as electrolytes, based on the needs. In conjunction with prior, the skin has other functions including thermoregulation, protection against severe environmental changes and the reduction of diseases by infection. In addition, the skin is considered as a wide area sensor which detects changes in the surroundings and conveys it to the brain. Besides, the skin is an indicator of human health [34]. As such, it is interesting to describe the skin structure.

1.2.1 Skin Anatomical Structure

Microscopically, the human skin is comprised of two main layers, from outside, the epidermis, and the dermis. The epidermis develops from the embryonic ectoderm, [33] while the dermis originates out of mesenchymal cells [33] as displayed in Figure 1-1 [35]. The human skin thickness varies with body location, where it ranges from 0.5 mm to 2 mm [36]. In structure basis, the skin epidermal layer has no blood vessels but has melanin. The epidermis melanin content is the main cause for the skin color. Hence, the skin colors of distinct races are due to variable amounts of melanin present in the epidermal layer. In addition, to being responsible for skin color, melanin is significantly absorbing the harmful ultra-violet (UV) spectra in sunlight. Hence, the more melanin is contained in the epidermis, the less suffering is endured from sunlight burning.

The skin dermis is the second and the last, major layer of the skin. This layer functions as a stress/strain release cushion against the surrounding physical pressure. It is dominantly occupied by blood capillaries, and in turn, the hemoglobin both parts (oxygenated & deoxygenated). Hemoglobin is an oxygen transporter to the surrounding tissues, where oxygen is self-contained in the red-blood cells. One hemoglobin molecule can bind up to four oxygen molecules. Oxygen loaded hemoglobin is termed oxyhemoglobin and has a dark red color. Once loaded oxygen is transported to tissues, oxyhemoglobin becomes deoxygenated and turns to be purple-blue in color. The oxygen-depleted hemoglobin or deoxyhemoglobin is named deoxyhemoglobin. The dermis layer sits on a tissue layer called hypodermis or subcutaneous layer. The hypodermis functions as an adhesive layer that allows the skin to adhere to both the musculature and skeletal tissues of the body, thereby, hypodermis is not considered a skin third layer [33], [34].

The skin contained pigments/ chromophores, melanin, and hemoglobin, are imperative components for optical investigation. The estimation of the concentration of both chromophores in skin is crucially important for skin health proper monitoring. As a result, an overview is given for skin major effective chromophores in the visible and near-infrared region.

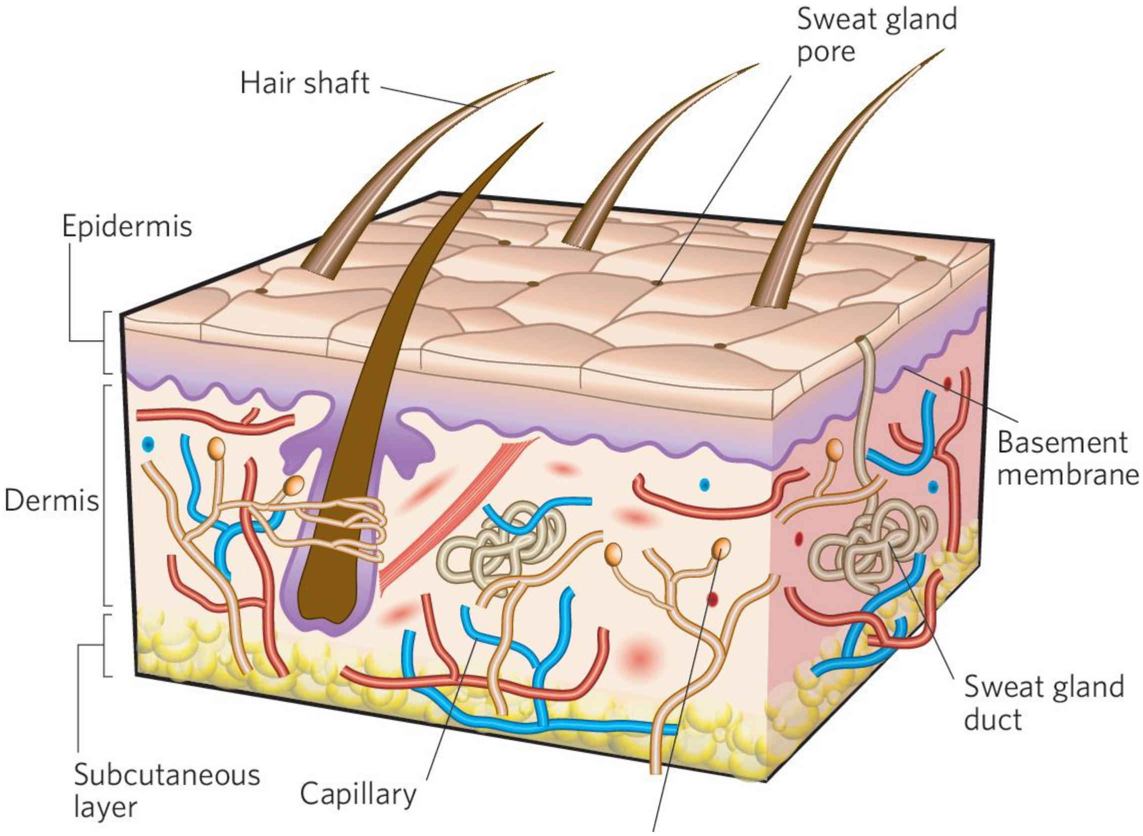

Figure 1-1: The structure of the skin is composed of two layers: (1) the epidermis and (2) the dermis. The skin is sitting on a subcutaneous layer that functions as an adhesive layer to connect the tissue to the body. The basement membrane is the boundary surface between the epidermis and the dermis. The epidermis melanin content is the cause of the skin color. The dermis layer contains the nourishing blood capillaries. [35]

1.2.2 Skin Chromophores

A chromophore is the part of a molecule that absorbs particular light due to an absorption spectrum. The skin has different chromophores encompassed in its structure. However, only three out of the skin chromophores, oxyhemoglobin, deoxyhemoglobin, and melanin, are dominating the skin reflectance spectra within 450:900 nm [37]. Each of the former chromophores has a specific wavelength dependent molar extinction coefficient measured in $cm^{-1}M^{-1}$ unit. For illustration, the formerly mentioned skin chromophores extinction coefficients spectral dependence along the range 450: 850 nm is displayed in Figure 1-2 [38]. In the figure, melanin shows a higher absorption in the ultraviolet (UV) which is approximately decaying in the visible (VIS) and near-infrared (NIR) spectral regions. Hence, an abundance of melanin in the epidermis accounts for the light loss in the early VIS region in skin reflectance measurements. Oxyhemoglobin, unlike melanin, is distinguished by two absorption peaks at 540 nm and 576 nm in the green region and absorption dip in the red region at ~686 nm. Deoxyhemoglobin, On the other hand, has a notable absorption peak at 560 nm in the green region, and an absorption dip in the NIR at ~736 nm. There are some wavelengths of matched absorption between hemoglobin both components called isosbestic points. The isosbestic wavelengths of oxygenated and deoxygenated hemoglobin components are 530 nm, 545 nm, 550 nm, 570 nm, 584 nm, and 797 nm. These wavelengths are used to measure oxygen saturation in the blood (StO_2) which ranges from 95% to 99% in a normal person.

As the skin is the body interface with the surrounding environment with all its disfavors, it is vulnerable to different diseases. One of the critical diseases that attack the skin is cancer. It is estimated that the main cause of skin cancer is the sunlight UV-A and UV-B exposure. Therefore, a tip is provided upon cancer.

1.2.3 Skin Cancer

Recent cancer statistics, in Canada, show that four out of ten Canadians might suffer from cancer during their lifetime and one out of four Canadians might succumb to cancer. To give a numerical example, it was expected in 2015 that approximately 200,000 people, only in Canada, will be added to the cancer patients list, where only 60.4% of them are expected to survive [39].

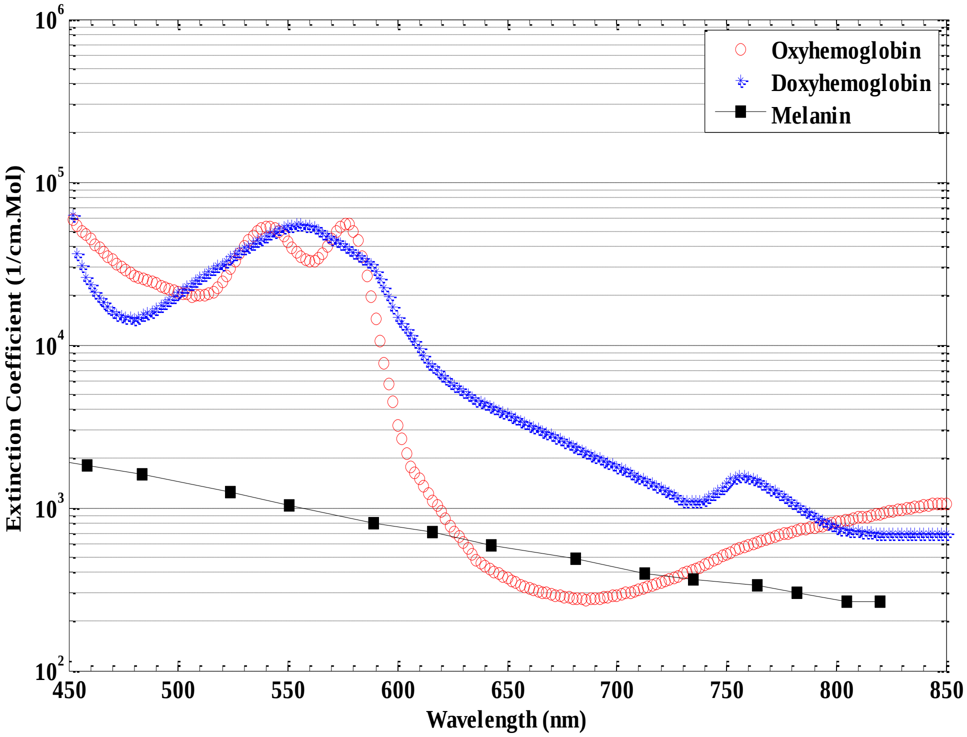

Figure 1-2: The molar extinction coefficients of human skin chromophores (Oxyhemoglobin, Deoxyhemoglobin, and Melanin) in the visible and early near infrared spectral region (450-850 nm) [38]. The melanin absorption is exponentially decreasing from the early visible toward the near-infrared region. The hemoglobin both parts show nonlinear wavelength dependent absorption behavior along the displayed region of spectra.

In gender basis, men are more likely to develop cancer than women, while in age basis, 89% of cancer patients are in their 6th decade of life [39]. As an example of one cancer type, skin cancer is reported to be the highest detected cancer in the American united states, where 3,000,000 people are estimated to contract skin cancer annually [40]. In general, skin cancer is classified into melanoma (MSC) and non-melanoma skin cancer (NMSC). Regarding NMSC, the Australians have the highest prevalence quota among all the whole world [41]. Canadian skin cancer estimates are not quite exact because NMSC cases including neoplasms of the skin (NOS), epithelial NOS, basal and squamous carcinomas are not included due to the lack of documentation in the majority of provincial and territorial cancer registries. There are rough estimates for Canadian NMSC established upon information from 4 Canadian provinces that new patients in 2015 are 78,300 people. It is of interest to know that MSC makes up less than 2% of all skin cancer cases [40]. Skin cancer is not majorly lethal but is annoying. Since it is a recurrent developing disease [41], [43]. The main risk factor, responsible for both skin cancer types, MSC, and NMSC is both the UV-A & UV-B radiation emitted by the sun, in addition to tanning beds and sunlamps [39], [42]. Therefore, a brief is introduced in the next section upon light-tissue interaction, focusing on light absorption and scattering.

1.3 Light-Tissue Interactions

1.3.1 Light Absorption

Atoms and molecules, by which tissue is structured, contain charged particles including electrons. The charge of molecules can be categorized according to its quantum energy into various levels. When a monochromatic light wave traverses a tissue, it loses a division of its energy due to the molecules' electronic clouds that oscillate at the light wave matching frequency. Consequently, a monochromatic light transmitted through a homogenous non-scattering medium material with intensity ($\boldsymbol{I}$), is attenuated relative to the original incident light intensity ($\boldsymbol{I_o}$). The light intensity attenuation is mainly dependent on the medium cross-sectional length ($\boldsymbol{l}$) and the molecules absorption coefficient ($\boldsymbol{\mu_a}$) governed by an exponential formula, shown in (1-1):

$$\boldsymbol{I = I_o\, e^{-\mu_a l}} \tag{1-1}$$

The absorption coefficient $\boldsymbol{\mu_a}$ is measured in cm^{-1} expressing the absorption probability for the propagating photon energy inside the medium cross section per unit length down to zero. A depiction of light absorption phenomena is shown in Figure 1-3. The opposite term to the light absorption is the light transmission which is expressed in transmission spectroscopy with the medium transmittance ($\boldsymbol{T}$) and is computed as in (1-2):

$$\boldsymbol{T = I/I_o} \tag{1-2}$$

The relevant expression of absorption in spectroscopy is named the absorbance ($\boldsymbol{A}$) which is equivalent to the inverse natural logarithm of transmittance as in (1-3):

$$\boldsymbol{A = ln\left(\frac{1}{T}\right) = ln\left(\frac{I_o}{I}\right)} \tag{1-3}$$

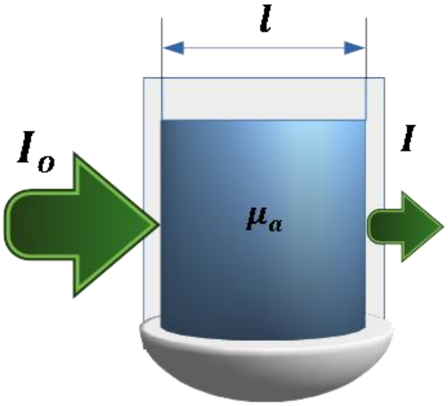

Figure 1-3: An illustration of the original light intensity ($\boldsymbol{I_o}$) attenuation by a homogenous non-scattering medium which has an absorption coefficient ($\boldsymbol{\mu_a}$) and a cross-sectional length ($\boldsymbol{l}$).

Replacing the right-hand side of (1-3) with its equivalent from (1-1), Beer's law can be reached as shown in (1-4).

$$\boldsymbol{A = \mu_a . l = \varepsilon_a . c . l} \tag{1-4}$$

The terms: $\boldsymbol{\varepsilon_a}$ is expressing the absorbent / chromophore extinction coefficient per mol (cm^{-1}M^{-1}), $\boldsymbol{c}$ is enunciating the molar concentration of the chromophore inside the attenuating medium and measured by (M) unit. Based on the previous equations, it is clear how Beer's law is important for quantifying chromophores encompassed in a medium. A clear example of Beer's law application is the estimation of hemoglobin concentration in a blood sample, by accounting for propagating light loss. However, absorption is not the only reason for light loss due to propagation in a medium.

1.3.2 Light Scattering

The scattering phenomenon is accounting for part of the propagating light intensity loss through a medium. In addition, it is explaining the directional deviation of the incident beam photons far from the original direction. This deviation occurs inside the propagation medium and is attributed to the non-homogenous refractive index space inside the medium. For human skin, suspended particles and fluctuating refractive index yield the deviation of the propagating photons from its original direction. In a hypothetical non-homogenous medium with no absorption, as simulated in Figure 1-4 (a), transmitted light intensity is attenuated in the original direction due to scattering and can be calculated by (1-5). The amount of scattered light is function of the scattering coefficient ($\boldsymbol{\mu_s}$), expressed in (cm^{-1}) unit. The scattering coefficient is dependent on the non homegenity of the medium (scattering particle cross section and concentration).

$$\boldsymbol{I = I_o\, e^{-\mu_s l}} \tag{1-5}$$

Fundamentally, a propagating light photon in a scattering medium experiences multiple scattering actions along its optical path length. For one scattering event, the direction of the traveling photon is deflected from its direction to a new one that is angularly separated by an angle ($\boldsymbol{\theta}$) as shown in Figure 1-4 (b).

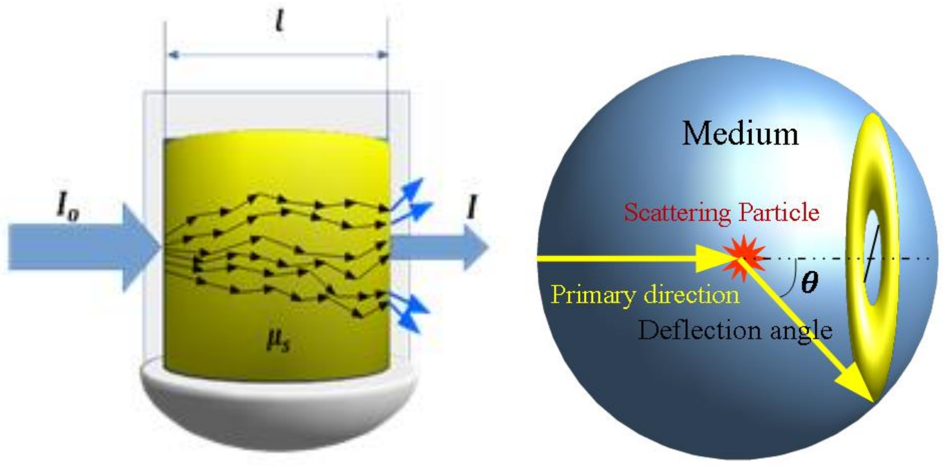

(a) (b)

Figure 1-4: (a) an illustration of light scattering in a hypothetical non-absorbing medium with a scattering coefficient ($\boldsymbol{\mu_s}$), however, it is suffering from intensity attenuation (b) Forward scattering simulation of a photon with a deflection angle (θ).

In an isotropic scattering medium, photons are scattered by an even distributed angular directions. For that reason, there is a coined term ($\boldsymbol{g}$) named anisotropy to express the mathematical average cosine of the photons scattering angles divided by the scattered light intensity associated with a specific scattering angle. The anisotropy $\boldsymbol{g}$ is a dimensionless parameter which ranges from [-1, 1]. The lowest value (-1) refers to the backward scattering medium, while the largest value (+1) refers to the forward scattering medium. The $\boldsymbol{g}$ term is mathematically calculated as follows [44]:

$$\boldsymbol{g} = \frac{\iint_{0}^{4\pi} \boldsymbol{I}(\boldsymbol{\theta})\boldsymbol{cos\theta}\ \boldsymbol{d\theta}}{\iint_{0}^{4\pi} \boldsymbol{I}(\boldsymbol{\theta})\ \boldsymbol{d\theta}} \tag{1-6}$$

It has been reported that human skin dermis layer is a highly forward scattering medium with a $\boldsymbol{g}$ factor ranges between [**0.74, 0.85**] value [45] in the spectral range of 415 nm-800nm. Mathematical models [46]–[49] for complex media like biological tissues employs, for simplicity, some assumptions to derive transport reduced coefficients for both scattering and attenuation. Based on these assumptions, reduced scattering coefficient ($\boldsymbol{\mu'_S}$) is calculated as shown in (1-7) and the total attenuation coefficient is calculated as shown in (1-8):

$$\boldsymbol{\mu'_S} = \boldsymbol{\mu_s}\,(\mathbf{1} - \boldsymbol{g}) \tag{1-7}$$

$$\boldsymbol{\mu_t} = \boldsymbol{\mu'_S} + \boldsymbol{\mu_a} \tag{1-8}$$

1.4 Contributions

The research project relevant to the thesis essentially aims to improve and increase the chances of cancer treatment based on radiotherapy. The adopted approach to treatment improvement is through an early estimation of individuals' irradiated tumor response and thus a close care of the patient can be taken. Toward this target, a hypothesis was proposed to study individuals irradiated skin reaction as assumed to be correlated with tumor's response. If this is the case, an individualized treatment plan might be altered based on the rapid skin reaction, compared with the tumor's response, to achieve a complete destruction cancer cells.

The primary phase of the project, which is relevant to the present thesis, aims to develop an objective optical technique for quantifying the acute skin reaction/ erythema induced due to radiotherapy. Based on the erythema assessment review, HSI was selected to be the candidate optical technique for quantifying erythema. Designating HSI for this challenge was not arbitrary, but to overcome few limitations of previously used techniques. Based on a review of current HSI technology, spectral scanning technique was selected. Accordingly, a dual channel AOTF-based-spectral scanning/ imaging spectrometer was developed. In terms of throughput, the developed dual channel imaging spectrometer was valued against the current single channel configurations. The evaluation exhibited higher performance of the developed imaging spectrometer an increment of 67% at least. Next to spectrometer calibration, characterization, and evaluation, it was used to classify artificially induced erythema, applying LDA, in an exploratory study on volunteers for. Afterward, a preliminary clinical study was conducted to check the feasibility of the developed HSI system to properly monitor, precisely quantify, and separately classify induced radiation dermatitis on cancer patients.

The onset of this study is a comprehensive review of skin erythema assessment techniques (**Chapter 2**). Based on the review, HSI was selected for objectively quantifying skin erythema. As such, HSI technology was expansively revised (**Chapter 3**). Following that, basic system requirements were outlined to be targeted through the process of developing the optical configuration of the new imaging spectrometer. In the design, a basic principle of microscopic imaging configuration innovated by John Oreopoulos, Peter Sinclair, and Richard Berman from Spectral Applied Research Company was adopted. This principle was modified toward the design and implementation of a wide field dual channel high throughput imaging spectrometer. Next to implementation, the spectrometer was fully calibrated, spatially and spectrally characterized. In addition, it is evaluated against a traditional corresponding LCTF system (**Chapter 4**).

Following hardware readiness, an exploratory study for artificially induced erythema on healthy volunteers is planned. The exploratory study, (**Chapter 5**), is an outcome of active co-operation between the thesis author, Lilian Doerwald, master student, Dr. Allison, previous alumni, and Ali Madooei, collaborating Ph.D. student. The workflow has the following sequence: HSI imaging, data acquisition, and primary image processing (detector noise reduction and normalization) were done by the thesis author, ground truth annotations were provided by Lilian Doerwald, image classification algorithm development by Ali Madooei, while classification was accomplished by the thesis author, with consultation of Ali Madooei, and Dr. Allison. A preliminary clinical study regarding objectively quantifying radiation dermatitis for skin cancer patients is explained in details in **Chapter 6**. HSI for radiation dermatitis objective assessment was accomplished as follows: HSI imaging, data acquisition, along with image processing were done by the thesis author, recruiting patients and ground truth annotations for the treated body parts were provided by Lilian Doerwald.

1.5 Thesis Organization

Chapter 1 describes, in the primary part, the motivation of the entire research project as well as the current thesis work specifically. Following the motivation, a brief overview of the human skin 1) anatomy, 2) major chromophores in the visible and near-infrared region and 3) cancer disease, is provided. Next to the skin brief, fundamental light absorption and scattering interactions are introduced. Finally, the chapter closes by the thesis contributions.

Chapter 2 reviews the existing methods related to skin erythema assessment. As a start, a brief description of skin erythema reaction is presented. In addition, erythema clinical origins that include cutaneous diseases and other non-disease causes are outlined. The existing techniques to assess skin erythema are described and discussed; going on a sequence from visual assessment, colorimetry, diffuse reflectance spectroscopy, digital imaging (RGB, polarized, fluorescence, spectral, MRI, and ultrasound), down to dielectric properties measurements. The strengths and weaknesses of each technique have been demonstrated. For quantitative evaluation of radiation dermatitis, HSI has been proposed as a possible candidate technique to come over reviewed methods limitations.

Chapter 3 provides an overview of HSI technology. It starts with HSI original definition and goes through its basic principle. Added to that, various HSI data acquisition schemes are illustrated. The chapter focuses on the distinct alternatives for hardware components involved in implementing an imaging spectrometer. More bias, in this chapter, exists toward AOTF-based-HSI as a feasible candidate for quantitative skin imaging. Over and above, a brief overview is given regarding the basic steps of spectral datacube analysis.

Chapter 4 presents the newly developed dual channel high throughput AOTF-HSI configuration. The chapter details the configuration design, performance characterization, and evaluation. Throughput characterization highlights the main advantage of the developed AOTF-HSI in comparison to the past single channel configurations as well as the liquid crystal tunable filter (LCTF) based technique.

Chapter 5 exhibits the feasibility of using the newly developed AOTF-HSI system to classify an artificially induced erythema, simulating radiation dermatitis, on healthy volunteers. For rating purposes, the developed AOTF-HSI was compared with digital color (RGB) imaging based on an originally developed LDA classification algorithm.

Chapter 6 presents the use of the high throughput AOTF-HSI and the LDA algorithm for monitoring radiation-induced dermatitis (erythema) on skin cancer patients. Erythema index, based on Dawson's model [19], was used to demonstrate the temporal development of radiation dermatitis through the course of radiotherapy treatment. Wilcoxon nonparametric two-tailed test was used to determine the time point at which significant change took place compared with the baseline measurement. Apparent hemoglobin concentration was estimated based on fitting the chromophore both parts extinction coefficients to the logarithm of the reciprocal reflection (LRR) data. LDA classification, once again, was used to rate the performance of the AOTF-HSI imaging spectrometer with digital RGB imaging in classifying radiation dermatitis.

Chapter 7 condignly presents the overall conclusions drawn out of the thesis work and proposes the future guidelines for the continuation phase of the contemporary research work.

References

[1] M. Garcia-Barros, F. Paris, C. Cordon-Cardo, D. Lyden, S. Rafii, A. Haimovitz-Friedman, Z. Fuks, and R. Kolesnick, "Tumor response to radiotherapy regulated by endothelial cell apoptosis," Science (80-.)., vol. 300, no. 5622, pp. 1155–1159, 2003.

[2] P. Wachsberger, R. Burd, and A. P. Dicker, "Tumor response to ionizing radiation combined with antiangiogenesis or vascular targeting agents: Exploring mechanisms of interaction," Clin. Cancer Res., vol. 9, no. 6, pp. 1957–1971, 2003.

[3] Z. Fuks and R. Kolesnick, “Engaging the vascular component of the tumor response,” Cancer Cell, vol. 8, no. 2, pp. 89–91, 2005.

[4] J. W. Denham, C. S. Hamilton, S. A. Simpson, P. M. Ostwald, M. O’Brien, T. Kron, D. J. Joseph, and K. B. G. Dear, “Factors influencing the degree of erythematous skin reactions in humans,” Radiother. Oncol., vol. 36, no. 2, pp. 107–120, 1995.

[5] G. N. Stamatas and N. Kollias, “In vivo documentation of cutaneous inflammation using spectral imaging.,” J. Biomed. Opt., vol. 12, no. 5, p. 051603, 2007.

[6] B. Jung, S. Kim, Y. Bae, H. Kang, Y. Lee, and J. S. Nelson, “Real-time measurement of skin erythema variation by negative compression: pilot study.,” J. Biomed. Opt., vol. 17, no. 8, pp. 081422–1, Aug. 2012.

[7] A. D. Ormerod, C. M. Dwyer, R. Weller, D. H. Cox, and R. Price, “A comparison of subjective and objective measures of reduction of psoriasis with the use of ultrasound, reflectance colorimetry, computerized video image analysis, and nitric oxide production,” J. Am. Acad. Dermatol., vol. 37, no. 1, pp. 51–57, 1997.

[8] M. Nischik and C. Forster, “Analysis of skin erythema using true-color images.,” IEEE Trans. Med. Imaging, vol. 16, no. 6, pp. 711–6, 1997.

[9] M. Baquie and B. Kasraee, “Discrimination between cutaneous pigmentation and erythema: Comparison of the skin colorimeters Dermacatch and Mexameter,” Ski. Res. Technol., vol. 20, no. 2, pp. 218–227, 2014.

[10] B. L. Diffey, R. J. Oliver, and P. M. Farr, “A portable instrument for quantifying erythema induced by ultraviolet radiation,” Br. J. Dermatol., vol. 111, no. 6, pp. 663–672, Dec. 1984.

[11] P. Simonen, C. Hamilton, S. Ferguson, P. Ostwald, M. O’Brien, P. O’Brien, M. Back, and J. Denham, “Do inflammatory processes contribute to radiation induced erythema observed in the skin of humans?,” Radiother. Oncol., vol. 46, no. 1, pp. 73–82, 1998.

[12] H. Hönigsmann, “Erythema and pigmentation,” Photodermatol. Photoimmunol. Photomed., vol. 18, pp. 75–81, 2002.

[13] K.-S. Suh, H.-J. Roh, S.-Y. Choi, Y.-S. Jeon, K.-S. Doh, J.-H. Bae, and S.-T. Kim, “A long-term evaluation of erythema and pigmentation induced by ultraviolet radiations of different wavelengths.,” Ski. Res. Technol., vol. 13, no. 4, pp. 360–8, 2007.

[14] S. D’haese, M. Van Roy, T. Bate, P. Bijdekerke, and V. Vinh-Hung, “Management of skin reactions during radiotherapy in Flanders (Belgium): a study of nursing practice before and after the introduction of a skin care protocol.,” Eur. J. Oncol.

Nurs., vol. 14, no. 5, pp. 367–372, 2010.

[15] J. Nyström, P. Geladi, B. Lindholm-Sethson, J. Rattfelt, A. C. Svensk, and L. Franzen, “Objective measurements of radiotherapy-induced erythema,” Ski. Res. Technol., vol. 10, no. 4, pp. 242–250, 2004.

[16] L. Diana L. Glennie, Joseph E. Hayward, Orest Z. Ostapiak, James Wright and T. J. F. Doerwald-Munoz, “Diffuse reflectance spectroscopy for monitoring erythema in head & neck intensity modulated radiation therapy,” J. Radiat. Oncol., 2014.

[17] D. Yohan, A. Kim, E. Korpela, S. Liu, C. Niu, B. C. Wilson, and L. C. Chin, “Quantitative monitoring of radiation induced skin toxicities in nude mice using optical biomarkers measured from diffuse optical reflectance spectroscopy.,” Biomed. Opt. Express, vol. 5, no. 5, pp. 1309–20, 2014.

[18] W. Maddocks-Jennings, J. M. Wilkinson, and D. Shillington, “Novel approaches to radiotherapy-induced skin reactions: A literature review,” Complement. Ther. Clin. Pract., vol. 11, no. 4, pp. 224–231, 2005.

[19] A. Bjorgan, M. Milanic, and L. L. Randeberg, “Estimation of skin optical parameters for real-time hyperspectral imaging applications.,” J. Biomed. Opt., vol. 19, no. 6, p. 066003, Jun. 2014.

[20] S. V. Panasyuk, S. Yang, D. V. Faller, D. Ngo, R. a. Lew, J. E. Freeman, and A. E. Rogers, “Medical hyperspectral imaging to facilitate residual tumor identification during surgery,” Cancer Biol. Ther., vol. 6, no. February 2015, pp. 439–446, 2007.

[21] J. B. Dawson, D. J. Barker, D. J. Ellis, E. Grassam, J. a Cotterill, G. W. Fisher, and J. W. Feather, “A theoretical and experimental study of light absorption and scattering by in vivo skin.,” Phys. Med. Biol., vol. 25, no. 4, pp. 695–709, 1980.

[22] S. Wan, J. a Parrish, and K. F. Jaenicke, “Quantitative evaluation of ultraviolet induced erythema.,” Photochem. Photobiol., vol. 37, no. 6, pp. 643–648, 1983.

[23] G. N. Stamatas, B. Z. Zmudzka, N. Kollias, and J. Z. Beer, “In vivo measurement of skin erythema and pigmentation: new means of implementation of diffuse reflectance spectroscopy with a commercial instrument.,” Br. J. Dermatol., vol. 159, no. 3, pp. 683–90, 2008.

[24] N. Kollias, I. Seo, and P. R. Bargo, “Interpreting diffuse reflectance for in vivo skin reactions in terms of chromophores,” J. Biophotonics, vol. 3, no. 1–2, pp. 15–24, 2010.

[25] K. Vishwanath, D. Klein, K. Chang, T. Schroeder, M. W. Dewhirst, and N. Ramanujam, “Quantitative optical spectroscopy can identify long-term local tumor control in irradiated murine head and neck xenografts.,” J. Biomed. Opt., vol. 14, no. 5, p. 054051, 2009.

[26] G. V. G. Baranoski, T. F. Chen, B. W. Kimmel, E. Miranda, and D. Yim, "On the noninvasive optical monitoring and differentiation of methemoglobinemia and sulfhemoglobinemia.," J. Biomed. Opt., vol. 17, no. 9, p. 97005, 2012.

[27] D. Ratner, C. O. Thomas, and D. Bickers, "The uses of digital photography in dermatology," J. Am. Acad. Dermatol., vol. 41, no. 5 I, pp. 749–756, 1999.

[28] M. Setaro and A. Sparavigna, "Quantification of erythema using digital camera and computer-based colour image analysis: a multicentre study.," Skin Res. Technol., vol. 8, no. 2, pp. 84–8, 2002.

[29] S. G. Coelho, S. A. Miller, B. Z. Zmudzka, and J. Z. Beer, "Quantification of UV-Induced Erythema and Pigmentation Using Computer-Assisted Digital Image Evaluation," Photochem. Photobiol., vol. 82, no. 3, pp. 651–655, 2006.

[30] Y. Bae and B. Jung, "Digital photographic imaging system for the evaluation of various facial skin lesions.," Conf. Proc. IEEE Eng. Med. Biol. Soc., vol. 2008, pp. 4032–4, 2008.

[31] W. K. Witmer and P. J. Lebovitz, "Clinical Photography in the Dermatology Practice," Semin. Cutan. Med. Surg., vol. 31, no. 3, pp. 191–199, 2012.

[32] A. Raina, R. Hennessy, M. Rains, J. Allred, D. Diven, and M. K. Markey, "Objective measurement of erythema in psoriasis using digital color photography with color calibration," in Annual International Conference of the IEEE Engineering in Medicine and Biology Society., 2014, vol. 2014, pp. 3333–3336.

[33] R. I. J . W . HOPEWELL (CRC Normal Tissue Radiobiology Research Group and H. (University of Oxford), The Churchill Hospital, "The skin : its structure and response to ionizing radiation," INT. J. RADIAT. BIOL ., vol. 57, no. 4, pp. 751–773, 1990.

[34] T. Chen, "Hyperspectral Imaging for the Remote Sensing of Blood Oxygenation and Emotions," 2011.

[35] S. MacNeil, "Progress and opportunities for tissue-engineered skin.," Nature, vol. 445, no. 7130, pp. 874–80, 2007.

[36] L. Y. and H. K., "Skin thickness of Korean adults," Surg. Radiol. Anat., vol. 24, no. 3–4, pp. 183–189, 2002.

[37] G. Zonios and A. Dimou, "Light scattering spectroscopy of human skin in vivo.," Opt. Express, vol. 17, no. 3, pp. 1256–1267, 2009.

[38] S. P. (Oregon M. L. Center), "Optical Absorption of Hemoglobin," 1999. [Online]. Available: http://omlc.org/spectra/hemoglobin/summary.html. [Accessed: 01-Nov-2015].

[39] C. C. S. Advisory and C. on C. Statistics, “Predictions of the future burden of cancer in Canada,” 2015.

[40] A. C. Society, “Cancer Facts and Figures 2015,” 2015.

[41] M. Veness and S. Richards, “Role of modern radiotherapy in treating skin cancer.,” Australas. J. Dermatol., vol. 44, no. 3, pp. 159–166; quiz 167–168, 2003.

[42] J. Maddams, M. Utley, and H. Møller, “Projections of cancer prevalence in the United Kingdom, 2010–2040,” Br. J. Cancer, vol. 107, no. 7, pp. 1195–1202, 2012.

[43] K. J. Zuzak, M. T. Gladwin, R. O. C. Iii, I. W. Levin, J. Karel, and R. O. Can-, “Imaging hemoglobin oxygen saturation in sickle cell disease patients using noninvasive visible reflectance hyperspectral techniques : effects of nitric oxide,” vol. 0510, pp. 1183–1189, 2003.

[44] E. S. Thiele and R. H. French, “Computation of Light Scattering by Anisotropic Spheres of Rutile Titania,” Adv. Mater., vol. 10, no. 15, pp. 1271–1276, 1998.

[45] V. V Tuchin, Tissue optics: light scattering methods and instruments for medical diagnosis. 2007.

[46] T. J. Farrell, “A diffusion theory model of spatially resolved, steady-state diffuse reflectance for the noninvasive determination of tissue optical properties in vivo,” *Med. Phys.*, vol. 19, no. 4, p. 879, 1992.

[47] B. C. Wilson, “A Monte Carlo model for the absorption and flux distributions of light in tissue,” *Med. Phys.*, vol. 10, no. 6, p. 824, 1983.

[48] S. T. Flock, M. S. Patterson, B. C. Wilson, and D. R. Wyman, “Monte Carlo modeling of light propagation in highly scattering tissue--I: Model predictions and comparison with diffusion theory.,” *IEEE Trans. Biomed. Eng.*, vol. 36, no. 12, pp. 1162–8, 1989.

[49] L. Yang and B. Kruse, “Revised Kubelka Munk theory. I. Theory and application,” *J. Opt. Soc. Am.*, vol. 21, no. 10, pp. 1933–1941, 2004.

Chapter 2: Skin Erythema and related Assessment Techniques

2.1 Skin Erythema

Skin erythema, or flare, is the reddening reaction of the skin as a result of external stimulus [1] or immunologically mediated cell reaction with/out hypersensitivity toward microbe [2], or viral infections [3]. The flare size depends on multiple parameters, for instance, the distribution of the neural fibers and vascularization of the stimulus region. Moreover, the strength and the essence of the stimulus are dominating factors by which the peak size of the flare is dependent. Normally, the flair's peak intensity is reached shortly after the stimulus onset unless the flare is a result of an accumulative process (such as radiotherapy in cancer treatments). Bruce and Lewis attributed the flare reaction to the axon reflex [4], [5]. Simply put, if a pernicious provocation occurred to the human skin's afferent nerve, it would alert skin fibers. The fibers, in turn, would respond to alarms in the format of action potentials sent mainly to the spinal cord and then expanded through the complementary axons. The consequence of the former scenario is the dispensation of neuropeptides like P /calcitonin gene-related peptide (CGRP) which causes a vasodilation and thereby skin erythema turns up [1]. In a second interpretation, skin erythema is described as an inflammatory cutaneous interaction associated with some cutaneous diseases such as acne, psoriasis, melasma, as well as fever. In severe skin reaction cases, skin erythema yields superficial blisters [6]–[8]. The formed blisters are relevant to wet desquamation which occurs due to irradiation with distinct electromagnetic waves (EMW).

EMW, be it ultraviolet (UV), visible (VIS), or infrared (IR) waves, is one of the erythema triggers. Each of the formerly mentioned spectral bands has an exposure threshold or 'minimal erythema dose' (MED) [7], [9]; if reached, skin erythema is directly induced [10]. An intriguing example of MED is the transient flush erythema which takes place rapidly with fair skin people in the summer upon exposure to sunlight. Other people with different skin types may show the same effect, but a couple of hours or one day later [10]. Excluding EMW exposure, physical pressure [11], skin ulcers [12], [13], application of cosmetic/medical topical agents and electrical stimulation [1], [14]–[17] are all possible causes for skin erythema. Furthermore, burns induce erythema around its scars [18].

Radiation dermatitis [19]–[23] is typically an equivalent term to radiotherapy-induced erythema. In this case, erythema is a cancer radiotherapy treatment linked side effect. The dermatitis reaction is interpreted as a skin response to the damaging effect regarding the basal cells present in the epidermal layer. Toward reducing the extent of damage, a rapid cell compensation goes on from skin deeper layers to replace destructed ones [24]. There is no clue of fixed dose-intensity to be the knife-cut threshold for triggering radiation dermatitis. However, there are few patients' parameters including skin type, age, and tumor specifications are highly dominating dermatitis conduction. [25], [19]. Despite dose-intensity ambiguity, there is a rough prerequisite dose threshold for skin erythema, where an extra dosage yields skin reactions progression [25]. It is of interest to know, permanent skin color change is likely to occur in the case of intensity-modulated radiation therapy (IMRT) due to the reduction of the melanocytes in the irradiated region [24],[22],[25],[29]. To put it briefly, radiation dermatitis deserves systematic assessment and monitoring with an objective technique, since it represents an imperative clinical flag not only for the skin's health and the patient's cosmetic style but also for treatment continuity such as radiotherapy cancer treatment [27].

The purpose of this chapter is to review the modalities that were utilized for skin erythema assessment. The review will produce a solid background and a launching base for developing new quantitative while being objective efficient erythema assessment techniques.

2.2 Assessment techniques

The ultimate goal for an ideal skin erythema assessment modality is to objectively quantify the skin reaction without the need for a biopsy or skin contact, for instance by generating a real time graded intensity map of skin erythema. Moreover, this modality should be high efficiency rated, size miniaturized, simply operated, and cost effective. In this section, a review of the procedures that have been employed, to date, to evaluate, grade or detect skin erythema in the literature is presented. The review begins with visual assessment (VA), which is the gold standard for skin erythema evaluation. Following VA, common optical modalities used for skin erythema assessment are introduced. However being uncommon, other erythema assessment modalities are highlighted in section 2.3. Next to erythema assessment modalities, different concepts of computing the erythema index are overviewed.

2.2.1 Visual Assessment

VA is the original [28] and the simplest modality for skin erythema assessment. VA's simplicity is a result of its tool/ equipment-free dependency. However, it depends on an experienced radiotherapist who provides a grade or score to distinct intensities of skin erythema [29]. The provided grade is one of a predetermined ordinal scale of grades. The erythema ordinal scale assigns a grade for distinct erythema intensities in a qualitative manner. There are various erythema scales depending on the precision between the minimum and the maximum erythema intensities. For example, there are three [29], four [30], [31], and ten [28] steps erythema scales were used earlier. One exemplary model of erythema scale is shown in Table 2-1 [28]. Although these scales are useful for rapid assessment, it lacks linear transitions between equidistant steps and thus it may miss or overact with skin erythema distinct intensities [32]. In addition to erythema scales nonlinearity, VA suffers from subjectivity, intra-observer variability dependence, and incapability of precise color communication. Despite all VA's mentioned disfavors, it is still heavily used in clinics compared to objectively engineered solutions. Since VA is (1) fast; which helps the clinician to serve more patients in a shorter time (2) simple; since clinicians do not need to worry about operating/ adjusting any equipment and (3) well-matched with the clinical environment; since the clinician can easily move back and forth from a room to the other to check different patients [28], [30].

Table 2-1: Example of an ordinal grading scale used for skin erythema visual assessment divided into 10 different qualitative reactions [78].

Grade	Erythematous reaction
0	No reaction
1	Marginal reaction
2	Slight perceptible erythema
3	A greater than slight reaction which is not sufficient to be classed as distinct
4	Distinct erythema
5	A greater than distinct reaction which is insufficient to be classed as well developed
6	Well developed, possibly spreading erythema
7	A greater reaction which is not sufficient to be classed as strong
8	Strong, deep erythema which may extend beyond the treatment site
9	A more intense reaction than above

2.2.2 Colorimetry Assessment

The color of an object is generally dependent on its surface optical properties and particularly on its spectral absorbance. In fact, the visually recognized color is simply the complementary wavelength to the absorbed spectrum in the case of polychromatic illumination. Two major parameters dominate the sensed color of any object; absorption and scattering. In terms of absorption, Beer-Lambert's law (BLL) mathematically models the light absorption. BLL states that a monochromatic light intensity passing through a cuvette with a solvent's extinction coefficient ($\boldsymbol{\alpha}$) and concentration (C), will endure an exponential intensity loss along the cuvette length (L) as shown in (2-1).

$$\boldsymbol{A = log(\frac{I_o}{I}) = \alpha CL} \tag{2-1}$$

Concerning scattering, the common method to measure colors optically is via computing the object's reflectance. The surface reflectance of objects varies according to the properties of the object's surface (highly polished like mirrors, glossy, semigloss, or diffuse), along with the used illumination spectra and angle of incidence. Divergent reflectance outcomes come out when a beam of light is incident on unlike surfaces as shown in Figure 2-1 [33]. There are few ways utilized to detect the object's surface reflectance and map it with its perceived color including, but not limited to, visual colorimeters, and spectrocolorimeters.

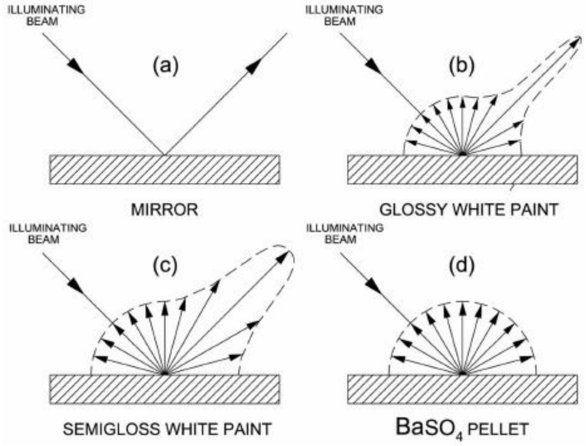

Figure 2-1: An illustration of the divergent reflection results upon an incident light beam on four categories of object's surfaces while preserving the same illumination conditions. [33]

The visual colorimeter (VC) is a circular plate made of a white standard material of high reflectance. The plate is divided into two halves. One-half of the VC plate is illuminated by three adjustable light sources spanning the color space. The second half plate of VC is illuminated by white polychromatic light. The formerly mention half plate is used to position the object under chromatic investigation. VC basically operates by fine tuning the three light sources intensities which illuminate the free half plate till well-matching occurs between the two plate halves based on visual judgment. VC has good attributes such as being: inexpensive, simply operated, and useful in distinguishing between real colors and turbidity. On the other side, it suffers from less reliability due to the variation in illumination intensity, coarse color scaling (resolution loss), and the operator's subjective judgment.[33]

Spectrocolorimeters, far from human subjectivity, are measuring the object's reflected light within specific bands through the visible spectrum. To compute the object's reflectance, a white standard target is required to establish a reference measurement. Both the object and the white reference are illuminated with a polychromatic light source such as xenon, tungsten-halogen, or white light emitting diode (LED). Xenon source has fair output over the entire ultraviolet, visible, and near-infrared spectrum. Tungsten-halogen, unlike xenon, has low output in the ultraviolet, and the blue regions which yields relatively small signal to noise ratio (SNR) in detection. White LED, dissimilar for both former sources, is limited to the visible region with low output in the green spectra. Spectrocolorimeter measures the object's reflected light intensity ($\boldsymbol{L(\lambda)}$), at specific wavelengths, which is divided by the corresponding ones regarding the white target reflected light ($\boldsymbol{L_W(\lambda)}$). In addition to the object and the white reference, a black reference ($\boldsymbol{L_B(\lambda)}$) is also utilized to eliminate the offset noise due to detection instrumentation. This black reference is made through light trap volume with one hole that allows its black walls observation. Based on the three formerly mentioned measurements, the object's spectral reflectance ρ(λ) is calculated as follows:

$$\boldsymbol{\rho(\lambda) = (\frac{[L(\lambda) - L_B(\lambda)]}{[L_W(\lambda) - L_B(\lambda)]})\rho_{ref}(\lambda)} \tag{2-2}$$

The computed spectral reflectance is utilized in combination with the color matching functions to obtain the matching tristimulus coefficients regarding one applicable color space such as CIE1931.

Regarding human skin, color is a critical informative descriptor for both the clinical and the research purposes [34]–[37]. However, the acquisition and communication of color information visually are limited by the time dependency, the describing language, and the means of communication. For instance, although the human eye is capable of distinguishing between an enormous amount of neighboring colors [38], linguistic description is far from the satisfactory precision of the distinct color tones. The lack of color descriptors to communicate the tissue color tones in a quantitative manner was the motivation to use the engineered colorimetry tools/ instruments to detect, analyze and archive distinct skin color changes.

Color standards are well-known tools used to assess the progression of some skin diseases associated with an erythematous reaction. One of the primary standards used for this purpose was red colored papers which have graded red intensities. A direct application of the red papers was to demarcate the skin erythema induced due to UV dose exposure. the use of the colored papers enabled the generation of UV dose–response curves [39]. However, red papers are not durable; as it wears easily nor reliable; since it was hard to be typically reproduced. To overcome red papers difficulties, red photographic filters were the alternative. Since photographic filters are reliable and relatively lasting longer. Unfortunately, neither the red papers nor filters were sufficiently robust to quantitatively grade the skin erythema. Thereby, both standards went out of use rapidly. As a result, the research was directed toward developing other reliable and inexpensive color scale that is appropriate to use.

Toward this direction, Taylor hyperpigmentation scale (THS) was developed. THS is based on an extensively conducted statistical study regarding different skin colors. The study employed a great number of people of different backgrounds to obtain maximum skin color divergence [40]. Consequently, THS ended up with 15 skin hue representative cards. Each card is divided into ten graded pigmented steps. As such, THS has a total of 150 different colors that are expected to well-match all skin types with a confidence of 95% [40], [41]. Other than THS, a Japanese group developed a new color tone scale based on Munsell color system [42]. The Japanese color tone was printed on flexible plastic bars. Each bar is divided into a number, >10, of color tones. The entire set of bars was used in a clinical study to assess the laser treatment of solar lentigo. The study was performed over approximately one year where it recruited eighty-one Japanese female patients [43]. Skin color tone matching, by the former color scales, is achieved in two steps. The first step is identifying the best hue that corresponds to the participant's skin color. The second step is scanning the identified hue-card to find the best matching hyperpigmented tone of the subject's skin as shown in Figure 2-2 [43].

The advantage of the former color scales is the simplicity of operation and the potential quantification of skin color change which, in turn, facilitates easy data communication and archiving. Although color scales, or color-order systems [44], increased the span of possible colors to describe, it is still far from being objective and vision acuity independent. Once again, color scales are vulnerable to wearing and thus making the color tones less discernible. Hence, there was a need to depend on technical solutions to function as robust colorimeters to come over subjectivity and attain more reliable outcomes.

In order to overcome the color charts' problems, systemic colorimeter devices were in demand. The colorimeter device function is to identify the tissue's apparent color using a 3-dimensional color space. One common color space is the standard CIELab (Commission Internationale de l'Eclairage), which is represented by three axes [45]. The first axis is the grey-scale and symboled by L*. The gray axis is divided into 100 divisions; starting from 0, (complete darkness), and ending at 100 (bright white). The second CIELab axis is the red-green one and symboled by a*. It has the red on the positive side and the green on the negative one. The third axis is the yellow-blue one and symboled by b*. It has the yellow on the positive side and the blue on the negative side.

Both CIELab axes a* and b* are, in principle, relevant to Hering's opponent color theory [46], which attributes the human vision to red-green, and yellow-blue channels. In the CIELab color system, the hue angle h^o is defined as the relevant psychometric of the visually perceived property of hue such as red, green, and magenta and calculated as in (2-3). Moreover, the perceived color is not only purely hue level but also is influenced by the color saturation. The color saturation is expressed by the displacement on the L* axis and termed as C, known also as chroma in the CIE. Chroma is calculated as in (2-4).

$$\boldsymbol{h^o = arctan(\frac{b^*}{a^*})} \tag{2-3}$$

$$\boldsymbol{C = \sqrt{(a^*)^2 + (b^*)^2}} \tag{2-4}$$

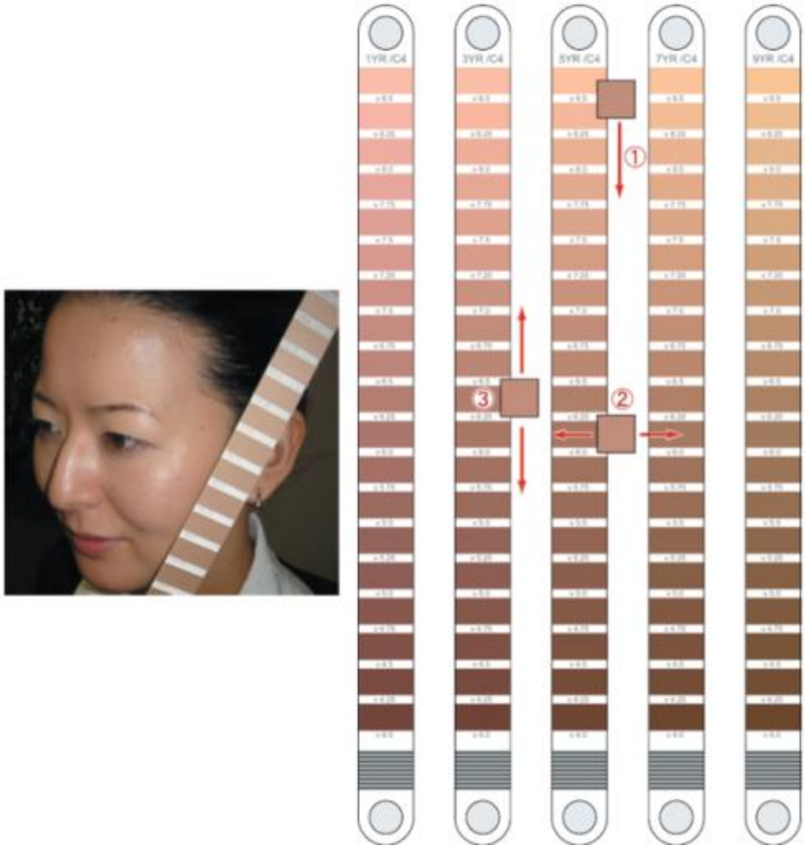

Figure 2-2: The process of allocating a color tone for human face commences with finding the closest possible match through the following steps, (1), a rough estimate is primarily determined by the operator and then (2) more precise pigmentation color is selected within left, right move, (3) followed by up and down adjustments. [43]

In general, the tissue perceived color information, in CIELab, is dependent on three factors, 1) the illumination characteristics, 2) the light modulation by the tissue under test, and 3) the human visual attributes. Accordingly, the CIELab standard color system delineates these three factors strictly. First, the CIELab specifies the standard illumination for color measurements. The spectral distribution of such standards are published in tabulated formats [45], [47], [33]. Second, the CIE system specified a standard for the spectrometer that is applicable to measure the light modulation in the range of the VIS region [47]. Third, the human visual system was investigated and the three color matching functions: $\bar{x}$, $\bar{y}$, and $\bar{z}$ were determined. The reason for being three is; in terms of color interpretation, human vision is a trichromatic system [33], [48], [49]. The CIELab color system is a convenient, robust way for communicating color information; moreover, it is able to measure the differences between perceived tissue colors. The difference (ΔE) between two colors is represented by the square root of the displacement of both colors in $L^*a^*b^*$ coordinates as shown in (2-5) [45].

$$\Delta \boldsymbol{E} = [(\Delta \boldsymbol{L}^*)^{\mathbf{2}} + (\Delta \boldsymbol{a}^*)^{\mathbf{2}} + (\Delta \boldsymbol{b}^*)^{\mathbf{2}}]^{\mathbf{1}/\mathbf{2}} \qquad \textbf{(2-5)}$$

2.2.3 Spectra-based-Assessment

Spectral reflectance concept has been involved in the objective assessment of the skin color for approximately six decades [41]. This concept was the basis for developing significant, robust, reliable, and compact instruments such as the tristimulus instruments and the narrow-band spectrometers. The tristimulus instruments, such as Minolta chromameter, took the name after since it depends mainly on the measurement of reflected light through three wavelength channels in their operation. Narrow-band spectrometers, unlike tristimulus instruments, such as the Dermaspectrometer, erythema meter, and Mexameter are measuring reflected light through specific-bands, mainly red and green.

Tristimulus Colorimetry instruments were originally developed to objectively and reliably measure color information in a manner similar to the human visual system. Simply, the method of measurement is illuminating the tissue under investigation with a polychromatic light source and detects the back-reflected intensity through three separate spectral channels. One or two-dimensional array of photodiodes are used for light detection. One of the prevalent tristimulus instruments is the Minolta chromameter [18], [50], [38], [51]–[55]. Minolta instrument frequently illuminates the object using a xenon light source and collects the diffusely back-reflected intensity at three central wavelength bands: 450, 560, and 600 nm. The instrument output is elucidated based on a mapping transformation to a standard color system such as CIELab. Minolta chromameter earned a good reputation in color measurement due to its robustness and repeatability [53]. In practice, Minolta chromameter output was valued to visual grading in a previous study for investigating the skin blanching onset when applying topical corticosteroid agent on volunteers for three subsequent days. The result of the evaluation exhibited superior performance of Minolta chromameter in distinguishing the blanching effect due to the applied agent. As the L* axis, but not the a* axis, was the most sensitive parameter in discriminating the skin blanching as shown in Figure 2-3 **[**52**]**.

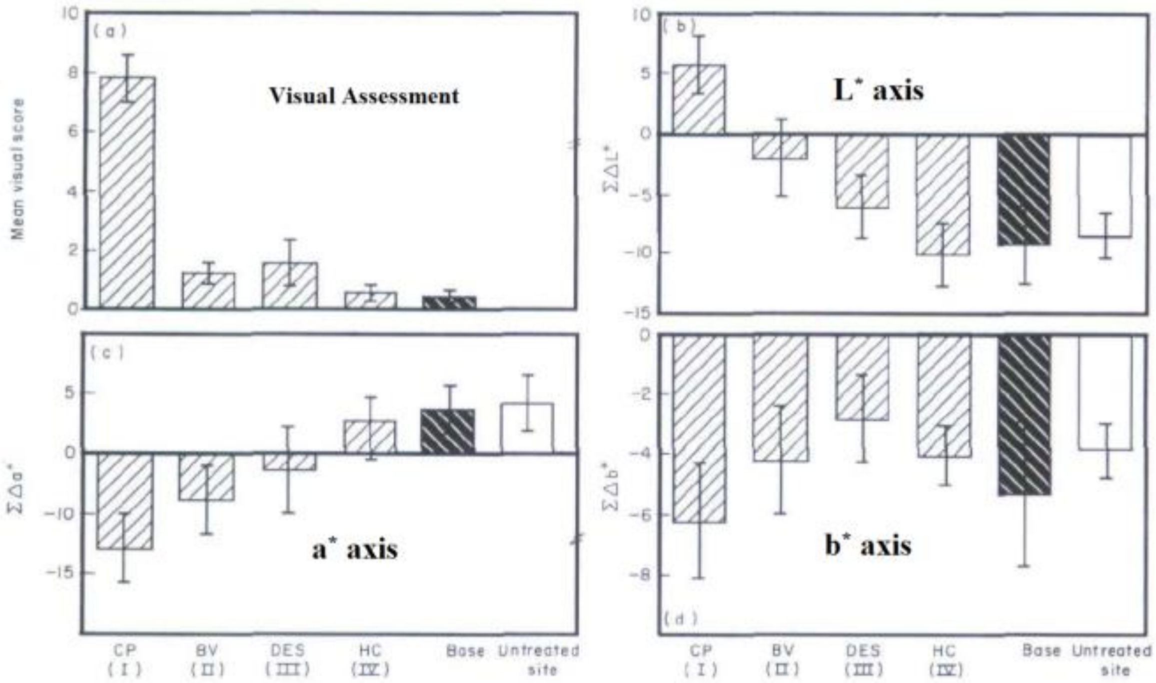

Figure 2-3: (a) Algebraic sum (mean ± std) for the visual assessment score, (b) the gray scale values $\sum \Delta \boldsymbol{L}^*$, (c) the red-green values $\sum \Delta \boldsymbol{a}^*$, and (d) the yellow-blue values $\sum \Delta \boldsymbol{b}^*$ for the skin color change induced by applying a topical corticosteroid agent using the Minolta Chromameter [51].

The Chromameter achieved the goal of providing an objective method and relatively cheap instrumentation for skin color measurement. However, these instruments need systemic calibration for each time before they are reused. Hence, an overhead time is required to prepare for the instrument operation. Thereby, it was not practical to become a bench-top instrument nor convenient to use for a clinician in the daily routine

Narrow-band spectrometers are based on the fact that the green and red portions of the visible spectrum suffice to estimate the skin visible pigmentation, hemoglobin, and melanin, in a quantitative approach [56]–[60]. Based on this fact, the skin redness/ erythema severity is quantitatively estimated by subtracting the melanin optical absorbance out of the green filter absorbance [41]. However, other studies interpreted erythema as a consequence of superficial microcirculation vasodilation and thus, it is less dependent on the epidermis melanin content [61], [62].

In conjunction with prior, a study reported the development of a portable device can be used for skin erythema measurement called the erythema meter [9], [63]. The basic principle of operation for the erythema meter is measuring the skin's back-reflected light within the red and the green spectral bands. The measured back reflected light out of a tissue allows a rough estimate of the skin's hemoglobin content. The hemoglobin content estimation is established based on calculating the erythema index (EI), as displayed in (2-6).

$$\boldsymbol{EI = \ log_{10}(\frac{Back\,reflected\,red\,light\,intensity}{Back\,reflected\,green\,light\,intensity})} \tag{2-6}$$

In conjunction with prior, two more common devices are using the narrow-band principle; the Dermaspectrometer [30], [54], and the Mexameter [64], [59]. The Dermaspectrometer device integrates two light-emitting diodes (LED); one emits at 568 nm (green band) and the other emits at 655 nm (red band) to illuminate the targeted skin ROI [56]. The skin's reflected intensities at the two former wavelengths are detected and analyzed to provide both the melanin and the erythema indices. The Mexameter, unlike the Dermaspectrometer, illumination part is composed of 16 integrated LED sources combined in one probe emitting at three different bands; green (568 nm), red (660 nm), along with near-infrared (NIR) (880 nm) bands. The Mexameter computes the skin's melanin index (MI) based on two bands; the red and the NIR back reflected light measurements. While the erythema index is computed based on the green and the red back reflected light as demonstrated in (2-7), and (2-8) [58], [65]:

$$\boldsymbol{MI = \frac{500}{log\,5 * [log({}^{NIR_{refl}}\!/\!{}_{Red_{refl}}) + \ log\,5]}} \tag{2-7}$$

$$\boldsymbol{EI = \frac{500}{log\,5 * [log({}^{Red_{refl}}\!/\!{}_{Green_{refl}}) + \ log\,5]}} \tag{2-8}$$

When it comes down to it, the Mexameter, shown in Figure 2-4 [66], is more sophisticated in contrast with the Dermaspectrometer. Since that, the Mexameter has a tolerance of ± 5% provided that three readings are obtained [41]. The Mexameter is commonly utilized for cosmetic and pharmaceutical cutaneous research work. However, it was recently approved to be employed in skin melasma investigation [64] and skin toxicity diagnosis along with delineating melanin content variation due to radiotherapy [8], [66].

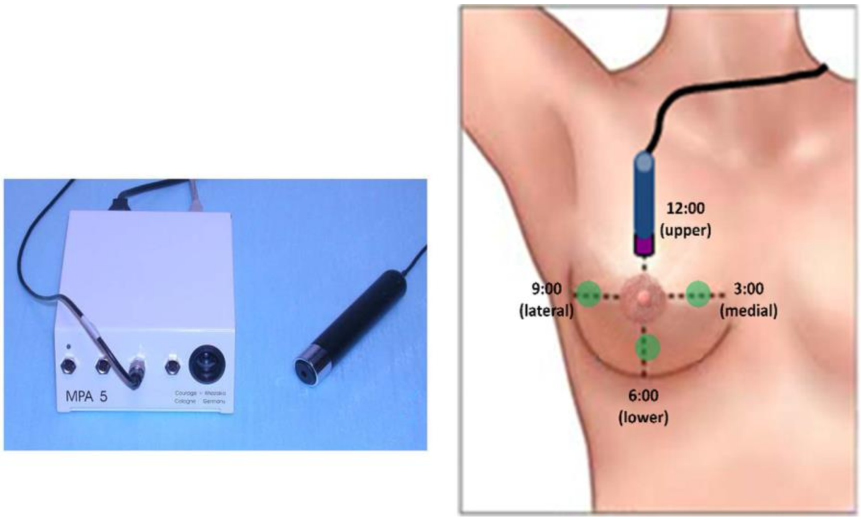

(a) (b)

Figure 2-4: (a) The Mexameter (MX) instrument. MX is equipped with a circular probe of 5 mm diameter and 20 mm^2 surface area. (b) MX was used to measure the skin reflectance in order to quantitatively assess the skin toxicity due to breast cancer radiotherapy treatment. [66]

The narrow-band principle is continuously developing. For instance, a real-time measurement of an artificially induced skin erythema was realized in a modern study [11]. The study succeeded to use an RGB sensor to identify and measure both the skin's erythematous response due to instantaneous applied negative pressure along with the temporal evolution of erythema as a result of constant negative pressure. In sum, the narrow-band devices are able to provide successful figures for the two skin pigmentation indices: the erythema and the melanin. Although the considerable performance of the narrow-band instruments, it lacks the potential to fully interpret the inherent changes of the skin color. Hence, the measurement of the skin's total diffuse reflectance was the approach to realize this interpretation.

Diffuse reflectance spectroscopy (DRS) systems are involved in the measurement of the total diffusely back-reflected light out of an illuminated object. Regarding human skin, the total diffusely reflected light is the summation of all the back-reflected light excluding the specular reflected light where the latter accounts for only 4:7 % of the total reflected light [41]. Specular reflection mainly probes the skin surface information such as the refractive index while conveys less information upon the underlying cutaneous structure. Oppositely, the diffusely back-reflected light conducts information upon the skin layers beneath the surface such as vascularization and pigments. Since the diffuse back-reflected light takes a pass inside the tissue before it bounces back. DRS measurements were accomplished using both time domain [67], [68], and frequency domain [69], [70] based techniques. Divergent skin symptoms associated with diseases were looked into using

DRS in a number of studies [17], [20], [31], [71]–[76]. DRS systems were implemented utilizing diverse optical configurations including the integrating sphere (IS)-based DRS [77]–[80], the spatially resolved steady-state DRS [81]–[83]. To get more in depth, the IS and the spatially resolved based DRS techniques use continuous-wave (CW) illumination sources and a spectrophotometer for measuring the back-reflected spectra. DRS systems are advantageous in measuring the tissue's optical properties, due to its simplicity, compactness, and low cost. For instance, an efficient, while being inexpensive, IS-based-DRS system schematic can be simply constructed as shown in Figure 2-5 [76]. The shown setup was used in a clinical study to detect the temporal development of skin erythema via computing the erythema index. Figure 2-6 displays the computed erythema index, in the study, based on the measurement of the daily skin diffuse reflectance for cancer patients. Based on the computed erythema index, DRS was able to detect the patients' skin color change earlier than visual assessment, however, both techniques were done synchronously [76]. Over and above, the acquired DRS data were able to quantify skin erythema via estimating the skin chromophores apparent concentrations during radiation treatment [76]. In sum, the simple and cheap IS-DRS system succeeded to properly detect and precisely quantify radiation dermatitis during cancer treatment before being even visible to radiotherapists. Unfortunately, DRS measurement techniques could be used only for relatively small ROI inspection with a lower demand on the spatial resolution. Moreover, it requires a direct contact with skin, which in some cases (dry and wet desquamation, burns) hard to achieve.

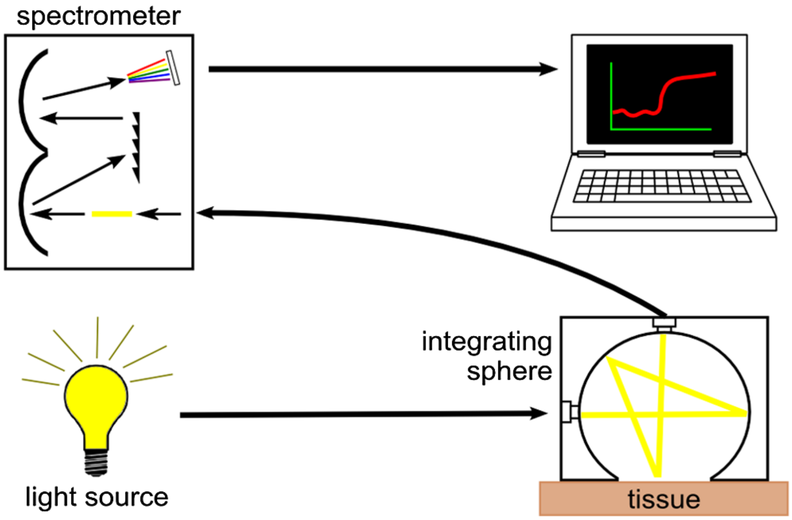

Figure 2-5: An inexpensive integrating sphere-based diffuse reflectance spectroscopy (DRS) configuration used for skin erythema measurement. The system is composed of a simple wide band light source coupled to an integrating sphere which connected to a PC controlled spectrometer. [112]

Unlike both IS and spatially resolved DRS techniques, the time domain (TD) based techniques utilize pulsed light for illumination and detect the skin's back reflection on a temporal basis. Moreover, the source-detector displacement in TD-DRS techniques should not exceed a couple of centimeters range to work properly [84]. To put it simply, the TD- DRS based techniques depend on sending a light pulse to the tissue and detect the back reflected return. Due to both the tissue's absorption and scattering, the reflected light pulse is modified in shape and decreased in amplitude [85]. Based on the detected light pulse shape modification and amplitude decrement, the tissue's optical properties can be estimated.

Contrasting TD-DRS, the corresponding frequency domain (FD) techniques of diffuse reflectance measurement utilize an amplitude-modulated light source and detect the phase and the amplitude modifications at one or more ROI sites. The less sensitivity to noise and being more straightforward in optical implementation are the strong motivations for using FD-DRS. Moreover, FD-DRS systems' reliability in data analysis is significantly larger than the corresponding TD techniques [85].

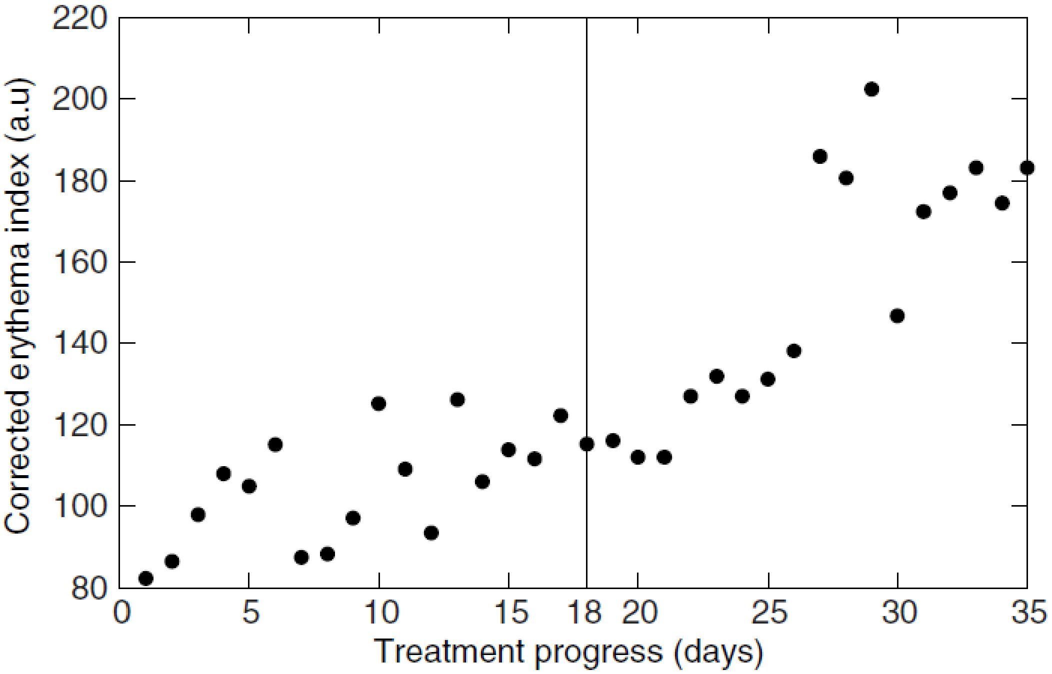

Figure 2-6: An illustration of the computed melanin-corrected skin erythema index on a daily basis during radiotherapy. The vertical black line at the 18th day indicates the first day for the skin erythema to be clinically observed by visual assessment. [112]

Laser Doppler Flowmeter (LDF) is also known as laser Doppler velocimetry. LDF is an optical instrument which enables measuring the frequency/ Doppler shift induced as a result of propagating laser beams in a moving fluid. For human skin, the moving red blood cells inside the superficial vessels cause a laser Doppler shift, by which an erythema could be quantified. Since the erythematous response is originally interpreted as microcirculation vasodilation dependent action [14], [15], [86]. Although LDF concept looks harmonious for erythema assessment, a past study reported its lower sensitivity in measuring the UVB-induced erythema in comparison to the Minolta colorimeter and the spectroradiometer [38]. The low sensitivity of LDF claimed in this study was attributed to the different phenomenon observed by each device [38]. The study furtherly explained that the blood perfusion's relative change measured by the LDF is not well correlated with the skin color change in contrast with diffuse reflectance spectra measurement [38]. Driven by the advance in technology, further development of LDF yields a new generation of devices named as laser Doppler imagers (LDI's). These devices are equipped with a CCD camera. Hence, LDI becomes capable of producing false color images for the region of interest which in turn facilitated the minimum erythema discernible (MED) easier to be visualized, as shown in Figure 2-7 [65]. Despite the advanced display in LDI, it is still limited to small area investigation. In addition, it lacks the potential of erythema quantification.

2.2.4 Imaging-based Assessment

In order to surpass the spectra-based measurement techniques disadvantages including direct skin contact, limited ROI investigation, and local region possible misguidance, imaging was the appropriate alternative. Since imaging-based techniques are: applicable for examining larger ROI, and contact-free.

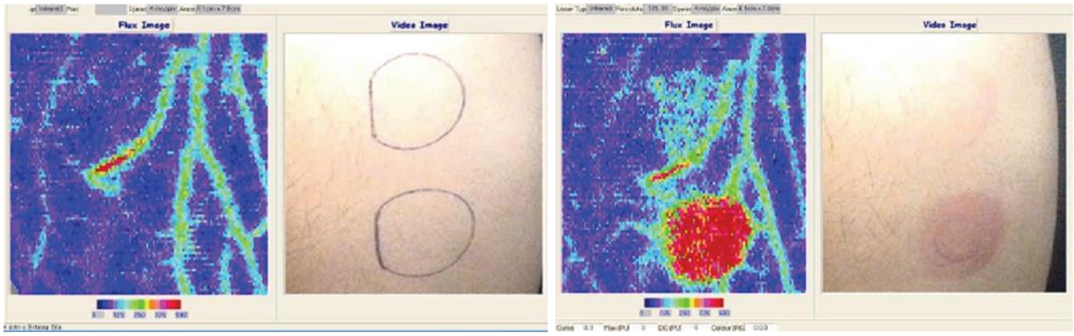

(a) (b)

Figure 2-7: Laser Doppler imager (LDI) captured images for (a) human skin before applying two different doses of UVB irradiation, and (b) after erythema was induced. [107]

Digital Color Imaging/ Photography is a well-suited approach to surmount visual assessment inter/ intra-observation particularity. In addition, it pushes further the existing limitation of the human memory which is incapable of retrieving the condition of the patient/s in former sessions. Moreover, digital photography is freeing the sensitive skin regions from any contact during clinical work or research studies such as in burn [87].

Taking all together, these former advantages offered by the imaging-based methods yield an advance in the dermatological research work. This advance was based on the current technological breakthroughs in electronics, communication, and photography that turned out incredible features of imaging with low-cost. For instance, digital imaging features, amongst others, have progressive capabilities including (1) autonomous color correction, (2) huge data storage, (3) wireless transfer of images via Bluetooth, and Wi-Fi, and (4) autofocusing. Likewise development in hardware, the innovation in image processing algorithms engendered significant steps in image registration, feature extraction, and classification. Hence, image analysis techniques were key solutions for skin pigments quantification [1], [87]–[94], and for other cutaneous diseases [95].

However, four factors need to be thoughtfully considered for realizing a successful photographic system for erythema analysis: (1) illumination; since it is very important to be constant in intensity and emitted spectra, (2) correct patient poses; as the skin is highly scattering tissue, and scattering is angularly dependent [96], (3) some special tools of photography, such as particular lenses, strong flashlights, spectral band filters, and color checkers, might be required to achieve optimum conditions for imaging, and (4) intellectual image analysis algorithms need to be developed; in order to retrieve embedded information inside the captured frames. On top of previous, photographic skills and continuous training play critical roles in acquiring informative photos. To reduce exerted effort in photography, some recent technologies provide high precise sophisticated photographic apparatus including the one in Figure 2-8, which is less dependent on human skills. Nonetheless, they are eminently expensive to afford.

Figure 2-8: An example of a high-end facial skin imaging station equipped with multiple illumination styles and a ready-made skin analysis software tool used for facial skin inspection [97],[98]. The equipment is immensely expensive due to its independence on human skills in imaging.

Regarding skin erythema imaging, Sergio Coelho et al. [90] reported the feasibility of using digital photography to quantify skin erythema induced due to a long-term UV-exposure. The study employed a digital color image analysis algorithm named “CADIE” to evaluate the skin erythematous response of volunteers from different backgrounds based on CIELab color system (see Figure 2-9). The study was able to monitor the induced skin erythema severity due to excessive exposure to multiple units of UV radiation. The UV radiation unit is defined as the dose linked to MED. However, MED is an individual property of skin type and person physiological nature. Albeit the study has few challenges, the use of CADIE algorithm enables better identification of the skin color changes in terms of Δa* relevant to the received MED units compared to the spectrometry. In spite of this efficacious work, it is of interest to know that photography loses clarity in revealing tissue surface/subsurface details, whenever polarization preference prevails. Accordingly, polarized light imaging was the key solution to retrieve the lost lucidity.

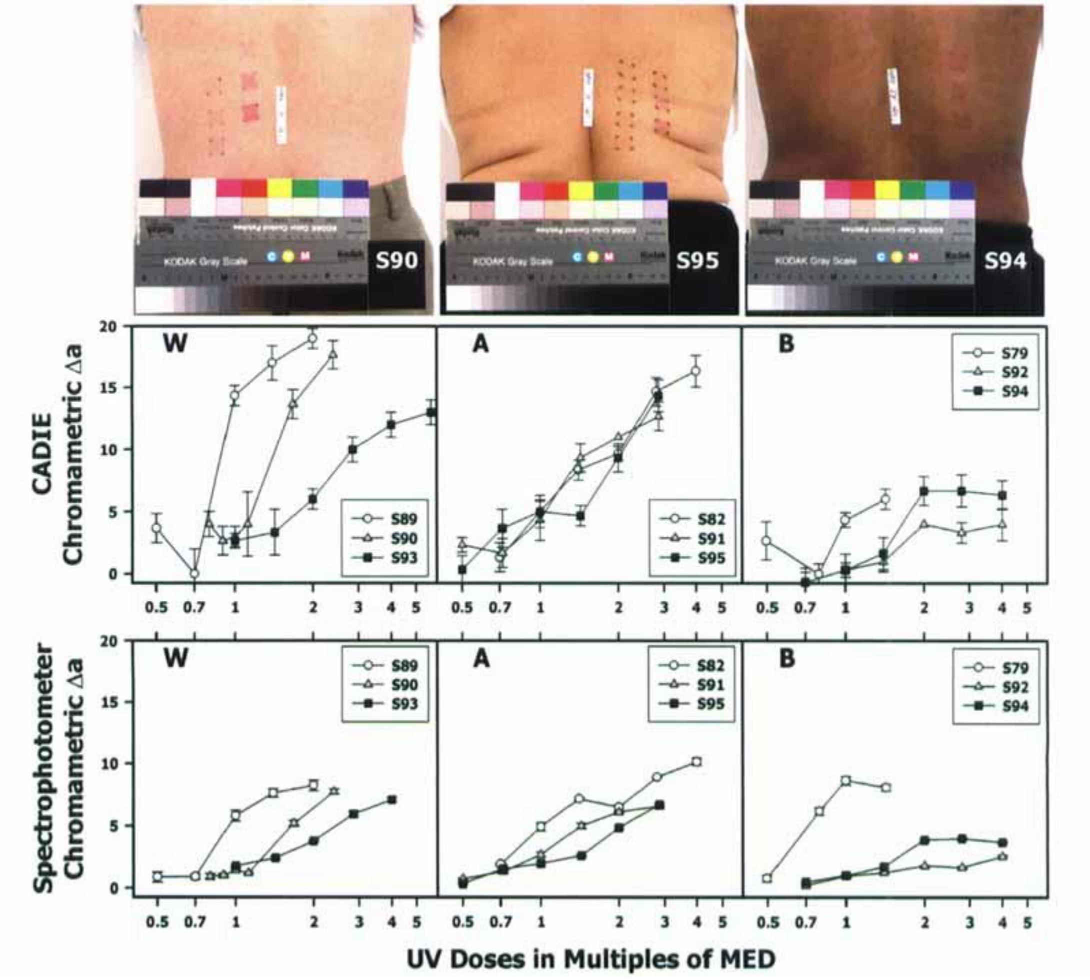

Figure 2-9: An illustration of the erythematous response in distinct backgrounds (W for white, A for Asian, B for African American) volunteers. The top row, color photos of ROI in one subject from each group of

the formerly mentioned backgrounds. The middle row, the relationships detected between the dose of UV radiation expressed in MED units (MED unit is the minimum required UV dose to induce a discernible erythema on the skin of a volunteer) and CADIE-assessed red-green axis Δa* after 1 day of UV exposure. The bottom row, the same relationships are computed based on DRS system using a spectrophotometer. [90]

Polarized light imaging provides the opportunity to selectively separate the surface and the surface underneath layers of tissue's ROI information [41], [99]. In fact, the light reflected back from any tissue's surface, in the case of linearly polarized illumination, is composed of two components. The first of which, specular reflection, is probing the tissue's surface and texture. This component retains the clone polarization type as the incident illumination. Oppositely, the second reflected component, diffusely reflected light, no longer conducts the same illumination polarization. The loss of polarization is accredited to the photons' scattering interactions within the tissue surface underneath layers before bouncing back. As such, the polarization difference between the two reflected components enables the extinction of one component while retaining the other.

To do that, a linear polarizer needs to be selectively oriented ahead of the imaging detector. Toward surface information acquisition, the linear polarizer should be well-matched to the incident illumination polarization. Quite the opposite, orthogonal orientation to illumination's one has to be chosen if the tissue's surface underneath layers information is compulsory. In practice, polarized imaging has a productive outcome where it improved the skin erythema visualization in acne lesions [100]. Furthermore, improved contrast was reported as a benefit for polarized imaging in monitoring the microcirculation, vasodilation, and vasoconstriction as shown in Figure 2-10 [101]. Inspired by the considerable improvement achieved by polarized imaging, a recent study claimed that, likewise linear, elliptically polarized light imaging is a potential approach for enhancing the contrast and the resolution depth of captured frames [102]. Although polarized imaging did a great job in visualizing particular polarization oriented tissue features, other tissue symptoms still can't become clear except if excited earlier, as in fluorescence imaging.

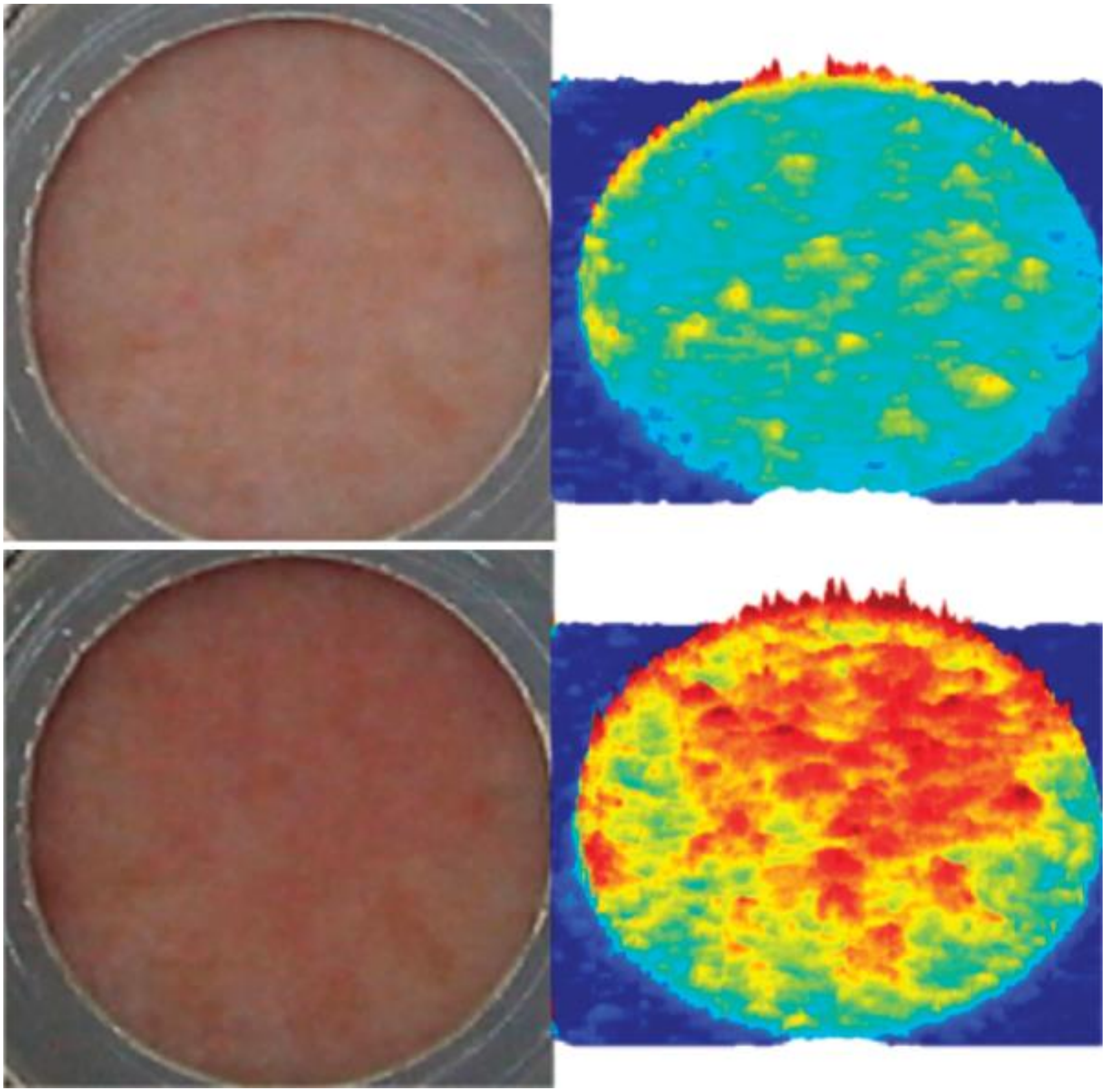

Figure 2-10: The top row, the normal skin image, for a bounded region, is displayed captured with digital photography on the left and with spectroscopy details on the right. The bottom row shows the same region of interest images, by both photography and detailed spectroscopy, however, showing the effects of using a vasodilator drug, induced by iontophoresis. Polarization spectroscopy imaging proved to be more efficient in displaying the heterogeneity of the microvasculature over the whole studied region of skin. [101]

Fluorescence imaging is mainly worried about biological tissues prompted emission detection, and mainly fluorescence. Since this tissue's prompted emission may be more valuable than absorption property in the scale of molecular structure [103]. Fluorescence imaging setup depends on the limited spectral band for both excitations including high energy UV or early VIS light, and a lower energetic spectral band for detection. Filters/ monochromators are always incorporated in the optical path to ensure only excitation and emission bands pass through. Fluorescence measurements on the human skin case are frequently done using optical fibers since excitation and emission bands are easily separated [37]. In general, the involved fiber bundle, in measurement, is divided into two pathways, one to deliver the excitation light while the other pathway is to collect the skin emission.

To give a practical instance, skin melanin displays a significant absorption of its excitation light at the range 340:400 nm and a lower absorption in the emission bands 360:560 nm [104]. Melanin optical properties provide fluorescence imaging a good likelihood to identify high concentrated melanin spots distribution within the skin. For the sake of erythema, fluorescence imaging was used in a couple of studies for examining the post-inflammatory hyperpigmentation (PIH) related to acne lesions and monitor the acne superficial spots development due to courses of treatment [105], [106].

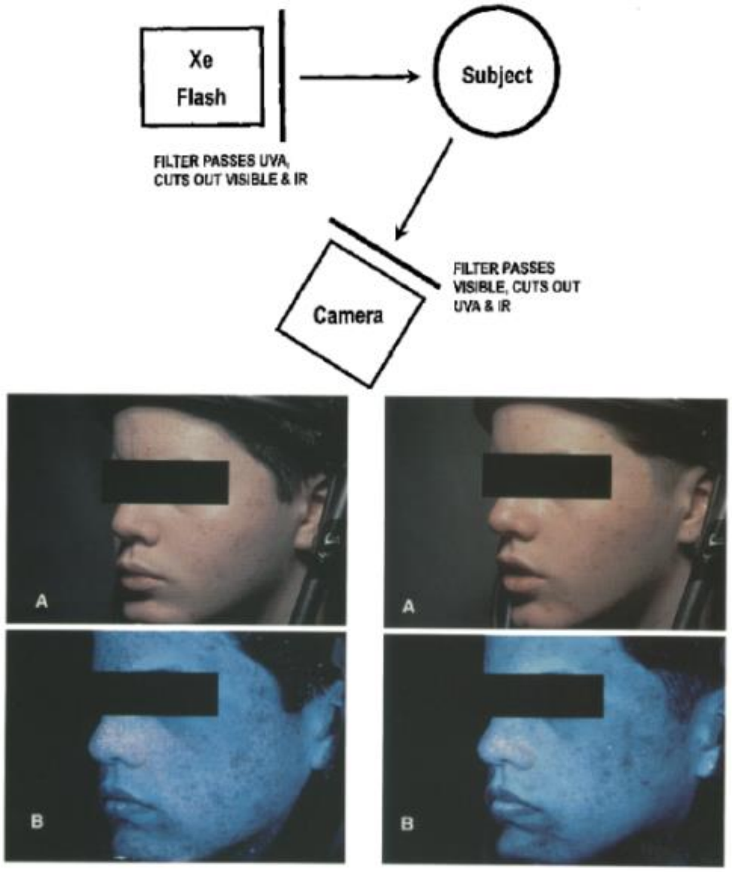

Figure 2-11: Top row, a schematic diagram of a fluorescence optical imaging configuration. Middle row, an acne patient’s images with flash photography is displayed at week-1 (left) and week-12 (right) of acne treatment. Bottom row, the images of the same patient, at the same weeks of treatment, however, captured by fluorescence imaging configuration are shown. The fluorescence images were delineating the acne lesions in the face more clearly than traditional photography. [106]

A simple schematic diagram for fluorescence imaging optical configuration is shown in the top row of Figure 2-11. The figure illustrates the basic principle fluorescence imaging equipment. A wideband light source (xenon in this case) filtered to excite the tissue under investigation. The prompted emission of the excited tissue is filtered by an emission filter to be imaged using a camera sensor.

In the same figure, the middle row shows two photographic pictures for a patient who has facial acne lesions on the first day at week-1 of treatment (prior treatment) and at week-12 of treatment. The bottom row shows the same patient at the same formerly mentioned time points, however, imaged by fluorescence imaging. By statistical analysis, the study, to which the images belong to, proved that fluorescence images of the patient were more capable of highlighting the facial erythematous regions' modified due to the used treatment in contrast with regular photography [106]. Even if fluorescence imaging is required to show molecular scale particles in biological tissue, it is neither the safest approach nor the only way to achieve such information. For instance, microscopic imaging is also intertwined with erythema assessment in order to create a deep understanding of the linked tissue microstructure.

Microscopic imaging is an approach to explore the skin diseases associated with erythematous symptoms on the cellular scale of resolution. Microscopic imaging enhances the assessment accuracy of the skin's inflammatory regions by permitting the visualization of the detailed structures encompassed in the skin layers. For instance, the stratum corneum and the interface junction between the epidermis and the dermis layers cannot be seen by macroscopic imaging but microscope. It is interesting how much details can be revealed potentially with a microscope like Dermoscopy type. For example, it is capable of disclosing three distinct skin properties: architecture, pigmentation, and divergent regions' perimeters. As a consequence, Dermoscopy provides a great opportunity for interpreting rare dermatological features such as the pattern of follicular red dots associated with scalp lesions [107].

Confocal microscopy is a distinguishable functioning microscopic imaging configuration [108]. It is capable of resolving microanatomic structures within the skin to a near histological resolution extent [109]. For instance, confocal scanning laser microscopy brings to the dermatologist's eyes skin detailed structure without the need for a biopsy. For illustration purposes, a schematic diagram of a confocal scanning laser microscopy system used for skin sample inspection is displayed in Figure 2-12 (a). This option is very productive in skin diseases such as contact dermatitis, as shown in [110], [111].

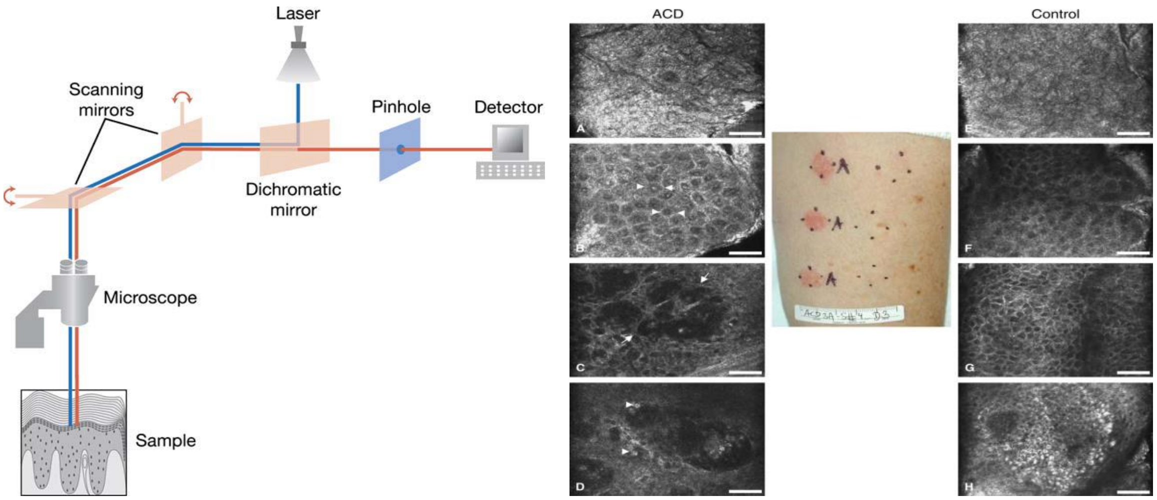

(a) (b)

Figure 2-12: (a) A schematic diagram of a confocal scanning laser microscopy system used for skin sample inspection [87]**,** (b) Sections of skin diagnosed with allergic contact dermatitis (ACD) and other sections for control healthy skin regions, where the confocal microscopy images show the differences in the skin structure between ACD skin regions and the normal ones at a near-histological level of resolution [110], [111].

Moreover, confocal microscopy was able to compete with both histology and patch testing, in diagnosing and monitoring allergic contact dermatitis (ACD), due to its high sensitivity and specificity in detection [112]. Although the high resolution offered by microscopic systems in dermatology, it still has some disfavors. The disfavors of microscopy are: (1) being bulky; which make it difficult to move from a place to another, (2) pricey; and thus it is not affordable in small dermatological clinics, and (3) most of the time invasive: therefore it is inconvenient for patients and time-consuming. Back to relatively less expensive and portable imaging technology, spectral imaging is an attractive technique because of its capability of acquiring a wealth of information in both the spatial and the spectral domains.

Spectral Imaging (SI) is an optical configuration used for acquiring multiple image frames for the object of interest, likewise photography, however, at distinct wavelengths. Thus, the object's field of view total spectral radiance is acquired in a 3-dimensional data set. SI is called differently in other references such as imaging spectrometry/ chemical imaging [113], [114]. Diverse parameters were used to categorize SI including the number of bands, resolution, and acquisition schemes. Regarding number of bands, for example, SI is mainly one of three; multispectral imaging (MSI, usually uses less than 10 bands) [12], [115], [116], hyperspectral imaging (HSI, > 10 and < 1000 bands) [117]–[119], and finally ultraspectral imaging (USI, ≥ 1000 bands) [120]. There are distinct schemes and technologies available for SI. However, spectral scanning SI scheme, based on tunable filters, is commonly used in different applications. Since the tunable filter has less vibration and the spectral scanning scheme require no movement between the object and the equipment. The tunable filter could be, for example, acousto-optic (AOTF) or liquid crystal (LCTF). The tunable filter, in such model, is responsible for the spectral dispersion and hence the resolution. Efficient use of tunable filter-based SI imposes the use of bright and broadband light sources such as tungsten-halogen or xenon lamps. The detector used, in typical models, is monochromatic with either CCD or CMOS sensor. For convergence sake, this section only focuses on HSI out of the other SI categories.

HSI produces a hybrid datacube that holds a wealth of information. This wealth of information offers a potential solution to arduous obstacles in a sundry of applications [121]. To give an example, HSI was used to address many challenges in the medical field as reviewed elsewhere [122]. Particularly, HSI is a technique of great potential for skin erythema assessment because of few reasons including being: contactless, objective, applicable for wide area imaging, and capable of mapping chromophores distributions. Take all together, HSI is likely an excellent candidate for skin erythema objective quantitative assessment challenge.

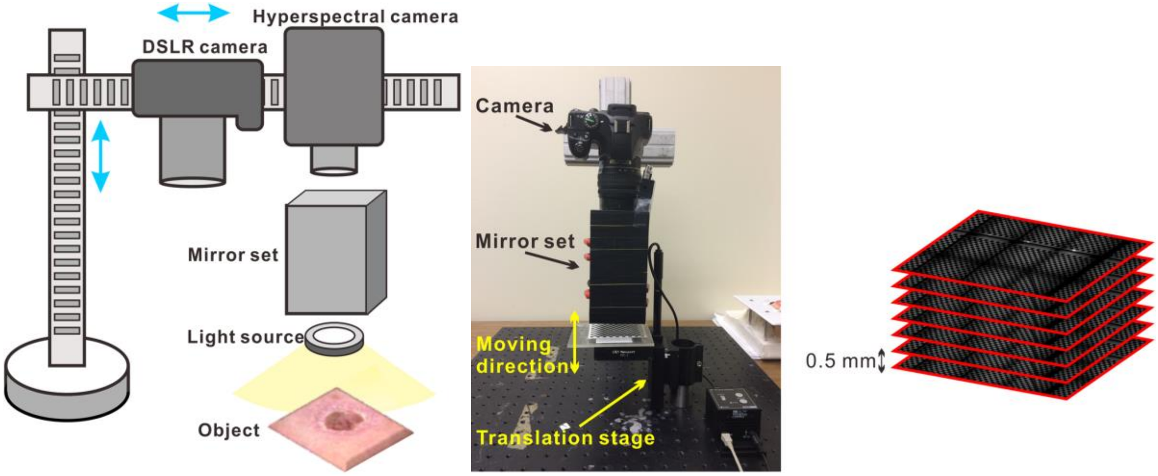

(a) (b) (c)

Figure 2-13: (a) Multiview HSI schematic diagram, (b) implementation and (c) a simulation of the sequence of images captured by the system at different heights with a step of 0.5 mm. The system is composed of two cameras; one is digital single-lens reflex (DSLR) and the other is hyperspectral, where both cameras are moving along a horizontal arm for positioning and the horizontal arm is leveled vertically with a step resolution of 0.5 mm. A mirror set is integrated between the object and the spectral camera to enable Multiview process. [123]

The challenge of objectively quantifying erythema distributed non-homogenously over a wide skin region can be resolved with a technique combining the advantages of imaging and spectroscopy in hybrid equipment. This hybrid equipment is doing hyperspectral imaging and producing spectral-spatial datacube. The intellectual analysis of the produced datacube enables mapping the skin color changes relevant to the induced erythema and the calculation of the apparent skin chromophores concentrations [124] [125]. HSI was used earlier to delineate the variable intensities of skin erythema accompanied with few skin problems [125]–[129]. For example, HSI was capable of mapping acne lesions, the skin's viral infections, and contact allergic dermatitis which are associated with erythematous symptoms as well as erythema temporal evolution [127]. HSI capability of mapping the variable intensity erythematous skin regions is better in terms of contrast compared to red-green-blue (RGB) digital imaging.

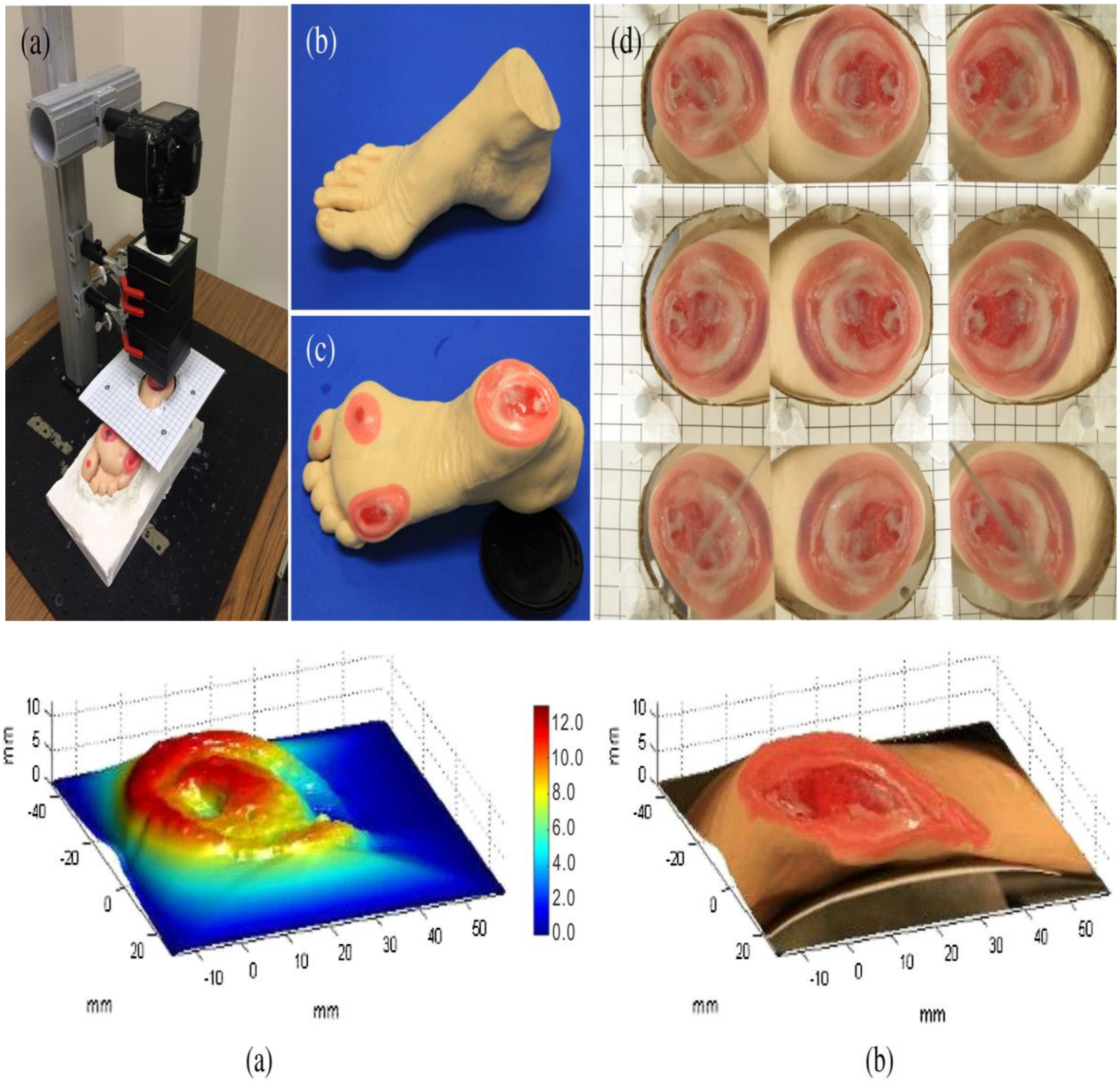

Figure 2-14: Top-row, (a): multiview-HSI system (b, c) the foot wound model, (d) digital color pictures taken by the multiview modality. Bottom-row, (a) 3-D wound model topology built from the multiview hyperspectral captured frames, (b) and the corresponding digital color 3-D wound model. [123]

Several studies ([101], [130], [131]) put an effort to obtain the erythematous maps from RGB images; however, the quality of these maps is still limited [99]. Since the skin's optical properties are dependent on the encompassed chromophores (both types of hemoglobin, melanin, water, etc.), which in turn are wavelength dependent. Therefore, it becomes difficult to optically monitor and precisely quantify chromophores concentration alterations using only red, green, and blue channels in photography. As a result, HSI ha been tagged the "gold standard" for skin erythema mapping [99]. Added to mapping, HSI has an impressive sensitivity to detect the onset of erythema before it becomes visible to the clinician eye [99].

A schematic diagram and implementation of a recently developed multiview HSI [123] used for studying the tissue structure and its functional attributes is shown in Figure 2-13. The novel multiview capability of HSI enabled the operator to outline the topography of a wound associated erythematous regions. In addition, it facilitates the construction of 3-dimensional image as shown for a wound model in Figure 2-14 [123].

2.3 Other Assessment Techniques

This section is dedicated to present an overview of the less frequently utilized techniques for skin erythema assessment including optical coherence tomography, ultrasound imaging, magnetic resonance imaging and dielectric constant measurement. The reasons for the low popularity of these techniques are diverse. For instance, these techniques are disfavored by lower sensitivity, higher cost, complexity, substantial size and weight, mobility problems, or a combination thereof.

2.3.1 Optical Coherence Tomography (OCT)

OCT is an optical technique that makes use of the interference of coherent light. To put it simply, OCT imaging uses a Michelson interferometer, as shown in Figure 2-15 top-row [132]. The information in OCT stems from the interpretation of the interference pattern generated by a low coherence laser beam. This laser beam is split into two arms, one of which is directed to the sample and the other is guided toward a mirror. In-phase interference generates bright fringes, constructive interference, otherwise, dark fringes, destructive interference, is found. The laser's short coherence length permits the determination of the penetration depth: images from subsurface layers can be drawn in analogy to A-scans in ultrasound [37]. While B-scans in OCT are formed by the combination of fringe intensities in adjacent A-scans.

In the past, OCT required a long time to build a tissue image due to slow scanning techniques. However, real-time imaging has become possible recently [133]. The penetration depth of OCT is mainly dependent on the laser's central wavelength. For example, the NIR wavelength of 1300 nm leads to a penetration of about 1.2 mm in comparison with 0.7 mm using light in the 700 nm red region. The typical lateral resolution may vary between 10-15μm, however, there are some special techniques that can reach 1-3μm, entering the region accessible with confocal microscopy [132]. OCT has the feasibility to detect the presence of skin diseases associated with tenderness and erythema. OCT detection for erythema is observed on the interference built images in the format of increased thickness in the epidermal layer, reduction in light scattering, and a dilated vasculature network [134], as shown in Figure 2-15 bottom-row [133]. Although some OCT systems are currently available as bench-top devices, its sensitivity is utterly vulnerable to change in case of slight movements during in vivo measurements. These unintentional movements of patients result in blurry images [133]. Two major differences exist between OCT and ultrasound; skin contact requirement and the sensitivity to patient movement.

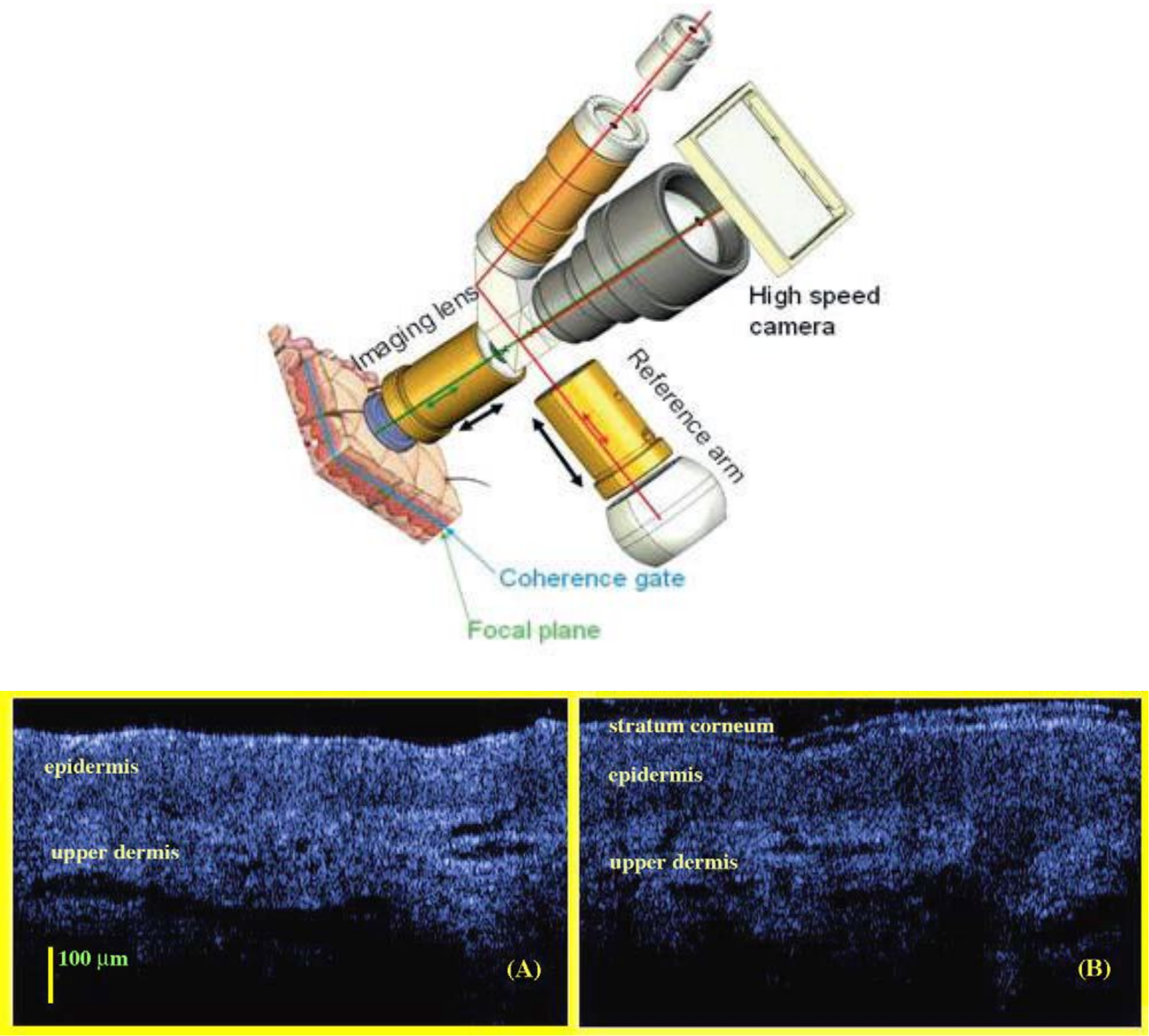

Figure 2-15: (top row), a schematic diagram of a high definition OCT [132]. Bottom row, (A) 2D-OCT scanned images of human back skin before UVB irradiation, (B) and after exposure to 4.5 UVB MED. The stratum corneum is often invisible on the none-glabrous skin surface as the case in the image (A). However, it is obviously delineated in the irradiated skin in the image (B). [133]

2.3.2 Ultrasound-Based Imaging

Ultrasound, likewise OCT, is supplementary equipment in the dermatological bench-top instrumentation. Ultrasound became a tool to measure the skin thickness since the late quarter of the 20th century [135]. Following that, ultrasound imaging expanded to different dermatological issues, including skin irritation and erythema [136]–[140]. The basic principle of ultrasonic imaging is detecting the reflected acoustic waves out of the different layers of the interesting tissue. The tissue components are quite often different in density and hence it responds to the transmitted acoustic waves individually. Distinct responses, from the different layers of the scanned tissue to the acoustic waves, are transformed into an image of the tissue's underlying structure in gray scale intensities displayed on the ultrasound monitor [141]. A wide range of acoustic frequencies is used in ultrasonic imaging, where lower frequencies are used to visualize structure deeper in tissue than when using higher frequencies. Examples of the used frequencies are shown in Table 2-2 [141]. In advanced ultrasonic imaging, the system is not only imaging stationary structures but also monitoring moving fluids like arterial/ venous blood by adopting Doppler ultrasound methodology.

Table 2-2: Ultrasonic imaging frequencies and associated penetration depth within visualized skin part [161]

Ultrasonic freq. (MHz)	Visual skin part	Penetration depth (cm)
7.5	Lymph nodes	~ > 4.00
13.5-50	Dermis and Epidermis	~ 3.0:0.3
20	Dermis and Epidermis	~ 0.6:0.7
50-100	Epidermis	~ 0.3:0.015

Ultrasonic imager is a noninvasive and portable device, used to measure the tissue thickness within the lesions area. The tissue thickness was found to be inversely proportional with skin erythema. This relationship between the skin thickness and the skin erythema due to irradiation was verified in a breast cancer study [136]. Another study showed the productive usage of ultrasound in a forearm dermatofibroma nodule surrounded by an erythematous region. The nodule is imaged, blue dot, before the removal surgery (see Figure 2-16 [138]) to alert the surgeon for the nearby vein. Although ultrasound was able to quantify erythema indirectly via skin thickness measurement, a contradicting study presented an experimental work that showed less efficiency of an acoustic equipment in erythema assessment [66]. The experiment accomplished in the contradicting study showed a low correlation between both the melanin and erythema indices with skin thickness measured by an ultrasound-based-device. Hence, the study concluded that skin thickness can't be a productive measure of the componential changes of the parenchyma to assess subcutaneous fibrosis. Therefore, ultrasound technique becomes a doubtful technique for studying skin erythema associated with different cutaneous diseases in contrast with, for example, spectral based modalities.

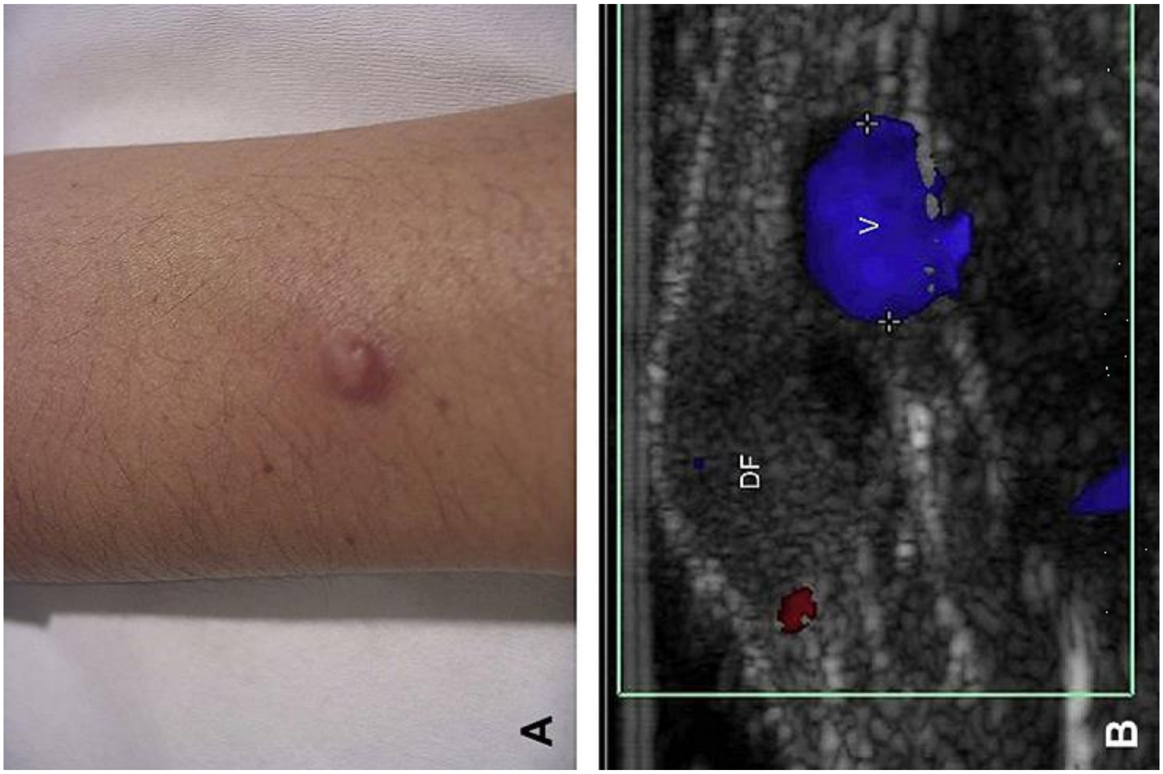

Figure 2-16: An illustration of Dermatofibroma (DF) case inspected by ultrasound instrument: (A) forearm erythematous nodule, (B) Ultrasonic transverse view image displays erythematous nodule near a large vein (blue spot) which assist in being avoided in surgery. [138]

2.3.3 Magnetic Resonance Imaging (MRI)

MRI is a distinguishable imaging technique by which high spatial resolution images for minute tissue components can be acquired [142]. Such highly sophisticated imaging modality is not commonly used for superficial skin disorders. However, in a previous study, MRI was used toward 3-D mapping of acne lesions and psoriasis as shown in Figure 2-17 [143]. The major disadvantages of such high-resolution imaging modality are; size, complexity, and ultimately the instrument costs.

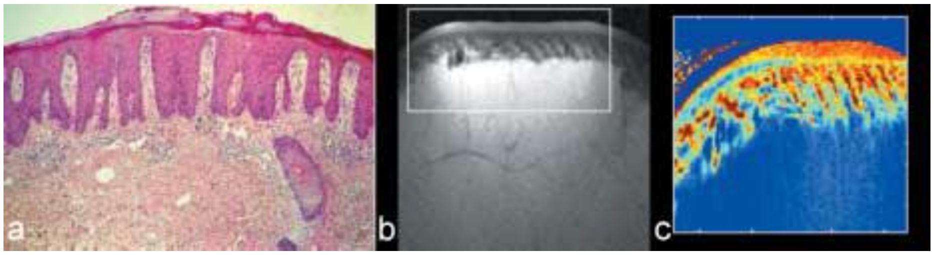

Figure 2-17: (a) Histological image of a severe psoriasis case, (b) anatomical view with the marked region of interest (ROI), (c) a relaxation time T1 map calculated for the ROI, where the increased red color intensity in the outer dermis layer is due to the skin inflammation. [143]

2.3.4 Dielectric constant

Dielectric constant measurement is used in diverse medical applications as reviewed elsewhere [144]. For instance, dielectric constant measurement was utilized to detect skin reactions induced by irradiation in breast cancer radiotherapy treatment [145]. The basic way to measure the dielectric constant of the skin is to connect an open terminal coaxial probe with a controlled network analyzer to transmit electromagnetic (EM) waves with harmless frequencies through the skin's ROI and measure its reflected return. It has been shown that the dielectric constant is inversely correlated to the clinically scored erythema. Hence, dielectric constant measurement proved to be capable of noninvasively quantifying skin erythema. However, the skin type variability and same skin inconsistent dielectric properties yield less repeatable results. Hence, it was less convincing for clinicians to use in their daily routine.

2.4 Erythema Indices

This section briefly describes the different computation approaches for the skin erythema index through a review of the literature. The purpose of this section is to hand over an overview of the skin erythema indices calculation guidelines in order to encourage more studies to validate and compare between them [146], to identify the optimal skin erythema estimation method.

2.4.1 Dawson Indices

The use of Dawson indices is a familiar approach for quantitative estimation of the skin color changes due to a disease's development [147], or a medical treatment [76], [148]. Dawson erythema index (DEI) is derived based on the assumption of a proportional relation between the hemoglobin optical absorption in the range of 510-610 nm and the erythema scores. The area under the curve for hemoglobin absorption, if a baseline is determined, is the parameter assumed to be related to the skin erythema variation and calculated as follows:

$$\boldsymbol{DEI = 50 * [2r + 3(q + s) - 4(p + t)]} \tag{2-9}$$

The terms, p, q, r, s, and t are the symbols expressing the logarithm of the reciprocal of the reflectance (LRR) measured at five predetermined wavelengths 510, 540, 560, 580, and 610 nm, respectively. Dawson melanin index (DMI) is computed based on two central wavelengths (650 and 700 nm). As it is assumed that melanin concentration is relative to the slope of the skin spectral curve of absorbance ($A_{xxx} = \log_{10}\frac{1}{R_{xxx}}$) bounded by the two formerly mentioned wavelengths. The formula used for computing melanin index is averaging the absorbance values for the wavelengths surrounding 650 nm and 700 nm (λ ± 5 nm) as seen in (2-10):

$$\boldsymbol{DMI = (100 * [Log_{10}\left(\frac{1}{(\bar{R}_{645,650,655}}\right) \text{-}Log_{10}\left(\frac{1}{(\bar{R}_{695,700,705}}\right)]) + 1.5} \tag{2-11}$$

The term R_{xxx} is the computed reflectance at certain wavelength xxxin nanometers. The constant at the end is an empirical correction constant. The DEI can be corrected (DEI$_c$) using the DMI by applying the formula as shown (2-12), where γ = 0.04 is an empirically derived balancing constant by Dawson to avoid negative values due to the other existing but not significant skin chromophores:

$$\boldsymbol{DEI_c = (50 * [2r + 3(q + s) - 4(p + t)]) * (1 + (\gamma * MEI))} \tag{2-12}$$

For the sake of evaluating a medical treatment's efficacy, subsequent reflectance measurements are taken. Following that, Dawson's relative erythema index (DEI$_r$) is computed to assess the skin color change. The term DEI$_r$ is basically equivalent to the difference in value between DEI$_c$ for two skin sites, one of which is the irradiated site while the other is for a control (not irradiated) site.

2.4.2 Diffey Index

Diffey index [32] was built on a simple observation of hemoglobin absorption attributes. Basically, Diffey realized that hemoglobin absorption is higher in the green spectral region with respect to the corresponding red region. Based on this fact, and as erythema is essentially a consequence of vasodilation, he proposed that erythema might be evaluated efficiently by computing the ratio of the inverse logarithm of the skin spectral reflectance at only two wavelengths: one of which is in the green band (565 nm) and the other is in the red band (635 nm) while not taking melanin into consideration. The formula which expresses Diffey index is given in (2-13).

$$\boldsymbol{E_{Dif} = -\log_{10}\left(\frac{R_g}{R_r}\right)} \tag{2-13}$$

2.4.3 Tronnier Index

Tronnier [149] had a similar approach to Diffey [32], but his principle is to compute the relative erythema rather than the absolute value. Consequently, he created his index (E$_T$) based on the variation between a UV-irradiated erythematous region (Er) versus a control (C) region. Tronnier, unlike Diffey, considered melanin in his computation. However, he assumed that the relative calculation should compensate for the melanin absorption in the skin tissue without the need for a separate calculation step. In sum, he used the back reflected light measurements at two wavelengths, one in green (545 nm) and the other in red (661 nm), for both the erythematous (Er_g, Er_r) and the control regions (C_g, C_r) to assess the skin's relative erythema, as shown in (2-14).

$$\boldsymbol{E_T = ((Er_g - Er_r) - (C_g - C_r))} \tag{2-14}$$

2.4.4 Ferguson-Hemoglobin content

Ferguson developed another computation technique of quantification for skin erythema named as the index of hemoglobin content (IHB) in the skin surface layer [150]. The developed technique is dependent on the use of the isosbestic absorption points of hemoglobin both components (i.e. spectral points of equal absorption for the oxygenated and deoxygenated components of hemoglobin). These wavelengths are the core input data for IHB computation. The term OD_{xxx} is the optical density of the skin at certain wavelengths of *xxx* nanometers.

$$IHB = \left[(1/_{16.5} * (OD_{544} - OD_{527.5}) - 1/_{29} * (OD_{573} - OD_{544}) \right] * 100 \qquad \text{(2-15)}$$

2.4.5 Hajizadeh Method

Hajizadeh made studies [151], [152] to correct for the melanin absorption effect on the spectrophotometric measurement of light backscattered from the epidermis, especially in highly pigmented people versus light skinned ones. To this end, the melanin index M_{675} was computed, as in (2-16) based on the absorption curve region, similarly to Dawson's method [71]. However, Hajizadeh had proposed a new compensation factor due to a synthetic melanin absorption measurement. This measurement is equivalent to the in vivo one, and thus he had developed the term named after him M_H where it is expressed in μg/cm^2 as shown in (2-17).

$$M_{675} = 100 * \left\{ \frac{OD_{700} - OD_{650}}{50} + \left(0.06 * \left[\frac{1 - SaO_2}{100} \right] + 0.01 \right) * IHB/80 \right\} \qquad \text{(2-16)}$$

$$M_H = (54 * 10^{-3} - M_{675}) * 120.1)\ \mu\text{g/cm2} \qquad \text{(2-17)}$$

Using the newly developed melanin index M_H, the approximately "true" hemoglobin content can be computed. This is done by applying an empirical constant as shown in (2-18):

$$IHB_{true} = IHB_{cor} + 0.000047 * M_H \qquad \text{(2-18)}$$

2.4.6 Helen Hayes Hospital

Helen Hayes Hospital method is an approach of erythema quantification mentioned elsewhere [146]. Basically, this method is using a standard in vitro measurement for standard melanin sample's absorption. The standard sample measured absorbance is tuned to match individuals' skin melanin content based on their skin absorption difference within the spectral range 500-625 nm. This method has the advantage of being consistent for both high and low pigmented skin people simultaneously. However, this method has a shortcoming due to its impotence to physiologically interpret the melanin content changes between the different locations in the same person, for example between an erythematous and control region [146].

2.5 Discussion

No doubt, VA is still the gold standard [41] and the primary method for the skin erythema assessment. It has not yet been supplanted by any other means, which still have some shortcomings. For instance, a study [30] provided an evidence of non-precise spectrometer results compared to the clinical visual assessment. Figure 2-18, belongs to the formerly mentioned study, shows that the erythema index (d IE) is not consistent with a clinical assessment in a formaldehyde-induced erythema [30]. However, VA is not perfect. It has several critical shortcomings. Primarily, VA is based on a subjective perspective, and thus suffers from inter- and intra-observation individuality, as well as being dependent on scene conditions. Secondly, in the ideal case, the human eye is capable of precisely detecting the difference between color levels, but it is unqualified to designate an absolute value for the detected color difference. Moreover, VA has no capability of delineating the margins between distinct erythematous levels precisely. Another point of critique against VA is color blindness, which may occur amongst operating clinicians without a declaration [153]–[155].

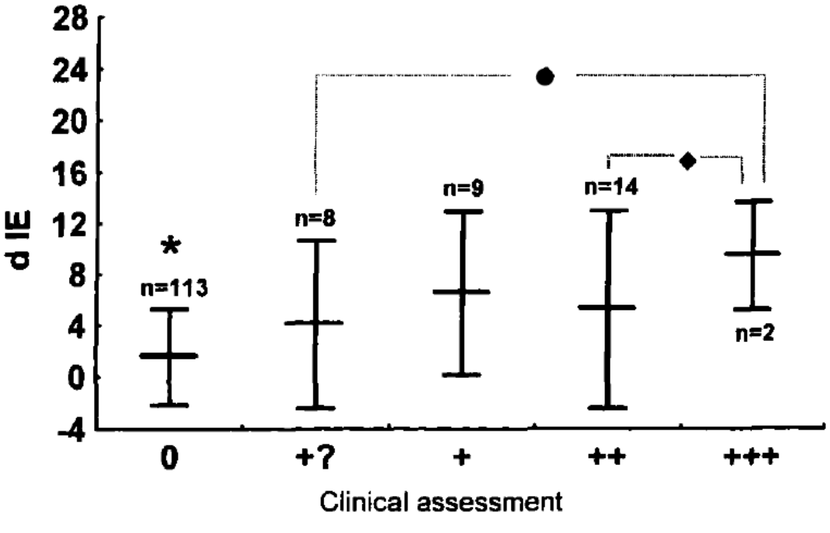

Figure 2-18: Comparison between the Dermaspectrometer delta erythema index (d IE) and the clinical assessment of formaldehyde patches applied to patients' skin. The term d IE is equivalent to the difference between the erythema reading of the Dermaspectrometer acquired for ROI and a control region. The horizontal axis is the clinical skin erythema score which ranges from 0 for normal skin and +++ for severe skin erythema. The vertical axis is the erythema index score. The term (n) is the number of people who have the same reaction, the (*) sign is indicating high correlation with positive patch test ($P<0.05$, ANOVA test), and the sign (♦) is pointing to separable categories ($P<0.05$, ANOVA test). [30]

For erythema assessment, it was convenient to use color charts as a supplementary tool in VA, since it is cheap and portable. Moreover, it helps the clinician to document the color tone of the skin which is hard to remember or to communicate verbally. However, using color charts is still a subjective method; thereby it suffers from VA shortcoming except for better documentation. Added to VA sole disadvantages, color comparison within tones may be vulnerable to metamerism phenomena, which is basically the matching of two colors under certain conditions including illumination type, geometrical position, and human-to-human color detection acuity.

Going far from subjective means, tristimulus instruments allowed objective assessment for the skin erythema and pigmentation measurements. However, these devices are heavy and pricey as well. Hence, they are difficult to be moved from room to another which is not typical in clinics. In terms of size and weight, the narrowband devices, Mexameter and Dermaspectrometer, are interesting. But they are dependent on fixed wavelengths which decrease the capability of these devices to consistently account for variability between distinct skin types to people with different backgrounds. Furthermore, all the early mentioned reflectance measurement devices require direct skin contact. Skin contact limits their usage in sensitive regions, like burns, and makes them susceptible local skin variations due to the limited region of inspection.

To overcome the spectral limitation of the tristimulus equipment, and the narrowband devices, continuous spectral measurement was introduced. To do that, DRS measurement techniques were utilized to scan the interesting spectra and find the changes in tissue’s diffuse reflectance. Although DRS measurement techniques are efficient in determining the optical properties of tissues, it still has few limitations. For instance, the typical IS-DRS configuration has less precision in the spatial domain. Hence IS-DRS becomes problematic in separating the particular influence of scattering and absorption in the absence of a predetermined scattering spectrum of the sample under test [85]. As well as IS-DRS, the spatially-resolved DRS is not flawless. It is dependent on few local point measurements which might yield indecisive outcomes [82]. Far from CW illumination, TD-DRS measurement techniques provide an advantage of acquiring both absorption and scattering coefficients data via a single measurement. Nonetheless, it requires a complex set of pricey instrumentation, which is not available everywhere. The prior DRS techniques disadvantages paved the way for imaging techniques to advance toward skin erythema quantitative assessment.

Photography enterprise, in erythema assessment, is a cumbersome process and needs firm constraints in order to achieve the expected efficiency. To give a brief, the illumination in photography is a critical issue that needs to be securely maintained to remain consistent in terms of intensity, emitted spectra, and relative position to object; if repeatable frames are considered. For illustration purposes, Figure 2-19 [97] displays two pictures of the same patient at two different illumination conditions. The taken pictures don’t look identical. As such, the two pictures may be falsely interpreted by the clinician as two distinct conditions.

Figure 2-19: Example of illumination conditions impact on the outcome of photographed pictures, which may lead to an error in clinical diagnosis. [97]

To rise above both illumination problems and specular glares, polarized imaging was solicited. However, polarized imaging requires the integration of additional optical components to pass and detect only polarized light. Such addition leads to raise the cost of the developed imager, and to grow system complexity in design and implementation. Besides, the more the number of system components in photography the more the illumination needs to be intense and/ or the detector to be more sensitive.

Although fluorescence imaging has a great potential in displaying skin structure in the molecular scale, it is limited in use due to the possible harm of UV light to the skin. In addition, fluorescence imaging requires special tools/ instrumentations, and personal protective equipment to be considered for both the patient and the imaging operator, which is an overhead cost. For instance, high sensitive detectors are required due to the low intensities of both exciting illumination and the fluorescence emission since band filters or monochromator are used in each way.

The microscope is the shortcut technique to extract the root information about diseases associated with the erythematous symptoms. Despite this fact, the microscope is expensive, and probably not easy to move instrument. Moreover, the microscope requires skin biopsy quite often to be analyzed in the laboratory. Hence, a change of optical properties is possible to take place due to the transfer from the clinic to the laboratory. Coupled with the relatively long time necessary for the lab analysis, microscopy is limited to the analysis of small skin regions. Far from common techniques, OCT, ultrasound, MRI, and dielectric constant measurements, are less attractive for dermatology clinics, due to different reasons such as the size, cost, and inconvenience.

Spectral imaging is a hybrid technique combining both the advantages of DRS and digital imaging and thus, it overcomes the limitations of each individually. HSI, one category of SI, is tagged as the gold standard in skin erythema mapping due to its distinguishable capability of contouring the distinct skin response intensities. Furthermore, HSI datacube analysis enables a precise estimation of skin componential chromophores temporal changes. However, HSI still requires a reasonable budget, for either case; building a custom-made spectral camera or purchasing a bench-top one. In addition to the required budget for HSI, one more challenge is to develop an intellectual image processing algorithm to achieve an efficient image registration and precise endmembers classification.

2.6 Conclusion

Optical science and technology have resulted in incredible advances in miniaturizing apparatus and full-systems to facilitate skin erythema quantification. Handheld colorimeters, single point spectroscopic devices, digital and spectral cameras are now mobile and can be carried in pocket size, ready to offer objective measures for various skin diseases associated with erythema. Larger imaging devices are equipped with high definition monitors and capable of producing real-time false color images, displaying the skin's epidermal and dermal symptoms. More sophisticated methods, such as confocal microscopy and OCT, offer almost histological spatial resolutions for details of the erythematous skin. This versatile array of objective tools to study cutaneous diseases associated with skin erythema definitely improve the clinical dermatology's daily routine in terms of both sensitivity and specificity.

However, the capabilities of the expert clinician's eyes will be hardly replaced for skin erythema inspection. Nevertheless, technology offered few solutions for eliminating subjectivity and reducing previously mentioned disadvantages of VA. In economic side, hiring a number of full-time radiotherapists might be more expensive than purchasing a technology on the long run. Therefore, clinicians who are equipped with an advanced technology are able to provide good service for more patients in a shorter time. In our point of view, HSI, as a developing optical modality, is expected to be in the near future a possible candidate to ease the work of clinicians. Since HSI is providing an objective precise approach for skin color pigmentation mapping in a contactless style for a relatively sizable tissue region.

In the next chapter, a brief will be introduced about the hyperspectral imaging definition, distinct classes, and its variable acquisition schemes. One common scheme will be addressed in more details. A strong focus will be on the different ways of wavelength dispersion and how tunable filters are distinguishable against others. The main purpose of the chapter is to establish more familiarity with the technique.

References

[1] M. Nischik and C. Forster, "Analysis of skin erythema using true-color images.,"

IEEE Trans. Med. Imaging, vol. 16, no. 6, pp. 711–6, 1997.

[2] G. Marchini, A. Nelson, J. Edner, S. Lonne-Rahm, A. Stavreus-Evers, and K. Hultenby, "Erythema Toxicum Neonatorum Is an Innate Immune Response to Commensal Microbes Penetrated into the Skin of the Newborn Infant," *Pediatr. Res.*, vol. 58, no. 3, pp. 613–616, 2005.

[3] S. L. Brice, S. S. Stockert, J. D. Bunker, D. Bloomfield, J. C. Huff, D. A. Norris, and W. L. Weston, "The herpes-specific immune response of individuals with herpes-associated erythema multiforme compared with that of individuals with recurrent herpes labialis," *Arch Dermatol Res*, vol. 285, pp. 193–196, 1993.

[4] A. N. BRUCE, "VASO-DILATOR AXON-REFLEXES," *Quat. J. Exp. Physiol*, vol. 6, pp. 339–354, 1913.

[5] and H. M. M. T. Lewis, R. T. Grant, "VASCULAR REACTIONS OF THE SKIN TO INJURY," *Heart*, vol. 14, pp. 139–160, 1927.

[6] H. Hönigsmann, "Erythema and pigmentation," *Photodermatol. Photoimmunol. Photomed.*, vol. 18, pp. 75–81, 2002.

[7] K.-S. Suh, H.-J. Roh, S.-Y. Choi, Y.-S. Jeon, K.-S. Doh, J.-H. Bae, and S.-T. Kim, "A long-term evaluation of erythema and pigmentation induced by ultraviolet radiations of different wavelengths.," *Ski. Res. Technol.*, vol. 13, no. 4, pp. 360–8, 2007.

[8] J. W. Shin, S. W. Yoon, J. B. Jeong, and K. C. Park, "Different responses of the melanin index to ultraviolet irradiation in relation to skin color and body site," *Photodermatol. Photoimmunol. Photomed.*, vol. 30, no. 6, pp. 308–315, 2014.

[9] Terence S. C. Poon, Johanna M. Kuchel, Aamir Badruddin, Gary M. Halliday, Ross StC. Barneston, Haruhi Iwaki, Masato Hatao, "Objective measurement of minimal erythemal and melanogenic doses using natural and solar simulated light," *Photochem. Photobiol.*, vol. 78, no. 4, pp. 331–336, 2003.

[10] L. R. Sklar, F. Almutawa, H. W. Lim, and I. Hamzavi, "Effects of ultraviolet radiation, visible light, and infrared radiation on erythema and pigmentation: a review," *Photochem. Photobiol. Sci.*, vol. 12, no. 1, pp. 54–64, 2013.

[11] B. Jung, S. Kim, Y. Bae, H. Kang, Y. Lee, and J. S. Nelson, "Real-time measurement of skin erythema variation by negative compression: pilot study.," *J. Biomed. Opt.*, vol. 17, no. 8, pp. 081422–1, Aug. 2012.

[12] L. Kong, D. Yi, S. Sprigle, F. Wang, C. Wang, F. Liu, A. Adibi, and R. Tummala, "Single sensor that outputs narrowband multispectral images.," *J. Biomed. Opt.*, vol. 15, no. 1, p. 010502, 2010.

[13] M. Denstedt, B. S. Pukstad, L. a. Paluchowski, J. E. Hernandez-Palacios, and L. L. Randeberg, “Hyperspectral imaging as a diagnostic tool for chronic skin ulcers,” vol. 8565, p. 85650N, Mar. 2013.

[14] G. Heyer, O. P. Hornstein, and H. O. Handwerker, “Skin reactions and itch sensation induced by epicutaneous histamine application in atopic dermatitis and controls,” *J Invest Dermatol*, vol. 93, no. 4, pp. 492–496, 1989.

[15] W. Magerl, R. a Westerman, B. Möhner, and H. O. Handwerker, “Properties of transdermal histamine iontophoresis: differential effects of season, gender, and body region.,” *J. Invest. Dermatol.*, vol. 94, no. 3, pp. 347–352, 1990.

[16] M. I. Thomas M. Chin, Fellner, “Allergic Hypersensitivity to Lidocaine Hydrochloride,” 1980.

[17] D. E. McKee, D. H. Lalonde, A. Thoma, D. L. Glennie, and J. E. Hayward, “Optimal Time Delay between Epinephrine Injection and Incision to Minimize Bleeding,” *Plast. Reconstr. Surg.*, vol. 131, no. 4, pp. 811–814, 2013.

[18] E. Van Den Kerckhove, K. Stappaerts, S. Fieuws, J. Laperre, P. Massage, M. Flour, and W. Boeckx, “The assessment of erythema and thickness on burn related scars during pressure garment therapy as a preventive measure for hypertrophic scarring,” *Burns*, vol. 31, no. 6, pp. 696–702, 2005.

[19] S. D’haese, M. Van Roy, T. Bate, P. Bijdekerke, and V. Vinh-Hung, “Management of skin reactions during radiotherapy in Flanders (Belgium): a study of nursing practice before and after the introduction of a skin care protocol.,” *Eur. J. Oncol. Nurs.*, vol. 14, no. 5, pp. 367–372, 2010.

[20] D. Yohan, A. Kim, E. Korpela, S. Liu, C. Niu, B. C. Wilson, and L. C. Chin, “Quantitative monitoring of radiation induced skin toxicities in nude mice using optical biomarkers measured from diffuse optical reflectance spectroscopy.,” *Biomed. Opt. Express*, vol. 5, no. 5, pp. 1309–20, 2014.

[21] L. Diana L. Glennie, Joseph E. Hayward, Orest Z. Ostapiak, James Wright and T. J. F. Doerwald-Munoz, “Diffuse reflectance spectroscopy for monitoring erythema in head & neck intensity modulated radiation therapy,” *J. Radiat. Oncol.*, 2014.

[22] N. Lee, C. Chuang, J. M. Quivey, T. L. Phillips, P. Akazawa, L. J. Verhey, and P. Xia, “Skin toxicity due to intensity-modulated radiotherapy for head-and-neck carcinoma,” *Int. J. Radiat. Oncol. Biol. Phys.*, vol. 53, no. 3, pp. 630–637, 2002.

[23] D. Porock and L. Kristjanson, “Skin reactions during radiotherapy for breast cancer: The use and impact of topical agents and dressings,” *Eur. J. Cancer Care (Engl).*, vol. 8, no. 3, pp. 143–153, 1999.

[24] M. McQuestion, “Evidence-Based Skin Care Management in Radiation Therapy,”

Semin. Oncol. Nurs., vol. 22, no. 3, pp. 163–173, 2006.

[25] J. W. Denham, C. S. Hamilton, S. A. Simpson, P. M. Ostwald, M. O'Brien, T. Kron, D. J. Joseph, and K. B. G. Dear, "Factors influencing the degree of erythematous skin reactions in humans," *Radiother. Oncol.*, vol. 36, no. 2, pp. 107–120, 1995.

[26] T. Olschewski, K. Bajor, B. Lang, E. Lang, and M. H. Seegenschmiedt, "[Radiotherapy of basal cell carcinoma of the face and head: Importance of low dose per fraction on long-term outcome].," *J. Dtsch. Dermatol. Ges.*, vol. 4, no. 2, pp. 124–30, 2006.

[27] H. R. Withers, D. Sc, B. Maciejewsiu, J. M. G. Taylor, D. Ph, and A. Hliniak, "Dose fractionation and regeneration in radiotherapy for cancer of the oral cavity and oropharynx: Tumor dose-response and repopulation," *Int. J. Radiat. Oncol.*, vol. 16, no. 831, pp. 831–843, 1989.

[28] D. Basketter, F. Reynolds, M. Rowson, C. Talbot, and E. Whittle, "Visual assessment of human skin irritation: a sensitive and reproducible tool.," *Contact Dermatitis*, vol. 37, pp. 218–220, 1997.

[29] M. Bruze, M. Isaksson, B. Edman, B. Björkner, S. Fregert, and H. Möller, "A study on expert reading of patch test reactions: inter-individual accordance," *Contact Dermatitis*, vol. 32, pp. 331–337, 1995.

[30] E. Held, H. Lorentzen, T. Agner, and T. Menné, "Comparison between visual score and erythema index (DermaSpectrometer) in evaluation of allergic patch tests," *Ski. Res. Technol.*, vol. 4, no. 4, pp. 188–191, 1998.

[31] S. Wan, J. a Parrish, and K. F. Jaenicke, "Quantitative evaluation of ultraviolet induced erythema.," *Photochem. Photobiol.*, vol. 37, no. 6, pp. 643–648, 1983.

[32] B. L. Diffey and P. M. Farr, "Quantitative aspects of ultraviolet erythema," *Clin. Phys. Physiol. Meas.*, vol. 12, no. 4, p. 311, 1991.

[33] Daniel Malacara, "Color Vision and Colorimetry theory and Applications," 2nd ed., Society of Photo-Optical Instrumentation Engineers (SPIE), 2011.

[34] M. H. Ahmad Fadzil, D. Ihtatho, A. Mohd Affandi, and S. H. Hussein, "Objective assessment of psoriasis erythema for PASI scoring.," *J. Med. Eng. Technol.*, vol. 33, no. 7, pp. 516–24, 2009.

[35] S. Banu, G. Toacse, and G. Danciu, "Objective erythema assessment of Psoriasis lesions for Psoriasis Area and Severity Index (PASI) evaluation," *EPE 2014 - Proc. 2014 Int. Conf. Expo. Electr. Power Eng.*, no. Epe, pp. 52–56, 2014.

[36] A. Raina, R. Hennessy, M. Rains, J. Allred, D. Diven, and M. K. Markey,

“Objective measurement of erythema in psoriasis using digital color photography with color calibration,” in *Annual International Conference of the IEEE Engineering in Medicine and Biology Society.*, 2014, vol. 2014, pp. 3333–3336.

[37] N. Kollias and G. N. Stamatas, “Optical non-invasive approaches to diagnosis of skin diseases,” *J. Investig. Dermatology Symp. Proc.*, vol. 7, pp. 64–75, 2002.

[38] M. H. A. Lahti, H. Kopola, A. Harila, R. Myllyla, “Assessment of skin erythema by eye, laser doppler flowmeter, spectroradiometer, two channel erythema meter, and Minolta chroma meter,” *Dermatological Res.*, pp. 278–282, 1993.

[39] and W. I. l. H. E. L. M. V. Hausser, karl Wilhelm, *Sunburn and suntanning*. London: Pergamon press, 1969.

[40] A. S. C. J. Taylor S.C., “The Taylor Hyperpigmentation Scale: A New Visual Assessment Tool for the Evaluation of Skin Color and Pigmentation,” *Ther. Clin.*, vol. 76, no. 4, pp. 270–274, 2005.

[41] S. Taylor, W. Westerhof, S. Im, and J. Lim, “Noninvasive techniques for the evaluation of skin color,” *J. Am. Acad. Dermatol.*, vol. 54, no. 5, pp. S282–S290, 2006.

[42] I. M. Gibson, “Measurement of skin colour in vivo,” *J. Soc. Cosmet. Chem*, vol. 22, pp. 725–740, 1971.

[43] N. Konishi, A. Kawada, Y. Morimoto, A. Watake, H. Matsuda, N. Oiso, and S. Kawara, “New approach to the evaluation of skin color of pigmentary lesions using Skin Tone Color Scale.,” *J. Dermatol.*, vol. 34, no. 7, pp. 441–446, 2007.

[44] R. G. Kuehni, *Color space and its divisions*, vol. 26, no. 3. Canada: John Wiley & Sons, Inc., Hoboken, New Jersey, 2003.

[45] I. L. Weatherall and B. D. Coombs, “Skin color measurements in terms of CIELAB color space values.,” *J. Invest. Dermatol.*, vol. 99, no. 4, pp. 468–473, 1992.

[46] M. R., *Color physics for Industry*. Society of Dyers and Colorists, Bradford, 1987.

[47] F. R. A. S. T. SMITH, M.A., F.INsT.P., J. GUILD, A.R.C.S., F.INsT.P., “THE C.I.E. COLORIMETRIC STANDARDS AND THEIR USE,” *Trans. Opt. Soc.*, vol. XXXIII, no. 3, 1932.

[48] R. P. C. O. Crick, L. E. in O. King’s College Hospital, London, S. of M. and D. of K. College, U. of L. P. T. K. of G. and W. Healing, C. O. Surgeon, W. H. R. U. Director, M. E. H. and I. of Ophthalmology, and L. University College, *A TEXTBOOK of CLINICAL OPHTHALMOLOGY*. World Scientific Publishing Co. Pte. Ltd., 2003.

[49] T. Root, *Ophthobook*. CreateSpace Independent Publishing Platform, 2009.

[50] J. Serup and T. Agner, "Colorimetric quantification of erythema-a comparison of two colorimeters (Lange Micro Color and Minolta Chroma Meter CR-200) with a clinical scoring scheme and laser-Doppler flowmetry," *Clin. Exp. Dermatol.*, vol. 15, no. 4, pp. 267–272, Jul. 1990.

[51] C. Queille-Roussel, M. Poncet, and H. Schaefer, "Quantification of skin-colour changes induced by topical corticosteroid preparations using the Minolta Chroma Meter," *Br J Dermatol*, vol. 124, no. 3, pp. 264–270, 1991.

[52] A. Fullerton, T. Fischer, A. Lahti, K. P. Wilhelm, H. Takiwaki, and J. Serup, "Guidelines for measurement of skin colour and erythema. A report from the Standardization Group of the European Society of Contact Dermatitis.," *Contact dermatitis*, vol. 35, no. 1. pp. 1–10, 1996.

[53] E. Van den Kerckhove, F. Staes, M. Flour, K. Stappaerts, and W. Boeckx, "Reproducibility of repeated measurements on healthy skin with Minolta Chromameter CR-300.," *Skin Res. Technol.*, vol. 7, no. 1, pp. 56–9, 2001.

[54] S. Park, C. Huh, Y. Choe, and J. Youn, "Time course of ultraviolet induced skin reactions evaluated by two different reflectance spectrophotometers : DermaSpectrophotometer A and Minolta spectrometer CM-2002," *Photodermatol. Photoimmunol. Photomed.*, vol. 18, pp. 23–28, 2002.

[55] C. K. Kraemer, D. B. Menegon, and T. F. Cestari, "Determination of the minimal phototoxic dose and colorimetry in psoralen plus ultraviolet A radiation therapy," *Photodermatol. Photoimmunol. Photomed.*, vol. 21, no. 5, pp. 242–248, 2005.

[56] M. D. Shriver and E. J. Parra, "Comparison of narrow-band reflectance spectroscopy and tristimulus colorimetry for measurements of skin and hair color in persons of different biological ancestry," *Am. J. Phys. Anthropol.*, vol. 112, no. 1, pp. 17–27, 2000.

[57] L. J. Draaijers, F. R. . Tempelman, Y. A. . Botman, R. W. Kreis, E. Middelkoop, and P. P. . van Zuijlen, "Colour evaluation in scars: tristimulus colorimeter, narrow-band simple reflectance meter or subjective evaluation?," *Burns*, vol. 30, no. 2, pp. 103–107, 2004.

[58] K. Yoshimura, K. Harii, Y. Masuda, M. Takahashi, T. Aoyama, and T. Iga, "Usefulness of a narrow-band reflectance spectrophotometer in evaluating effects of depigmenting treatment," *Aesthetic Plast. Surg.*, vol. 25, no. 2, pp. 129–133, 2001.

[59] M. Baquie and B. Kasraee, "Discrimination between cutaneous pigmentation and erythema: Comparison of the skin colorimeters Dermacatch and Mexameter," *Ski. Res. Technol.*, vol. 20, no. 2, pp. 218–227, 2014.

[60] A. R. Matias, M. Ferreira, P. Costa, and P. Neto, “Skin colour, skin redness and melanin biometric measurements: Comparison study between Antera-3D, Mexameter and Colorimeter,” *Ski. Res. Technol.*, pp. 346–362, 2015.

[61] B. L. Diffey, R. J. Oliver, and P. M. Farr, “A portable instrument for quantifying erythema induced by ultraviolet radiation,” *Br. J. Dermatol.*, vol. 111, no. 6, pp. 663–672, Dec. 1984.

[62] P. M. Farr and B. L. Diffey, “Quantitative studies on cutaneous erythema induced by ultraviolet radiation.,” *Br. J. Dermatol.*, vol. 111, no. 6, pp. 673–682, 1984.

[63] J. R. Trevithick, H. Xiong, S. Lee, D. T. Shum, S. E. Sanford, S. J. Karlik, C. Norley, and G. R. Dilworth, “Topical tocopherol acetate reduces post-UVB, sunburn-associated erythema, edema, and skin sensitivity in hairless mice,” *Arch. Biochem. Biophys.*, vol. 296, no. 2, pp. 575–582, 1992.

[64] E. S. Park, J. I. Na, S. O. Kim, C. H. Huh, S. W. Youn, and K. C. Park, “Application of a pigment measuring device - Mexameter - for the differential diagnosis of vitiligo and nevus depigmentosus,” *Ski. Res. Technol.*, vol. 12, no. 4, pp. 298–302, 2006.

[65] K. S. Cheng, M. W. Huang, and P. Y. Lo, “Objective assessment of sunburn and minimal erythema doses: Comparison of noninvasive in vivo measuring techniques after UVB irradiation,” *EURASIP J. Adv. Signal Process.*, vol. 2010, pp. 1–7, 2010.

[66] E. J. Yoshida, H. Chen, M. A. Torres, W. J. Curran, and T. Liu, “Spectrophotometer and ultrasound evaluation of late toxicity following breast-cancer radiotherapy.,” *Med. Phys.*, vol. 38, no. 10, pp. 5747–55, 2011.

[67] M. S. Patterson, B. Chance, and B. C. Wilson, “Time resolved reflectance and transmittance for the non-invasive measurement of tissue optical properties,” *Appl. Opt.*, vol. 28, no. 12, pp. 2331–2336, 1989.

[68] D. T. Delpy, M. Cope, P. van der Zee, S. Arridge, S. Wray, and J. Wyatt, “Estimation of optical pathlength through tissue from direct time of flight measurement.,” *Phys. Med. Biol.*, vol. 33, no. 12, pp. 1433–1442, 1988.

[69] M. S. Patterson, J. D. Moulton, B. C. Wilson, K. W. Berndt, and J. R. Lakowicz, “Frequency-domain reflectance for the determination of the scattering and absorption properties of tissue,” *Appl. Opt.*, vol. 30, no. 31, pp. 4474–4476, 1991.

[70] M. S. Patterson and B. W. Pogue, “Mathematical model for time-resolved and frequency-domain fluorescence spectroscopy in biological tissues,” *Appl. Opt.*, vol. 33, no. 10, pp. 1963–1974, 1994.

[71] J. B. Dawson, D. J. Barker, D. J. Ellis, E. Grassam, J. a Cotterill, G. W. Fisher, and

J. W. Feather, “A theoretical and experimental study of light absorption and scattering by in vivo skin.,” *Phys. Med. Biol.*, vol. 25, no. 4, pp. 695–709, 1980.

[72] G. N. Stamatas, B. Z. Zmudzka, N. Kollias, and J. Z. Beer, “In vivo measurement of skin erythema and pigmentation: new means of implementation of diffuse reflectance spectroscopy with a commercial instrument.,” *Br. J. Dermatol.*, vol. 159, no. 3, pp. 683–90, 2008.

[73] N. Kollias, I. Seo, and P. R. Bargo, “Interpreting diffuse reflectance for in vivo skin reactions in terms of chromophores,” *J. Biophotonics*, vol. 3, no. 1–2, pp. 15–24, 2010.

[74] K. Vishwanath, D. Klein, K. Chang, T. Schroeder, M. W. Dewhirst, and N. Ramanujam, “Quantitative optical spectroscopy can identify long-term local tumor control in irradiated murine head and neck xenografts.,” *J. Biomed. Opt.*, vol. 14, no. 5, p. 054051, 2009.

[75] G. V. G. Baranoski, T. F. Chen, B. W. Kimmel, E. Miranda, and D. Yim, “On the noninvasive optical monitoring and differentiation of methemoglobinemia and sulfhemoglobinemia.,” *J. Biomed. Opt.*, vol. 17, no. 9, p. 97005, 2012.

[76] D. L. Glennie, J. E. Hayward, D. E. Mckee, and T. J. Farrell, “Inexpensive diffuse reflectance spectroscopy system for measuring changes in tissue optical properties,” *J. Biomed. Opt.*, vol. 19, no. December, pp. 105005–1–105005–6, 2014.

[77] A. H. Taylor, “The measurement of diffuse reflection factors and a new absolute reflectometer,” *J. Opt. Soc. Am.*, vol. 4, no. 1–2, p. 9, 1920.

[78] J. a. Jacquez and H. F. Kuppenheim, “Theory of the Integrating Sphere,” *J. Opt. Soc. Am.*, vol. 45, no. 6, p. 460, 1955.

[79] J. W. Pickering, C. J. M. Moes, H. J. C. M. Sterenborg, S. A. Prahl, and M. J. C. van Gemert, “Two integrating spheres with an intervening scattering sample,” *J. Opt. Soc. Am. A*, vol. 9, no. 4, pp. 621–631, 1992.

[80] J. W. Pickering, S. a Prahl, N. van Wieringen, J. F. Beek, H. J. Sterenborg, and M. J. van Gemert, “Double-integrating-sphere system for measuring the optical properties of tissue.,” *Appl. Opt.*, vol. 32, no. 4, pp. 399–410, 1993.

[81] T. J. Farrell, “A diffusion theory model of spatially resolved, steady-state diffuse reflectance for the noninvasive determination of tissue optical properties in vivo,” *Med. Phys.*, vol. 19, no. 4, p. 879, 1992.

[82] a Kienle, L. Lilge, M. S. Patterson, R. Hibst, R. Steiner, and B. C. Wilson, “Spatially resolved absolute diffuse reflectance measurements for noninvasive determination of the optical scattering and absorption coefficients of biological

tissue.,” *Appl. Opt.*, vol. 35, no. 13, pp. 2304–2314, 1996.

[83] R. M. Doornbos, R. Lang, M. C. Aalders, F. W. Cross, and H. J. Sterenborg, “The determination of in vivo human tissue optical properties and absolute chromophore concentrations using spatially resolved steady-state diffuse reflectance spectroscopy.,” *Phys. Med. Biol.*, vol. 44, no. 4, pp. 967–981, 1999.

[84] A. Pifferi, J. Swartling, E. Chikoidze, A. Torricelli, P. Taroni, A. Bassi, S. Andersson-Engels, and R. Cubeddu, “Spectroscopic time-resolved diffuse reflectance and transmittance measurements of the female breast at different interfiber distances.,” *J. Biomed. Opt.*, vol. 9, no. 6, pp. 1143–51, 2004.

[85] D. F. Moscu, “Quantifying chromophore concentration in tissue simulating phantoms using an optical detection system based on an integrating sphere,” p. 153, 2010.

[86] K. Wårdell, H. K. Naver, G. E. Nilsson, and B. G. Wallin, “The cutaneous vascular axon reflex in humans characterized by laser Doppler perfusion imaging.,” *J. Physiol.*, vol. 460, pp. 185–199, 1993.

[87] G. V Oliveira, D. Chinkes, C. Mitchell, G. Oliveras, H. K. Hawkins, and D. N. Herndon, “Objective assessment of burn scar vascularity, erythema, pliability, thickness, and planimetry.,” *Dermatol. Surg.*, vol. 31, pp. 48–58, 2005.

[88] M. Setaro and A. Sparavigna, “Quantification of erythema using digital camera and computer-based colour image analysis: a multicentre study.,” *Skin Res. Technol.*, vol. 8, pp. 84–88, 2002.

[89] B. Jung, B. Choi, A. J. Durkin, K. M. Kelly, and J. S. Nelson, “Characterization of Port Wine Stain Skin Erythema and Melanin Content Using Cross-Polarized Diffuse Reflectance Imaging,” *Lasers Surg. Med.*, vol. 34, no. 2, pp. 174–181, 2004.

[90] S. G. Coelho, S. A. Miller, B. Z. Zmudzka, and J. Z. Beer, “Quantification of UV-Induced Erythema and Pigmentation Using Computer-Assisted Digital Image Evaluation,” *Photochem. Photobiol.*, vol. 82, no. 3, pp. 651–655, 2006.

[91] Y. Bae and B. Jung, “Digital photographic imaging system for the evaluation of various facial skin lesions.,” *Conf. Proc. IEEE Eng. Med. Biol. Soc.*, vol. 2008, pp. 4032–4, 2008.

[92] J. Lu, J. H. Manton, E. Kazmierczak, and R. Sinclair, “ERYTHEMA DETECTION IN DIGITAL SKIN IMAGES,” in *17th International Conference on Image Processing*, 2010, pp. 2545–2548.

[93] D. Hossam, A. Sadek, A. Wagih, and M. Malik, “Clinical photography of skin diseases Photographic Techniques [1],” *Egypt. Dermatology Online J.*, vol. 11,

no. 1, pp. 1–10, 2015.

[94] A. Raina, R. Hennessy, M. Rains, J. Allred, D. Diven, and M. K. Markey, “Objective measurement of erythema in psoriasis using digital color photography with color calibration,” *Ski. Res. Technol.*, no. 7, pp. 1–6, 2015.

[95] D. Ratner, C. O. Thomas, and D. Bickers, “The uses of digital photography in dermatology,” *J. Am. Acad. Dermatol.*, vol. 41, no. 5 I, pp. 749–756, 1999.

[96] A. C. Halpern, A. A. Marghoob, T. W. Bialoglow, W. Witmer, and W. Slue, “Standardized positioning of patients (poses) for whole body cutaneous photography,” *J. Am. Acad. Dermatol.*, vol. 49, no. 4, pp. 593–598, 2003.

[97] W. K. Witmer and P. J. Lebovitz, “Clinical Photography in the Dermatology Practice,” *Semin. Cutan. Med. Surg.*, vol. 31, no. 3, pp. 191–199, 2012.

[98] “CANFIELD.” [Online]. Available: http://www.canfieldsci.com/imaging-systems/visia-cr/.

[99] A. K. CC Zouboulis, AD Katsambas, *Pathogenesis and Treatment of Acne and Rosacea*. Springer-Verlag Berlin Heidelberg, 2014.

[100] S. B. Phillips, N. Kollias, R. Gillies, J. A. Muccini, and L. A. Drake, “Polarized light photography enhances visualization of inflammatory lesions of acne vulgaris,” *J. Am. Acad. Dermatol.*, vol. 37, no. 6, pp. 948–952, 1997.

[101] J. O’doherty, J. Henricson, C. Anderson, M. J. Leahy, G. E. Nilsson, and F. Sjoberg, “Sub-epidermal imaging using polarized light spectroscopy for assessment of skin microcirculation,” *Ski. Res. Technol.*, vol. 13, no. 4, pp. 472–484, 2007.

[102] S. Sridhar and A. Da Silva, “Enhanced contrast and depth resolution in polarization imaging using elliptically polarized light,” *J. Biomed. Opt.*, vol. 21, no. 7, p. 071107, 2016.

[103] Z. Huang, H. Zeng, I. Hamzavi, A. Alajlan, E. Tan, D. I. McLean, and H. Lui, “Cutaneous melanin exhibiting fluorescence emission under near-infrared light excitation.,” *J. Biomed. Opt.*, vol. 11, no. 3, p. 34010, 2006.

[104] J. M. Gallas and M. Eisner, “Fluorescence of Melanin-Dependence Upon Excitation Wavelength and Concentration,” *Photochem. Photobiol.*, vol. 45, no. 5, pp. 595–600, 1987.

[105] N. Kollias, R. Gillies, C. Cohen-Goihman, S. B. Phillips, J. A. Muccini, M. J. Stiller, and L. A. Drake, “Fluorescence photography in the evaluation of hyperpigmentation in photodamaged skin,” *J. Am. Acad. Dermatol.*, vol. 36, no. 2, pp. 226–300, 1997.

[106] R. J. T. Leslie C. Lucchina, Scott B. Phillips, “Fluorescence photography in the evaluation of acne,” *Am. Acad. Dermatology*, 1996.

[107] A. Tosti, F. Torres, C. Misciali, C. Vincenzi, M. Starace, M. Miteva, and P. Romanelli, “Follicular Red Dots,” *Arch Dermatol*, vol. 145, no. 12, pp. 1406–1409, 2009.

[108] A. N. Yaroslavsky, J. Barbosa, V. Neel, C. DiMarzio, and R. R. Anderson, “Combining multispectral polarized light imaging and confocal microscopy for localization of nonmelanoma skin cancer.,” *J. Biomed. Opt.*, vol. 10, no. 1, p. 14011, 2005.

[109] M. Rajadhyaksha, S. González, J. M. Zavislan, R. R. Anderson, and R. H. Webb, “In vivo confocal scanning laser microscopy of human skin II: advances in instrumentation and comparison with histology.,” *J. Invest. Dermatol.*, vol. 113, no. 3, pp. 293–303, 1999.

[110] S. Astner, E. Gonzalez, A. Cheung, F. Rius-Diaz, and S. González, “Pilot study on the sensitivity and specificity of in vivo reflectance confocal microscopy in the diagnosis of allergic contact dermatitis,” *J. Am. Acad. Dermatol.*, vol. 53, no. 6, pp. 986–992, 2005.

[111] S. Astner, N. Burnett, F. Rius-Díaz, A. G. Doukas, S. González, and E. Gonzalez, “Irritant contact dermatitis induced by a common household irritant: A noninvasive evaluation of ethnic variability in skin response,” *J. Am. Acad. Dermatol.*, vol. 54, no. 3, pp. 458–465, 2006.

[112] J. a Suárez-Pérez, “Pathogenesis and diagnosis of contact dermatitis: Applications of reflectance confocal microscopy,” *World J. Dermatology*, vol. 3, no. 3, p. 45, 2014.

[113] R. Proc, S. Vol, W. A. Vii, H. H. Szu, M. Vetterli, W. J. Campbell, J. R. Buss, E. Invited, and N. Gat, “Imaging Spectroscopy Using Tunable Filters: A Review,” Apr. 2000.

[114] D. a Glenar, J. J. Hillman, B. Saif, and J. Bergstralh, “Acousto-optic imaging spectropolarimetry for remote sensing.,” *Appl. Opt.*, vol. 33, no. 31, pp. 7412–24, Nov. 1994.

[115] L. Kong, S. Sprigle, M. G. Duckworth, D. Yi, J. J. Caspall, J. Wang, and F. Zhao, “Handheld erythema and bruise detector,” *Proc. SPIE*, vol. 6915, p. 69153K–69153K–7, 2008.

[116] D. Jakovels, J. Spigulis, and I. Saknite, “Multi-spectral mapping of in vivo skin hemoglobin and melanin,” *SPIE Proc.*, vol. 7715, p. 77152Z–77152Z, 2010.

[117] J. M. Beach, M. a. Lanoue, K. Brabham, and B. Khoobehi, “Portable hyperspectral

imager for assessment of skin disorders: preliminary measurements," in *Photonic Therapeutics and Diagnostics, Proc. of SPIE*, 2005, vol. 5686, pp. 111–118.

[118] Z. Nie, R. An, J. E. Hayward, T. J. Farrell, and Q. Fang, "Hyperspectral fluorescence lifetime imaging for optical biopsy.," *J. Biomed. Opt.*, vol. 18, no. 9, p. 096001, Sep. 2013.

[119] C. Zhang and H. Wang, "The narrow band AOTF based hyperspectral microscopic imaging on the rat skin stratum configuration," *J.Europ.Opt.Soc.*, vol. 14034, 2014.

[120] a. D. Meigs, I. Otten, L.J., and T. Y. Cherezova, "Ultraspectral imaging: a new contribution to global virtual presence," in *1998 IEEE Aerospace Conference Proceedings (Cat. No.98TH8339)*, 1998, vol. 2, no. October.

[121] A. F. H. Goetz, "Three decades of hyperspectral remote sensing of the Earth: A personal view," *Remote Sens. Environ.*, vol. 113, no. SUPPL. 1, pp. S5–S16, 2009.

[122] G. Lu and B. Fei, "Medical hyperspectral imaging: a review.," *J. Biomed. Opt.*, vol. 19, no. 1, p. 10901, Jan. 2014.

[123] S. Zhang, P. Liu, J. Huang, and R. Xu, "Multiview hyperspectral topography of tissue structural and functional characteristics," *J. Biomed. Opt.*, vol. 21, p. 85530P–85530P–7, 2016.

[124] N. Kollias, R. Gillies, J. A. Muccini, R. K. Uyeyama, S. B. Phillips, and L. A. Drake, "A Single Parameter, Oxygenated Hemoglobin, Can Be Used to Quantify Experimental Irritant-Induced Inflammation," *J. Invest. Dermatol.*, vol. 104, no. 3, pp. 421–424, 1995.

[125] G. N. Stamatas, C. J. Balas, and N. Kollias, "Hyperspectral Image Acquisition and Analysis of Skin," in *Spectral Imaging: Instrumentation, Applications, and Analysis II, Proceedings of SPIE*, 2003, vol. 4959, pp. 77–82.

[126] G. N. Stamatas, M. Southall, and N. Kollias, "In vivo monitoring of cutaneous edema using spectral imaging in the visible and near infrared.," *J. Invest. Dermatol.*, vol. 126, no. 8, pp. 1753–1760, 2006.

[127] G. N. Stamatas and N. Kollias, "In vivo documentation of cutaneous inflammation using spectral imaging.," *J. Biomed. Opt.*, vol. 12, no. 5, p. 051603, 2007.

[128] M. S. Chin, B. B. Freniere, Y.-C. Lo, J. H. Saleeby, S. P. Baker, H. M. Strom, R. a. Ignotz, J. F. Lalikos, and T. J. Fitzgerald, "Hyperspectral imaging for early detection of oxygenation and perfusion changes in irradiated skin," *J. Biomed. Opt.*, vol. 17, no. 2, p. 026010, 2012.

[129] G. V. G. Baranoski, S. Member, T. F. Chen, and S. Member, "On the Identification

and Interpretation of Human Skin Spectral Responses Under Adverse Environmental Conditions," pp. 845–848, 2015.

[130] M. Setaro and A. Sparavigna, "Quantification of erythema using digital camera and computer-based colour image analysis: a multicentre study.," *Skin Res. Technol.*, vol. 8, no. 2, pp. 84–8, 2002.

[131] J. Nyström, P. Geladi, B. Lindholm-Sethson, J. Rattfelt, A. C. Svensk, and L. Franzen, "Objective measurements of radiotherapy-induced erythema," *Ski. Res. Technol.*, vol. 10, no. 4, pp. 242–250, 2004.

[132] M. Boone, G. B. E. Jemec, and V. Del Marmol, "High-definition optical coherence tomography enables visualization of individual cells in healthy skin: Comparison to reflectance confocal microscopy," *Exp. Dermatol.*, vol. 21, no. 10, pp. 740–744, 2012.

[133] T. Gambichler, G. Moussa, M. Sand, D. Sand, P. Altmeyer, and K. Hoffmann, "Applications of optical coherence tomography in dermatology," *J. Dermatol. Sci.*, vol. 40, no. 2, pp. 85–94, 2005.

[134] J. W. Elke Sattler, Raphaela Kastle, "Optical coherence tomography in dermatology," *J. Biomed. Opt.*, vol. 18, no. 6, 2013.

[135] D. L. M. Harold Alexander, "Determining Skin Thickness with Pulsed Ultra Sound," *J. Invest. Dermatol.*, vol. 72, no. 1, pp. 17–19, 1979.

[136] A. Warszawski, E. M. Röttinger, R. Vogel, and N. Warszawski, "20 MHz ultrasonic imaging for quantitative assessment and documentation of early and late postradiation skin reactions in breast cancer patients," *Radiother. Oncol.*, vol. 47, no. 3, pp. 241–247, 1998.

[137] E. Szymańska, a Nowicki, K. Mlosek, J. Litniewski, M. Lewandowski, W. Secomski, and R. Tymkiewicz, "Skin imaging with high frequency ultrasound - preliminary results.," *Eur. J. Ultrasound*, vol. 12, pp. 9–16, 2000.

[138] X. Wortsman and J. Wortsman, "Clinical usefulness of variable-frequency ultrasound in localized lesions of the skin," *J. Am. Acad. Dermatol.*, vol. 62, no. 2, pp. 247–256, 2010.

[139] S. Wong, A. Kaur, M. Back, K. M. Lee, S. Baggarley, and J. J. Lu, "An ultrasonographic evaluation of skin thickness in breast cancer patients after postmastectomy radiation therapy.," *Radiat. Oncol.*, vol. 6, no. 1, p. 9, 2011.

[140] X. Wortsman, J. Wortsman, C. Orlandi, G. Cardenas, I. Sazunic, and G. B. E. Jemec, "Ultrasound detection and identification of cosmetic fillers in the skin," *J. Eur. Acad. Dermatology Venereol.*, vol. 26, no. 3, pp. 292–301, 2012.

[141] R. Kleinerman, T. B. Whang, R. L. Bard, and E. S. Marmur, “Ultrasound in dermatology: Principles and applications,” *J. Am. Acad. Dermatol.*, vol. 67, no. 3, pp. 478–487, 2012.

[142] a B. Kimball, R. M. Summers, M. Turner, E. M. Dugan, J. Hicks, F. W. Miller, and L. G. Rider, “Magnetic resonance imaging detection of occult skin and subcutaneous abnormalities in juvenile dermatomyositis. Implications for diagnosis and therapy.,” *Arthritis Rheum.*, vol. 43, no. 8, pp. 1866–73, 2000.

[143] B. Querleux, “Magnetic resonance imaging and spectroscopy of skin and subcutis,” *J Cosmet Dermatol*, vol. 3, no. 3, pp. 156–161, 2004.

[144] E. Burdette, F. Cain, and J. Seals, “In vivo probe measurement technique for determining dielectric properties at VHF through microwave frequencies,” *IEEE Trans. Microw. Theory Tech.*, vol. MTT-28, no. 4, pp. 414–427, 1980.

[145] J. Nuutinen, T. Lahtinen, M. Turunen, E. Alanen, M. Tenhunen, T. Usenius, and R. Kolle, “A dielectric method for measuring early and late reactions in irradiated human skin,” *Radiother. Oncol.*, vol. 47, no. 3, pp. 249–254, 1998.

[146] B. Riordan, S. Sprigle, and M. Linden, “Testing the validity of erythema detection algorithms.,” *J. Rehabil. Res. Dev.*, vol. 38, no. 1, pp. 13–22, 2001.

[147] I. Diebele, A. Bekina, A. Derjabo, J. Kapostinsh, I. Kuzmina, and J. Spigulis, “Analysis of skin basalioma and melanoma by multispectral imaging,” *Biophotonics*, vol. 8427, no. May, pp. 842732–842732–5, 2012.

[148] T. G. Levitskaia, S. A. Bryan, J. A. Creim, T. L. Curry, T. Luders, K. D. Thrall, and J. M. Peterson, “Optical spectroscopy and multivariate analysis for biodosimetry and monitoring of radiation injury to the skin,” *Drug Dev. Res.*, vol. 73, no. 5, pp. 252–273, 2012.

[149] H. Tronnier, “Evaluation and measurement of ultraviolet erythema,” *Biol. Eff. Ultrav. Radiat.*, pp. 255–266, 1969.

[150] M. Ferguson-Pell and S. Hagisawa, “An empirical technique to compensate for melanin when monitoring skin microcirculation using reflectance spectrophotometry,” *Med. Eng. Phys.*, vol. 17, no. 2, pp. 104–110, 1995.

[151] J. W. Feather, M. Hajizadeh-Saffar, G. Leslie, and J. B. Dawson, “A portable scanning reflectance spectrophotometer using visible wavelengths for the rapid measurement of skin pigments.,” *Phys. Med. Biol.*, vol. 34, no. 7, pp. 807–820, 1989.

[152] M. Hajizadeh-Saffar, J. W. Feather, and J. B. Dawson, “An investigation of factors affecting the accuracy of in vivo measurements of skin pigments by reflectance spectrophotometry,” *Phys. Med. Biol. Phys. Med. Biol*, vol. 35, no. 9, pp. 1301–

1315, 1990.

[153] D. M. Cockburn, “Confessions of a colour blind optometrist,” *Clin. Exp. Optom.*, vol. 87, no. 4–5, pp. 350–352, 2004.

[154] T. Pramanik, M. T. Sherpa, and R. Shrestha, “Color vision deficiency among medical students: an unnoticed problem.,” *Nepal Med. Coll. J.*, vol. 12, no. 2, pp. 81–83, 2010.

[155] T. Pramanik, B. Khatiwada, and R. Pandit, “Color vision deficiency among a group of students of health sciences,” *Nepal Med. Coll. J.*, vol. 14, no. 4, pp. 334–336, 2012.

Chapter 3: Tunable Filter-based-Hyperspectral Imaging

3.1 Hyperspectral Imaging (HSI)

Hyperspectral Imaging (HSI), also known as imaging spectroscopy/ chemical imaging [1], [2], is a highly informative imaging technique. Since HSI allows the acquisition of spectral radiance across a relatively wide spatial area. The acquired data is organized in a 3-dimensional structure called datacube. The datacube is composed of a stack of monochromatic images. Each image is built from the captured light reflected back from the object at a distinct spectral band. HSI has been used in many research fields such as agriculture [3], food industry [4], archeology [5], forensic medicine [6], medical diagnosis [7], etc. However, there are individual parameters need to be satisfied for the former fields of research to have a productive use of HSI. These parameters include the acquisition scheme, the operating spectral range, the spectral / spatial resolution, and particular hardware components. As a result, HSI has various categories.

The current chapter discusses the basics of HSI including HSI definition and the intersection between HSI and multispectral imaging (MSI). Next, an overview of HSI various optical schemes is illustrated. Considering a particular scheme as an example, a display for basic HSI optical components is presented. Towards the end of the chapter, a brief description of HSI datacube and commonly utilized datacube analysis methods including, for example, feature selection and image classification are exposed.

3.1.1 HSI Definition

Originally, HSI was introduced in 1985 by Goetz for remote detection and sensing of the earth resources as "*The acquisition of images in* ***hundreds*** *of contiguous, registered, spectral bands, such that for each pixel a radiance spectrum can be derived* [8], [9]. The close imaging style to HSI is multispectral imaging (MSI). However, there are three major differences between HSI and MSI. For instance, the number of bands ranges from 3 to 10 bands in MSI while greater than that in HSI. The number of bands in HSI is originally defined to be in the range of 3-digits figure. However, HSI was involved in many studies with varying numbers of bands including those with less than one hundred bands [10]–[16] and one hundred plus bands [17]–[21]. This variability created an undefined boundary between HSI and MSI. Linguistically, the definition of the word *Multi* means two or more without a limit, while *Hyper* refers to the extremity. Although the lingual definitions specify more bands for HSI relevant to MSI, there is still no crystal clear boundary.

To come over the number of bands intersection, there are two other parameters distinguishing between HSI and MSI; the spectral resolution, and the spectral continuity. Although HSI is often qualified by high spectral resolution and contiguous bands, no clear resolution figure is associated with neither HSI nor MSI. Based on this ambiguity, in a number of bands and resolution, we suggest an updated definition for HSI as; *"*Hyperspectral imaging is the process of capturing tens of consecutive, spectral, co-registered images within thin bandwidths, such that for each captured object spatial point an uninterrupted spectral line of information can be acquired*"*.

3.1.2 HSI basic principle

HSI is a hybrid optical imaging technique formed out of two essential scientific strategies for object investigation; digital imaging and spectroscopy. Digital imaging emerged in the mid of the 20th century. This strategy assisted the researchers in storing and retrieving their visual observations for subsequent analysis. As a result, digital photography allowed advances in education, training, telediagnosis and limited the subjectivity and inter-observer variability in documenting observational data [22]. Since then, digital imaging has become integral to research largely due to the advances in the silicon and optics industry. For example, medical imaging (either via camera-based modalities such as microscopy or through non-camera-based imaging techniques like ultrasound and computed tomography) had a critical role in disease diagnosis [23]–[26]. However, the main limitations with digital imaging are the restriction of the operating spectral bands and its poor spectral resolution. Consequently, HSI is outperforming digital color imaging in the spectral resolution.

The second optical strategy used to form HSI is spectroscopy. In general, spectroscopy investigates the distinct interactions between light and matter. In other words, it studies the behavior of photons as they propagate through tissue structures. More specifically, it studies the light propagation and its loss via absorption and scattering due to objects' optical properties. Besides, it is also involved in light interactions including energy exchange as in the case of fluorescence/ phosphorescence [27]–[29]. Although spectroscopy is doing a great job, it is limited to a point or small area for investigation. Therefore, great effort and lengthy time are required in order to study large tissue's region. One of the intimate techniques relevant to spectroscopy is diffuse reflectance spectra (DRS) measurement. DRS measurement techniques are disfavored by the need for direct contact with the investigated tissue. In some cases, such as burns, direct contact with skin is hard to achieve. Thus, HSI is superior to DRS measurement techniques in the former disfavors; since it is analogous to a *remote* spectroscopic strategy but in large 2-dimensional spatial scale.

HSI essentially produces a datacube which incorporates a wealth of information [30] concerning the object reflectance image (2-dimensions) within the dispersed spectra (one dimension). The spectral radiance of each object's spatial point $S_{(x,y)}(\lambda)$, in (3-1), is the integration of the reflectance upon the operating spectra from the initial wavelength (λ_i), to the final wavelength (λ_f) as illustrated in Figure 3-1. The acquired spectral radiance allows for finding the apparent concentration of the local chromophores existing in the investigated object. Note that the chemical and physical nature of the chromophore (molecular, atomic, or crystal) affects its spectral radiance. Hence, each chromophore, in theory, has a unique spectral radiance.

$$S_{(x,y)}(\lambda) = \int_{\lambda_i}^{\lambda_f} I(x,y) \tag{3-1}$$

The accurate design of HSI requires a proper selection of the spectral region if unique identity for the object's ingredients needs to be found. The choice of the proper spectral region depends on the optical properties of the existing ingredients of the investigated target. The human eye sclera, for example, is a high-density connective tissue encompassing > 80% of the eye surface. Sclera comprises different types of collagen such as type I, III, V, and VI [31], [32]. Scleritis, sclera disease, can cause discoloration of the sclera (white to bluish) [32]–[35], thus investigating the sclera in the visible and NIR spectral regions allows for successful discrimination between the colored symptoms based on the sclera encompassed chromophores [34], [36].

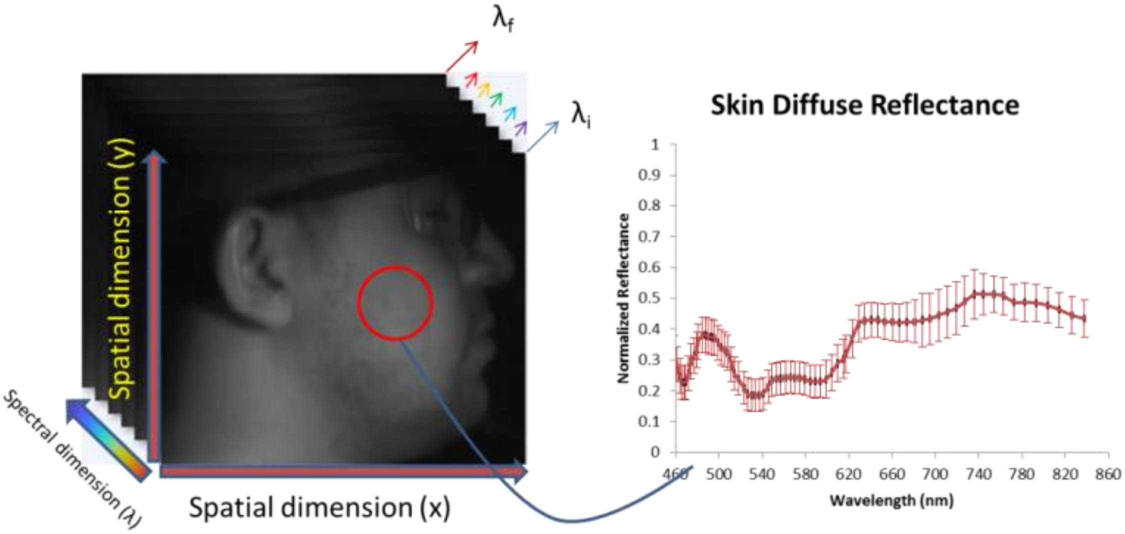

Figure 3-1: An illustration of HSI output datacube, where each pixel can be used to retrieve an uninterrupted spectral radiance of the object under test.

HSI is a progressive technique that is evolving alongside advances in research, technology, and software development. For instance, advances in hardware such as image detectors, filters, and dispersive elements have improved the spectral and the spatial resolution of HSI. In conjunction with hardware advances, intellectual algorithms for image processing paved the way toward robust and real-time analysis of spectral datacube [22]. The choice between distinct hardware alternatives in building HSI configuration resulted in developing various acquisition schemes. Hence an overview of distinct HSI schemes is exhibited in the next section.

3.1.3 HSI spectrometer acquisition schemes

There are few approaches to acquire the 3-dimensional datacube. The two main approaches are the scanning and non-scanning acquisition schemes. For instance, the point scanning scheme is the primary configuration of imaging spectrometers. It is based on engaging a linear digital detector array to collect reflected light intensities from the region of interest point by point on a spatial scanning regime. Significantly rapid readout rates are achieved by dispersing the interested spectrum through a line of sensors. Two galvo mirrors are used to scan the tissue in order to produce 2D slices which then combined at different spectra to create the object datacube. Next to point scanning, the push-broom spectrometer was the second step in the spatial scanning imaging spectrometers. It replaced the point scanning scheme to one-dimensional line imager in which complete spectral data is collected for each line [6]. This configuration employs a slit monochromatic-camera based spectrograph, where a scanning motion is required by either the instrument or the object. A popular application of the push-broom scheme is the scanning airborne HSI platform used in agriculture inspection for crops. Although the precise performance, of the spatial scanning schemes, they suffer from the vibration generated by the scanning movement. In addition, they demand fancy step motors to achieve smooth movement. Furthermore, the output data of the spatial scanning techniques needs a concatenating code to form the datacube.

Fourier Transform (FT) imaging spectrometer scheme applies the concept of Michelson interferometry. In this technique, readings are acquired at distinct optical path differences (OPD) representing a frequency domain tantamount of a filter based camera model [18], [22], [37]. A couple of years ago, an FT improved technique called birefringent FT imaging spectrometer was revealed. The advantage of this spectrometer is its decreased susceptibility to vibration-induced artifacts [38], [39]. Fourier transform infrared (FTIR) spectrometers are known for their high throughput and multiplexing advantages. However, FTIR typically requires pricey pieces of equipment in addition to the high degree of mechanical stability to achieve great performance [40], [41].

Masked aperture imaging spectrometer is a distinct scheme of HSI since it offers FT spectrometer advantages and overcomes FT associated time delay and pricey parts. The basic principle of this spectrometer is replacing the input slit used in the push-broom scheme with a 2-D mathematically coded aperture. This irregular aperture permits both spatial and spectral scanning of the source using bolometer [40]. A bolometer is a transducer that converts the incident light at the detector into thermal and electrical energy corresponding to the optical power. Although the formerly mentioned advantages provided by this scheme, it suffers from various sources of noise such as pattern noise, flickering noise, and photon noises [40], [41].

Snapshot spectral imaging methodology, far from spatial scanning, uses an optical configuration that varies significantly from common HSI setups. The snapshot configuration exhibits a hike in optical signal collection extent. The earliest model of a snapshot imager, as thought to be , was based on Bowen’s invention of his slicing imager

[42]. Over the years, there has been an advance of computational methodologies and hardware development which resulted in the innovation of computed tomography imaging spectrometer (CTIS). Simply, this imager uses a dispersion plane to construct a spectrally painted projection upon an imaging array of sensors permitting the spectral-spatial multiplex [43]. It is of interest to know, snapshot imaging technique doesn’t imply imaging rapidness in itself [37] however, the main advantage of this scheme is the ability to capture the entire datacube in one integration cycle whether taking a minute or longer. Although these advantages of relative time reduction and imaging efficiency, the snapshot imager still requires large sensor formats to capture wide areas in multiple spectral bands and this, in turn, requires an expensive detector. Moreover, it needs significant computational resources to be able to process its output data in a precise manner [37], [44]–[46].

The stare looking, spectral scanning, HSI scheme has the advantage of mechanical stability where no movement is required between the object and the imaging system. The spectral scanning configuration uses a tunable filter to disperse the optical input. The tunable filter is either dynamic, such as the filter wheel [5], [11], or static such as the remotely tunable filters. The filter types have distinct wavelength access speeds. For instance, the wavelength access speed varies from the fastest to the slowest as follows; tens of microseconds in case of acousto-optic tunable filter (AOTF) [2], [47]–[53], tens to hundreds of milliseconds for the liquid crystal tunable filters (LCTF) [54], [55] and mechanically adjusted Fabry-Perot element [5], [37], and approximately one second for the filter wheel.

The other advantage of the stare looking scheme is the capability of imaging wide region in comparison with the whiskey broom, push-broom, and snapshot imaging spectrometers. In addition, it saves large funds required in case of snapshot large sensor size format and digital micromirrors in the case of the FT-based imaging spectrometer. Furthermore, The stare scheme is more compatible with the field environment due to its less sensitivity to mechanical instability [1], [2]. An illustration of the distinct ways of data acquisition in both the scanning and the non-scanning schemes is shown in Figure 3-2. The next section briefly discusses HSI hardware elements in a tunable filter (TF) based stare looking scheme.

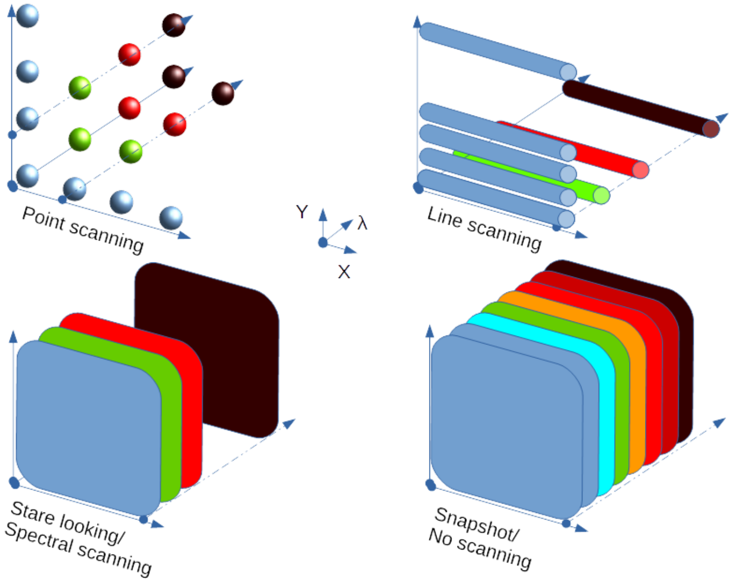

Figure 3-2: An illustration of HSI output datacube various scanning and non-scanning acquisition schemes utilized in hyperspectral imaging setup.

3.2 HSI Hardware Elements

HSI design is an elaborate workflow that starts with a deep understanding of the research problem. Based on the proper understanding, an array of specifications is prepared as objective goals for the planned imaging system design while also dictating the requisite hardware. Figure 3-3 displays a schematic diagram of a basic spectral scanning HSI optical configuration. Illumination for the object under investigation is the first element of the hardware discussion list. Next to illumination, guidelines for the integrated optics in HSI setup are introduced. A key element in this discussion is the tunable filter. Two examples of tunable filters, LCTF and AOTF, are considered in details as common options displaying favor and disfavor of each technology. TF's are convenient in the stare looking schemes due to their electronic control facility, no vibration is produced, and high-speed wavelength random access. Towards the end of this section, the two competing detector technologies; charge-coupled device (CCD), and complementary metal-oxide-semiconductor (CMOS) are briefly discussed in HSI context.

3.2.1 Illumination sources

The choice of the light source for HSI is imperative since it should be relevant to the optical properties of the object of interest. For instance, if the visible spectra (VIS) are more interesting for the study [29], [35], [56]–[62], then the HSI designer should ensure that the illumination source has a high VIS emission. In some cases, the use of filters helps delineate the required spectra while also reduces the optical noise. In VIS, for instance, the common options of illumination are 1) tungsten-halogen, 2) xenon, and 3) white light emitting diodes (LED) sources. Currently, the white LED sources are widely used given their remarkably low power consumption and in turn its heat dissipation.

Unfortunately, LED sources have poor output in the yellow-green spectral region. Xenon illumination, in contrast with LED, has a reasonable spectral emission in the near UV and VIS regions. A smoothing filter is usually coupled with xenon source since the spectral optical output has ripples. With xenon illumination, there is a risk for eye and skin harm due to UV exposure at certain levels of emission. The third option of illumination used in the VIS region of spectra is the tungsten-halogen source. Tungsten-halogen smoothly provides a rising spectral output emission proportional to the wavelength in VIS region and a distinguishable high output in the near infrared. The disadvantages of halogen light are the low output in the blue VIS wavelengths (380-480 nm) which is critical to some applications. In addition, halogen light sources consume high power and dissipates more heat [63], [64] than LED for example. Consequently, the merits and disadvantages of each light source have to be carefully considered alongside the imaging requirements, before an appropriate light choice can be selected.

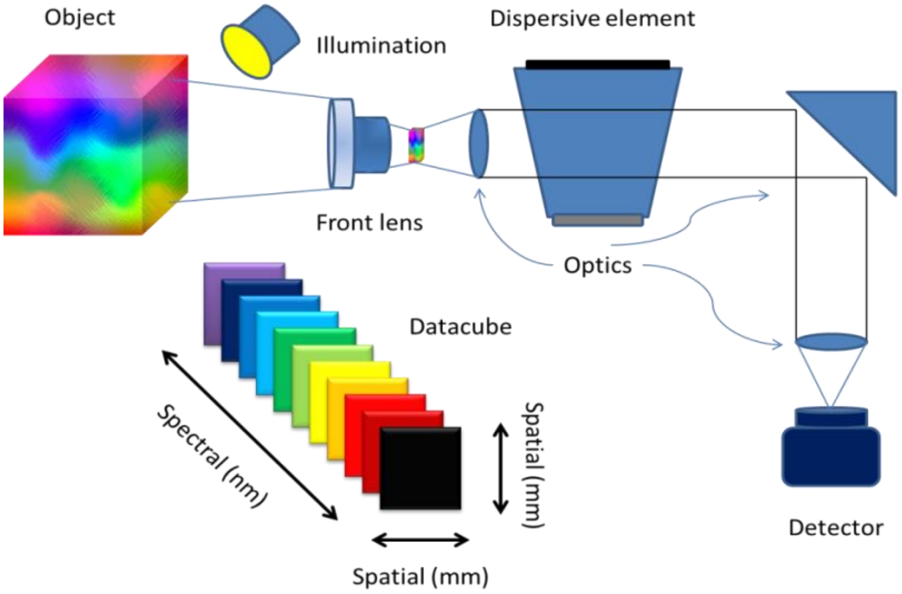

Figure 3-3: A stare looking acquisition scheme of HSI showing the involved main hardware components including lenses, spectral dispersion tool, and detector.

3.2.2 Optical elements

In conjunction with illumination, precise consideration must be given to the optical elements that are integrated into the HSI setup. To satisfy this consideration, optical simulation software is used to virtually test the HSI design. The simulation saves the designer time, effort, and money. Since simulation software models physically unapproachable optical elements such as lenses, mirrors, polarizer plates, etc. Verification of the primary system design is done by numerous tests of system validation. These tests include aberration tests (chromatic aberration, distortion, spherical aberration, etc.) and spatial resolution tests such as contrast transfer function (CTF). The system is then optimized to achieve the maximal design performance. For instance, the relay lenses engaged in HSI to convey the captured images from the object side to the detector stage might need to be achromatic to avoid chromatic aberration artifact. Furthermore, the lenses are recommended to be fast ones (small f-number / large aperture) to collect maximum light. Finally, two extra factors are considered; the field of view and the magnification where both contribute in restricting the imaged ROI and the involved spatial resolution.

3.2.3 Wavelength slicing tools

Along with the formerly mentioned HSI components, a substantial concern should be steered toward the spectral slicing tools selection in HSI design. There are distinct options for spectral chopping tools, however, sticking to one is application-matching based. This diversity of tools can be clustered into four major classes relevant to the imaging spectrometer as follows [65]:

1. Dispersive means
2. Fourier Transform based interferometers
3. Interference filters wheels
4. Remotely-tuned filters

Dispersive means based imaging spectrometer has two available optical elements to diffract the input light; be it a prism or grating. The dispersive tool needs a mechanism to scan the operating band since it generates one image row at a time. In order to acquire all the image rows, a relative displacement should occur between the target and the spectrometer. The displacement takes place in one direction to form one spectral frame and in two directions to build the entire datacube. The great favor of the prism is the high diffraction efficiency while keeping inferior optical scattering. The prism is not the optimum dispersive tool in all cases since it suffers from design complexity versus the corresponding grating model. The grating-based-spectrometer model achieves high optical output for a specific interference order within an interested wavelength. In this case, the linewidth is correlated to the grating number of lines. The direct benefit of replacing a prism with a grating is system simplicity and design compactness. In an effort to construct a hybrid tool, the prism, and the grating were integrated into a compact format, prism-grating-prism (PGP), to achieve the advantage of each and overcome their individual limitations. PGP is structurally a sandwiched grating between two specifically manufactured prisms (almost identical prisms with reversed orientation). PGP has the advantage of sustaining the incident beam direction which facilitates its operation in various medical applications [18], [66], [67]. Nevertheless, PGP decreases the light transmittance due to the increased absorption of the dispersive tool which yields a lower entire system throughput [68].

Fourier Transform (FT) is a second approach for constructing imaging spectrometers. FT-based spectrometers have two common configurations; Michelson and Sagnac architectures. The basic principle of both interferometers, Michelson / Sagnac, is to split the input coherent beam into two parts and commingle them later upon a relative phase difference occurrence due to tested object scanning. The two beam divisions interfere together fulfilling superposition principle. The regenerated beam is then focused at the detector plane, where the optical amplitude is modulated by the two beam divisions' route difference. Sampling the commingled beam at a pertinent sample rate provides FT the opportunity to convey the amplitude modulated beam into the spectral domain.

The major distinction between the two interferometers schemes lies in the beam-mirrors' relative angle. Michelson has a perpendicular angle relative to the beam path and in most cases, there are two, one static and one dynamic, mirrors which are responsible for the path difference. Sagnac beam-mirror angle is mainly fixed ($< 90^o$) while there is no moving mirror in that scheme. The beam splitter in Sagnac configuration induces a phase difference between the two coherent interfered beam divisions. The optical route is altered linearly with beam incidence angle relative to the optical axis of the interferometer. Sagnac design without moving components offers the advantage of high mechanical stability at the expense of only scanning one spatial dimension. Michelson based spectrometer has the privilege of two ways scanning capability with pixel based interferogram (pattern formed due to the interferometer's dual light beams interference). However, Michelson's is more time consuming (moving mirror translation time) with respect to Sagnac [65]. Far from hardware, developing the Fast Fourier Transform (FFT) algorithm combined with technology advances in superior data processing equipment contributed in significantly decreasing the computational time for Fourier transform. Here and now, FT commercial spectrometers become bench-top instruments in research laboratories.

Interference filters are optical windows functioning as band transmitters. The transmitted band is dependent on the applied coating deposited on the filter circular substrates. Moreover, the transmitted band varies proportionally with the angular orientation of the substrate or the embedded dielectric material cross section as shown in Figure 3-4. The transmittance of interference filters is approximately 27.5 ± 2.5 % out of the original beam intensity [65]. Filter wheel imaging spectrometers commonly install 6 to 10 exclusive band-pass filters in a moving wheel. The detector read-out and integration time should be synchronized with the rotation velocity of the filter wheel. The advantage offered by employing variable linear band-pass filters is optical setup modesty. However, it suffers from low spectral resolution, moving part vibration, and extended acquisition time with respect to the corresponding static tunable filters based spectrometers [5], [65], [69].

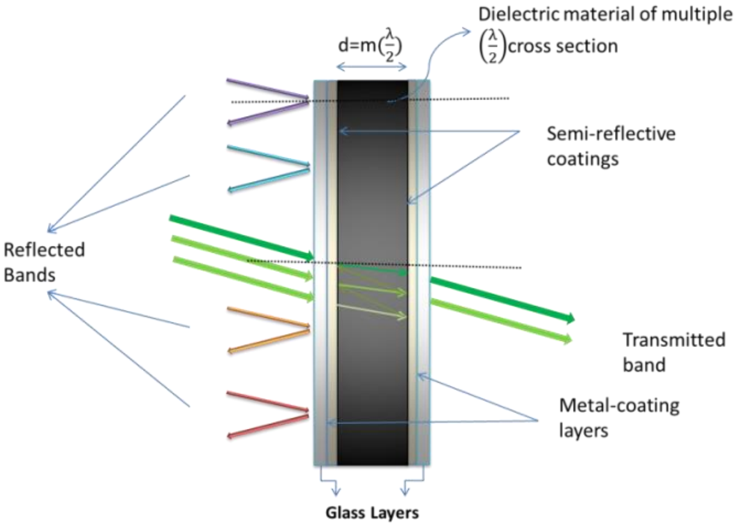

Figure 3-4: An illustration of the interference filter structure and its optical transmission for a single band while suppressing the others.

Tunable Filters are devices that selectively transmit optical waves depending on received control signals. The control signals might be electrical (voltage wave) as in LCTF case, or acoustic as in AOTF. Since there is no flawless equipment; each technology has its favors and disfavors. Hence, HSI setup design should be built on the basis of close matching between the filter specifications and the application requirements. The following section presents three types of tunable filters; Tuned Etalon, LCTF, and AOTF. Comprehensive details of AOTF basic principles are introduced in this section.

Fabry and Perot developed the vertebrae etalon which is named after them in a common optical setup called Fabry-Perot interferometer. The etalon architecture comprises two parallel planes with semi reflective surfaces displaced by a well-determined spacing. The material of the two parallel planes could be glass or transparent structure. Given a certain angle, incident beam will interface a series of transmissions and reflections in the trap between the parallel planes contracting amplitude loss. The phase difference between both the transmitted and reflected beams yields a constructive and destructive interference. The Fabry-Perot interferometer transmitted beam reaches maximal intensity at the instant of the unity order (smallest phase shift) event is achieved.

The Fabry-Perot interferometer qualitatively performs in a similar way to a grating-based spectrometer. However, the grating-based spectrometer is quantitatively beating the Fabry-Perot interferometer. Since the grating provides a smaller order of interference that reaches unity and thus becomes more spectrally selective. The productive operating spectral range of Fabry-Perot interference setup, along with its spectral resolution is based on its order. Lower order Fabry-Perot, which is highly desired, function on a wide spectral range with higher resolution equipment. However, as the order of Fabry-Perot gets lower, the etalon planes spacing needs to be smaller. The Small spacing between the etalon planes requires a complex manufacturing process which in turn is very expensive. One more difficulty of the etalon is the tricky tuning, which can be performed either through plane spacing or beam incidence angle with adjusting the primary etalon surface. Etalon-based spectral imaging systems are limited due to its low throughput which is a consequence of engaging multiple elements in the optical setup. Furthermore, the etalon performance is temperature sensitive [56], [65], [70], [71].

LCTF, the second TF option, is electrically operated. LCTF structure is composed of multiple units of Lyot filter. Lyot filter unit is essentially a birefringent liquid crystal attached to glass and quartz layers and confined between two polarizer plates. The polarizer plates incorporated in LCTF architecture accounts for polarization sensitivity of the LCTF device. LCTF incorporates multiple units attached together to achieve a specific spectral linewidth as shown in Figure 3-5. The central wavelength of the tuned spectral band is linked to the applied voltage signal. Once the input light comes across the birefringent crystal, it is split into two paths since the crystal has two refraction indices; extraordinary beam index of refraction ($\mathbf{n_{ex}}$), and ordinary beam index of refraction ($\mathbf{n_{or}}$). The crystal birefringence property $\mathbf{b = n_{ex}\text{-}n_{or}}$, offers a delay between the two beam paths. The delay caused by the crystal stands behind the retardance (R) concept of LCTF. The retardance is interpreted in angular format as:

$$\boldsymbol{R = 2\pi bl/\lambda} \tag{3-2}$$

The term $\boldsymbol{l}$ is the path length of the light through the crystal. LCTF retardance is a basic factor on its transmission function (T) along with light path length, and eventually light wave number (1/λ) as shown in (3-3).

$$\boldsymbol{T = cos^2(\frac{\pi bl}{\lambda})} \tag{3-3}$$

LCTF maximal transmission condition is (($\frac{\pi bl}{\lambda}$) = nπ) and minimal transmission condition is (($\frac{\pi bl}{\lambda}$) = 2n+1(π/2)) where n is a positive integer. The tunable parameter in LCTF device is the crystal retardance. The crystal retardance is correlated to the applied voltage signal. The crystal offers the facility of succedent and arbitrary wavelength access in the spectral operating range in tens of milliseconds time range. LCTF finds its way in high spatial resolution imaging applications because of its high quality imaging. Furthermore, LCTF is distinguished by its wide acceptance angle, large input/ output apertures, simple operation, and compactness. However, since the electro-optic property of the liquid crystal has limited chance to exist in distinct materials, the spectral range of operation is limited per single crystal. In general, the longest wavelength range of operation for LCTF is the near infrared region (NIR ≃ 1-1.7 µm) [3], [20], [65], [72], [73].

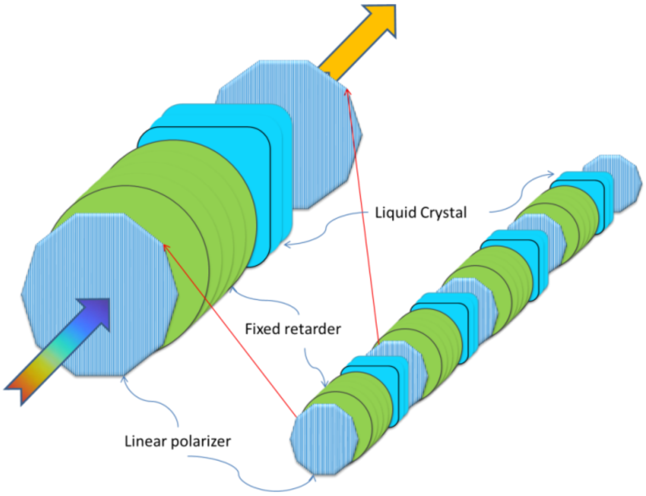

Figure 3-5: A schematic diagram for LCTF basic structure. The filter structure is composed of a sequence of Lyot filter units, where each Lyot unit is formed of a fixed retarder sandwiched between the linear polarizer and liquid crystal plates.

The third tunable filter in the contemporary discussion, AOTF, is based on the Photoelastic phenomenon. This phenomenon is responsible for the acousto-optics (AO) interactions taking place between the traversing mechanical waves (acoustic signals) and the incident electromagnetic waves (optical beam). AO interactions take place if high speed, acoustic range, oscillation stress is applied to a particular birefringent crystal. More often than not, tens/ hundreds megahertz operated-piezoelectric transducer is responsible for initiating the propagation of the acoustic waves through the crystal structure from one side to be absorbed in the other. This high vibrating stress wave produces a traveling disturbance in the crystal structure. This disturbance develops a fluctuating recurrent refractive index inside the material. The fluctuation of the refractive index is due to the transfer of energy bundles named as Phonons [71]. The photon-phonon interactions unfold while only momentum matching comes to pass. The AO interactions are either isotropic or anisotropic [74]. Highlights are shed on both, isotropic and anisotropic, types of interactions.

Isotropic AO interactions produce single/ multiple diffracted optical rays without altering the incident optical beam polarization. Raman-Nath diffraction is named after two scientists had explained the multiple-order isotropic AO interactions, illustrated in Figure 3-6. Raman-Nath multiple-order isotropic AO interaction suffers from low diffraction efficiency, thereby; it didn’t succeed commercially. Bragg diffraction, as with Raman-Nath, is the designated name for the single-order isotropic diffraction, exhibited in Figure 3-7, which is remarkable for high diffraction efficiency. For this specific sense, Bragg diffraction becomes widely applied and employed in the AO bench-top commercial devices [74].

In isotropic acousto-optic interactions, the diffracted optical beams coming out of an AO device can be estimated by solving the wave equation that expresses the optical beam propagation through the AO crystal path length. The isotropic interactions take place because the utilized crystal exhibits the same refractive index for all the diffracted orders. Thereby, an appreciable extent of the zero order optical power is conveyed to the diffracted bands based on a parameter (Q**)** [75], prescribed as follows:

$$\boldsymbol{Q = \frac{K_a(K_aL)}{K_i cos\theta_i} = \frac{2\pi\lambda_i L}{\Lambda(n\Lambda cos\theta_i)}} \tag{3-4}$$

The terms: K_a is the acoustic wave number, L is the crystal length along the optical axis, K_i is the incident optical beam wave number in free space, θ_i is the optical beam incidence angle, λ_0 is the optical beam wavelength in free space, n is the refractive index of the incident optical beam, and Λ is the acoustic signal wavelength. The jth optical diffracted order, out of AOTF crystal, is oriented distinctly with an angle (θ_j) relative to the incident beam. The angle θ_j can be calculated as follows:

$$\theta_j \approx \pm \frac{j\lambda_i}{n\Lambda} \tag{3-5}$$

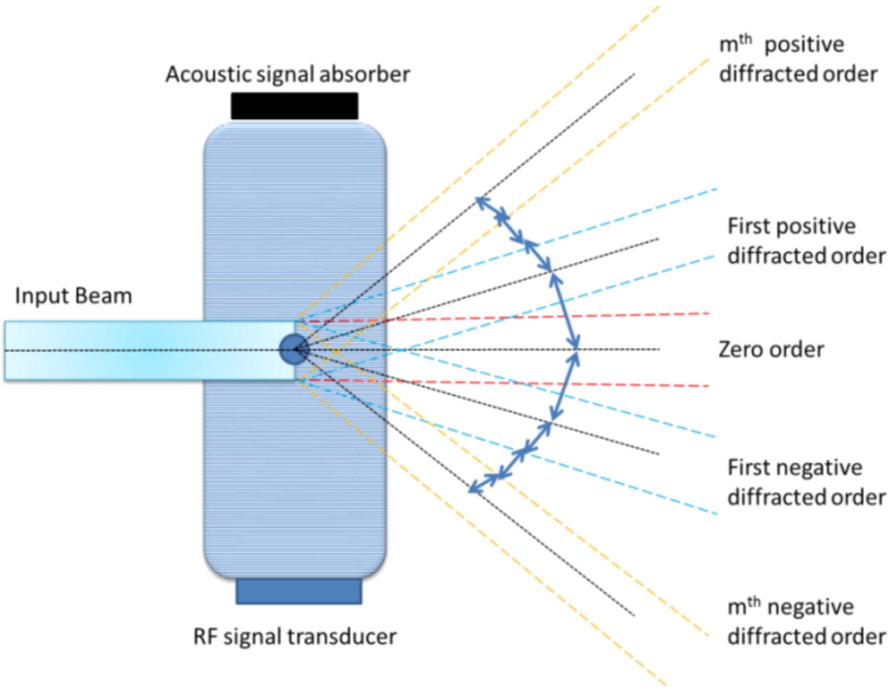

Figure 3-6: A schematic drawing illustrating Raman-Nath multiple-order isotropic acousto-optic interactions in a simplified geometrical form.

It is important to know that the optical diffracted beam intensity would be maximal in the case of satisfying the condition $\theta_j = jQ/2K_aL$. For a single optical diffracted order, angular separation can be calculated as follows:

$$\boldsymbol{\sin\theta_i = \sin\theta_B = \frac{K_a}{2K_i} = \frac{\lambda_0}{2n\Lambda}} \tag{3-6}$$

The Bragg angle θ_B condition is likewise derived by considering photon-phonon interaction phenomenon. This interaction produces a distinct diffracted frequency ω_d and momentum hK_d photon and a phonon vibration frequency Ω_a with momentum hK_a. Engaging both terms energy and momentum conservation laws outturns the following relation:

$$\boldsymbol{\omega_d = \omega_i \pm \Omega_a} \tag{3-7}$$

$$\boldsymbol{\widehat{K}_d = \widehat{K}_i \pm \widehat{K}_a} \tag{3-8}$$

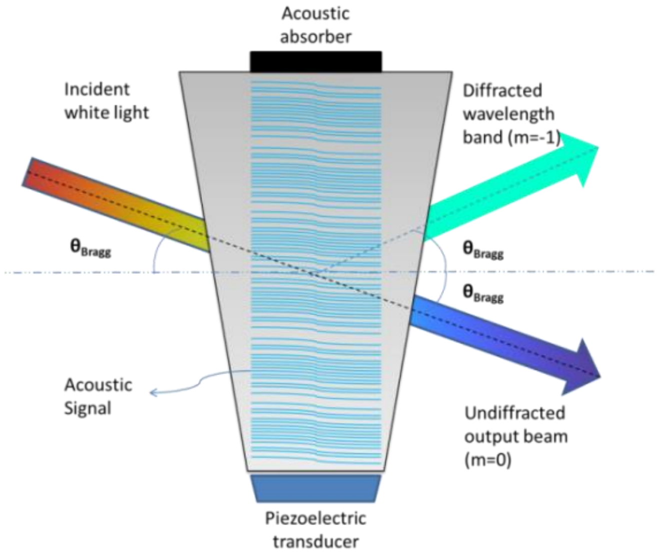

Figure 3-7: A schematic drawing illustrating Bragg single-order isotropic acousto-optic interaction in a simplified geometrical form

It is interesting to realize that different momentum matching cases could take place at various optical wavelengths as illustrated in Figure 3-8. The (±) sign in (3-7) and (3-8) are direction indicators for optical wave propagation versus traversing acoustic wave direction respectively. The relation (3-7) displays the Doppler shift effect that yields the diffracted optical beam based on the relative propagation direction of the incident optical and phase matching of the acoustic signal through the crystal. The wave vector relation between the incident optical wave and the transmitted shear wave, acoustic signal, is expressed in vector form in (3-8).

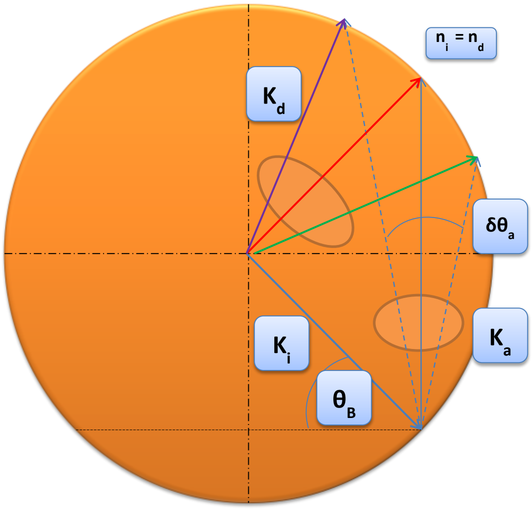

Figure 3-8: An illustration diagram for Bragg different momentum matching cases that could take place at various optical wavelengths diffraction.

Anisotropic AO interactions, dissimilar to isotropic, modify the polarization direction of the diffracted optical beam to become orthogonal in comparison to its incident parent. For example, if the parent beam is vertically polarized the diffracted beam will be horizontally polarized, and vice versa. In fact, the polarization alteration for the incident optical beam comes to pass due to a transient crystalline lattice change. This change is a particular response to the applied vibrating stress. Despite polarization changes, anisotropic crystals exhibit greater efficiencies, accept wider acoustic frequency range, and operate in a wider spectral range. Consequently, Majority of the high-end deflectors and tunable filters take the advantage of anisotropic crystals [71]. Other than AO interactions, deflectors, and TF's efficiency are accentuated by a material-related factor called time-bandwidth product (TBWP). The term TBWP is mainly dependent on the acoustic damping property of the crystal, and in special cases, AO crystal dimensions also play a limiting role [2], [74].

To illustrate more, anisotropic AO interactions generate diffraction for ordinary and extraordinary optical beams traveling through the anisotropic AO crystals. Since ordinary/ extraordinary beams interface distinct refractive indices, due to AO materials birefringence, the diffracted output for each beam confronts polarization rotation of 90^o degrees relative to the incident parent beam. Diffracted optical outputs, in anisotropic crystal, have two different wave vectors K_d magnitude that satisfy the momentum matching for the same incident wave vector K_i. Figure 3-9 displays the wave vector diagram in the case of a negative single axis crystal in which ordinary beam refractive index (n_o) > extraordinary refractive index (n_e) with (n_i=n_o & n_{d}=n_e). This fact illustrates the availability of two disparate acoustic frequencies that are able to satisfy the exact momentum condition for particular spectral band diffraction. In the same figure, it has been illustrated that diffracted wave vector has been modified from K_d to K_d' through acoustic wave vector magnitude alteration from K_a to K_a'. This property gives leverage for the anisotropic AO crystals versus isotropic ones to achieve extended operation bandwidths with fixed diffraction efficiencies. Reorganizing (3-8) for diffracted wavelength encompassing incidence angle θ_i and diffraction angle θ_d in the case of parallel components to acoustic signals leads to the relation (3-9). Processing (3-9) at certain constraints [74] an expression for both incidence, and diffraction angles as a function of acoustic signal frequency are acquired as exhibited in (3-10), and (3-11).

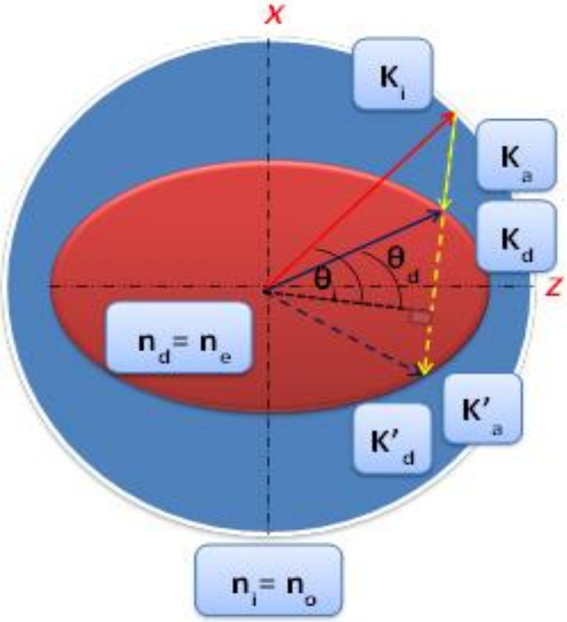

Figure 3-9: displays the wave vector diagram in the case of a negative single axis crystal in which ordinary beam refractive index (n_o) > extraordinary refractive index (n_e) with (n_i=n_o & n_{d}=n_e).

$$\boldsymbol{k_d sin\theta_d + k_i sin\theta_i = k_a} \quad \textbf{(3-9)}$$

$$\boldsymbol{sin\,\theta_i = \frac{f\lambda_0}{2n_iV}\left[1+\left(\frac{V}{f\lambda_0}\right)^2\left(n_i^2-n_d^2\right)\right]} \quad \textbf{(3-10)}$$

$$\boldsymbol{sin\,\theta_d = \frac{f\lambda_0}{2n_dV}\left[1-\left(\frac{V}{f\lambda_0}\right)^2\left(n_i^2-n_d^2\right)\right]} \quad \textbf{(3-11)}$$

It is obvious, the first parts in (3-10) and (3-11) are akin to what ensued in Bragg isotropic diffraction phenomenon, (3-6), except that the last part is the consequence of the anisotropic diffraction [74]. Based on anisotropic interactions, AOTF crystal is confronting refractive indices variation. This variation creates particularly two distinct indices n_o and n_e that interface both ordinary and extraordinary beams correspondingly. Revisiting (3-5), supposing that incident beam is an e-ray; the angular frequency for both optical and acoustic wave vectors can be deducted as shown in (3-12). Mathematically processing the formerly mentioned relation putting the wavelength on the left-hand side and incorporating incidence angle produces the formulae in (3-13).

$$\frac{2\pi n_e}{\lambda} \pm \frac{2\pi f}{v} = \frac{2\pi n_o}{\lambda} \tag{3-12}$$

$$\lambda = \frac{v\Delta n}{f}\sqrt{sin^4\theta_i + sin^2 2\theta_i} \tag{3-13}$$

The relation (3-14) highlights the parameters that control the diffracted wavelength in anisotropic AOTF crystal. Where the acoustic frequency acts as a tuning factor while the optical incidence angle performs as a limiting criterion [71]. The main target of AOTF devices is to free the more interesting wavelength band, diffracted order, from the original incident beam. To do that, there are two common manufacturing configurations for AOTF devices: collinear and non-collinear devices.

The collinear configuration of AOTF has the propagation path for both the incident light waves and the tuning acoustic waves. The purpose of the similar direction of propagation is to increase the photon-phonon interaction chance. In AOTF collinear configuration, polarization rotation for the diffracted output takes place in the crystal; however, diffracted and incident photons are departing in the same direction. Thereby, the collinear AOTF configuration imposes utilizing an external polarizer for the diffracted and the incident beams to be separated.

Non-collinear AOTF configuration, on the other hand, has two nearly perpendicular traveling pathways; one of which is for the optical input while the other is for the tuning acoustic signals [2], [74], [76], [77]. Non-collinear AOTF crystals force the diffracted and the incident beams to depart the crystal in an angularly separated directions. The separation angle, for the non-collinear AOTF crystals, is determined by (3-15) [71]. Hence, the use of non-collinear crystals demands less optical components in comparison to the corresponding collinear ones.

$$\Delta\theta = \Delta n sin\theta_i \tag{3-15}$$

A schematic diagram of the non-collinear AOTF is displayed in Figure 3-10. A piezoelectric transducer is attached to the AOTF crystal. The transducer is operated by an RF driving signal which yields the emission of the shear waves. The shear waves are traversing the crystal structure from one side and killed by the acoustic absorber at the other. AOTF is a polarization sensitive optical element, so the consequence of an incident random polarized white light will be a divergence of both ordinary and extraordinary beams inside the crystal. the beams are obeying Snell's law tailored for the current circumstance in (3-16) [71]. It is of the interest to mention that both beams, ordinary and extraordinary, encompass the diffracted wavelength with the incident momentum M_i. The interaction between these two wavelength photon groups and the acoustic phonons with momentum M_a yields an angle 90^o polarization rotation.

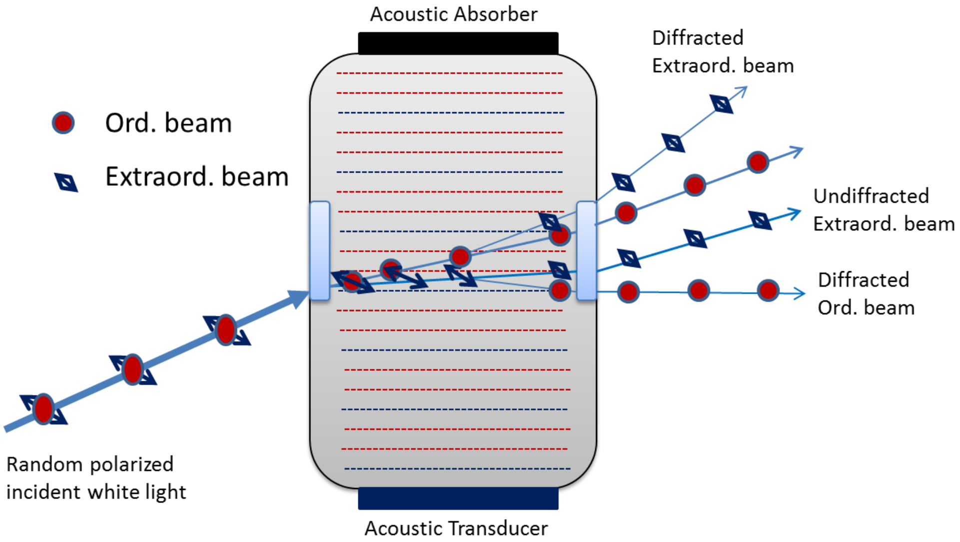

Figure 3-10: A schematic diagram displays a noncollinear AOTF crystal operating in the case of a randomly polarized incident white light.

$$\boldsymbol{n_i \sin\theta_i = n_o \sin\theta_o = n_e \sin\theta_e} \tag{3-16}$$

The two diffracted beams exit the crystal with a distinct angular propagating direction relative to undiffracted beams. One group momentum is equal to its original undiffracted beam plus the phonon momentum which is named the positive first order diffracted beam. The other beam momentum is equal to the undiffracted beam minus the phonon momentum and is called the negative first order. Higher diffracted orders take place in this procedure, although it has lower significance. In the case of an incident polarized light, there is a single first order diffracted output exiting the crystal.

Two crucial factors influencing the operation of AOTF in spectroscopy; the bandwidth, and the angular aperture. The bandwidth of AOTF is identified as the spectral displacement between the middle waist of the diffracted band, full-width half maximum (FWHM or Δλ). FWHM is calculated by an approximated relation shown in (3-17):

$$\Delta\boldsymbol{\lambda} = \frac{\mathbf{0.9}\,\boldsymbol{\lambda}^{2}}{\Delta\boldsymbol{n}\,\boldsymbol{L}\,\boldsymbol{sin}^{2}\boldsymbol{\theta}_{i}} \tag{3-17}$$

Based on (3-17), it is simple to scrutinize the controlling factors for the diffracted bandwidth computation. Basically, the two main factors are the operating wavelength (λ), and the AO interaction length L. Over and above, the angular aperture / acceptance angle is a restriction that needs to be considered in AOTF-based imaging system design to determine the field of view (FOV). The AOTF angular aperture is an urgent parameter in design in the cases of gas monitoring experiments / atomic spectra by which extremely high spectral resolution is required. Next to spectral slicing tools, image detectors are the coming hardware member in HSI setup to be discussed.

3.2.4 Image detectors

The pixel is the basic unit of the detector focal plane array (FPA) used in HSI optical train [7]. FPA encompassed in cameras operates, usually, in a wide spectral region based on its specific quantum efficiency. Employing the most potent detector is essential in spectral imaging system design since it provides an opportunity to detect the low-intensity optical signals. An application-based checklist for detector characteristics should be met for a successful HSI design. These characteristics might include some/ all of the following properties; high signal to noise ratio (SNR), high quantum efficiency, large sensor size/ pixel pitch, long range of exposure time, the large scale of gain and extended digitization [78].

Charge–coupled devices (CCD's) are the common technology used for light detection in the medical applications of imaging spectrometers. The popularity of CCD's comes from its high quantum efficiency, minimal inherent dark current, larger dynamic range, and high fill factor [7] [79] [80]. The advance in technology yields distinct categories of CCD to be used for scientific imaging and spectroscopic applications.

Regarding CCD's categories, the front-illuminated CCD receives photons at the front surface, silicon dioxide, where the significant ratio of these photons didn't survive in the depleted region due to high absorption. Consequently, this category of CCD's can maximally produce 50% quantum efficiency, thereby, it is restricted to tenacious light conditions as in reflection, absorption, and transmission work [79]. To improve the CCD quantum efficiency, back-illuminated CCD's were developed to receive the incident light from the opposite direction as a way for decreasing light loss. As with photons hit the back substrate side minute cross section, it suffers no photons loss, thereby yields higher quantum efficiency that approaches 90% level. This advantage opens the gate for CCD's to detect very low signal levels in applications such as stimulated emissions (luminescence, fluorescence, phosphorescence) measurements. Despite the significant enhancement in quantum efficiency achieved, back illuminated CCD faces an etalon effect in NIR. This effect is basically due to the NIR photons capability to traverse the depletion region and reflect back from silicon dioxide layer causing interference patterns which are difficult for image post-processing to eliminate [79]. Therefore, the deep depletion back illuminated CCD was a good approach to reduce the disadvantage of the traditional back-illuminated CCD category. This manufacturing solution proposes thickening the depletion region, which in turn means longer path length for NIR photons. This path length elongation provided two advantages; the first of which is the NIR higher quantum efficiency and the second is the elimination of etalon effect. However, the disadvantage of the deeply depleted CCD category is its high dark current with respect to its predecessor CCD categories. In terms of applications, deep depletion back illuminated CCD is used in Raman signal measurements with cooling levels reaching -90 to -130^{o}C with thermoelectric cooler/ liquefied nitrogen [79]. Although the improvement in the quantum efficiency in this category of CCD, it was insufficient to serve in ultralow photon counts conditions.

Accordingly, the electron multiplying CCD (EMCCD) is designed to have an enhanced detection technique which is peculiarly light compatible with an ultra low number of photons [7], [79]. The improvement, in EMCCD, detection is based on the signal amplification for each individual pixel likewise the avalanche photodiode procedure. The famous application for EMCCD is the single- molecule excited emission spectroscopy and imaging [7], [79], [81]. Likewise, EMCCD was improved in detection, Intensified CCD (ICCD) is the term coined for the detector used to serve for the high-speed applications in the spectroscopic research field [7], [27], [79]. Basically, ICCD is a product of coupling CCD and a microchannel plate (MCP) image intensifier which is fundamentally a multichannel photomultiplier tube. In ICCD, the photon hits the photocathode which leads to the generation of accelerated electrons which subjected to multiplication process in the MCP. Phosphor screen is used as a transducer that converts the received electrons back to light that detected by the coupled CCD. Since, the intensifying action is simulating the shutter performance, rapid change of applied potential on the photocathode can allow high-speed shutter effect. The formerly mentioned high frame rate is the major advantage of the ICCD versus EMCCD; however, ICCD is not only a pricey instrument but also lifetime limited [7], [79].

In this day and age, the other major approach for manufacturing detectors is depending on complementary metal oxide semiconductor (CMOS). CMOS has proceeded to divergent applications, nowadays, in imaging market due to its cheap cost, high-speed readout and significantly low power consumption. Moreover, CMOS quantum efficiency has been improved in the last two decades which provided this technology a chance to compete in some applications that were solely reserved for CCD's [82]. In spite of CMOS obvious advantages, a recent review of medical hyperspectral applications [7] has mentioned only a single study employing this technology of detectors [83]. The reason of CMOS less attractiveness is the sensor higher inherent dark current noise, less quantum efficiency, lower dynamic range in comparison with corresponding CCD detector [78]. Despite all the CMOS challenges, research and technology don't stop to push the limitations of CMOS sensors further steps to improve its performance. For instance, recent SNR enhancement in CMOS fabrication has paved the way for CMOS to be a feasible option for HSI detector position [84]. In addition, a new generation of the scientific CMOS (sCMOS) is currently competing with EMCCD to be utilized in the very low light conditions and other highly light sensitive applications [85]. In sum, HSI designer needs to determine which of the two technologies is more close to the application requirements? Following proficient image detection, intellectual spectral data processing and analysis are required to extract the valuable information out of the captured data.

3.3 Spectral datacube analysis

HSI produces a 3-dimensional data format called datacube. Two of the captured datacube dimensions are spatial information by which the field of view is represented. The third dimension is the operating spectral range. The cube size is dependent on both the captured field of view area and the operating spectral range combined with the spectral resolution. In general, the HSI output datacube incorporates a huge amount of data. This data includes both significant and insignificant information. The insignificant part is due to the redundancy of information since contiguous bands are highly correlated. The goal of HSI datacube analysis, in the medical field, is not limited to the differentiation between tissues (healthy/ non-healthy) but also mapping, and monitoring individual tissue species based on their current concentrations. HSI data mining is a workflow of image processing stages as step-wise displayed in Figure 3-11. The flow starts with initial data processing (noise reduction and normalization) in order to obtain noise-reduced registered datacube. Once the captured frames are registered, feature (variable) selection, and finally decomposition or classification can be implemented [7].

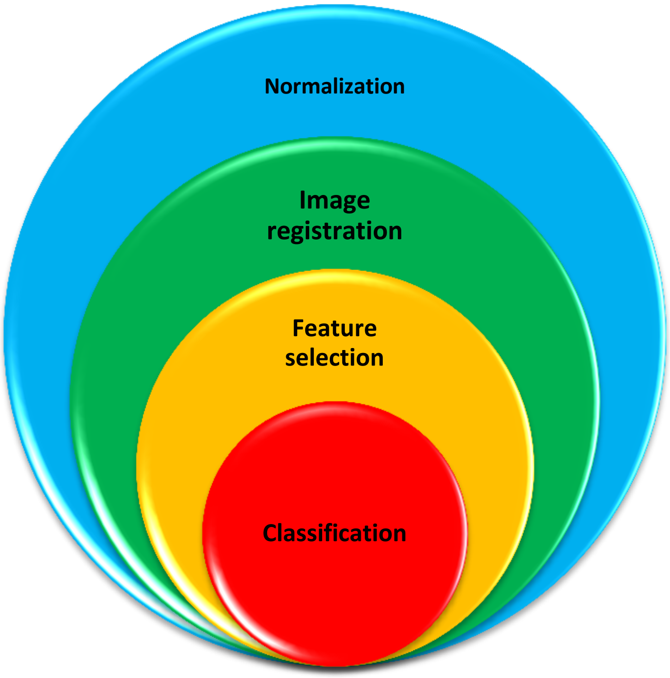

Figure 3-11: displays a flow of hyperspectral imaging output datacube sequence of image processing.

In the beginning, HSI datacube requires initial processing. This processing comprises image normalization in the case of reflectance measurement. Next to normalization, frames registration is essential to maintain the same field of view. To get more in-depth, image normalization is a process accomplished to obtain the spectral radiance be it in the format of absorbance [86], [87] or reflectance based on the application [7], [88]–[90]. Image normalization, in addition, involves the elimination of both system noise and formed image artifacts due to unevenly distributed illumination. For instance, toward eliminating the detector inherent noise (dark current), dark image (S_{dark}) cubes are captured with each individual object datacube. For compensation of uneven distributed illumination, high reflectance standard surface ($S_{white\ Standard}$) are captured with each individual object datacube. In reflectance measurement, the raw detected signal for each sample (S_{object}) is often converted to reflectance R_I as displayed in (3-18) [7], [16], [29]. In contrast, absorbance (A_I) computation is basically the inverse logarithm for the division output of the measured radiance of object of interest upon the white standard, as shown in (3-19). Furthermore, the normalization process is skipping the need to account for the spectral dependence of the different optical elements integrated in the HSI optical setup in the absorbance and reflectance computations [7]. Upon normalization, datacube frames need to be registered to maintain the same field of view.

$$\boldsymbol{R_I = \frac{S_{object} - S_{dark}}{S_{white\ Standard} - S_{dark}}} \qquad \textbf{(3-18)}$$

$$\boldsymbol{A_I = -log_{10}(\frac{S_{sample}}{S_{white\ Standard}})} \qquad \textbf{(3-19)}$$

Image registration is the key solution for achieving precise coincidence among distinct datacube spectral frames. Moreover, registration is necessarily required in the case of acquiring series of measurements through a timeline axis. This is the case for which monitoring a developing phenomenon / disease / treatment efficacy takes place [7]. In practice, image registration is based on selecting a reference band and relatively registering the other bands to the reference one. The reference band quite often lies in the mid-range of operating spectra taking into consideration the overall system efficiency. In order to implement image registration, distinct approaches were used, one of which is utilizing phase correlation between the divergent bands [87], [91]. Once the frames are registered to the reference frame, a refinement process for encompassed data is done to properly designate the potentially more informative bands in the datacube.

Feature extraction and variables selection in HSI is a process implemented to exclude the minor potential informative bands in the captured datacube [7]. Feature extraction often precedes data classification since it provides a better chance for data clustering [92]. It has been shown that hyperspectral datacube includes both rich and poor informative bands, where poor ones contribute less in recognizing the interested features [93]. The capability of reducing the datacube frames is a time-saving process. Principal component analysis (PCA) is a common regime of variable selection among the majority of hyperspectral imaging studies in medical applications [7]. PCA, in general, eliminates the redundancy involved in the highly correlated bands while keeping the most demonstrative and distinguishing features carrying bands [94], [95]. There are some other methods that are based on PCA for feature extraction such as individual component analysis (ICA), where it works on the hypothesis of a linear mixture of independent variables [36], [96]. One more method for multidimensional data decomposition is the linear discriminant analysis (LDA). LDA is used for dimensionality reduction, as well as classification, but with a different implementation. LDA is looking for the knife-cut transformation plane which maximizes the distinction between the intra-categories displacement while preserving the inter-category elements attachment [97].

Classification of data is often the final step in datacube analysis flow. It is employed to draw separate boundaries between the encompassed species in the investigated tissue. Classification of data is based on the information encompassed in the image pixel level as well as the subpixel. Pixel-based classification may adopt parametric or nonparametric techniques. The parametric technique usually speculates normal distribution of features involved in the captured images, such as the maximum likelihood estimation. Support vector machine (SVM) [62], [98], and artificial neural networks (ANN) [67], [99] are popular examples of the nonparametric classifiers that have been widely used in the medical application of HSI. Subpixel-based techniques consider either a linear/nonlinear relationship among endmember components [7].

Pixel and subpixel dependent classifiers are used in both the supervised and unsupervised categories of classification. Supervised techniques, fundamentally, are based on ground truth data for all embedded features in the captured datacubes. Supervision in classification indicates the presence of a certain expertise that is able to accurately identify different clusters in the input data. This expertise is the teacher for the supervised classification algorithm to learn from (training data) and applying later on unclassified data (test data). Unsupervised classification approach, on the other side, has no clue on what sort of features embedded in the input data. Efficient Unsupervised classifiers may yield to decision regions coincident with supervised ones although it is unlabeled [100].

3.4 Summary

In the research work related to this thesis, I decided to engage HSI to address the macroscopic skin acute reaction, skin erythema, induced by radiotherapy treatment. The arguments that motivate my decision for picking HSI are summarized as follows:

1- HSI is an objective technique of its own, where it is based on non-humanoid observations, but extensive data analysis, and reproducible outcomes. HSI is not replacing human experience; however, it works toward the elimination of the subjectivity, and inter/intra-observability full dependence.

2- HSI is a contact-free optical technique. This advantage is imperatively in demand for the severe skin injuries; where skin contact yields unbearable pain such as in dry/wet desquamation reaction or burns.
3- HSI is not limited to a small region of interest, compared to DRS measurement techniques, where a local variation may turn out into a false assessment.
4- HSI, in contrast with traditional digital imaging, has a higher spectral resolution with a contiguous radiance spectrum output which offers a spectral sensation for skin ingredients alteration.
5- Literature work supports the feasibility of addressing skin toxicity due to irradiation employing HSI technique [16].

Based on prior HSI technology discussion, a new configuration of AOTF-HSI was developed, characterized in spatial and spectral domains. Moreover, it is evaluated against a corresponding LCTF configuration. The main purpose of HSI system development is to achieve quantitative while being objective, skin erythema assessment (**Chapter 4**).

References

[1] [1] R. Proc, S. Vol, W. A. Vii, H. H. Szu, M. Vetterli, W. J. Campbell, J. R. Buss, E. Invited, and N. Gat, “Imaging Spectroscopy Using Tunable Filters: A Review,” Apr. 2000.

[2] D. a Glenar, J. J. Hillman, B. Saif, and J. Bergstralh, “Acousto-optic imaging spectropolarimetry for remote sensing.,” *Appl. Opt.*, vol. 33, no. 31, pp. 7412–24, Nov. 1994.

[3] W. Wang, C. Li, E. W. Tollner, G. C. Rains, and R. D. Gitaitis, “A liquid crystal tunable filter based shortwave infrared spectral imaging system: Design and integration,” *Comput. Electron. Agric.*, vol. 80, pp. 126–134, 2012.

[4] H. Huang, L. Liu, and M. O. Ngadi, “Recent developments in hyperspectral imaging for assessment of food quality and safety.,” *Sensors (Basel).*, vol. 14, no. 4, pp. 7248–76, Jan. 2014.

[5] H. Liang, “Advances in multispectral and hyperspectral imaging for archaeology and art conservation,” *Appl. Phys. A*, vol. 106, no. 2, pp. 309–323, Nov. 2011.

[6] G. Edelman, T. G. van Leeuwen, and M. C. G. Aalders, “Hyperspectral imaging for the age estimation of blood stains at the crime scene,” *Forensic Sci. Int.*, vol. 223, pp. 72–77, 2012.

[7] G. Lu and B. Fei, “Medical hyperspectral imaging: a review.,” *J. Biomed. Opt.*, vol. 19, no. 1, p. 10901, Jan. 2014.

[8] B. N. R. A.F.H.Goetz, J.E. Solomon, “Imaging spectrometry for earth remote

sensing," *Science (80-.).*, vol. 228, p. 11471153, 1985.

[9] V. S. A.F.H.Goetz, "Mineralogical mapping in the Cuprite mining district, Nevada," in *Airborne Imaging Spectrometer Data Analysis workshop*, 1985, pp. 22–29.

[10] S. G. Kong, M. Martin, and T. Vo-Dinh, "Hyperspectral Fluorescence Imaging for Mouse Skin Tumor Detection," *ETRI J.*, vol. 28, no. 6, pp. 770–776, Dec. 2006.

[11] Z. Liu, H. Wang, and Q. Li, "Tongue tumor detection in medical hyperspectral images.," *Sensors (Basel).*, vol. 12, no. 1, pp. 162–74, Jan. 2012.

[12] Z. Nie, R. An, J. E. Hayward, T. J. Farrell, and Q. Fang, "Hyperspectral fluorescence lifetime imaging for optical biopsy.," *J. Biomed. Opt.*, vol. 18, no. 9, p. 096001, Sep. 2013.

[13] B. S. Sorg, B. J. Moeller, O. Donovan, Y. Cao, and M. W. Dewhirst, "Hyperspectral imaging of hemoglobin saturation in tumor microvasculature and tumor hypoxia development.," *J. Biomed. Opt.*, vol. 10, no. 4, p. 44004, 2014.

[14] S. Kiyotoki, J. Nishikawa, T. Okamoto, K. Hamabe, M. Saito, A. Goto, Y. Fujita, Y. Hamamoto, Y. Takeuchi, S. Satori, and I. Sakaida, "New method for detection of gastric cancer by hyperspectral imaging: a pilot study.," *J. Biomed. Opt.*, vol. 18, no. 2, p. 26010, Feb. 2013.

[15] N. MacKinnon, F. Vasefi, E. Gussakovsky, G. Bearman, R. Chave, and D. L. Farkas, "In vivo skin chromophore mapping using a multimode imaging dermoscope (SkinSpect™)," vol. 8587, p. 85870U, Feb. 2013.

[16] M. S. Chin, B. B. Freniere, Y.-C. Lo, J. H. Saleeby, S. P. Baker, H. M. Strom, R. a Ignotz, J. F. Lalikos, and T. J. Fitzgerald, "Hyperspectral imaging for early detection of oxygenation and perfusion changes in irradiated skin.," *J. Biomed. Opt.*, vol. 17, no. 2, p. 026010, Feb. 2012.

[17] M. Denstedt, B. S. Pukstad, L. a. Paluchowski, J. E. Hernandez-Palacios, and L. L. Randeberg, "Hyperspectral imaging as a diagnostic tool for chronic skin ulcers," vol. 8565, p. 85650N, Mar. 2013.

[18] B. Khoobehi, "Hyperspectral Imaging for Measurement of Oxygen Saturation in the Optic Nerve Head," *Invest. Ophthalmol. Vis. Sci.*, vol. 45, no. 5, pp. 1464–1472, May 2004.

[19] E. L. P. Larsen, L. L. Randeberg, E. Olstad, O. a Haugen, A. Aksnes, and L. O. Svaasand, "Hyperspectral imaging of atherosclerotic plaques in vitro.," *J. Biomed. Opt.*, vol. 16, no. 2, p. 026011, Feb. 2011.

[20] L. Prisme, P. Orléans, U. Orléans, and D. B. Bp, "Calibration and test of a

hyperspectral imaging prototype for intra-operative surgical assistance," vol. 11, 2013.

[21] Q. Li and Z. Liu, "Tongue color analysis and discrimination based on hyperspectral images.," *Comput. Med. Imaging Graph.*, vol. 33, no. 3, pp. 217–21, Apr. 2009.

[22] Y.-J. Kim, T. Brox, W. Feiden, and J. Weickert, "Spectral Imaging: Principles and Applications," *Cytometry. A*, vol. 71, no. 1, pp. 8–15, 2006.

[23] X. Mao, S. Zhang, H. Chen, L. Du, and G. Li, "Corneal Permeability Assay of Topical Eye Drop Solutions in Rabbits by MRI," vol. 30, no. 6, pp. 804–808, 2010.

[24] R. E. Norman, J. G. Flanagan, S. M. K. Rausch, I. a. Sigal, I. Tertinegg, A. Eilaghi, S. Portnoy, J. G. Sled, and C. R. Ethier, "Dimensions of the human sclera: Thickness measurement and regional changes with axial length," *Exp. Eye Res.*, vol. 90, no. 2, pp. 277–284, 2010.

[25] J. L. Barker, A. S. Garden, K. K. Ang, J. C. O'Daniel, H. Wang, L. E. Court, W. H. Morrison, D. I. Rosenthal, K. S. C. Chao, S. L. Tucker, R. Mohan, and L. Dong, "Quantification of volumetric and geometric changes occurring during fractionated radiotherapy for head-and-neck cancer using an integrated CT/linear accelerator system," *Int. J. Radiat. Oncol. Biol. Phys.*, vol. 59, no. 4, pp. 960–970, 2004.

[26] J. R. Weber, D. J. Cuccia, W. R. Johnson, G. H. Bearman, A. J. Durkin, M. Hsu, A. Lin, D. K. Binder, D. Wilson, and B. J. Tromberg, "Multispectral imaging of tissue absorption and scattering using spatial frequency domain imaging and a computed-tomography imaging spectrometer.," *J. Biomed. Opt.*, vol. 16, no. 1, p. 011015, 2011.

[27] Q. Fang, T. Papaioannou, J. a. Jo, R. Vaitha, K. Shastry, and L. Marcu, "Time-domain laser-induced fluorescence spectroscopy apparatus for clinical diagnostics," *Rev. Sci. Instrum.*, vol. 75, no. 1, pp. 151–162, 2004.

[28] G. Yu, "Near-infrared diffuse correlation spectroscopy in cancer diagnosis and therapy monitoring," *J. Biomed. Opt.*, vol. 17, no. 1, p. 010901, 2012.

[29] D. L. Glennie, J. E. Hayward, D. E. Mckee, and T. J. Farrell, "Inexpensive diffuse reflectance spectroscopy system for measuring changes in tissue optical properties," *J. Biomed. Opt.*, vol. 19, no. December, pp. 105005–1–105005–6, 2014.

[30] A. F. H. Goetz, "Three decades of hyperspectral remote sensing of the Earth: A personal view," *Remote Sens. Environ.*, vol. 113, no. SUPPL. 1, pp. S5–S16, 2009.

[31] P. G. Watson and R. D. Young, "Scleral structure, organisation and disease. A review," *Exp. Eye Res.*, vol. 78, no. 3, pp. 609–623, 2003.

[32] a. N. Bashkatov, E. a. Genina, V. I. Kochubey, and V. V. Tuchin, “Optical properties of human sclera in spectral range 370–2500 nm,” *Opt. Spectrosc.*, vol. 109, no. 2, pp. 197–204, 2010.

[33] P. J. Lanting, P. C. Borsboom, G. J. te Meerman, and L. P. ten Kate, “Decreased scattering coefficient of blue sclerae.,” *Clin. Genet.*, vol. 27, no. 2, pp. 187–190, 1985.

[34] K. L. S. Therese Yamuna Mahesh, “Detection of Diseases based on Vessel Structure and colour changes as viewed on the Sclera Region of the Eye,” in *2014 International Conference on Circuit, Power and Computing Technologies [ICCPCT]*, 2014, pp. 1480–1483.

[35] S. Crihalmeanu and A. Ross, “On the use of multispectral conjunctival vasculature as a soft biometric,” in *2011 IEEE Workshop on Applications of Computer Vision, WACV 2011*, 2011, pp. 204–211.

[36] N. P. Bannister, M. J. Wakefield, a. Tatham, S. L. Bugby, P. M. Molyneux, and J. I. Prydal, “Spectroscopic measurements in scleritis: Bluish-red or deep red?,” *Br. J. Ophthalmol.*, vol. 98, no. 12, pp. 1761–1764, 2014.

[37] N. Hagen and M. W. Kudenov, “Review of snapshot spectral imaging technologies,” *Opt. Eng.*, vol. 52, no. 9, p. 090901, Sep. 2013.

[38] A. Harvey and D. Fletcher-Holmes, “Birefringent Fourier-transform imaging spectrometer.,” *Opt. Express*, vol. 12, no. 22, pp. 5368–5374, 2004.

[39] M. W. Kudenov and E. L. Dereniak, “Compact real-time birefringent imaging spectrometer,” *Opt. Express*, vol. 20, no. 16, p. 17973, 2012.

[40] C. Fernandez, B. D. Guenther, M. E. Gehm, D. J. Brady, and M. E. Sullivan, “Longwave infrared (LWIR) coded aperture dispersive spectrometer.,” *Opt. Express*, vol. 15, no. 9, pp. 5742–5753, 2007.

[41] M. E. Gehm, M. S. Kim, C. Fernandez, and D. J. Brady, “High-throughput, multiplexed pushbroom hyperspectral microscopy.,” *Opt. Express*, vol. 16, no. 15, pp. 11032–11043, 2008.

[42] I. S. Bowen, “The Image-Slicer a Device for Reducing Loss of Light at Slit of Stellar Spectrograph.,” *Astrophys. J.*, vol. 88, p. 113, 1938.

[43] T. Okamoto and I. Yamaguchi, “Simultaneous acquisition of spectral image information.,” *Opt. Lett.*, vol. 16, no. 16, pp. 1277–1279, 1991.

[44] D. J. Mordant, I. Al-Abboud, G. Muyo, a Gorman, a Sallam, P. Ritchie, a R. Harvey, and a I. McNaught, “Spectral imaging of the retina.,” *Eye (Lond).*, vol. 25, no. 3, pp. 309–20, Mar. 2011.

[45] A. Gorman, D. W. Fletcher-Holmes, and A. R. Harvey, “Generalization of the Lyot filter and its application to snapshot spectral imaging.,” *Opt. Express*, vol. 18, no. 6, pp. 5602–8, Mar. 2010.

[46] N. Hagen, “Snapshot advantage: a review of the light collection improvement for parallel high-dimensional measurement systems,” *Opt. Eng.*, vol. 51, no. 11, p. 111702, 2012.

[47] L.-J. C. Tien-Hsin Chao, Jeffrey Yu, George Reyes, David Rider, “ACOUSTO-OPTIC TUNABLE FILTER IMAGING SPECTROMETERS,” *IEEE*, vol. 1, pp. 585–588, 1991.

[48] D. R. Suhre and J. G. Theodore, “White-light imaging by use of a multiple passband acousto-optic tunable filter.,” *Appl. Opt.*, vol. 35, no. 22, pp. 4494–4501, 1996.

[49] I. B. Kutuza, V. E. Pozhar, and V. I. Pustovoit, “AOTF-based Imaging Spectrometer for Research of Small-Size Biological Objects,” *Nov. Opt. Instrum. Biomed. Appl.*, vol. 5143, p. 5143_165, 2003.

[50] M. E. Martin, M. Wabuyele, M. Panjehpour, B. Overholt, R. Denovo, S. Kennel, G. Cunningham, and T. Vo-Dinh, “An AOTF-based dual-modality hyperspectral imaging system (DMHSI) capable of simultaneous fluorescence and reflectance imaging.,” *Med. Eng. Phys.*, vol. 28, no. 2, pp. 149–155, Mar. 2006.

[51] H. Liu, Q. Li, Y. Guan, J. Liu, and Y. Xue, “An AOTF-Based Molecular Hyperspectral Imaging (MHSI) System,” *2011 5th Int. Conf. Bioinforma. Biomed. Eng.*, pp. 1–4, May 2011.

[52] Q. Li, D. Xu, X. He, Y. Wang, Z. Chen, H. Liu, Q. Xu, and F. Guo, “AOTF based molecular hyperspectral imaging system and its applications on nerve morphometry.,” *Appl. Opt.*, vol. 52, no. 17, pp. 3891–901, Jun. 2013.

[53] F. Li, Y. Xu, and Y. Ma, “Design of hyper-spectral and full-polarization imager based on AOTF and LCVR,” in *Intl. Symposium on Optoelectronic Technology and Application*, 2014, vol. 9298, p. 92980U.

[54] S. V. Panasyuk, S. Yang, D. V. Faller, D. Ngo, R. a. Lew, J. E. Freeman, and A. E. Rogers, “Medical hyperspectral imaging to facilitate residual tumor identification during surgery,” *Cancer Biol. Ther.*, vol. 6, no. February 2015, pp. 439–446, 2007.

[55] D. Nouri, Y. Lucas, and S. Treuillet, “Calibration and test of a hyperspectral imaging prototype for intra-operative surgical assistance,” vol. 8676, no. 0033, p. 86760P, Mar. 2013.

[56] E. G. Bucher and J. W. Carnahan, “Characterization of an Acousto-optic Tunable Filter and Use in Visible Spectrophotometry,” *Appl. Spectrosc.*, vol. 53, no. 5, pp.

603–611, May 1999.

[57] K. J. Zuzak, M. D. Schaeberle, E. N. Lewis, and I. W. Levin, “Visible Reflectance Hyperspectral Imaging: Characterization of a Noninvasive, in Vivo System for Determining Tissue Perfusion,” *Anal. Chem.*, vol. 74, no. 9, pp. 2021–2028, May 2002.

[58] K. J. Zuzak, M. T. Gladwin, R. O. C. Iii, I. W. Levin, J. Karel, and R. O. Can-, “Imaging hemoglobin oxygen saturation in sickle cell disease patients using noninvasive visible reflectance hyperspectral techniques : effects of nitric oxide,” vol. 0510, pp. 1183–1189, 2003.

[59] K. Grieve, P. Tiruveedhula, Y. Zhang, and A. Roorda, “Functional imaging with the multi-wavelength imaging with the adaptive optics scanning laser Ophthalmoscope.,” in *Optics express*, 2007, vol. 14, no. 25, pp. 12230–12242.

[60] H. Proença, “Iris recognition: On the segmentation of degraded images acquired in the visible wavelength,” *IEEE Trans. Pattern Anal. Mach. Intell.*, vol. 32, no. 8, pp. 1502–1516, 2010.

[61] S. L. Jacques, J. C. Ramella-Roman, and K. Lee, “Imaging skin pathology with polarized light.,” *J. Biomed. Opt.*, vol. 7, no. 3, pp. 329–340, Jul. 2002.

[62] S. Vyas, A. Banerjee, and P. Burlina, “Estimating physiological skin parameters from hyperspectral signatures.,” *J. Biomed. Opt.*, vol. 18, no. 5, p. 57008, May 2013.

[63] M. Csele, *Fundamentals of light sources and lasers*, vol. 1. 2004.

[64] S. Kitsinelis, *Light Sources technologies and Applications*. CRC press, 2011.

[65] R. T. O. T. Report, *Survey of Hyperspectral and Multispectral Imaging Technologies (Etude sur les technologies d ’ imagerie*, vol. 323, no. May. 2007.

[66] J. M. Beach, M. a. Lanoue, K. Brabham, and B. Khoobehi, “Portable hyperspectral imager for assessment of skin disorders: preliminary measurements,” in *Photonic Therapeutics and Diagnostics, Proc. of SPIE*, 2005, vol. 5686, pp. 111–118.

[67] F. Blanco, M. López-Mesas, S. Serranti, G. Bonifazi, J. Havel, and M. Valiente, “Hyperspectral imaging based method for fast characterization of kidney stone types.,” *J. Biomed. Opt.*, vol. 17, no. 7, p. 076027, Jul. 2012.

[68] P. W. Yuen and M. Richardson, “An introduction to hyperspectral imaging and its application for security, surveillance and target acquisition,” *Imaging Sci. Journal*, vol. 58, no. 5, pp. 241–253, 2010.

[69] J. E. Burger, “HYPERSPECTRAL CHEMICAL IMAGING,” in *UNIVERSITY OF*

STRATHCLYDE'S SECOND ANNUAL ACADEMIC HYPERSPECTRAL IMAGING CONFERENCE, 2011, no. May.

[70] Paras N.Prasad, *Introduction to Biophotonics*. John Wiley & Sons, Inc., 2003.

[71] L. Bei, "Acousto-optic tunable filters: fundamentals and applications as applied to chemical analysis techniques," *Prog. Quantum Electron.*, vol. 28, no. 2, pp. 67–87, 2004.

[72] I. PerkinElmer, "Liquid Crystal Tunable Filters DATA SHEET," 2013. [Online]. Available: http://www.perkinelmer.ca/CMSResources/Images/44-140156DTS_010053A_01_VariSpec_DTS.pdf.

[73] W. Wang, C. Li, E. W. Tollner, G. C. Rains, and R. D. Gitaitis, "A liquid crystal tunable filter based shortwave infrared spectral imaging system: Calibration and characterization," *Comput. Electron. Agric.*, vol. 80, pp. 135–144, 2012.

[74] A. P. (Westinghouse S. and technology center) Goutzoulis and I. . R.Pape, Dennis (Photonic Systems, *Design and fabrication of Acousto-Optic devices*. MARCEL DEKKER INC., 1994.

[75] B. D. Klein, W.R., Cook, "Unified approach to ultrasonic light diffraction," *IEEE Trans.*, vol. SU-14, pp. 123–134, 1967.

[76] C. Zhang, H. Wang, and Y. Qiu, "Study of the Imaging Performance for a Noncollinear Acousto-Optic Tunable Filter," in *Symposium on Photonics and Optoelectronics*, 2010, pp. 1–4.

[77] Y. Zhu, C. Zhang, and B. Zhao, "Design and analysis of a novel noncollinear acousto-optic tunable filter," *Opt. Commun.*, vol. 285, no. 9, pp. 2332–2334, May 2012.

[78] A. Rogalski, "Progress in focal plane array technologies," *Prog. Quantum Electron.*, vol. 36, no. 2–3, pp. 342–473, 2012.

[79] R. Liang, *Biomedical Optical Imaging Technologies: Design and Applications*. 2012.

[80] U. of Arizona) William L.Wolfe(Optical sciences center, *Introduction to imaging spectrometers*. SPIE Optical Engineering Press, 1997.

[81] J. Hernandez-Palacios and L. L. Randeberg, "Intercomparison of EMCCD- and sCMOS-based imaging spectrometers for biomedical applications in low-light conditions," vol. 8215, p. 82150Q, Feb. 2012.

[82] I. Grulkowski, M. Gora, M. Szkulmowski, I. Gorczynska, D. Szlag, S. Marcos, A. Kowalczyk, and M. Wojtkowski, "Anterior segment imaging with Spectral OCT

system using a high-speed CMOS camera.," *Opt. Express*, vol. 17, no. 6, pp. 4842–4858, 2009.

[83] J. Katrašnik, F. Pernuš, and B. Likar, "Illumination system characterization for hyperspectral imaging," *Des. Qual. Biomed. Technol.*, vol. 7891, p. 78910T–78910T–10, 2011.

[84] K. D. Stefanov, B. J. Dryer, D. J. Hall, A. D. Holland, J. Pratlong, M. Fryer, and A. Pike, "A global shutter CMOS image sensor for hyperspectral imaging," vol. 9602, p. 96020K, 2015.

[85] P. Bedggood and A. Metha, "Optical imaging of human cone photoreceptors directly following the capture of light," *PLoS One*, vol. 8, no. 11, 2013.

[86] G. N. Stamatas, B. Z. Zmudzka, N. Kollias, and J. Z. Beer, "In vivo measurement of skin erythema and pigmentation: new means of implementation of diffuse reflectance spectroscopy with a commercial instrument.," *Br. J. Dermatol.*, vol. 159, no. 3, pp. 683–90, 2008.

[87] I. Kuzmina, I. Diebele, D. Jakovels, J. Spigulis, L. Valeine, J. Kapostinsh, and A. Berzina, "Towards noncontact skin melanoma selection by multispectral imaging analysis.," *J. Biomed. Opt.*, vol. 16, no. 6, p. 060502, Jun. 2011.

[88] J. Daugman, "New methods in iris recognition.," *IEEE Trans. Syst. Man. Cybern. B. Cybern.*, vol. 37, no. 5, pp. 1167–1175, 2007.

[89] J. M. Fonville, C. Carter, O. Cloarec, J. K. Nicholson, J. C. Lindon, J. Bunch, and E. Holmes, "Robust data processing and normalization strategy for MALDI mass spectrometric imaging," *Anal. Chem.*, vol. 84, no. 3, pp. 1310–1319, 2012.

[90] R. Koprowski, S. Wilczyński, Z. Wróbel, S. Kasperczyk, and B. Błońska-Fajfrowska, "Automatic method for the dermatological diagnosis of selected hand skin features in hyperspectral imaging.," *Biomed. Eng. Online*, vol. 13, p. 47, 2014.

[91] B. Srinivasa Reddy and B. N. Chatterji, "An FFT-based technique for translation, rotation, and scale-invariant image registration," *IEEE Trans. Image Process.*, vol. 5, no. 8, pp. 1266–1271, 1996.

[92] D. Landgrebe, "Hyperspectral image data analysis," *Signal Process. Mag. IEEE*, vol. LXIII, no. 7, pp. 859–867, 2002.

[93] E. G. B. Costas, P, Christos, *Handbook of Biomedical Optics: Light scattering Methods and Instruments for Medical Diagnosis*. CRC Press, 2011.

[94] L. L. Randeberg, E. L. P. Larsen, and L. O. Svaasand, "Hyperspectral imaging of blood perfusion and chromophore distribution in skin," in *Photonic Therapeutics and Diagnostics V*, 2009, vol. 7161, p. 71610C–1.

[95] F. Palsson, J. R. Sveinsson, M. O. Ulfarsson, and J. A. Benediktsson, “Model-BasedFusion of Multi-and Hyperspectral Images using PCA and Wavelets,” *IEEE Trans. Geosci. Remote Sens.*, vol. 53, no. 5, pp. 2652–2663, 2015.

[96] J. Wang and C. I. Chang, “Independent component analysis-based dimensionality reduction with applications in hyperspectral image analysis,” *IEEE Trans. Geosci. Remote Sens.*, vol. 44, no. 6, pp. 1586–1600, 2006.

[97] Q. Du and H. Ren, “Real-time constrained linear discriminant analysis to target detection and classification in hyperspectral imagery,” *Pattern Recognit.*, vol. 36, no. 1, pp. 1–12, 2003.

[98] H. Akbari, L. V Halig, D. M. Schuster, A. Osunkoya, V. Master, P. T. Nieh, G. Z. Chen, and B. Fei, “Hyperspectral imaging and quantitative analysis for prostate cancer detection.,” *J. Biomed. Opt.*, vol. 17, no. 7, p. 076005, Jul. 2012.

[99] H. Ding, Q. Lu, H. Gao, and Z. Peng, “Non-invasive prediction of hemoglobin levels by principal component and back propagation artificial neural network.,” *Biomed. Opt. Express*, vol. 5, no. 4, pp. 1145–52, 2014.

[100] Y. S. A. (California I. of T. Mostafa, M. Magdon-Ismail (Rensselaer Polytechnic Institute), and H.-T. (National T. U. Lin, *Learning from Data*, vol. XXXIII, no. 2. 2012.

Chapter 4: High Throughput AOTF-based-Hyperspectral Imaging Development

Hyperspectral imaging (HSI) was originally used for remote sensing applications by the National Aeronautics and Space Administration (NASA) agency more than three decades ago [1]. HSI has been known for being capable of remotely identifying visually indistinguishable species within a sizable region based on their spectral features [2],[3]. Therefore HSI finds applications in many research fields including food industry [4], [5], archeology [6], forensic medicine [7], [8], security [9], geology [1], [10]–[12], and medicine [13]. Medical researchers, for example, have incorporated HSI for inspection/ detection purposes in different clinical problems, such as retinal vascular inspection [14], gastric cancer detection [15], tongue lesion classification [16], and tumors residuals precise recognition [17].

The basics of HSI technique have been reviewed in Chapter 3. In fact, it is recognized that robust HSI system design requires its close matching with the targeted application constraints. In this project, I devoted my effort to design a hyperspectral imager, to study skin erythema, bounded by the following system requirements:

1. Sufficient spatial resolution to ensure high-quality imaging of details of the skin surfaces; in order to enable clear decision of skin phenomenon spreading.
2. Working in the visible and near infrared range (450-800 nm) with high spectral resolution; since this range opens the gate for more understanding of the intrinsic chromophores (hemoglobin and melanin) alteration due to irradiation.
3. A field of view (FOV) not less than 10 x10 cm and up to 20x20 cm on the target, while the working distance is no more than 50 cm close to the patient; as the former FOV is the average size of the body treated area taking into consideration part of the surrounding healthy region, while the latter distance is the relative patient-equipment spacing restriction for patient safety.
4. Imaging patients in a clinical setting requires short procedure time; to ensure that patient has less movement during the imaging time, in addition, to causing less inconvenience for participating subjects.
5. The cost of the instrument should also be taken into consideration; hence, it becomes an affordable and attractive instrument in small clinics.

Among current HSI technologies, acousto-optics tunable filter (AOTF) based HSI technique was more appealing for our application due to few reasons:

1. AOTF crystal has fair image quality and can use high-resolution imagers for read-out, thereby it was used for imaging small species and molecules in microscopic applications [18]–[21].

2. AOTF crystals have a good spectral resolution in the visible and near-infrared region; it is also capable of scanning wavelengths randomly or sequentially, therefore it permits operating either in multispectral imaging (MSI) or HSI mode.
3. AOTF crystals with larger apertures enable inspection of a sizable FOV which is a great advantage relevant to the spatial scanning techniques.
4. A significant strength of AOTF is its capability of spectral switching/scanning at high-speed; as such enabling the operation in real time [22], [23] where AOTF speed of wavelength transitions is in the microsecond range .
5. AOTF-HSI is one of the configurations that allow the detector gain and integration time dynamically altered to enhance imaging performance. In contrast, other configurations, such as snapshot HSI imagers, lack this option.
6. In addition, Compact size [11], [24], [25], and no mechanical movement are two significant factors which permit integrating AOTF-HSI with other optical configurations [26], [18], [27], [28].

4.1 AOTF-HSI system design

Typically, the AOTF crystals used in imaging are optimized to be polarization sensitive, to a single polarization, in order to maximize the angular aperture. However, this crystal optimization resulted in a lower system throughput due to the inherent loss in the case of randomly polarized input light. I report, here, the development of a new dual channel AOTF-HSI configuration. The new configuration improves the imager throughput by injecting two polarized input components rather than one. In contrast with existing configurations of: (1) single input beam of randomly polarized light [10], [29]–[32], or (2) single input beam of AOTF matching polarization, past developed AOTF- imagers [18], [33], the added share of the optical input yields a relative increase in the diffracted output by 67.55% for the first case and 147.08 % in the other. Furthermore, this configuration provides an evidence on the feasibility of replacing the most commonly used charge-coupled device (CCD) [13] with its less-often used cheaper alternative complementary metal-oxide-semiconductor (CMOS) in HSI medical applications.

In this section, the detailed description of the design and implementation of the newly developed high throughput AOTF-HSI optical configuration is provided. The schematic diagram of the newly developed AOTF-HSI dual channel configuration is displayed in Figure 4-1.

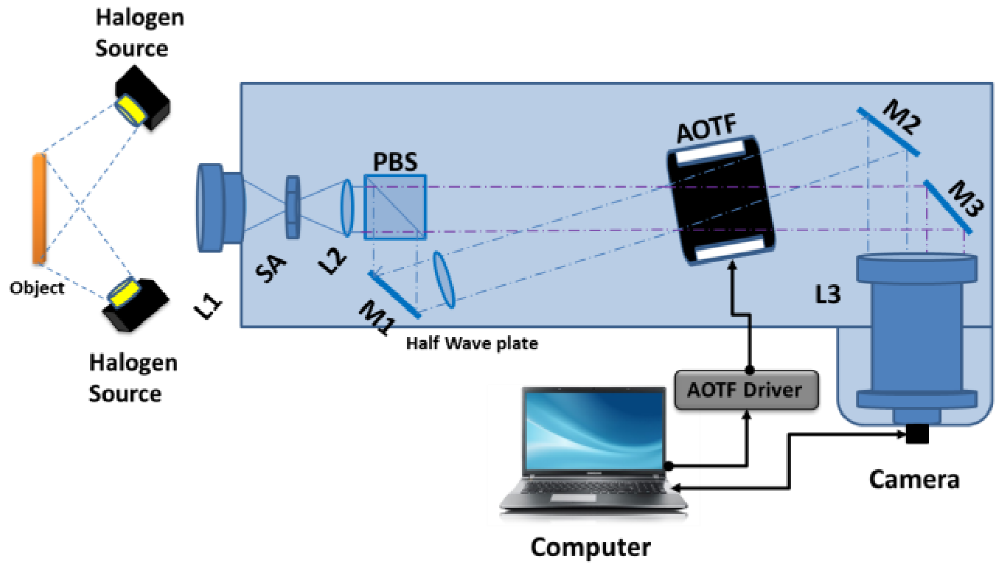

Figure 4-1: A schematic drawing displays the acousto-optic tunable filter (AOTF)-based hyperspectral imaging (HSI) system new configuration. L1: zoom lens; SA: square aperture acting as field aperture; L2, L3: achromatic lenses; M1, M2, M3: flat mirrors; PBS: polarizing beam splitter; AOTF: acousto-optic tunable filter; camera for capturing images, and computer for system control and data storage, all the components are tightly fixed to a metal platform to ensure portability.

4.1.1 AOTF-HSI optical design

Once the light shines on the region of interest, it reflects back in the form of specular and diffuse reflections. The specular reflection probes the surface information, while the diffuse reflection probes the underneath tissue layers. Since the diffusely reflected photons have a propagation path underneath the object's surface before it bounces back. In my work, I was more interested in the diffused reflected light. To acquire the interested portion of reflected light with less shadow effect, illumination and detection were positioned with an acute angle (~ 45^o degrees) relative to each other. The diffusely reflected portion of the light is collected by a zoom lens L1 and focused to form the object image at the AOTF-HSI first focal plane. A square aperture (8 mm x8 mm) is placed at the focal plane to clear any optical noise out of the object image. The formed image is conveyed via a collimated beam by the primary relay achromatic lens L2 toward the polarizing beam splitter (PBS**)**. To this end, the entire diffusely reflected light would suffer a great reduction in intensity if passed toward AOTF since the former is polarization sensitive. Therefore, it is required to have a polarizing optical element ahead of the AOTF crystal. The polarizing plate option, ideally, will let a sole polarization pass, and thus the diffusely reflected light intensity will be significantly reduced.

To overcome the low throughput of the contemporary configurations, I integrated a PBS which divides the collimated input beam into two orthogonal polarized rays. One ray is transmitted parallel to the system's optical axis while the other ray is reflected perpendicularly. The PBS was oriented such that the transmitted ray polarization matches the AOTF crystal one, while the PBS reflected ray is orthogonally polarized to the former. Rather than losing the orthogonally polarized input light, it was guided, via a deflecting mirror, toward a half-wave ($\lambda/2$) plate. The plate rotates the PBS reflected ray polarization 90^o degrees. Thereby, both PBS output rays become matching the AOTF crystal. In order to fit PBS output rays into the AOTF crystal angular aperture ($\pm 2^0$ degrees), the crystal was tilted relative to the system's optical axis. The two PBS rays were planned to be forced to traverse the same path length. The purpose for that is taking to maintain similar magnification as demonstrated below in details. According to the design and computation, shown in Figure 4-2, a non-significant difference, ~ 1mm, was found as the total change in the path length between the two rays which is less than 0.2%. Thus negligible magnification difference exists between the dual arms' images.

Transmitted beam path length = $28.1 + 245.3 + (24.5 * \cos(2^o)) + 216.8 + 26.8 = 541.48$ mm

Reflected beam path length = $28.1 + 19.9 + 218 + (24.5 * \cos(2^o)) + 203.8 + 46 = 540.29$ mm

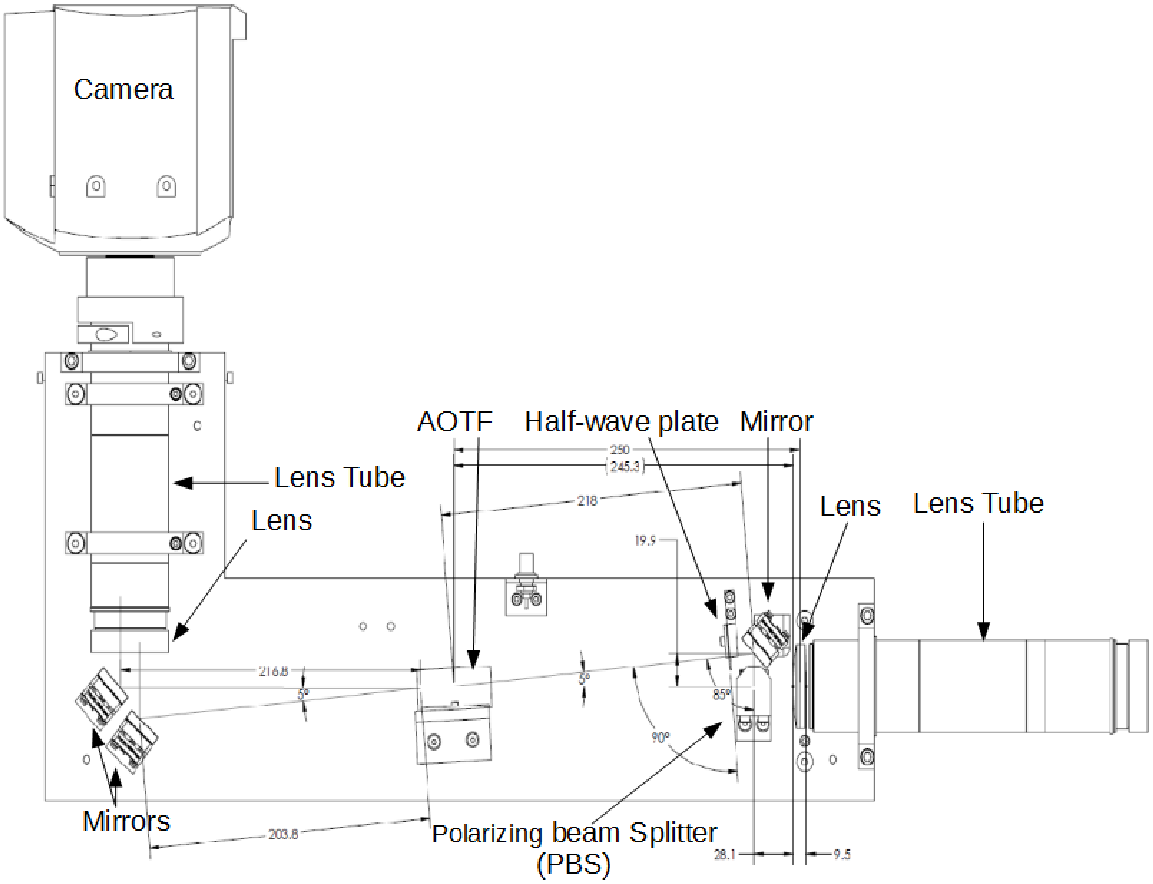

Figure 4-2: A detailed design diagram showing the positions including the angles and displacements of the integrated optical elements in the developed AOTF-HSI system excluding the front zoom lens.

Consequently, the tunable filter, now, has two input polarized rays incident within the angular acceptance of the crystal. As such, AOTF diffracts, ideally, two typical monochromatic bands in wavelength and linewidth but with different directions. Thus, two mirrors M2 and M3 are precisely positioned to skip the original, undiffracted, beams while deflecting the diffracted AOTF beams toward the second relay achromatic lens L3. The optical relay lenses L2 and L3 are selected to be identical in order to convey the object image formed at the square aperture with 1:1 magnification to the sensor. A 3-dimensional system model illustrating the AOTF-HSI real implementation and the optical flow is displayed in Figure 4-3.

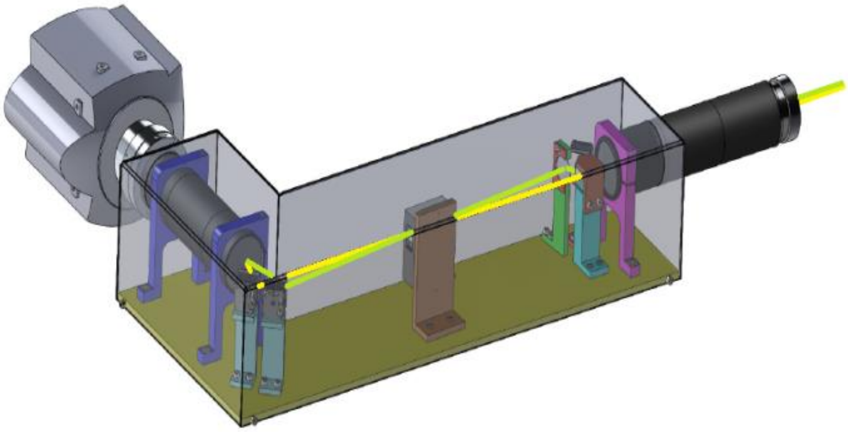

Figure 4-3: A model illustrating the implementation of the developed AOTF-HSI and the optical input flow throughout the entire system optical train of elements.

4.1.2 Electronics and acquisitions

The spectral dispersion is accomplished using a polarization sensitive AOTF filter (TF625-350-2-11-BR1A, Gooch & Housego, FL, USA) with a relatively large aperture window (11 mmx12 mm); as such it is suitable for imaging applications. To illustrate more on AOTF, the filter tellurium dioxide (TeO2) crystal is optimized to operate with high pointing stability of diffraction for a specific polarized input. The purpose of optimization is to permit imaging of wide field of view. The filter is operating in the range of 450:800 nm and thus allows the operation within the visible-near infrared (VIS-NIR) spectral region. Along the range of operation, AOTF has a variable spectral resolution (FWHM) ranges from < 1 nm @ 450 nm, and up to ~4 nm @ 800 nm, with an average of < 3 nm at 625 nm. The high spectral resolution of AOTF enables the operator to distinguish between the close spectral features relevant to an object. The filter is controlled by an 8-channel digital radio frequency (RF) synthesizer (MSD040-150-0.2ADM-A5H-8 x 1, Gooch & Housego, FL, USA). The RF signal used for AOTF operation ranges from 65-135 MHz to span the whole spectral range, however, the RF synthesizer range of operation is wider. As an option, the driver is capable of transmitting eight distinct frequencies simultaneously and thus provides the opportunity to diffract eight different bands.

The imager detector (MQ042RG-CM, Ximea, Munster, Germany) incorporated in the setup is a monochromatic CMOS sensor which is enhanced for infrared detection. It has an active sensor area of (11.27 mm x 11.27 mm), since then it permits capturing the entire field of view. The sensor has a high spatial resolution of 2048 x 2048 pixels with 5.5 µm pixel pitch. The camera exposure time ranges from $26{:}10^6$ µsec and supports up to 90 frames per second at 1x1 binning. The detection sensor was chosen due to several advantages: (1) compactness (26.4x26.4x30.25 mm), (2) lightweight (32.1 g), (3) large sensor format 1 inch^2, (4) signal to noise ratio (SNR) equals to 41 dB and (5) low cost with respect to the corresponding CCD alternative. Aside from the detector, a workstation was used to control the camera detector and the AOTF driver. The workstation is an Intel i7 dual-core processor ASUS laptop operated by Windows 7 Enterprise and equipped with a touch screen to make the control more convenient. A schematic diagram, of the integrated electronic components and its interconnectivity, is displayed in Figure 4-4.

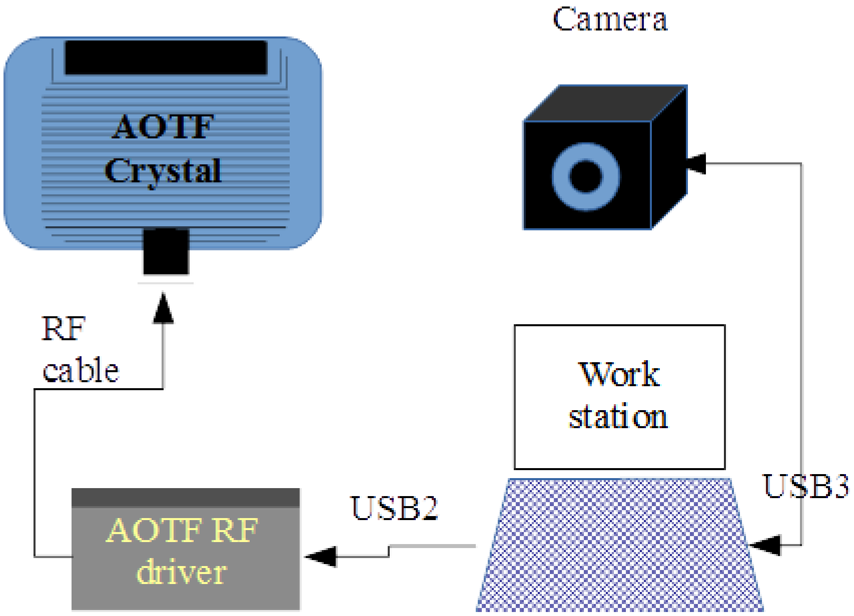

Figure 4-4: A schematic diagram displays AOTF-HSI system electronic parts communication. The workstation is controlling both the camera shutter speed; in order limit the exposure time along with the gain value, and the RF driver; frequency, amplitude, phase, and a number of operating channels. The RF driver, in turn, controls the AOTF crystal tuning through transduced acoustic signals that yield to the diffraction of specific band/s.

A C-language program was developed in order to fully automate and synchronize the operation of the AOTF device along with the camera. To establish the harmony between AOTF wavelength switching and the sensor shutter speed, the predefined sensor's integration time, AOTF transition speed, and delay due to workstation intercommunication are taken into consideration. The objective of the data acquisition and control program design is to ensure (1) the modesty of operation needed by non-professionals, and (2) clarity of parameters (ranges, and default values). Therefore, the developed program's interface was created to provide the user with the straightforward operation. The developed interface program has various options for operating the imaging spectrometer. For instance, it allows the user to randomly or sequentially access distinct spectral bands in single or sweep modes. In sweep mode, the user selection of fixed or dynamic integration time is passed to the detector in order to sequentially adapt for the system response at different wavelengths. Furthermore, there are several parameters available for the user to control the procedure of spectral imaging including the RF signal amplitude (0-0.2 watt), the phase difference between the AOTF driver channels, and the number of operating channels (1-8 channels) for the AOTF driver. For the sensor, the integration times along with sensor gain (0-6 dB) are also tunable. The goal of the system's synchronization is to prompt AOTF, and the detector shutter to operate in the correct time window for each synchronously.

4.2 Imaging System Characterization

In this section, we introduce the characterization procedure steps accomplished in order to identify the major operating parameters of the newly developed AOTF-HSI system. The procedure is divided into three stages; (1) throughput evaluation versus existing configurations, (2) spectral characterization including RF tuning, measurement of the diffracted beam linewidth/ bandwidth, and the impact of the RF signal amplitude on the diffracted band, (3) spatial characterization involving delineating the optimum distance between the object and HSI first lens, the spatial resolution, and the depth of focus (DOF).

4.2.1 Throughput evaluation

The dual channel imaging AOTF-HSI configuration was evaluated in order to compare its performance to the current single channel configurations. The single channel configurations are based on either capturing random polarized reflected light and then capture one out of two diffracted beams [10], [26], [29], [11], [34], [20], [31], [32] or to capture a linearly polarized input which has only one diffracted output [18], [35], [33]. For evaluation purposes, a continuous wave diode laser source emitting at $\lambda = 650$ nm was used to shine directly toward the imaging spectrometer. The laser diffracted intensity was collected via a collimating lens coupled to an optical fiber that is connected to the optical multimeter (1830C, Newport, Irvine, CA, USA). This procedure is repeated in the next three different configurations and displayed in Figure 4-5:

1- No PBS; randomly polarized input beam to the AOTF crystal

2- Linear polarizer; matching polarized input beam to the AOTF crystal

3- PBS; two matching polarized input beams to the AOTF crystal

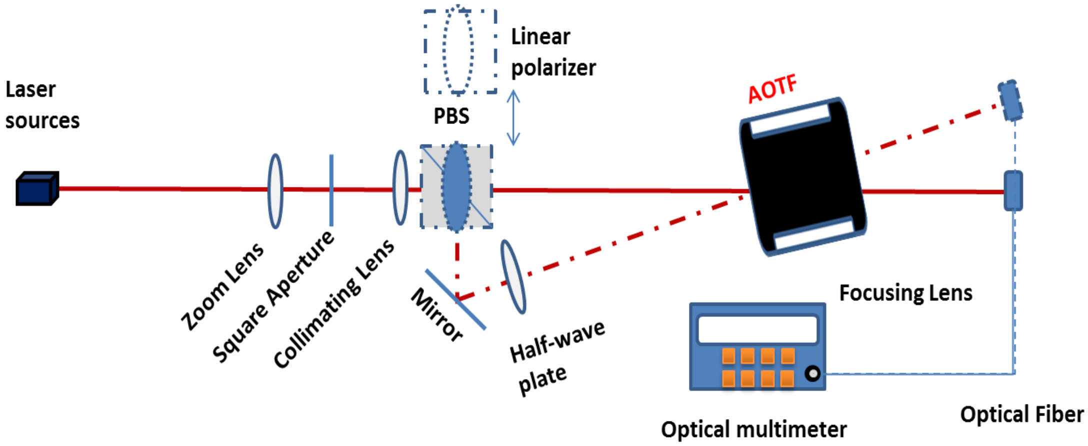

Figure 4-5: A schematic diagram shows the procedure of evaluating the newly developed AOTF-HSI dual channel configuration, in terms of throughput, in contrast with the two current AOTF-based-single configurations. First case: when randomly polarized input light is allowed to go through the AOTF crystal and thus the crystal diffracts two orthogonally polarized beams excluding the incident one. Second case: when a linear polarizer plate (blue oval) is positioned ahead of the AOTF crystal and thus a single beam is diffracted out of the crystal.

In the case of randomly polarized beam is input to the AOTF crystal, higher diffracted beam intensity was produced. However, this configuration might require two separate detectors for both positive and negative orders to be collected; as such it becomes more complex and expensive. Moreover, this configuration either loose diffraction stability (whenever employing polarization sensitive AOTF crystals), or loose wide angular acceptance in non-optimized AOTF crystals.

In the second case, where the linear polarizer is positioned ahead of the AOTF crystal, the plate permits, ideally, nothing to pass but the AOTF crystal matching polarized portion of the input beam. Thus, this configuration yields the lowest diffracted output intensity since the polarizer plate significantly cut the intensity of the input beam before AOTF diffraction. Consequently, this configuration needs a high sensitive sensor to detect the captured low level of diffracted light.

Aside from the previous AOTF-HSI configurations, integrating PBS allows two orthogonally polarized beams to pass. Adding the half-wave plate in the way of the reflected PBS beam permits the combination of both the transmitted and reflected beams intensities. However, the two beams, now match the AOTF polarization. In turn, this optical setup resulted in significant increase in the total diffracted intensity out of the AOTF crystal. This relative increase in the intensity was quantitatively computed and found to be 67.55 % against the randomly polarized input and 147.08 % against the linearly polarized input. Hence, the newly developed dual channel AOTF-HSI configuration provided an evidence of higher throughput versus the current AOTF-HSI configurations as illustrated in Figure 4-6.

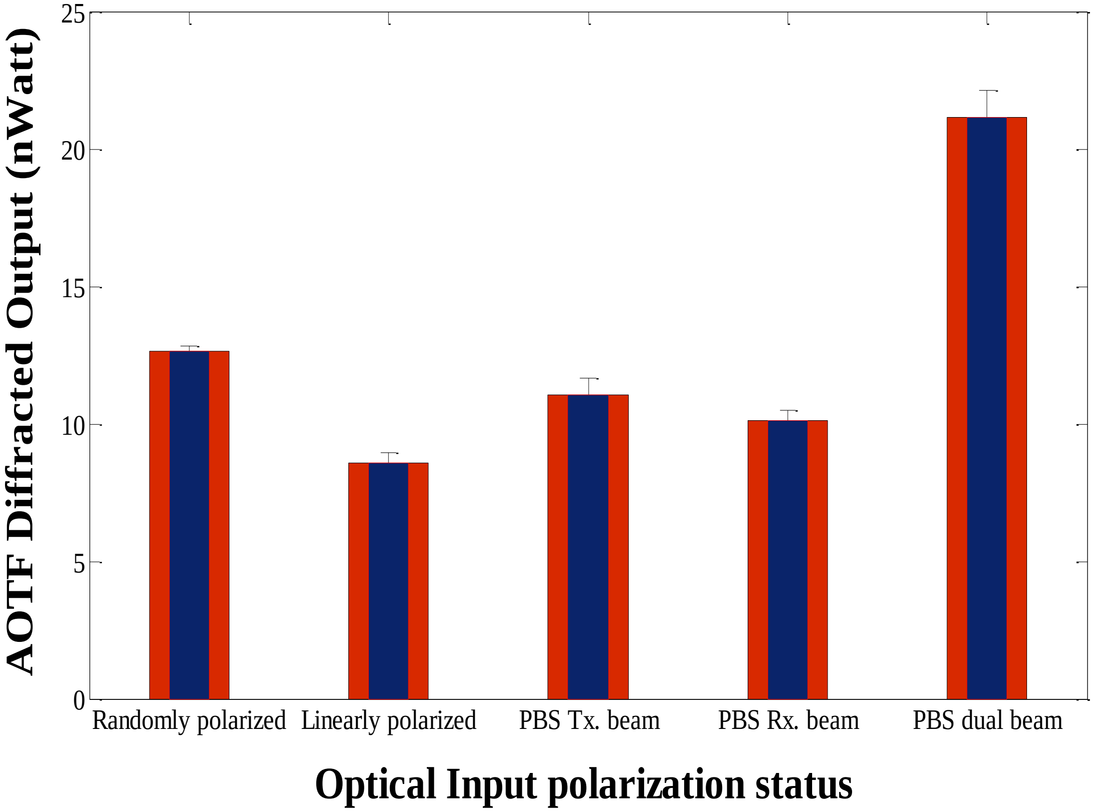

Figure 4-6: The diffracted light intensity of the AOTF crystal in three cases: 1) randomly polarized incident beam, 2) linearly polarized incident beam, and 3) PBS transmitted, reflected, and dual beams, respectively.

The fundamental attributes for the developed imaging spectrometer were identified via a precise spectral and spatial characterization. I present in my characterization various system parameters such as (a) the spectrometer's tuning relation, (b) the spectrometer's linewidth, (c) RF signal amplitude variation impact on the diffracted intensity, (d) the measured difference between the spectrometer's dual channels linewidth (e) the optimum object distance to the first imaging lens, (f) The imaging spectrometer's DOF, and (g) the imaging spectrometer's spatial resolution. In the following two subsections, the detailed spectral and spatial characterizing procedures of the newly developed AOTF-HSI configuration are explained, taking into consideration the standard methods and tools published earlier for similar systems characterization [10], [26], [27], [36], [37].

4.2.2 Spectral characterization

The majority of the optical components, integrated into the dual channel imaging spectrometer, have a share in delineating the system's spectral performance **M**, starting from the wide band illumination and ending by the detector.

$$\boldsymbol{M} = \int_{\lambda_i}^{\lambda_f} \boldsymbol{S}(\boldsymbol{\lambda})\boldsymbol{L}(\boldsymbol{\lambda})\boldsymbol{A}(\boldsymbol{\lambda})\boldsymbol{C}(\boldsymbol{\lambda})\boldsymbol{d\lambda} \qquad \textbf{(4-1)}$$

The terms included in the former equation are: $\boldsymbol{S}(\boldsymbol{\lambda})$ is representing the light source's spectral output, $\boldsymbol{L}(\boldsymbol{\lambda})$ is the installed lens's spectral transmission, $\boldsymbol{A}(\boldsymbol{\lambda})$ is the AOTF's spectral response, and $\boldsymbol{C}(\boldsymbol{\lambda})$ is the camera's quantum efficiency.

The beam shaping optics; lenses and polarizing beam splitter (PBS) (Thorlabs Inc., New Jersey, USA), were selected based on their high transmission (less than 5% loss due to reflectivity) throughout the entire AOTF-HSI range of operation. The developed imaging spectrometer characterization was performed based on a previously published methodology [26]. The procedure includes the following measurements: (1) AOTF-HSI tuning, (2) the AOTF-HSI spectral linewidth upon the operating range, (3) the RF signal amplitude effect on the diffracted beam intensity, (4) the spectral difference between the newly developed system dual channels. The developed AOTF-HSI spectral characterization was accomplished by using auxiliary instruments such as a high-resolution spectrophotometer (OSM-400, Newport, Irvine, CA, USA) and a halogen light source (A20500 Fostec, ACE light source with EKE lamp, Mainz, Germany) which emits out along the interested spectral region.

The tuning relation is the first parameter in the characterization row to consider. The AOTF-HSI tuning relation aims to determine the single driving RF signal required to trigger the TeO_2 crystal's piezoelectric transducer in order to diffract a particular band. To attain such relation, the driver RF entire range was skimmed, by 1 MHz frequency step. Upon each frequency step the diffracted output peak corresponding wavelength is recorded using a high-resolution spectrophotometer. The driving RF frequencies are plotted against the recorded wavelengths in Figure 4-7.

The formerly mentioned figure shows an inverse proportionality between the AOTF driving RF frequencies and the diffracted wavelengths. To give an example, the highest RF frequency (~135 MHz) in the driver range is the frequency required to diffract the shortest wavelength (450 nm) for AOTF cell and vice versa. For evaluation purposes, the attained tuning data was plotted against the AOTF manufacturer's tuning data. The manufacturer tuning relation is relevant to the case where input light is perpendicularly incident to the crystal's input aperture. As obvious, in Figure 4-7, the new developed AOTF-HSI tuning data showed similar behavior to the manufacturer's but with a slight shift. This shift is attributed to the non-perpendicular incidence of the input optical beams upon the AOTF crystal interface. For evaluation purposes, the impact of different incident angles relative to the crystal optical axis, (0, ±2, ±4 degrees), upon the AOTF's tuning has been computed, based on (4-2) [38], [39], and plotted in Figure 4-7. The identified values, in MHz, of the RF frequencies required diffracting all bands was insignificantly shifted from the theoretically computed one. Eventually, a look-up table, relating the RF signal and the diffracted wavelength, was established in order to call up in data analysis.

$$\lambda = \frac{v\Delta n}{f}\sqrt{\sin^4\theta_i + \sin^2 2\theta_i} \tag{4-2}$$

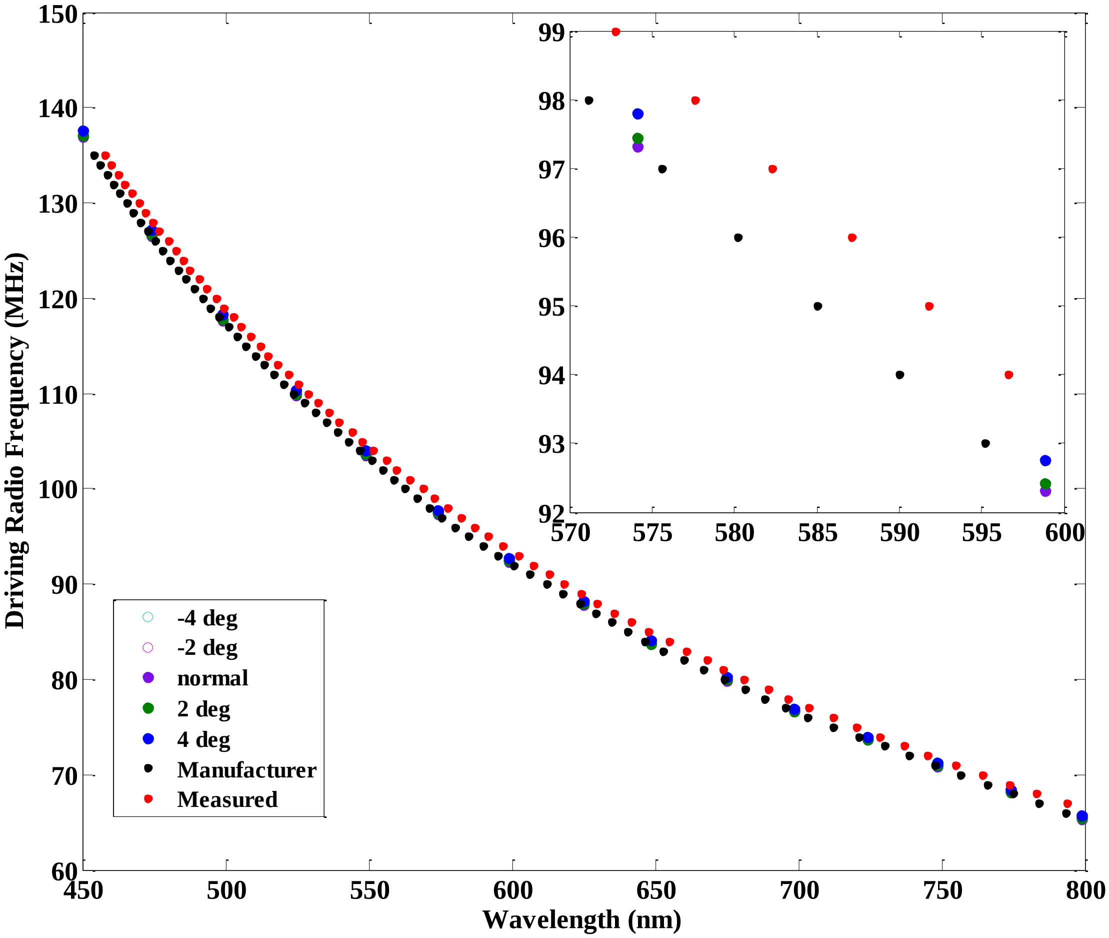

Figure 4-7: The AOTF-HSI imaging spectrometer tuning relationship compared with the manufacturer tuning data, in addition to a theoretical computational data for optical input at different incident angles (0, ±2, ±4 degrees). A zoom was accomplished in the spectral region of 570:600 nm of the figure to show how data points are in relevance to each other. The tuning data of both negative and positive incident angles but equal in value (±2, ±4 degrees) are identical.

Second, in the row, the AOTF-HSI spectral linewidth along the entire operating range was computed using MATLAB (Mathworks Inc., Natick, MA, USA). The computed linewidth of the developed AOTF-HSI is plotted against the AOTF crystal manufacturer's linewidth data. In addition, beams of different incident angles (0, ±2, ±4 degrees) relative to the AOTF crystal optical axis linewidth were theoretically computed, employing the relation in (4-3):

$$\Delta\boldsymbol{\lambda} = \mathbf{1.8}\boldsymbol{\pi}\boldsymbol{\lambda}^{\mathbf{2}}/\boldsymbol{bLsin}^{\mathbf{2}}\boldsymbol{\theta}_{\boldsymbol{i}} \tag{4-3}$$

The line width ($\boldsymbol{FWHM} = \Delta\boldsymbol{\lambda}$) of the diffracted band out of AOTF crystal is proportional to the square value of the central wavelength ($\boldsymbol{\lambda}^{\mathbf{2}}$) of the same band when other parameters are constants based on the relation (4-3). This fact interprets the reduction of the spectrometer spectral resolution/ linewidth along with the wavelength increment. The AOTF-HSI linewidth was computed for both single and dual channel/s, using the diffracted data along the RF frequency range of the AOTF's driver. Figure 4-8 shows the computed linewidth side by side with the manufacturer's data along with the linewidths for typical incident angles ($\pm 2^o, \pm 4^o$) computed theoretically.

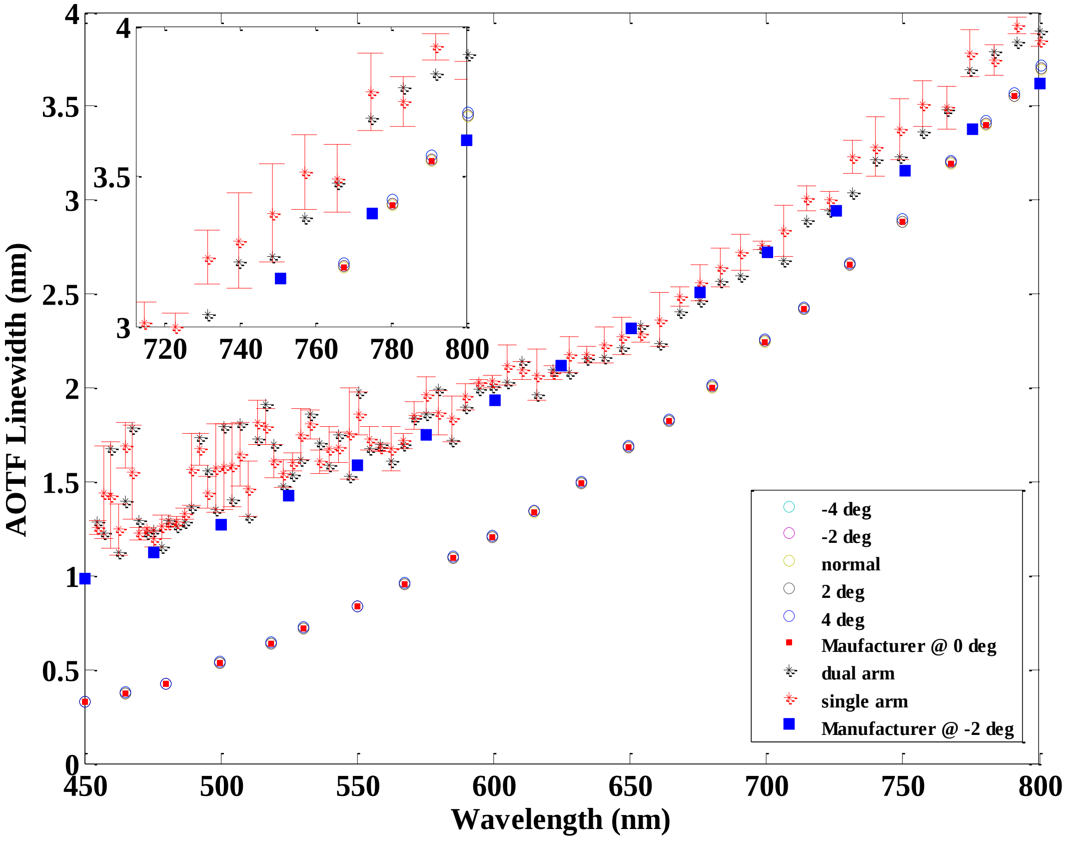

Figure 4-8: The AOTF-HSI imaging spectrometer linewidth (FWHM) compared with the manufacturer linewidth data in addition to a theoretical computational data for different optical input incident at angles (0, ±2, ±4 degrees). A zoom is accomplished on the part of the figure to show how data points are in relevance to each other.

It is of interest to know, the computed FWHM for the newly developed dual channel AOTF-HSI configuration is larger, which means less resolution, than the solely AOTF crystal manufacturer’s linewidth. The reason for that difference in linewidth is attributed to the difference in the angle of incidence for each case. However, for the input light beam which is incident at ± 2 degrees relative to normal: the computed linewidth of the developed AOTF-HSI and the AOTF crystal manufacturer’s linewidth data, obtained from the company technical support, have no substantial resolution difference.

The ideal linewidth for a light beam incident at 2 degrees drifted from normal incidence to the input aperture of the AOTF crystal is found to be different compared with the actual AOTF-HSI system and TeO_2 crystal manufacturer’s linewidths. In fact, this difference is attributed to the AOTF crystal structure design. Since this AOTF crystal is designed to be polarization sensitive. As such, only single diffracted order (1^{st} negative order) is recommended to be utilized. The reason for this recommendation is the high pointing stability which is not guaranteed for the other diffracted beam. In practice, such optimization aimed essentially to increase the angular acceptance of the AOTF crystal, which serves better in wide FOV imaging spectrometry.

Third in a row is the AOTF-HSI dual channels’ linewidth comparison. It was utterly interesting to investigate the diffracted output linewidth for each individual channel and compute how close they are to each other. Therefore, the system was operated in such a way allowing only one channel to function at a time. Based on linewidth computation, we found the FWHM for each channel is not completely identical to the other as was obvious from the error bars of AOTF-HSI single arm in Figure 4-8. The FWHM difference of both channels of the developed AOTF-HSI is plotted through the operating range in Figure 4-9. The maximum difference computed turned to be ± 0.8 nm between the two channels, which is acceptable, compared to the spectrometer global linewidth.

Final parameter in the spectral characterization is examining the RF signal amplitude variation impact on the AOTF-HSI diffracted light intensity. The purpose of such RF characterization was to delineate the optimum RF signal amplitude which can be used to obtain the highest diffracted intensity while saturation is dodged. Toward achieving this purpose, a broadband halogen source was used to shine directly toward the imaging spectrometer. Once the light passes through the system AOTF is tuned to permit a single band to pass. The RF signal amplitude full-scale deflection (FSD) amplitude was stepped in 6 equal up steps evenly as follows: 17%, 33%, 50%, 66%, 83%, and 100% FSD.

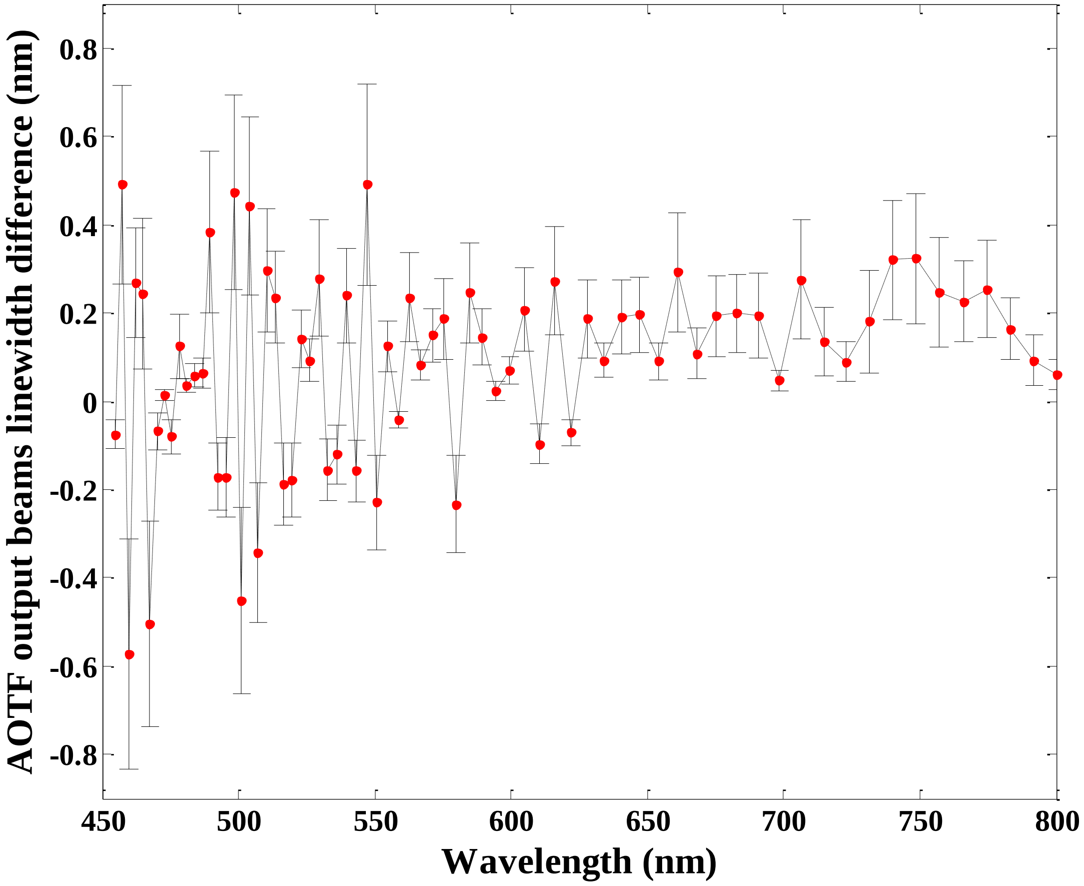

Figure 4-9: The AOTF-HSI imaging spectrometer dual channels linewidth difference plotted along the entire operating spectral range of the developed equipment.

At each RF signal amplitude step, the diffracted light intensity was recorded using an optical multimeter, tuned to the diffracted band central wavelength. For verification purposes, the former procedure was done repeatedly at five different bands sampling the operating range of the developed imaging spectrometer. Figure 4-10 displays the impact of RF amplitude variation on the AOTF-HSI diffracted output intensity. A positive proportional increase in the diffracted light intensity was obvious with each the RF signal amplitude increment toward FSD. The diffracted light intensity was not only the single parameter altered with RF amplitude increasing steps but also, the FWHM was altered as well but with less significance. The FWHM for the formerly mentioned five wavelengths spanning the developed spectrometer operating range were examined at different RF amplitudes and the same results were verified, data is shown here for one band out of the five examined bands.

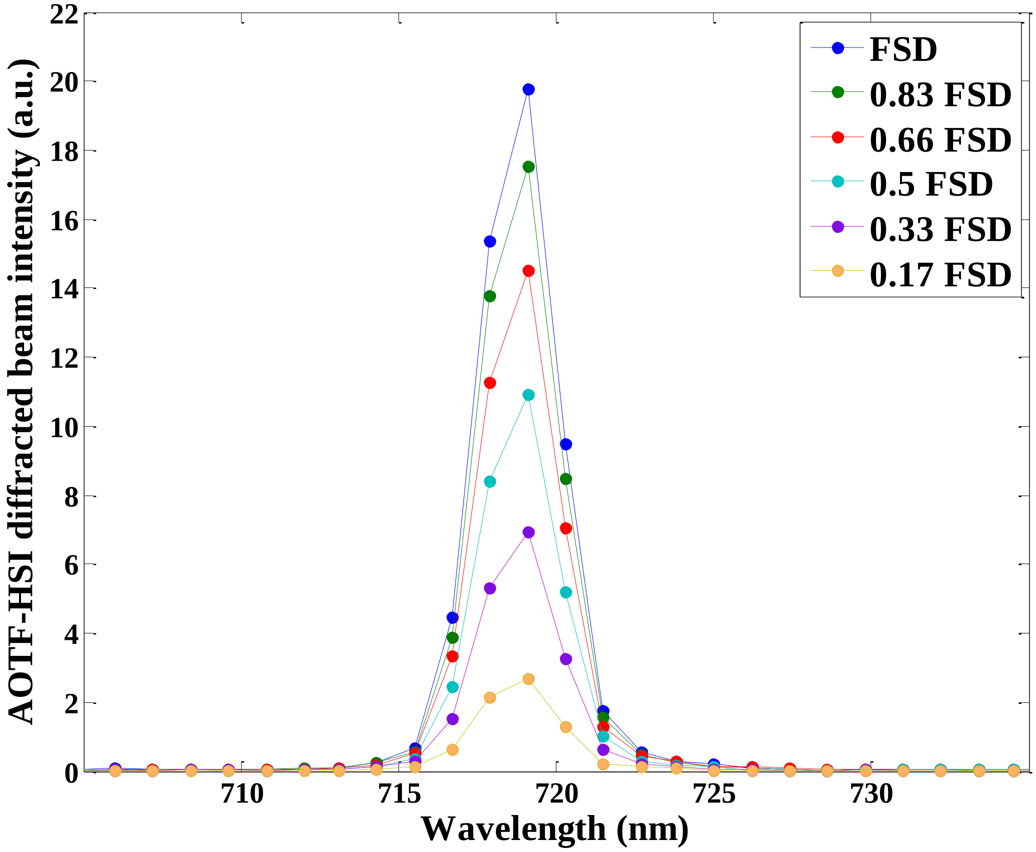

Figure 4-10: AOTF-HSI diffracted beam intensity tuned to single wavelength at different RF amplitude levels

4.2.3 Spatial Characterization

In this section, three parameters are studied: 1) The optimum location for the object under investigation relative to the AOTF-HSI first lens, 2) the AOTF-HSI depth of focus, and 3) the spatial limitation/ resolution for the developed AOTF-HSI system.

Identifying the optimum location for the investigated target relative to the imaging system is important in the sense of attaining high-definition frames. Thus, it was appealing to identify how far should be my subject seated to acquire high-resolution images for his/her ROI. Aside from subject displacement, the DOF for the developed imaging system needs to be recognized to identify how much details can come to focus within the field of view (FOV). In the captured FOV, it is required not only to capture the subject's ROI but also to include a part of the surrounding area. Since the surrounding region of ROI is useful in image registration and data analysis. For example, the surrounding region might contain natural/ artificial landmarks which are extremely valuable in registering distinct spectral and distant temporal captured frames. Moreover, the spatial resolution is a matter of concern for the developed imaging instruments in order to outline resolution barriers.

In order to find the optimum location for the object required to be studied, a standard reflection target United States Air Force (USAF-1951, 38-710, Edmund Optics) was imaged. The target was imaged at 57 points along a straight line from the center of the AOTF-HSI first lens. The displacement of the first and the end points are 500 mm, and 780 mm far from the imaging system's first lens respectively. At each point, the contrast transfer function (CTF) was calculated, based on the acquired image, according to (4-4) for the entire elements of groups zero and one.

$$\boldsymbol{CTF = \frac{Max_I - Min_I}{Max_I + Min_I}} \tag{4-4}$$

The terms $\mathbf{Max_I}$, $\mathbf{Min_I}$ are the maximum and minimum light intensities, respectively, detected in the rectangular region surrounding the spatial element as shown in Figure 4-11. The significant element of consideration for each displacement step was based on the highest spatial frequency element which has CTF is greater or equal to one-half. Figure 4-11 shows the USAF-1951 image and the intensity plot for the highest spatial frequency element which was resolved by the system at a displacement of 700 mm separation [40].

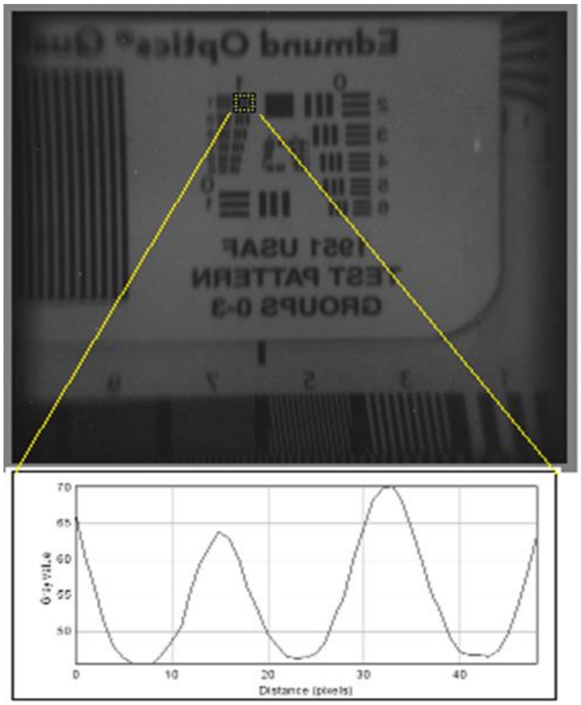

Figure 4-11: A United States air force (USAF-1951) target is imaged by the AOTF-HSI system at 700mm displacement. Group1/element1 is enclosed in a yellow dotted rectangle, the intensity was plotted, where maximum, and minimum intensities are identified to calculate the contrast transfer function (CTF) at this range.

On the other hand, Figure 4-12 exhibits the calculated CTF values of the highest frequency element (group 1/ element1 = 2 LP/mm) resolved by the AOTF-HSI system in the translation range 500:780 mm. A quadratic curve was fitted to the scattered CTF results. The fitting equation was solved at the value = 0.5 and two solutions were output. The identified solutions limit the range for object-system displacement to achieve the best focus. The optimal range was bounded in between 668 mm and 702 mm. Since DOF, for an imaging system, is defined as the displacement range in which the best focus is maintained [41]. Thereby, the developed dual channel AOTF-HSI system is found to have DOF equal to 34 mm.

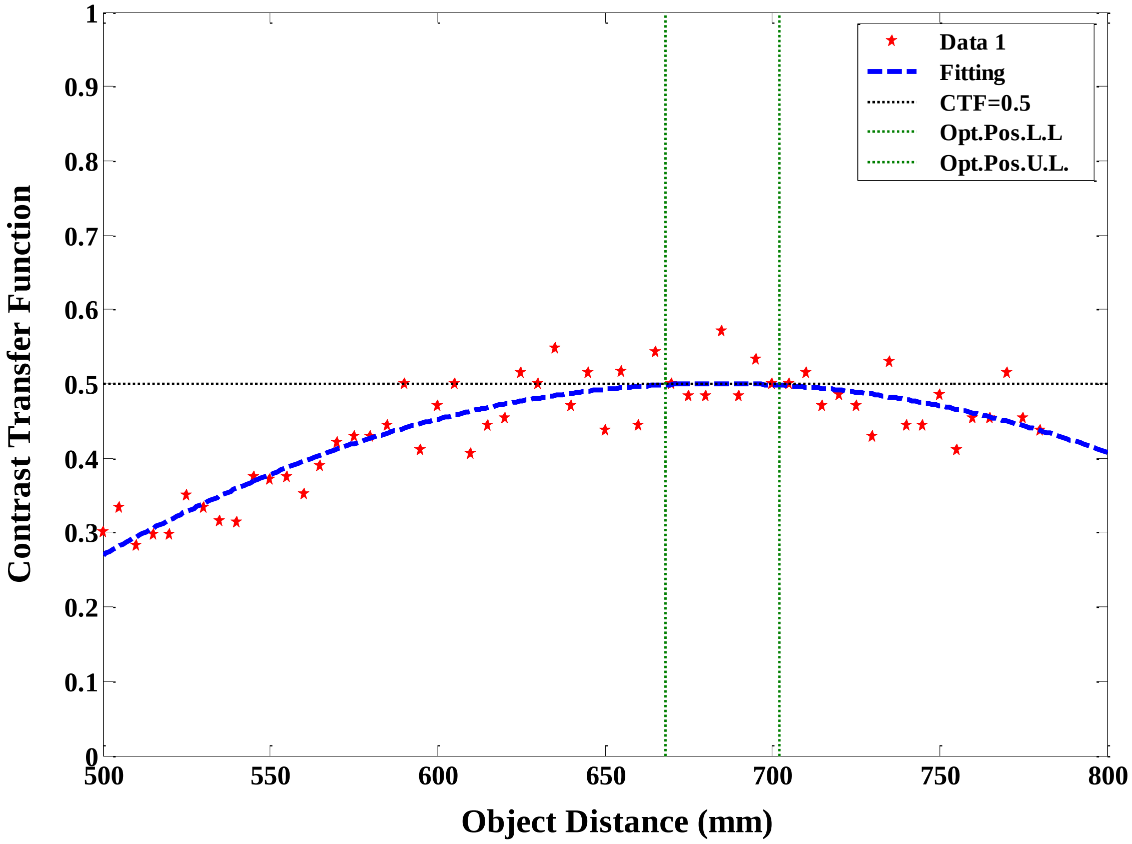

Figure 4-12: Contrast transfer function (CTF) values, for the spatial target group1/element1, are plotted at 57 locations lying in the range of 500:780mm displaced relative to the AOTF-HSI imaging system (red stars). The blue dashed line is the data-fitting curve used to identify the object best position based on the highest CTF. The green vertical dashed lines (Optimum object position both lower and upper limits) are intersecting with the fitting curve at CTF = 0.5 to bound the optimum location of the object under test.

The modulation transfer function (MTF) measurement is commonly computed to characterize the spatial resolution of an optical system. To compute an imaging system's

MTF, the ratio of the acquired image modulation and the original object modulation is accounted as demonstrated in (4-5) [42].

$$\boldsymbol{MTF = \frac{Mod_{image}}{Mod_{object}}} \tag{4-5}$$

The term **Mod$_{\mathbf{image}}$** is the contrast transfer function of the object image captured by the developed imaging setup and **Mod$_{\mathbf{object}}$** is the contrast function provided for the original object/ test chart by the manufacturer. When using a standard test chart (**Mod$_{\mathbf{object}}$ = 1**), the system MTF is considered as the modulation of the object captured image. This test characterizes the system's capability to resolve tiny features, which might be interesting in the clinical domain. Figure 4-13 illustrates the AOTF-HSI imaging system's MTF using the USAF-1951 target at an object distance equal to 685 mm.

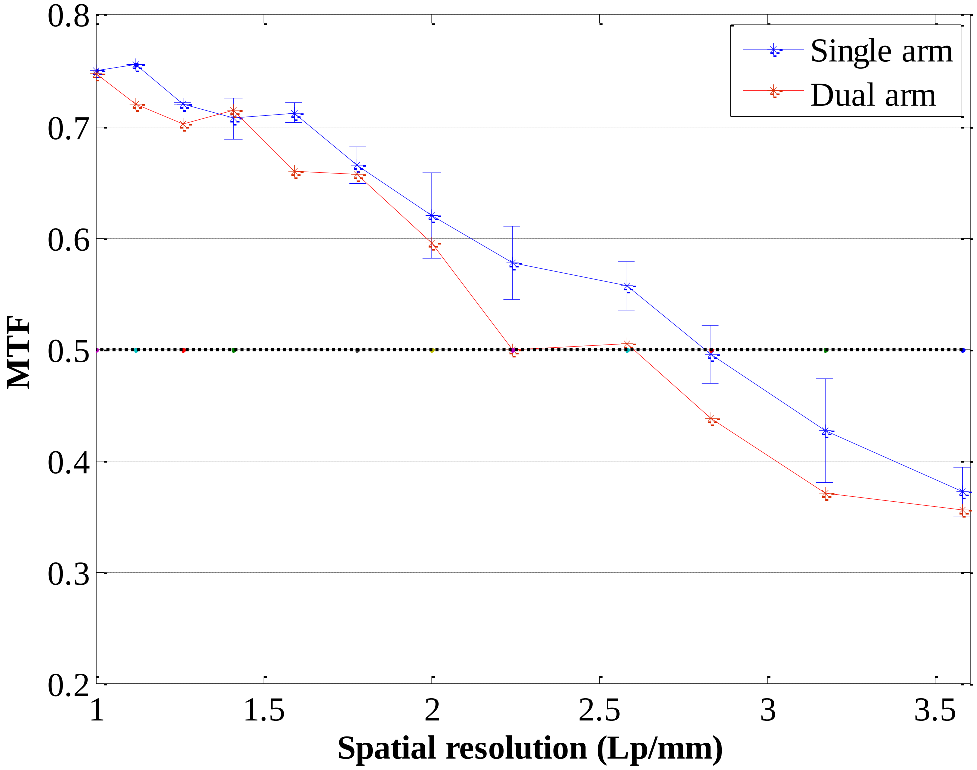

Figure 4-13: The AOTF-HSI imaging spectrometer MTF plot obtained by imaging USAF-1951 spatial target.

The minimum size for an object structure could be resolved by the AOTF-HSI imaging spectrometer is figured by the spatial frequency limit and the optical magnification. The size ratio of the real object and its image on our sensor (M) was measured by imaging a precisely graduated test target, and the spatial frequency of the image ($\boldsymbol{f_I}$) is calculated according to (4-6) and found to be 23 (lp/mm).

$$\boldsymbol{f_I = \frac{f_{Obj}}{M} = f_{Obj} * \frac{D_{Obj}}{D_I}} \tag{4-6}$$

The term $\boldsymbol{f_{Obj}}$ is the USAF-1951 test chart spatial frequency (Lp/mm), $\boldsymbol{D_{Obj}}$ is the dimension of the real test chart size, and $\boldsymbol{D_I}$ is the dimension of the corresponding object image size. The integrated zoom lens contributes in optimizing the interesting FOV in hyperspectral imaging systems. The specifications of the zoom lens in our newly developed imaging system were concluded based on clinical considerations for in-vivo skin inspection. At each focal length, the FOV and the spatial resolution limit were defined. Conceptually, the FOV and the image spatial resolution are inversely proportional to each other.

To this end, it is essential to mention the presence of a shift angle between the dual channels' focused images on the camera sensor. This shift is thought to be due to the tolerance of manufacturing and implementation of the optical design for the AOTF-HSI system platform. This shift was measured to be 3.89^o degrees. This shift is slightly observed only on the combined frame extremities while the rest of the frame has a quite coincidence.

4.3 Performance comparison of the dual channel AOTF to LCTF

AOTF and LCTF have been compared previously for specific applications; fluorescence and Raman microscopy [28], and laser induced breakdown spectroscopy [32]. In this study, I report comparing both filters for hyperspectral imaging in the sense of 1) spectral resolution, 2) spectral selectivity, 3) reliability & image quality, and 4) spatial resolution. Since these parameters represent the major interesting specifications for HSI designers/ operators to satisfy the requirements of various applications.

4.3.1 Evaluation set up

The involved LCTF (VIS-10-20, Cambridge research & instrumentation, MA, USA) is operating in the visible region 400-720 nm with a wavelength dependent spectral resolution. LCTF is compact in size, simple to operate, and easy to control via an RS-232 communication protocol. In addition to LCTF, a wavelength calibration target, Erbium oxide (WCS-EO-010, Labsphere, NH, USA), and white standard reflectance target (SRS-99, Labsphere, NH, USA) were used for spectral imaging quality and reliability assessment. A tungsten-halogen light source and two laser lines, He-Ne laser emitting at λ = 633 nm and a diode laser emitting at λ = 675 nm, were used in the characterization experiments. For control purposes, a developed program was built in C-language to fully automate and synchronize the filter operation with the image detector similar to AOTF.

4.3.2 Spectral resolution

The spectral operating range of each filter is marginally different, however, the common overlap, 450: 720 nm was adequate for spectral resolution investigation. For investigation purposes, a wide band tungsten-halogen source is used to radiate directly towards the optical configuration, where one individual filter is installed at a time. For each filter, the tuned spectra are collimated by a lens and coupled to an optical fiber Ø400 µm, 0.22 NA connected to the input of a high-resolution spectrophotometer. The spectrophotometer is serially connected to the workstation for control and data storage. In terms of the filter function, LCTF passes only the selected band; however, AOTF allows both the incident and the diffracted beams to go through. Since AOTF diffracted output is angularly separated with ~4.5^o vertically below the undiffracted beam. Consequently, switching filters needs no change in the optical configuration except for adjusting the two rear mirrors (M2, M3) shown in Figure 4-1. Given that these mirrors are reflecting the diffracted/filtered beams toward the focusing lens which precedes the spectrophotometer detection fiber.

Automatic sweeping through the spectral range was the way for sequential band-to-band transition while employing both filters. The developed control program utilizes the programmable RF signal in the case of AOTF, and the programmable voltage level in LCTF case for tuning. Spectrophotometer intensity saturation was avoided by adjusting its integration time to ensure the maximum received photons are below 95 % of its saturation value. Averaging the measurements at each single tuned band, for three repeated trials, was accomplished twice on two separate days. The average data computed out of the repeated experiments produces the raw data for analysis. A look-up table relating the central wavelength filtered and the corresponding intensity profile for each tuned band was realized. A developed MATLAB function was used to calculate the FWHM at each band and plot it as shown in Figure 4-14.

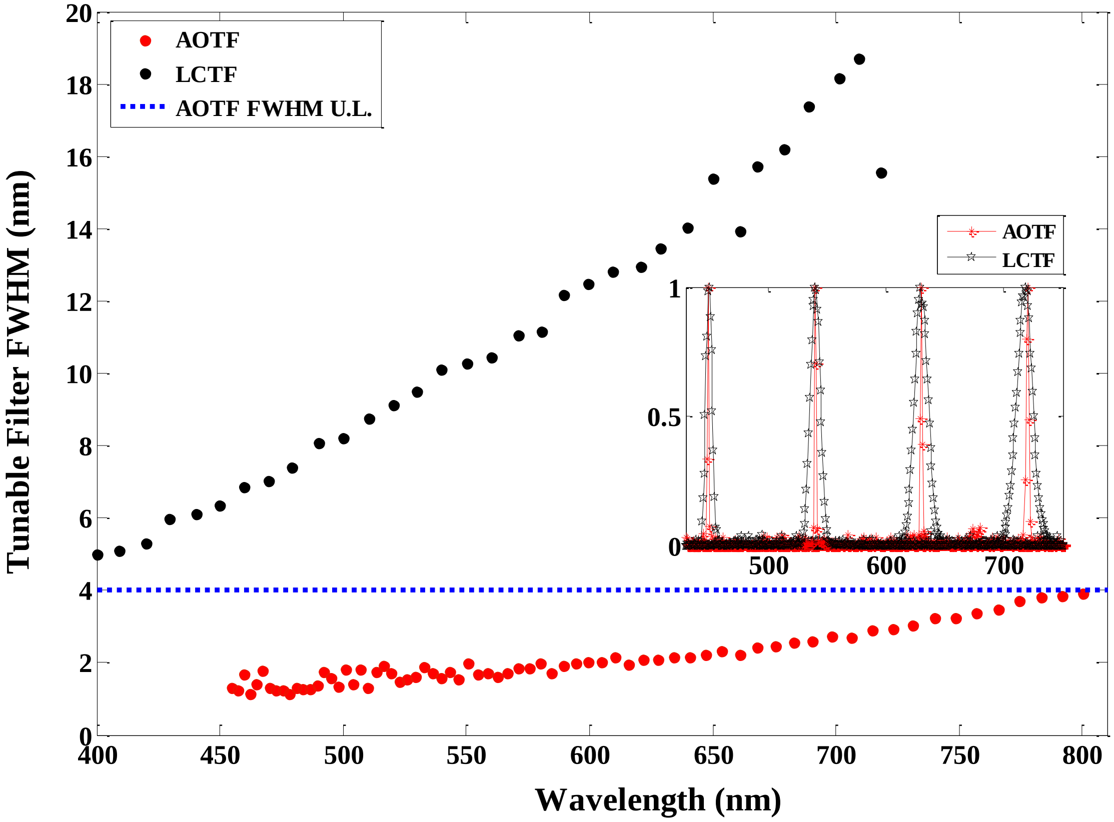

Figure 4-14: The imaging spectrometer spectral resolution evaluation in the case of switching between AOTF (red circles) and LCTF (black circles) along the operating range for each filter. Samples of filtered/diffracted bands are also included in the embedded figure. A blue dotted line is bounding the lower resolution limit of the AOTF-HSI. This line shows that AOTF has superior linewidth in contrast with LCTF.

4.3.3 Spectral selectivity

An ideal tunable filter is infinitely selective, which means it suppresses all the bands except the designated one. In practice, real filters are far from ideal. Hence filter practical suppression needs to be assessed in both challenging tunable filters. For assessment purposes, two wavelength-nearby laser lines were engaged together and radiate directly toward the developed HSI configuration. The first engaged laser is a He-Ne laser source emitting at 633 nm with an FWHM of 2.0 nm bandwidth while the second is a diode laser radiating at 675 nm with a 1.2 nm FWHM. Both laser lines were transmitted at once with one tunable filter installed at a turn. In this work, the spectral range of 600: 700 nm was stepped over by ~ 2 nm jump and filtered/diffracted output was captured. Figure 4-15 displays a plot for the two laser lines in blue, the AOTF diffracted output in red, and the LCTF filtered output in black. The intensity of each is normalized to the maximum detected level.

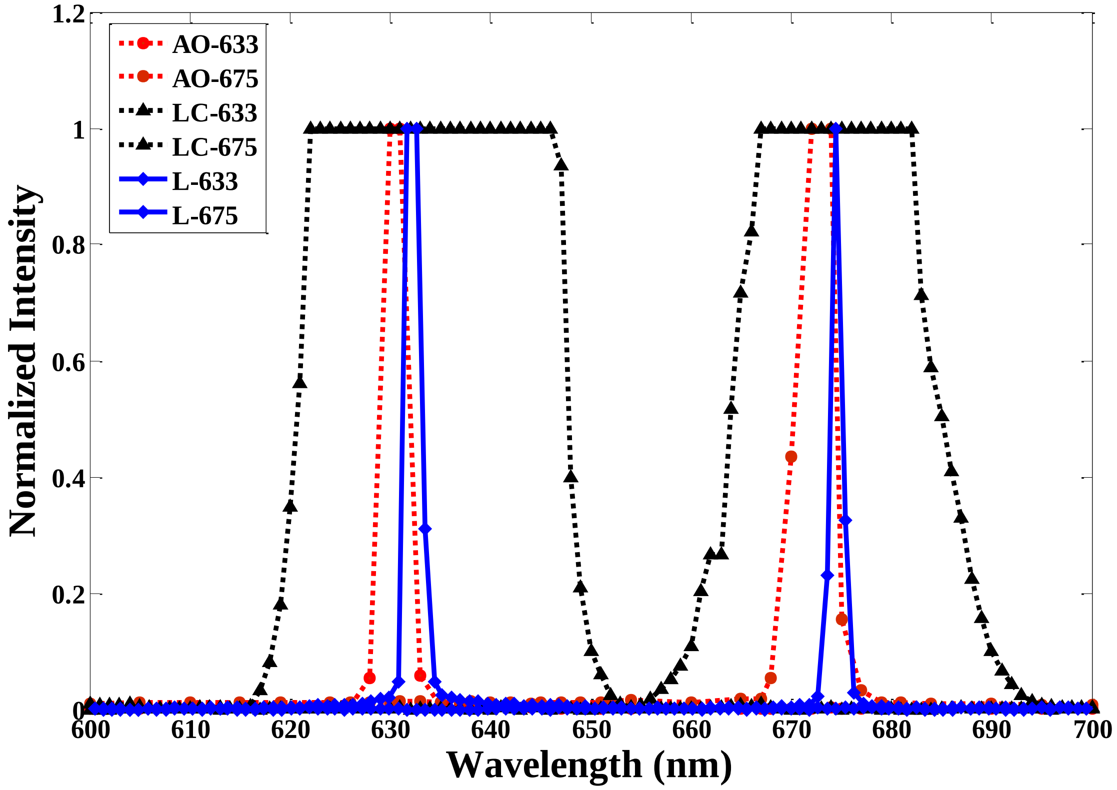

Figure 4-15: Spectral selectivity comparison of AOTF (red) and LCTF (black) while using direct transmission of He-Ne laser emitting @ 633nm and Diode laser emitting @ 675nm lines (blue).

4.3.4 Reliability and Image quality

For spectral assessment validation and quality of imaging purposes, a doped Erbium oxide calibrated wavelength target was imaged by both tunable filters. The imaging was repeated four times to reduce human error possibility. The target datacube processing commences with the detector dark current noise removal. Noise, related to the dark current, is removed by subtracting the dark datacube (R_d) from both the target and the reference datacubes. The dark datacube is captured while the zoom lens cap was on and the illumination sources were off. The reference data is taken for a white standard target in the same imaging conditions of the object under test. Following noise removal, the target datacube was normalized to the reference datacube to accommodate for uneven illumination effects and the optical setup spectral dependence applying the relation in (4-7).

$$\boldsymbol{R_n = \frac{R_{EO} - R_d}{R_{s99} - R_d}} \qquad \textbf{(4-7)}$$

The term R_n is the normalized reflectance of the wavelength calibration target, R_{s99} is the back reflected datacube of the white standard target, and R_{EO} is the back reflected datacube of the Erbium oxide target. Figure 4-16 displays the spectral signature of the erbium oxide target by using both filters the AOTF (top-row) and the LCTF (middle-row). The visible spectral range within 500:720 nm was used as a common range between the involved AOTF and LCTF. The error bars represent the standard deviation for the average normalized pixel intensities. Reliability based on reproducible spectral output was checked by imaging the erbium oxide target for three successive days, three times a day at different daytimes to evaluate both filters reproducibility. The arithmetic mean and the standard deviation, for the captured datacube pixels, were calculated to identify the imaging reproducibility for each filter all over the entire operating range. The results for these measurements are displayed, as shown in Figure 4-16 (bottom-row).

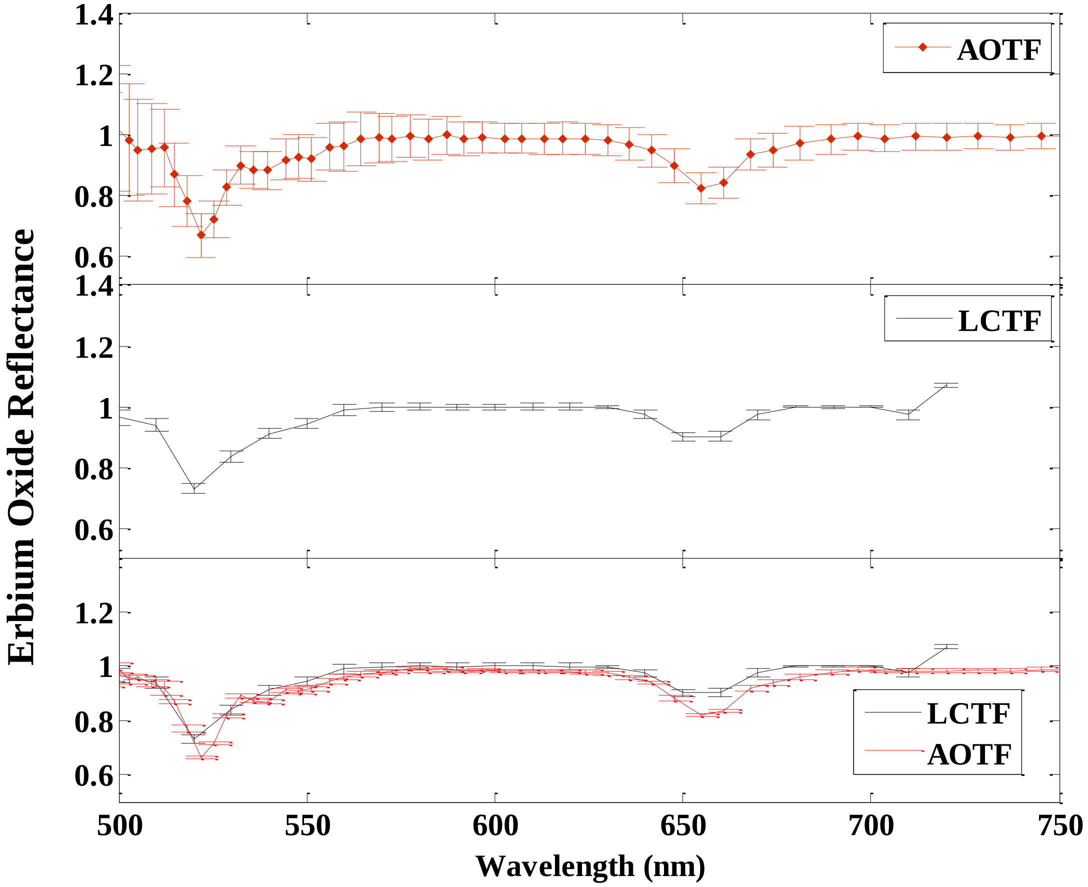

Figure 4-16: A standard wavelength calibration target, Erbium oxide, (top) imaged by AOTF- HSI, (middle) by LCTF-HSI configuration, and (bottom) by both tunable filters for reproducibility purpose.

4.3.5 Spatial resolution

In order to examine our queried filters spatial resolution limitation, a standard USAF-1951 test chart with graduated spatial frequency elements is used for imaging purpose as shown in Figure 4-17 [43]. The modulation transfer function (MTF), for each element in two groups, 0 and 1, for the USAF-1951 was calculated and plotted as shown in Figure 4-18. Notably, LCTF was remarkably higher in spatial resolution relative to AOTF, in either the case of vertical or horizontal spatial frequency. As such, LCTF image quality is particularly smoother in terms of heterogeneity.

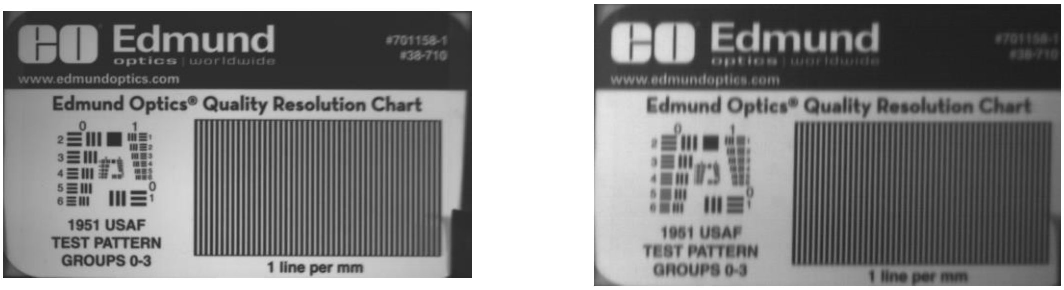

(a) (b)

Figure 4-17: USAF-1951 imaged at 690 nm employing (a) LCTF and (b) AOTF tunable filters in HSI platform one at a time.

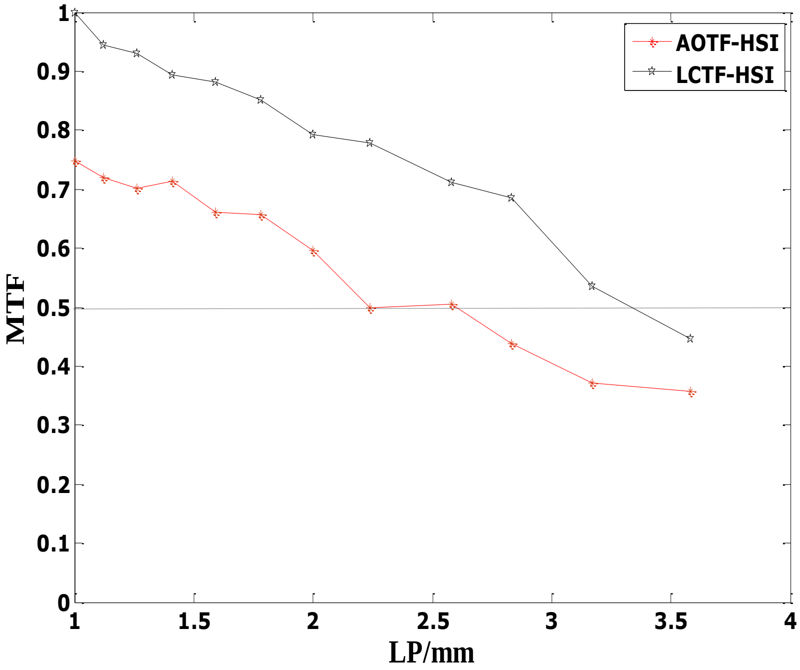

Figure 4-18: MTF plot for both tunable filters, LCTF & AOTF, imaging a USAF-1951 reflection pocket target; group 0 and 1, noting that diffraction resolution limit @ 500nm is equal to 4.88 µm.

4.4 Discussion

We report the development of a new dual-channel high throughput AOTF-based hyperspectral imaging system. The system essentially operates in the range of 450: 800 nm. However, the range of operation could be slightly extended up to 430: 850 nm, in the case of using an extended RF range. The spectral resolution for the innovated configuration is nonlinearly varying from ~1.5 to 4.1 nm. The newly developed configuration has an increased overall throughput since it makes use of two components of the randomly polarized input light rather than one in the existing single beam configurations.

The novelty of this configuration is achieved, in terms of hardware; by incorporating a polarizing beam splitter and a half-wave plate ahead of the AOTF crystal. The two integrated components contributed in increasing the input light into the AOTF cell, which in turn yields to a higher diffracted light intensity. Therefore the developed configuration allowed injecting both orthogonal polarizations reflected back from the object into AOTF. As a result, the system's throughput is increased compared to single channel configurations using polarizer plates [18].

The second potential advantage of my developed configuration becomes apparent in the case of using polarized illumination. For instance, a simple modification of the used illumination to be linearly polarized light would permit cross-polarized imaging. Cross-polarized imaging can be realized at the expense of 50% field of view reduction, where two images can be displayed simultaneously on one single detector. One of which is on the tissue's surface (specular reflection) while the other is for the underneath layers (diffuse reflection) information. The formerly mentioned advantage provides a cheap alternative for the conventional cross-polarized imaging systems, as less number of elements are installed [44]. It spares also employing a rotor to change the polarizer orientation in order to capture parallel and perpendicular reflected lights one at a time. To this end, the global improvement measured due to the new developed AOTF-HSI configuration is 67.55% in the case of randomly polarized light injected to AOTF for a single beam and 147.08 % if AOTF is preceded with a polarizing plate in lieu of the PBS.

The detailed characterization of the developed AOTF-HSI system identified the major specifications in both spectral and spatial domains. Spectral specifications, in particular, were remarkable in the newly developed configuration due to selecting AOTF. To give an example, long range of spectral operation comprising visible and near-infrared is applicable. Moreover, the high spectral resolution is available which facilitate differentiation between distinct but close spectral peaks. Furthermore, the high-speed option of wavelength access allows both HSI and MSI mood of operation. In terms of spatial domain, accepted the spatial resolution, ~2 Lp/mm, is available with a reasonable depth of focus was determined experimentally. Although the developed imaging spectrometer was fully characterized, performance assessment was required to prove competence. Hence, a competent tunable filter, LCTF, was employed to be installed in place of AOTF for filters assessment in spectral and spatial attributes.

The spectral assessment accomplished for both questioned tunable filters provided clear evidence of AOTF outstanding spectral performance in contrast with LCTF. First evidence, the AOTF's spectral linewidth is significantly lower than the LCTF over the entire operating range since the AOTF has a linewidth of 1.5: 4.1 nm while the LCTF linewidth is ~5: 19 nm as clear in Figure 4-14. Thereby, AOTF is more compatible in detecting tiny spectral peaks rather than LCTF in the visible spectra. Second evidence, the AOTF's spectral selectivity is superior relative to the LCTF's, where significant suppression is expressed by AOTF for undesired bands. Table 4-1 documents the AOTF capability to suppress wavelengths outside two laser lines; within a range of ~ 3.11 nm neighborhoods in the case of He-Ne laser and 4.36 nm in the case of the diode laser. On the contrary, the LCTF has failed to suppress the He-Ne laser within 27.1 nm and 21.10 nm for the diode laser.

Table 4-1: Spectral comparison of band suppression for AOTF and LCTF performance based on a He-Ne laser (633 nm) and a diode laser emitting at 675nm

Laser type	Beam Bandwidth	AOTF Bandwidth	LCTF Bandwidth
He-Ne laser @633 nm	2.01 nm	3.11 nm	27.10 nm
Diode laser @ 675 nm	1.20 nm	4.36 nm	21.10 nm

In spite of the great advantages owned by AOTF in the spectral domain, LCTF competes very strongly in the spatial domain. For example, the imaging quality is a positive advantage for the LCTF relative to the AOTF. Capturing spectral data sets for the Erbium oxide doped wavelength calibration target along the common operating range for both filters returned lower standard deviation values in LCTF compared with AOTF spectral imaging. The standard deviation, in these measurements, is expressing the heterogeneity of the pixel intensities, within the imaged sector. As such, LCTF has smoother images. Although LCTF misses tiny spectral details due to the lower spectral resolution, it is capable of resolving vertical and horizontal high spatial frequency elements with high MTF values. For instance, Figure 4-18 shows that AOTF-based-HSI is only resolving features in the scale of $\simeq 2$ lp/mm while the correspondent LCTF is resolving features in the scale of $\simeq 3.17$ lp/mm for an object displaced at 700 mm far. This difference is partially contributing in high definition quality imaging of the LCTF, versus slightly blurred imaging of the AOTF as shown in Figure 4-17.

Reliability check for both tunable filters revealed that both filters have an approximately ~ 50 nm of less stable spectral output at the short end. This was deducted in the sense of large error bars while imaging Erbium-oxide wavelength calibration target for multiple times at separate days. Other than prior attributes, there are some performance differences among both filters should be mentioned. For example, AOTF has no warm-up time while LCTF needs at least 30 seconds every shut-off. Moreover, LCTF based configuration requires a wavelength-exposure time look-up table for the detector in order to avoid saturation. This lookup table should be checked and updated whenever illumination intensity or object relative location is changed to avoid falling into saturation. One distinguishable advantage of AOTF is the rapid switching between spectral bands that exceeds **1000** times LCTF one and makes it more applicable to real-time imaging. On the other hand, LCTF has a larger aperture of Ø 20 mm versus 11 mm x12 mm square aperture for AOTF. Eventually, AOTF has slightly longer range of operation relative to LCTF; however, the former operating procedure is simpler.

4.5 Conclusion

A novel high throughput dual channel AOTF-hyperspectral imaging configuration was developed and fully characterized to determine both its capabilities and limitations. The newly developed system is operating in (1) VIS-NIR spectral range, with a (2) relatively high spectral resolution 1.5:4.1 nm, (3) high spectral selectivity, and (4) high throughput versus traditional configurations, and (5) is relatively cheaper than the market-available hyperspectral imaging systems. However, at this point, the developed AOTF-HSI instrument has two shortcomings; (1) the relatively large size of the entire imaging instrument, (2) a small angle (3.89^o) between the dual channels' images focused on the camera sensor. Currently, this angle is corrected by image post processing.

Concisely, the tunable filters comparison presented here for performance evaluation tagged each filter with few favors and displayed its limitations as well. The decision of incorporating one of the two filters in an optical design should be based on how close the filter attributes are matching the application's requirements and constraints. In sum, the major advantages of each filter are documented below:

1- The incorporated AOTF is distinguished by:
   a. High spectral resolution
   b. Significant spectral selectivity (out of tuned band suppression)
   c. Expeditious random wavelength access, where video rate is feasible
   d. High diffraction efficiency (90%)
   e. Long range of operation
   f. Simultaneous diffraction of 8-distinct bands is feasible

2- The LCTF is remarkable by:
   a. High spatial resolution (vertical and horizontal)
   b. High image quality (smaller variability of close pixel intensities)
   c. Large aperture size
   d. Simple operation

Ultimately, we need to emphasize that the presented comparison among the two involved tunable filters is representative for the mentioned models. And thus, altered results might come up dependent upon the utilized particular devices properties. In general, the tunable filter-based-HSI system robust design is majorly dependent on targeted application. For instance, if the interested biological object of the study has unknown optical properties, or characterized by close spectral peaks, AOTF might be the superlative option. On the other hand, LCTF would be more convenient and simpler to grab in the case of image quality is critical for the study.

The newly developed imaging spectrometer is planned to be used in the clinical investigation of the human skin inflammation (erythema). For this purpose, the AOTF-HSI system's FOV was planned to be within 10: 20 cm^2, where 13.5 cm^2 FOV was achieved by the developed instrument for a ~70 cm far object. The DOF for the newly developed system, 3.4 cm, is expected to keep the targeted non-flat regions, such as cheeks and forehead regions, in the best focus. According to Nyquist sampling theorem, in the case of imaging 13.5 cm^2 (achieved FOV) onto a sensor size of 11.27 mm^2 with a pixel pitch of 5.5 µm, the system is capable of resolving details > 13 µm which are greater than the diffraction limit of the developed system. This resolution should be adequate in skin superficial features investigation. In order to check the sensitivity of the newly developed system is detecting skin color changes. An exploratory study was planned to examine the feasibility of HSI in detecting distinct skin erythema levels induced artificially on volunteers. The exploratory study is detailed in the coming chapter.

References

[1] [1] A. F. H. Goetz, "Three decades of hyperspectral remote sensing of the Earth: A personal view," *Remote Sens. Environ.*, vol. 113, no. SUPPL. 1, pp. S5–S16, 2009.

[2] Q. Tong, B. Zhang, and L. Zheng, "Hyperspectral remote sensing technology and applications in china," *Proc. 2nd CHRIS/Proba Work. ESA/ESRIN, Frascati, Italy*, no. July, pp. 1–10, 2004.

[3] R. Proc, S. Vol, W. A. Vii, H. H. Szu, M. Vetterli, W. J. Campbell, J. R. Buss, E. Invited, and N. Gat, "Imaging Spectroscopy Using Tunable Filters: A Review," Apr. 2000.

[4] H. Huang, L. Liu, and M. O. Ngadi, "Recent developments in hyperspectral imaging for assessment of food quality and safety.," *Sensors (Basel).*, vol. 14, no. 4, pp. 7248–76, Jan. 2014.

[5] a Gowen, C. Odonnell, P. Cullen, G. Downey, and J. Frias, "Hyperspectral imaging – an emerging process analytical tool for food quality and safety control," *Trends Food Sci. Technol.*, vol. 18, no. 12, pp. 590–598, Dec. 2007.

[6] H. Liang, "Advances in multispectral and hyperspectral imaging for archaeology

and art conservation," *Appl. Phys. A*, vol. 106, no. 2, pp. 309–323, Nov. 2011.

[7] G. J. Edelman, E. Gaston, T. G. van Leeuwen, P. J. Cullen, and M. C. G. Aalders, *Hyperspectral imaging for non-contact analysis of forensic traces.*, vol. 223, no. 1–3. 2012.

[8] Z. Zalevsky, A. Ilovitsh, and Y. Beiderman, "Usage of cornea and sclera back reflected images captured in security cameras for forensic and card games applications," in *Optics and Photonics for Counterterrorism, Crime Fighting and Defence IX; and Optical Materials and Biomaterials in Security and Defence Systems Technology, proc. of SPIE*, 2013, vol. 8901, p. 89010I.

[9] P. W. Yuen and M. Richardson, "An introduction to hyperspectral imaging and its application for security, surveillance and target acquisition," *Imaging Sci. Journal*, vol. 58, no. 5, pp. 241–253, 2010.

[10] D. a Glenar, J. J. Hillman, B. Saif, and J. Bergstralh, "Acousto-optic imaging spectropolarimetry for remote sensing.," *Appl. Opt.*, vol. 33, no. 31, pp. 7412–24, Nov. 1994.

[11] L.-J. C. Tien-Hsin Chao, Jeffrey Yu, George Reyes, David Rider, "ACOUSTO-OPTIC TUNABLE FILTER IMAGING SPECTROMETERS," *IEEE*, vol. 1, pp. 585–588, 1991.

[12] F. Huang and L. Yan, "Hull vector-based incremental learning of hyperspectral remote sensing images," *J. Appl. Remote Sens.*, vol. 9, no. 1, p. 096022, 2015.

[13] G. Lu and B. Fei, "Medical hyperspectral imaging: a review.," *J. Biomed. Opt.*, vol. 19, no. 1, p. 10901, Jan. 2014.

[14] D. J. Mordant, I. Al-Abboud, G. Muyo, a Gorman, a Sallam, P. Ritchie, R. Harvey, and I. McNaught, "Spectral imaging of the retina.," *Eye (Lond).*, vol. 25, no. 3, pp. 309–20, Mar. 2011.

[15] S. Kiyotoki, J. Nishikawa, T. Okamoto, K. Hamabe, M. Saito, A. Goto, Y. Fujita, Y. Hamamoto, Y. Takeuchi, S. Satori, and I. Sakaida, "New method for detection of gastric cancer by hyperspectral imaging: a pilot study.," *J. Biomed. Opt.*, vol. 18, no. 2, p. 26010, Feb. 2013.

[16] Z. Liu, H. Wang, and Q. Li, "Tongue tumor detection in medical hyperspectral images.," *Sensors (Basel).*, vol. 12, no. 1, pp. 162–74, Jan. 2012.

[17] S. V. Panasyuk, S. Yang, D. V. Faller, D. Ngo, R. a. Lew, J. E. Freeman, and A. E. Rogers, "Medical hyperspectral imaging to facilitate residual tumor identification during surgery," *Cancer Biol. Ther.*, vol. 6, no. February 2015, pp. 439–446, 2007.

[18] C. Zhang and H. Wang, "The narrow band AOTF based hyperspectral microscopic

imaging on the rat skin stratum configuration," *J.Europ.Opt.Soc.*, vol. 14034, 2014.

[19] I. B. Kutuza, V. E. Pozhar, and V. I. Pustovoit, "AOTF-based Imaging Spectrometer for Research of Small-Size Biological Objects," *Nov. Opt. Instrum. Biomed. Appl.*, vol. 5143, p. 5143_165, 2003.

[20] Q. Li, D. Xu, X. He, Y. Wang, Z. Chen, H. Liu, Q. Xu, and F. Guo, "AOTF based molecular hyperspectral imaging system and its applications on nerve morphometry.," *Appl. Opt.*, vol. 52, no. 17, pp. 3891–901, Jun. 2013.

[21] E. S. Wachman, W. Niu, and D. L. Farkas, "AOTF Microscope for Imaging with increased speed and spectral versatility," *Biophys. J.*, vol. 73, no. September, pp. 1215–1222, 1997.

[22] D. R. Suhre and E. Villa, "Imaging spectroradiometer for the 8-12-num region with a 3-cm(-1) passband acousto-optic tunable filter," *Appl. Opt.*, vol. 37, no. 12, pp. 2340–2345, 1998.

[23] D. Kim, S. Kim, H. J. Kong, and Y. Lee, "Measurement of the thickness profile of a transparent thin film deposited upon a pattern structure with an acousto-optic tunable filter," *Opt. Lett.*, vol. 27, no. 21, pp. 1893–1895, 2002.

[24] N. Gupta, R. Dahmani, and S. Choy, "Acousto-optic tunable filter based visible- to near-infrared spectropolarimetric imager," *Opt. Eng.*, vol. 41, no. 5, pp. 1033–1038, 2002.

[25] E. Dekemper, D. Fussen, D. Pieroux, J. Vanhamel, B. Van Opstal, F. Vanhellemont, N. Mateshvili, G. Franssens, V. Voloshinov, C. Janssen, and H. Elandaloussi, "ALTIUS: a spaceborne AOTF-based UV-VIS-NIR hyperspectral imager for atmospheric remote sensing," *Proc. SPIE*, vol. 9241, p. 92410L, 2014.

[26] Z. Nie, R. An, J. E. Hayward, T. J. Farrell, and Q. Fang, "Hyperspectral fluorescence lifetime imaging for optical biopsy.," *J. Biomed. Opt.*, vol. 18, no. 9, p. 096001, Sep. 2013.

[27] M. E. Martin, M. Wabuyele, M. Panjehpour, B. Overholt, R. Denovo, S. Kennel, G. Cunningham, and T. Vo-Dinh, "An AOTF-based dual-modality hyperspectral imaging system (DMHSI) capable of simultaneous fluorescence and reflectance imaging.," *Med. Eng. Phys.*, vol. 28, no. 2, pp. 149–155, Mar. 2006.

[28] H. R. Morris and C. C. Hoyt, "Imaging Spectrometers for Fluorescence and Raman Microscopy : Acousto-Optics and Liquid Crystal Tunable Filters," *Appl. Spectrosc.*, vol. 48, no. 7, p. 847, 1994.

[29] S. G. Kong, M. Martin, and T. Vo-Dinh, "Hyperspectral Fluorescence Imaging for Mouse Skin Tumor Detection," *ETRI J.*, vol. 28, no. 6, pp. 770–776, Dec. 2006.

[30] H. Liu, Q. Li, Y. Guan, J. Liu, and Y. Xue, "An AOTF-Based Molecular Hyperspectral Imaging (MHSI) System," *2011 5th Int. Conf. Bioinforma. Biomed. Eng.*, pp. 1–4, May 2011.

[31] Y. Yuan, J. Hwang, M. Krishnamoorthy, K. Ye, Y. Zhang, J. Ning, R. C. Wang, M. J. Deen, and Q. Fang, "time-resolved fluorescence spectrometer for optical biopsy," vol. 34, no. 7, pp. 1132–1134, 2009.

[32] D. I. M. I. N. Stratis, K. L. Eland, J. C. Carter, S. A. M. Uel, J. T. O. M. Linson, and S. M. I. Angel, "Comparison of Acousto-optic and Liquid Crystal Tunable Filters for Laser-Induced Breakdown Spectroscopy," *Appl. Spectrosc.*, vol. 55, no. 8, pp. 999–1004, 2001.

[33] J. D. Ward, S. Valle, C. Pannell, and N. P. Johnson, "Acousto-Optic Tunable Filters (AOTFs) Optimized for Operation in the 2-4µm region," *J. Phys. Conf. Ser.*, vol. 619, p. 012054, 2015.

[34] D. R. Suhre and J. G. Theodore, "White-light imaging by use of a multiple passband acousto-optic tunable filter.," *Appl. Opt.*, vol. 35, no. 22, pp. 4494–4501, 1996.

[35] F. Li, Y. Xu, and Y. Ma, "Design of hyper-spectral and full-polarization imager based on AOTF and LCVR," in *Intl. Symposium on Optoelectronic Technology and Application*, 2014, vol. 9298, p. 92980U.

[36] J. Katrašnik, M. Bürmen, F. Pernuš, and B. Likar, "Spectral characterization and calibration of AOTF spectrometers and hyper-spectral imaging systems," in *Design and Quality for Biomedical Technologies III,Proc. of SPIE*, 2010, vol. 7556, no. 1, pp. 23–29.

[37] N. J. Chanover, D. a. Glenar, D. G. Voelz, R. Tawalbeh, P. J. Boston, W. B. Brinckerhoff, P. R. Mahaffy, S. Getty, I. ten Kate, and A. McAdam, "An AOTF-LDTOF spectrometer suite for in situ organic detection and characterization," *2011 Aerosp. Conf.*, pp. 1–13, Mar. 2011.

[38] E. G. Bucher and J. W. Carnahan, "Characterization of an Acousto-optic Tunable Filter and Use in Visible Spectrophotometry," *Appl. Spectrosc.*, vol. 53, no. 5, pp. 603–611, May 1999.

[39] A. P. (Westinghouse S. and technology center) Goutzoulis and I. R.Pape, Dennis (Photonic Systems, *Design and fabrication of Acousto-Optic devices*. MARCEL DEKKER INC., 1994.

[40] Y. Qin, H. Hua, and M. Nguyen, "Characterization and in-vivo evaluation of a multi-resolution foveated laparoscope for minimally invasive surgery," *Biomed. Opt. Express*, vol. 5, no. 8, p. 2548, 2014.

[41] D. Nouri, Y. Lucas, S. Treuillet, L. Prisme, P. Orléans, U. Orléans, and D. B. Bp, "Calibration and test of a hyperspectral imaging prototype for intra-operative surgical assistance," vol. 11, no. 0033, p. 86760P, Mar. 2013.

[42] X. Zhang, T. Kashti, D. Kella, T. Frank, D. Shaked, R. Ulichney, M. Fischer, and J. P. Allebach, "Measuring the modulation transfer function of image capture devices: what do the numbers really mean? " vol. 8293, pp. 829307–829307, 2012.

[43] O. Sengul, M. Turkmenoglu, and L. B. Yalciner, "MTF Measurements for the Imaging System Quality Analysis," *Gazi Univ. J. Sci.*, vol. 25, no. 1, pp. 19–28, 2012.

[44] L. L. Randeberg, E. L. P. Larsen, and L. O. Svaasand, "Hyperspectral imaging of blood perfusion and chromophore distribution in skin," in *Photonic Therapeutics and Diagnostics V*, 2009, vol. 7161, p. 71610C–1.

Chapter 5: Skin Erythema Classification based on Hyperspectral Imaging

5.1 Preface

Skin erythema is an accompanied symptom for multiple cutaneous diseases [1] including psoriasis [2], [3], acne lesions [4], as well as injuries [5], [6]. It also acts as the early indicator for skin severe complications in cancer radiotherapy treatment [7]–[10]. Moreover, cutaneous inflammation is claimed to be a cause of hemorrhaging which is life-threatening during thrombocytopenia [11]. Consequently, there is a pressing need for the development of an objective quantitative method to assess skin erythema progression. The contact-free technique would be more recommended to investigate sensitive skin injuries [6].

Erythema has been investigated by different techniques as formerly detailed in Chapter 2. These techniques include colorimetry [12], [13], diffuse reflectance spectroscopy [14], laser Doppler flowmeter [15], digital photography [16], [17], confocal microscopy [18], optical coherence tomography [19], ultrasound [20], and magnetic resonance imaging [21]. Although the literature techniques are versatile and some of them are advanced, visual assessment (VA) is still considered the gold standard for the clinical evaluation of skin erythema. Unfortunately, even VA has its own lapses that make it far from optimal. These lapses involve; expertise versatility, inter/intra-observation variability, lack of precise quantification, and perhaps visual acuity deficiency [22], [23].

Other than VA, two major modalities are, in literature, deeply entangled in quantitative assessment of skin erythema; diffuse reflectance spectroscopy [24], [8], [25], [26], [10] and digital imaging [3], [4], [27], [28]. However, diffuse reflectance measurement techniques require direct contact with patients' skin and apply only for small area investigation. Digital imaging modality, on the other hand, is poor in the spectral interpretation of skin color change. Since it is mainly constrained to the three major visible bands (red, green, and blue) and thus it is non-precise in differentiating between tissues' constituents that have close spectral features. Inspired by the literature [29], hyperspectral imaging (HSI) is proposed on the basis of being a hybrid combination of the two formerly mentioned modalities. Since HSI is capable of overcoming the individual limitations for each particular modality while combining their advantages. For instance, HSI requires no skin-contact and is capable of studying considerably large regions of interest while being not limited to the trichromatic, red-green-blue, channels of digital color imaging.

The goal of this exploratory study, detailed in this chapter, is to investigate the feasibility of the new high-throughput acousto-optic tunable filter (AOTF)-HSI configuration to be utilized for carrying out a precise classification of an artificial skin induced erythema. The main checkpoints addressed in this study are; 1) investigating HSI sensitivity to detect subtle erythematous regions in skin, 2) delineating the major imperative spectral region for erythema differentiation, 3) classifying skin erythema, and 4) use the employed classifier to contrast digital and spectral imaging for erythema assessment.

5.2 Materials and Methodology

5.2.1 Volunteers

A control experiment was designed to examine the feasibility of HSI sensitivity toward detecting skin erythema. This experiment is considered an exploratory study prior to being involved in radiation dermatitis quantification. The studied erythema was artificially induced on healthy volunteers' forearms for investigation purpose. Three people, two male and one female from different backgrounds; Asian, North African, and South American, volunteered to participate in the exploratory study. The volunteers' age ranges from 35 to 50 years and they have neither cutaneous disease nor injury in the selected region of interest. Participation was based on a verbal consent of volunteers to induce transient skin erythema at the inner side of their ventral forearms simulating the erythematous linked effect of radiotherapy treatment for skin cancer (SC) patients.

5.2.2 Hyperspectral Imaging

The stare-looking HSI used to monitor the artificially induced erythema on participating volunteers is a newly developed AOTF-based configuration which has been fully characterized and evaluated previously in Chapter 4. In brief, the developed AOTF-HSI incorporates two halogen sources of total 300 W for illumination. The optical setup is comprised of a zoom lens to admit the object back reflectance. The former lens is followed by a 1:1 optical relay to propagate the object image through the entire system. In between the two optical relay lenses, an AOTF cell is utilized to disperse the propagating beams into separate bands. These beams are finally focused by the optical relay on a CMOS detector. The acquired images are then transferred to a workstation that holds the developed control program for synchronizing the performance of both the filter and the CMOS detector. The dedicated workstation computer, in addition, is used for data analysis. A schematic diagram of AOTF-HSI optical setup for skin erythema imaging is shown in Figure 5-1.

AOTF-HSI system is employed to capture a determined number of spectral images based on user selection of radio frequency (RF) step. The radio frequency signal is responsible for generating the acoustic signal frequency by which diffraction of a particular band takes place. The highest spectral resolution of the HSI system is 1.5: 4 nm varying inversely and nonlinearly with the operating visible-near-infrared (VIS-NIR) range of 450: 800 nm. The CMOS sensor format is 1-inch^2 with a resolution of 2048 x 2048 pixels and pixel pitch of 5.5 µm. The digital color camera involved in the current study is a 16-megapixel compact video camera (HYUNDAI, HDMI-768, China). A white standard calibration surface with 99% reflection (SRS-99, Labsphere, NH, USA) was used for image normalization.

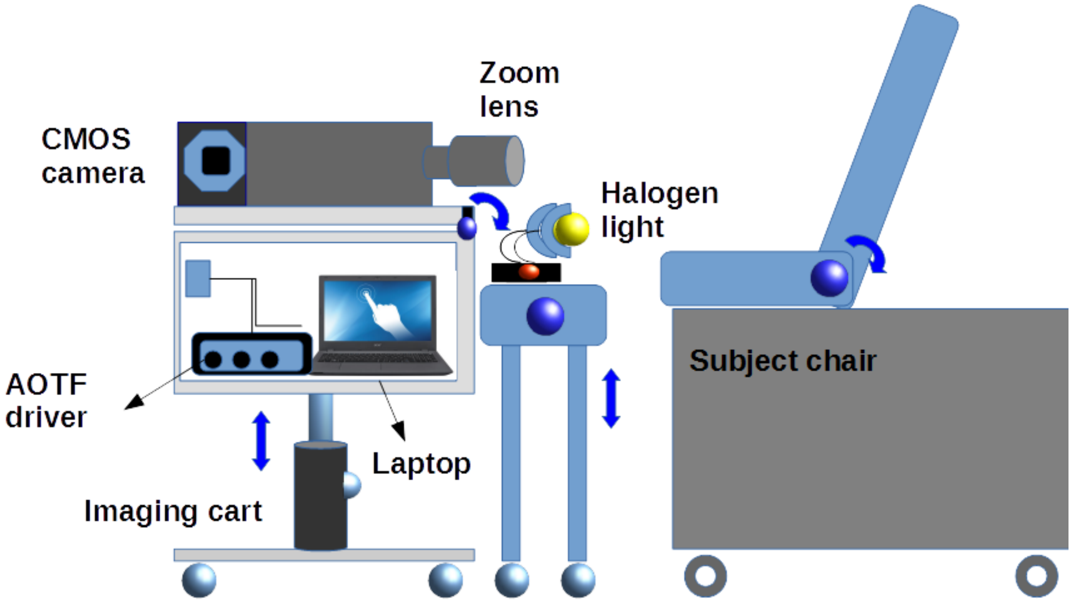

Figure 5-1: The configurational setup for imaging artificially induced erythema contains the spectral camera mounted to a custom-made moving cart which encloses the control unit (laptop and AOTF driver). Ahead of the camera, two commercial halogen light sources exist to illuminate the ROI from both sides. Both the cart and the light sources carrying table are height adjustable and the camera surface has an angular rotation degree of freedom. A clinical chair was used to seat the volunteer facing the spectral camera.

5.2.3 Artificial skin erythema induction

The artificially induced skin erythema/ flare is planned to be bounded by a predetermined marked ROI using green / blue markers at the perimeters. Although green/blue markers might not be as convenient as red ones; they were used to seizing any possible confusion with induced skin erythema in image analysis. The skin erythema reaction is initiated by instructing the participating volunteers to strike the marked ROI for a time period of approximately three minutes utilizing a plastic bar. An expert radiotherapist is involved in the experiment from the beginning to the end. The radiotherapist monitors and grades the volunteer’s induced erythema within the marked ROI, as shown in Figure 5-2. The induced skin erythema intensity and rate of development was variable among the three participating volunteers. For instance, the less melanin content skin type was the fastest to display a visual reaction and vice versa.

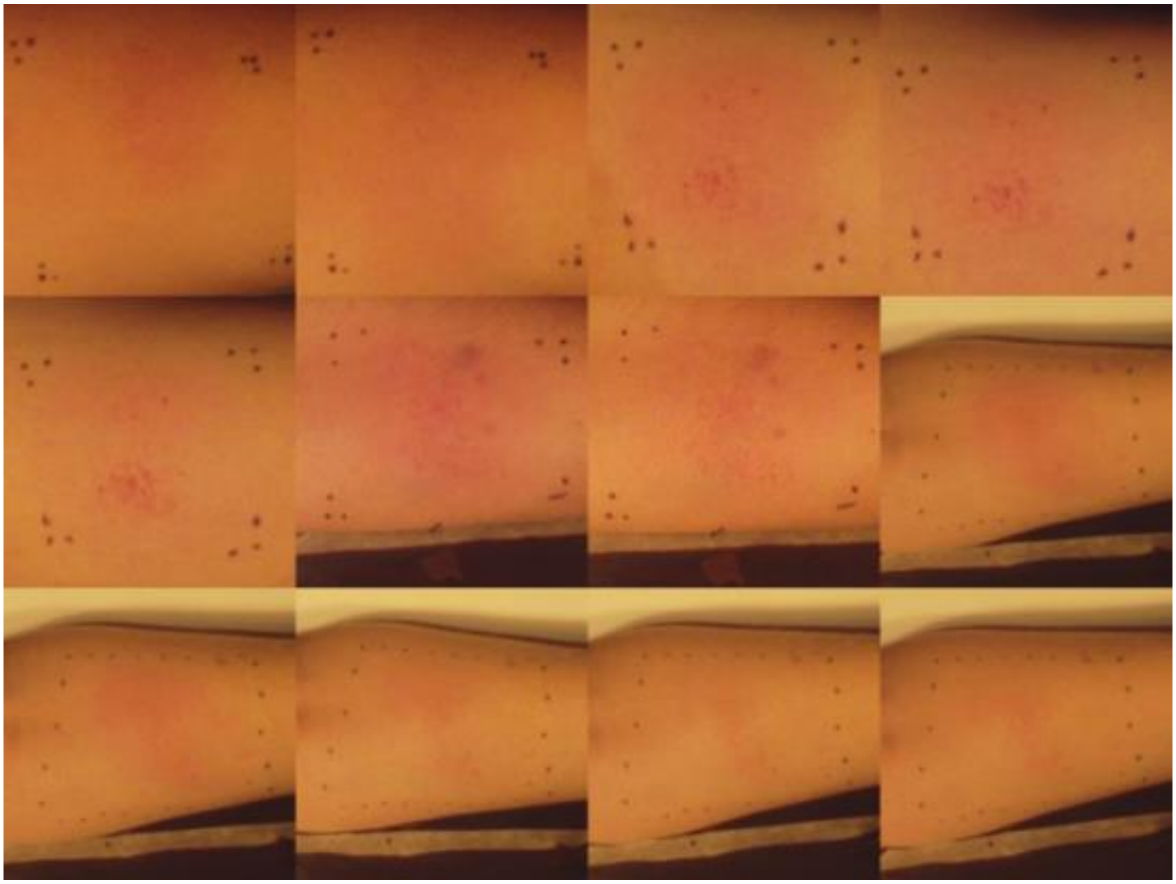

Figure 5-2: Artificially induced skin erythema developed on the skin of three participating volunteers' ventral side arms. Images are captured by the digital color video camera involved in the study at a sequence after the striking action.

5.2.4 Experimental procedure

Prior to artificial erythema induction, the assigned field of view was imaged by both HSI and the digital color camera for each participant volunteer. This data was captured and stored as an individual volunteer corresponding baseline. Moreover, the dark and the white standard hyperspectral datacubes were collected sequentially taking into consideration the same illumination and room conditions. The dark datacube was utilized to account for the dark current noise in the CMOS sensor while the white standard datacube is used to compensate for possible uneven illumination and instrumentation spectral dependence. An overview of the experimental procedure and data analysis track is simply illustrated in the flow chart drawn in Figure 5-3.

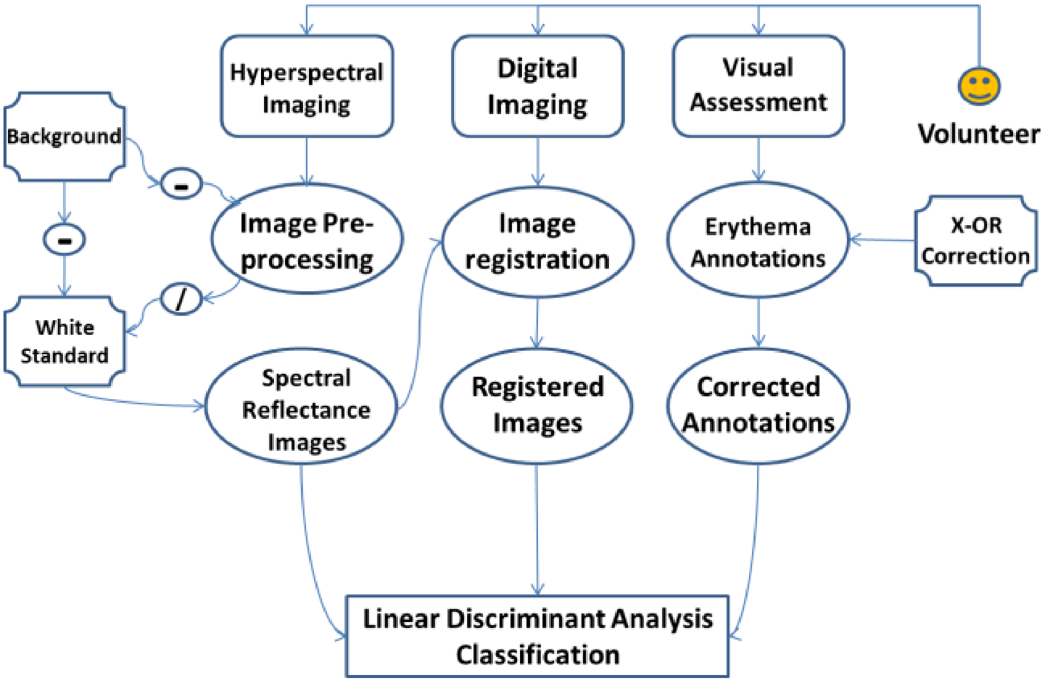

Figure 5-3: Overview of the workflow of the artificially induced erythema exploratory study accomplished on healthy volunteers.

Once the skin erythema was visually graded by the research team's radiotherapist, according to a predetermined ordinal scale for skin erythema displayed in Table 5-1, digital and spectral imaging proceeded. Initially, the ROI was digitally imaged by the color video camera for at least three consecutive times preserving the same scope of the spectral camera. Next to the digital color imaging, the same ROI was imaged spectrally by the HSI system. This process was repeated orderly as the aforementioned sequence; each round lasts approximately three minutes until the induced skin erythema/ flare fades away and can no longer be visually detected by the radiotherapist.

Table 5-1: The visual assessment ordinal scale for skin erythema assessment developed by an expert radiotherapist

Name	**Score**	**Description**
No erythema	0%	No observable difference relative to normal skin
Very faint erythema	25%	Skin has a very light pink color
Faint erythema	50%	Skin reaction is more apparent with clear borders but is still pink with more intensity.
Bright erythema	75%	Erythema is apparent in bright pink and borders are clearly defined.
Very bright erythema	100%	Skin is bright red, borders are very well defined, capillaries and bruising may be visible.

5.3 Data processing

To achieve visual assessment, the radiotherapist gives grade/s for the artificially induced skin erythema based on the clinical experience, which is subjective but gold standard, out of the former table of skin reactions. These grades are considered to be the ground truth of the skin reaction in this exploratory study. The induced skin erythematous reaction in the provoked region was nonhomogeneous. As a result, the radiotherapist drew contours to bound visually individual induced skin erythema grade disjointedly. The graded contours were drawn using ImageJ freeware and saved as separate files and named with skin annotations. The skin annotations are overlaid frames, which can be printed on both digital color and spectral frames without affecting the original image frame contained information. A sample of skin annotations provided by the radiotherapist is shown in the top row of Figure 5-4.

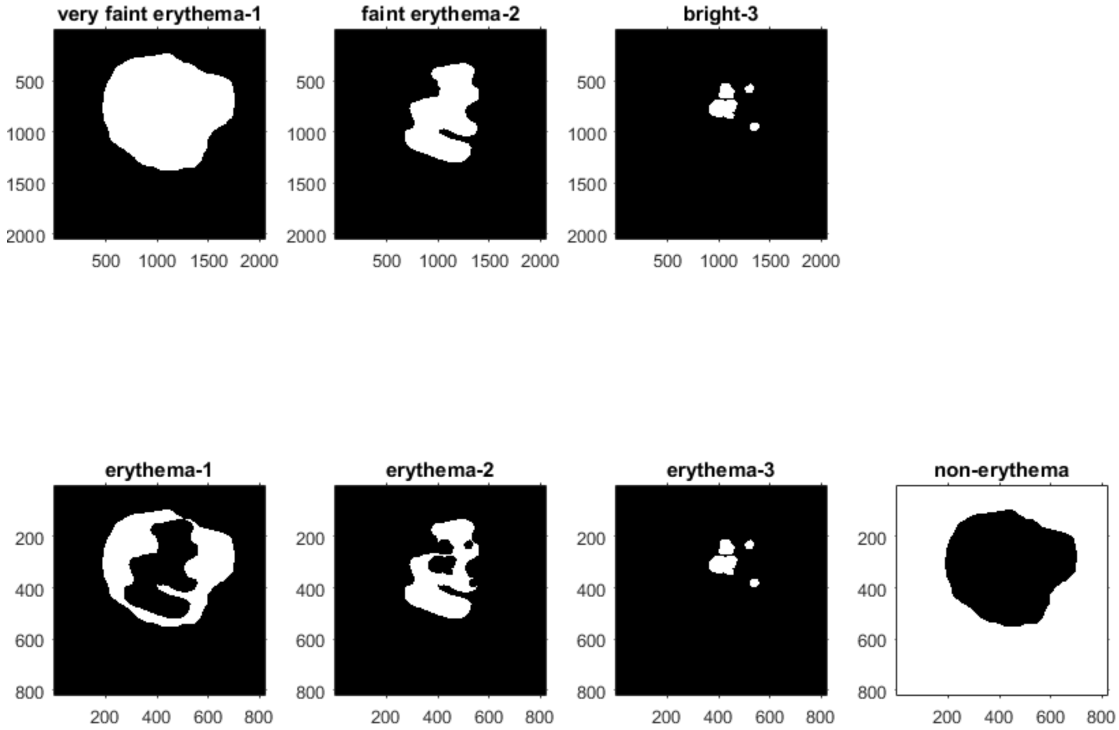

Figure 5-4: (top) Skin erythema overlapped annotations provided by the radiotherapist for one volunteer. (Bottom) XOR process was accomplished for correcting the overlap effect, and thus, the correction process yields exclusive annotations. A new annotation of the non-erythematous region was generated to count for normal skin.

Since the erythematous annotations are signifying the ground truth skin reaction classes, they need to be exclusively separate, not as shown in the top row of Figure 5-4. As a result, XOR process was executed among skin annotations to correct for the overlap effect as shown in the bottom row of Figure 5-4. Along with the erythematous classes, a supplementary class for the non-erythematous region was created. The created class used to identify the normal skin region within the captured frames. The normal region is computed as the difference between the entire image and the union of the annotated regions. Taking all together, the exclusive skin annotations enabled monitoring both the spatial and temporal recovery of the erythematous regions toward normal status on volunteers' skin. The graded contours for the artificially induced erythema on the arm of one volunteer displayed the stages of the temporal and the spatial changes of the skin reaction intensity along the duration of the study. The displayed data was attained via few steps. The first step is grading the induced erythematous reaction by the radiotherapist. The former step is replicated for all the consecutive imaging cycles for the same individual. Following the grading, the second step is computing the ratio of individual erythematous reactions to the total area of ROI. The final step is plotting the erythematous graded contours at the corresponding imaging cycle which represents the temporal evolution as shown in Figure 5-5. The intensity of the induced erythema was gradually decreasing over time from the first imaging cycle going to the last. In addition, the annotations are used to allocate the different erythema grades on both the color and spectral reflectance images.

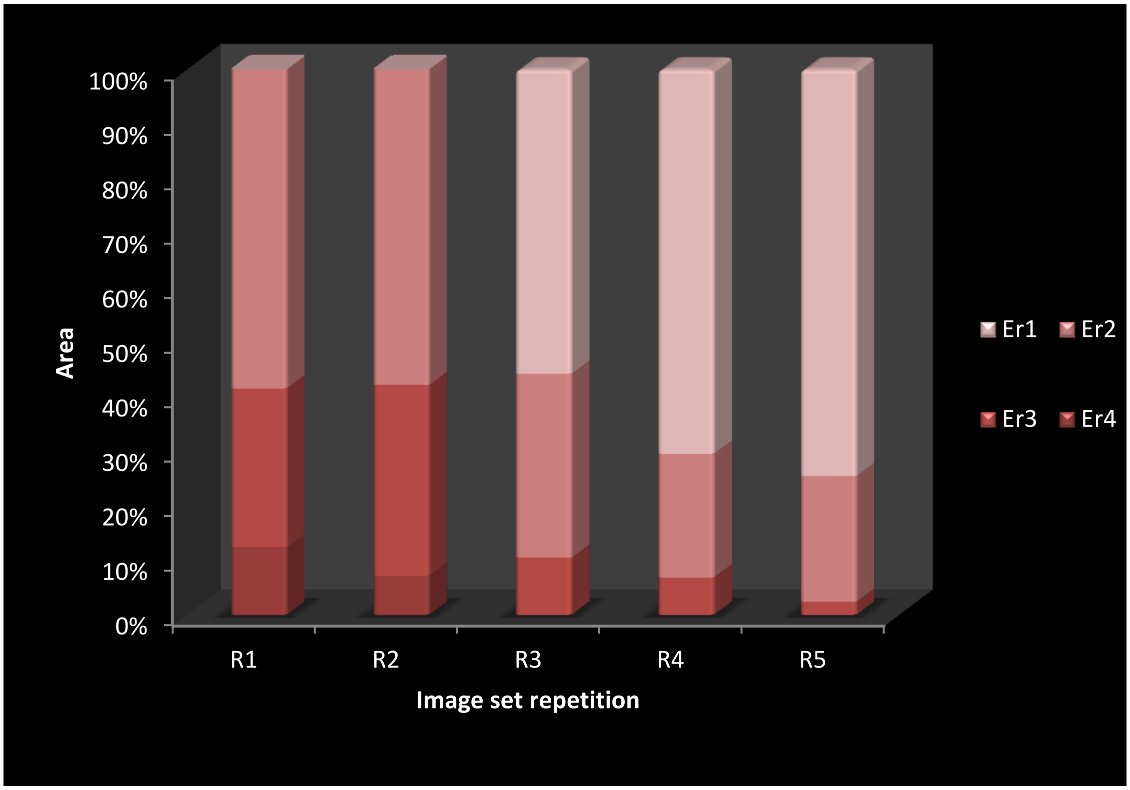

Figure 5-5: The skin artificially induced erythema provoked on a single volunteer ventral arm side evolution through multiple image sequence cycles. The first imaging cycle R1 showed the development of the highest erythema intensities (Er4, Er3, and Er2). By the time of R5, most of the volunteer's ROI was occupied by the lowest discernible erythema intensity (Er4).

Spectral reflectance data are computed by an initial processing of the acquired hyperspectral datacubes. Simply, the acquired raw spectral data ($\boldsymbol{I_{ROI}}$) is adapted to become noise-free by subtracting the sensor dark current ($\boldsymbol{I_{dark}}$) datacube. Following the removal of noise, variation of illumination was corrected by normalizing the datacube to a white standard reflectance target ($\boldsymbol{I_{ws}}$) datacube. Both the white standard target and the dark noise datacubes were collected, taking into consideration the same conditions of imaging volunteers' ROI. The former two-step process does not only contribute in the skin reflectance but also amends for the captured spectral data due to systemic artifacts. In other words, this process arises above the need to account for the spectral response of the hyperspectral camera individual optical components. Hence, the skin ROI reflectance (R_{ROI}) is computed as follows;

$$\boldsymbol{R_{ROI}} = \frac{\boldsymbol{I_{ROI}} - \boldsymbol{I_{dark}}}{\boldsymbol{I_{ws}} - \boldsymbol{I_{dark}}} \tag{5-1}$$

Next to the skin reflectance computation, the captured spectral frames are ready to be registered. The registration process was executed using a freeware (ImageJ [30]) plugin. Simply put, the executed image registration depends on a predefined reference band selected by the user. Selecting the reference band is governed by the peak of the computed histogram for a specific location in the captured frame. This location contains a well-determined feature/ landmark; be it natural (skin freckle or mole) or artificial (green or blue marked dots). The spectral bands in the datacube are registered to this band provided that pixel shift is set to minimum. Likewise spectral images, digital color images are registered to the corresponding spectral reference bands. This process essentially aimed to sustain the same field of view under investigation for both spectral and digital imaging, and thus, data is prepared for further processing.

Spectral reflectance data, which is also registered, were furtherly processed to achieve particular aims. The first aim is to enhance the signal to noise ratio. To achieve that, Wiener filter was applied [31], [32]. The formerly mentioned filter is basically a low pass window which conducts all, but high-frequency noise. Weiner filter runs in an adaptive way governed by the level of variance of the image's pixels intensities. Weiner's filtered image has pixel intensity $\boldsymbol{I_w(x)}$, where $\boldsymbol{x}$ indexes frame pixels. The former term, $\boldsymbol{I_w(x)}$**,** is computed adaptively based on the level of noise contained in the original pixel intensity $\boldsymbol{I_0(x)}$.

$$\boldsymbol{I_w(x)} = \boldsymbol{\mu} + \frac{\sigma^2 - \nu^2}{\sigma^2}(\boldsymbol{I_0(x)} - \boldsymbol{\mu}) \tag{5-2}$$

The term ν expresses the data variance, and μ and σ^2 are the image locally computed mean and standard deviation [31].

The second aim is to classify the distinct clusters of pixels contained in the datacube in order to distinguish between skin erythema grades. Toward realizing this aim, linear discriminant analysis (LDA) [33]–[35] was selected to be the statistical method of classification. Moreover, based on LDA results both digital and spectral imaging techniques performance are weighed for skin erythema assessment.

Briefly, LDA classifies the observation data based on the basic assumption of a normal distribution occurring within each particular class. Given a number (n) of labeled set of observations (x, y) where the term: $x \in \mathbb{R}^m$ and the term **m** is the spectral datacube dimension, and y is a single class out of S discrete classes [35]. LDA aims to identify the transformation matrix G that linearly reduces the experimental multidimensional spectral data to a smaller s-dimensional vector (a), where $a = G^T x \in \mathbb{R}^s$, provided that s < m. The purpose of transformation to small dimensional vector space is to achieve the maximum separability among distinct existing classes in the multidimensional observations according to an accustomed criterion. This criterion is a mathematical function used for discrimination between groups of data points that come together around a central mean. For instance, a discrimination function (f_d) can be determined as follows:

$$\boldsymbol{f_d(X) = arg\,\max_{S} P(y = S|X)} \tag{5-3}$$

Where Bayes rule has been employed to determine individual class posterior:

$$\boldsymbol{P(y = S|X) = \frac{P(X|y = S)P(y = S)}{P(X)}} \tag{5-4}$$

An empirical assignment for the prior probability is used in this classification to be equal to ns/n. The P (X) is a utilized as a normalization constant process and is delineated as the summation over the number of discrete classes S as follows:

$$\boldsymbol{P(x) = \sum_{1}^{s} P(x|y = s)P(y = s)} \tag{5-5}$$

LDA modeled particular class conditional probability (x|y=s) by applying multivariate normalized density function (f_{mul}):

$$\boldsymbol{f_{mul}(X|\mu_S\,, \textstyle\sum_S) = \frac{exp\{-\frac{1}{2}(X - \mu_S)^T \sum_S^{-1}(X - \mu_S)\}}{\sqrt{2\pi|\sum_S|}}} \tag{5-6}$$

Where μ_S and $\sum_S$ are particular class mean and covariance, and the two mathematical formats $|\ \ |$, $[\ \ ]^{-1}$ are expressing the matrix determinant and inverse, respectively. A further assumption used in the discriminant analysis is that the embedded distinct classes in the provided observation data share a common covariance matrix $\Sigma s = \Sigma \forall s$ which yields a linear boundaries decision. The previous assumptions assisted in the inference of both the mean $\hat{\mu s}$ and the covariance matrix $\widehat{\Sigma s}$ specifications based on the training ratio of the observation data.

5.4 Results

Once color images were registered with the corresponding spectral data set, the skin corrected exclusive annotations were overlaid on both digital color and spectral images. For illustration purposes, the distinct induced erythematous grades were contoured for one participating volunteer from the moment the skin provocation halted until induced erythema becomes no more discernible by human eye. The different levels of erythema used in contouring are; very faint erythema (Er1) in yellow, faint erythema (Er2) in orange, bright erythema (Er3) in red and very bright erythema (Er4) in magenta, as indicated in Figure 5-6. The indicated images demonstrate the gradual decrease of the skin erythematous reaction from the start to the end time, where erythema became hard to observe visually.

The skin reflectance was computed based on the pixel intensities (mean ± std.) for each ROI for the different skin contoured response for individual participants. This process was repeated for all instances of the repeated imaging sequence. Skin erythematous levels in addition to normal healthy skin reflectance were congregated and averaged for the three volunteers' altogether and plotted against the operating spectral range of HSI system, as shown in Figure 5-7 (a). The plotted result identified a spectral region of maximum separation between the healthy and erythematous skin. This region is confined within the range of ~520: 650 nm.

Zooming more on the formerly mentioned spectral zone using only a single volunteer's data enabled the differentiation between the healthy skin reflectance, in blue circles, and the very faint erythematous skin, in red circles. This particular spectral region is majorly affected by the intrinsic absorption of hemoglobin chromophores. Where the intensity of skin reflectance is dependent on the present hemoglobin concentration; be it oxygenated or deoxygenated. The reflectance data was smoothed utilizing Savitzky-Golay low pass filter and plotted in Figure 5-7 (b). The error bars involved in the shown figure is representing the heterogeneity of the erythematous zone which is interpreted mathematically in standard deviation. Only error bars for the normal healthy skin, very faint erythema, and very bright erythema are displayed for contrast purposes.

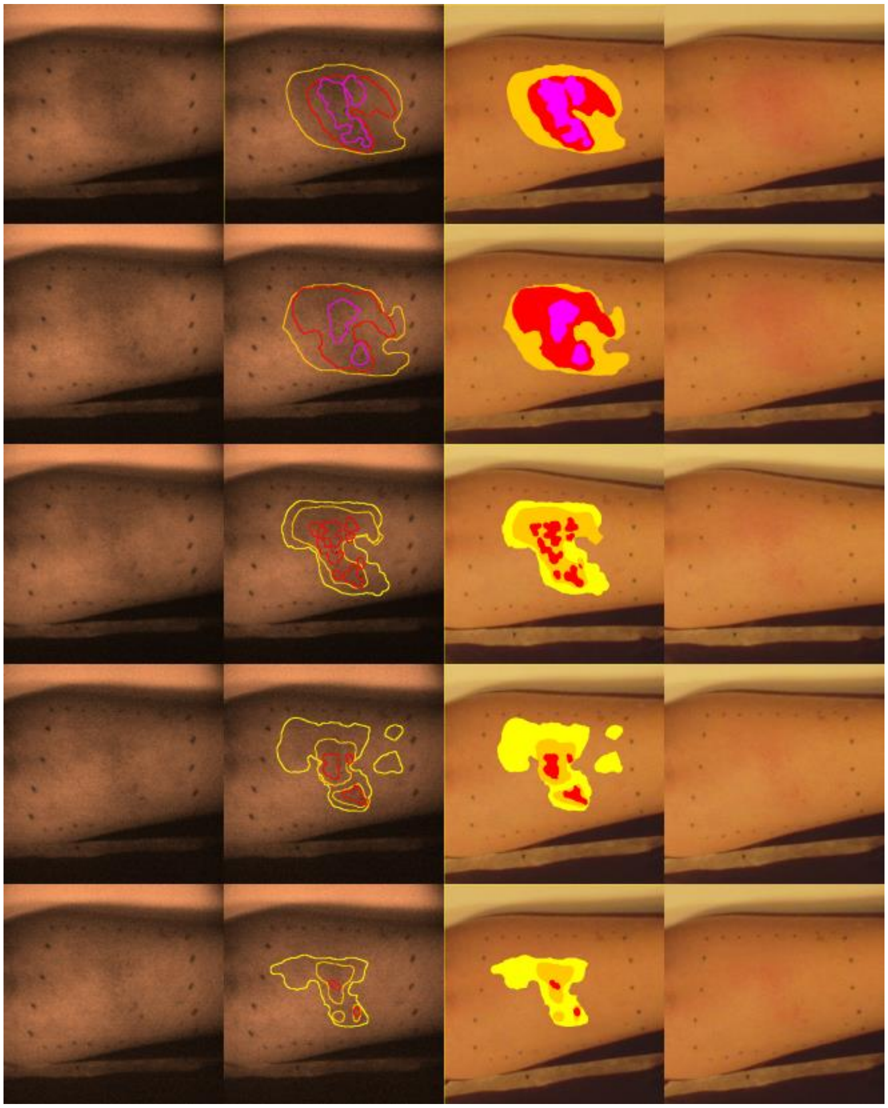

	🟨	🟧	🟥	🟪
Control	**Er1**	**Er2**	**Er3**	**Er4**

Figure 5-6: Skin annotations for the distinct erythematous levels are printed on digital and spectral images for one volunteer. The sequence from top to bottom is based on the time scale of imaging. The displayed spectral images were captured at 540nm since this wavelength is one absorption peak for oxyhemoglobin in the green region (extreme-left). Corrected annotations are printed in the same set of images (middle-left). The corresponding digital color images are displayed (extreme right), and again corrected filled annotations are printed for the same set (middle right). The different levels of erythema used in contouring are very faint erythema (Er1) in yellow, faint erythema (Er2) in orange, bright erythema (Er3) in red and very bright erythema (Er4) in magenta.

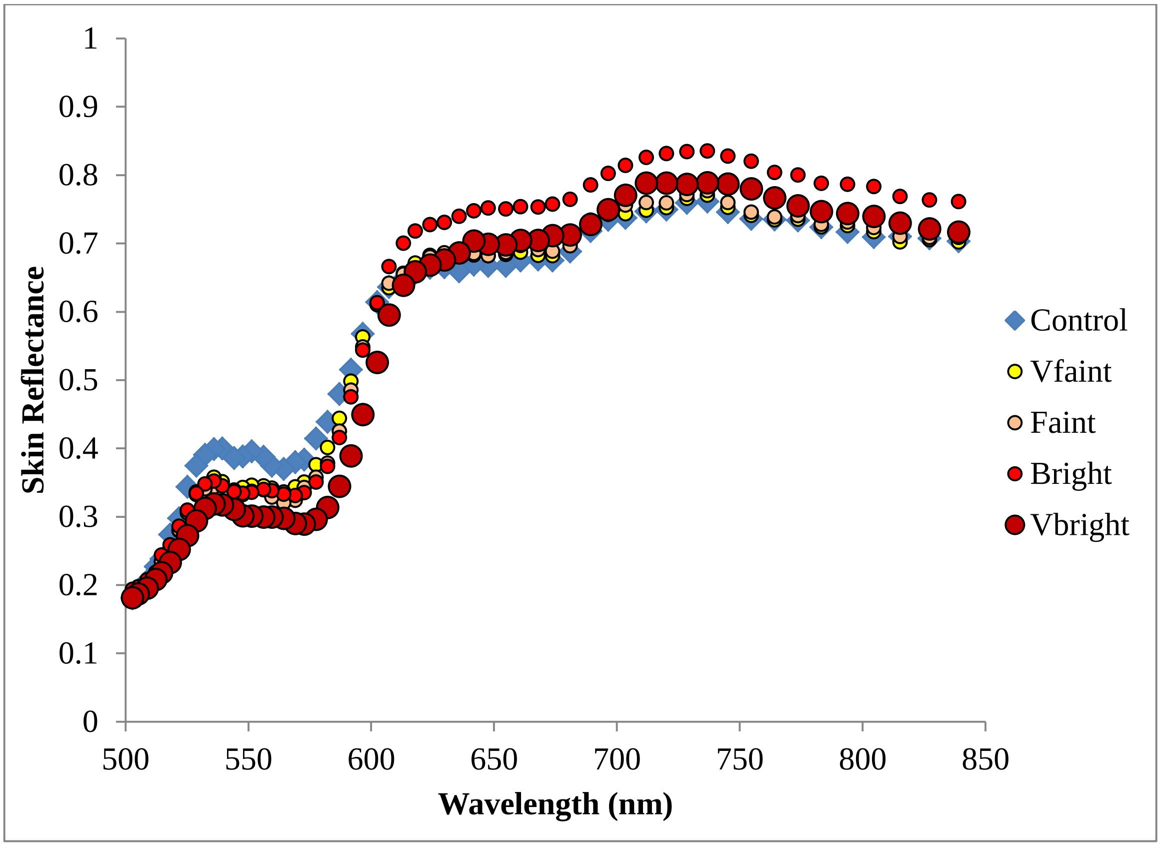
Skin Reflectance
1
0.9
0.8
0.7
0.6
0.5
0.4
0.3
0.2
0.1
0
500
550
600
650
700
750
800
850
Wavelength (nm)
Control
Vfaint
Faint
Bright
Vbright

(a)

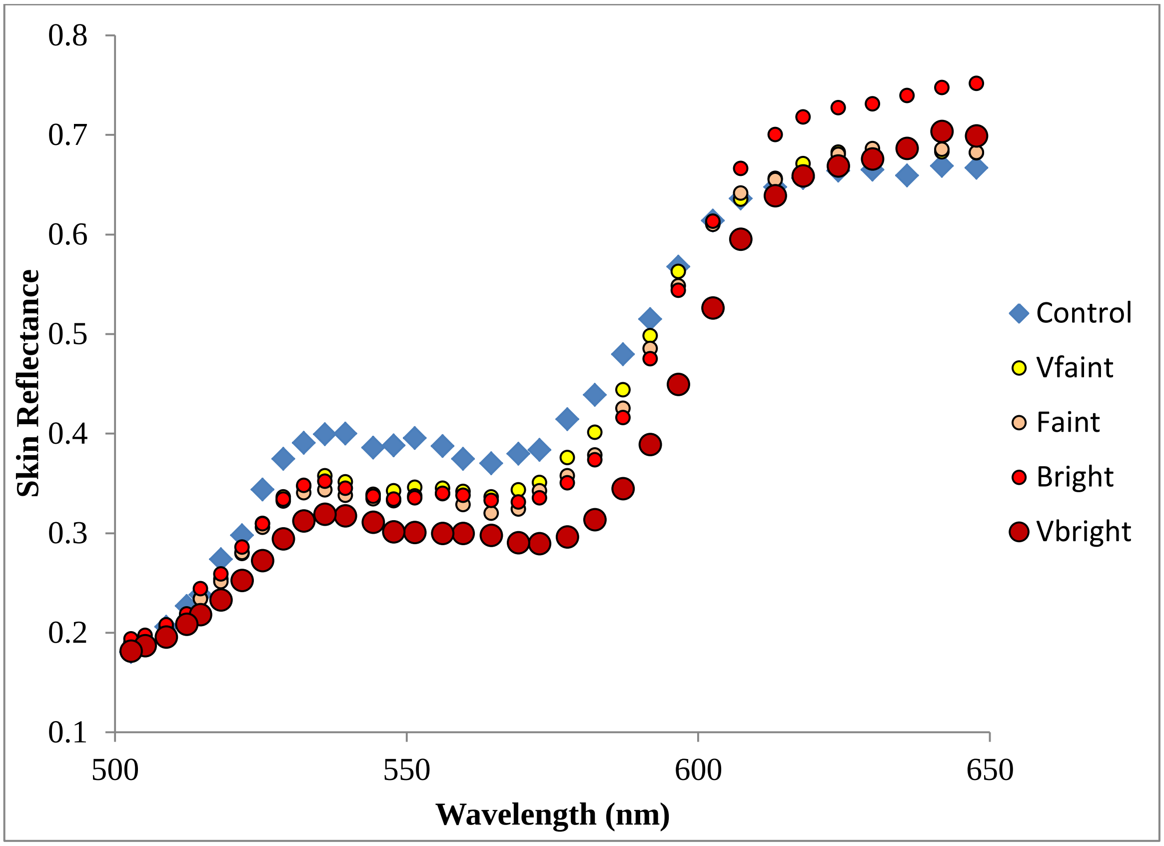

(b)

Figure 5-7: (a) the skin reflectance all over the operating range averaged for the three participating volunteers for different levels of induced skin erythema, (b) the skin reflectance for one single volunteer in the range of 500: 650 nm, which is apparently the main region of distinguishable difference between healthy and the erythematous zones.

One more time, the skin reflectance was computed for the typical healthy and erythematous skin contoured regions, but this time using the volunteers' digital color images. Primarily, each color image was split into its basic components red, green, and blue layers. Then the skin annotated ROI's pixel intensities were averaged individually for each color channel. The digital color data was able to provide a supporting evidence to verify that the green zone is the most sensitive visible region for the development of skin erythema. Since the green reflectance component was decreasing proportionally with the skin erythema intensity increment. Figure 5-8 displays the three color channels, blue, green, and red, reflectance averaged for the three participating volunteers, for different skin erythematous grades.

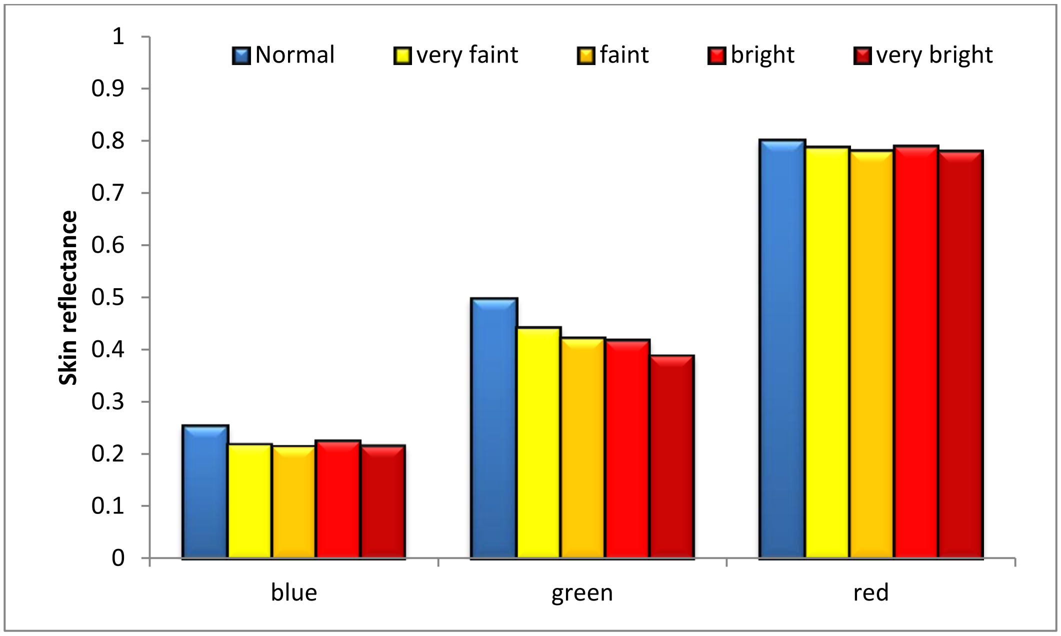

Figure 5-8: Skin reflectance computed from the digital color images blue, green, red channels to examine the most sensitive part of the visible region to erythema development.

Applying LDA statistical method on both the spectral and the digital images in a supervised parametric approach exploiting the ground truth made available by the radiotherapist was the way to evaluate both imaging modalities in erythema assessment. Twelve data sets were collected in this study from the participating volunteers. These data sets were divided into two groups; training and test sets. The ratio between the training group and the test group data sets, according to the Pareto principle, was set to ~ 20: 80%, respectively. A random selection of the training set was accomplished by a random key generator function. Since the number of data samples was huge, ~ 50,000,000 pixels, we performed down sampling for the acquired data by a factor 0.6 to reduce the size in order to speed up the classification processing time. The classification process was run for 10 consecutive times to verify the output results. Six parameters were reported to weigh classification results; accuracy, precision, sensitivity, specificity and geometrical mean [36].

Table 5-2: Classification parameters clinical meaning in erythema context

Parameter	**Clinical meaning**
Accuracy	How much true erythema and true normal skin were classified within the sample
Precision	How much of the classified erythema was true erythema
Sensitivity	How much of the true erythema was classified
Specificity	How much of the true normal was classified
Geometrical mean	$= \sqrt{\text{Sensitivity} * \text{Specificity}}$

The average values for the entire formerly mentioned classification parameters were higher in hyperspectral imaging against digital color imaging. Moreover, the hyperspectral imaging achieved an outstanding performance in accuracy and precision as exhibited in Figure 5-9. The difference between the HSI and RGB imaging in classification parameters combined with the corresponding P-values are demonstrated in

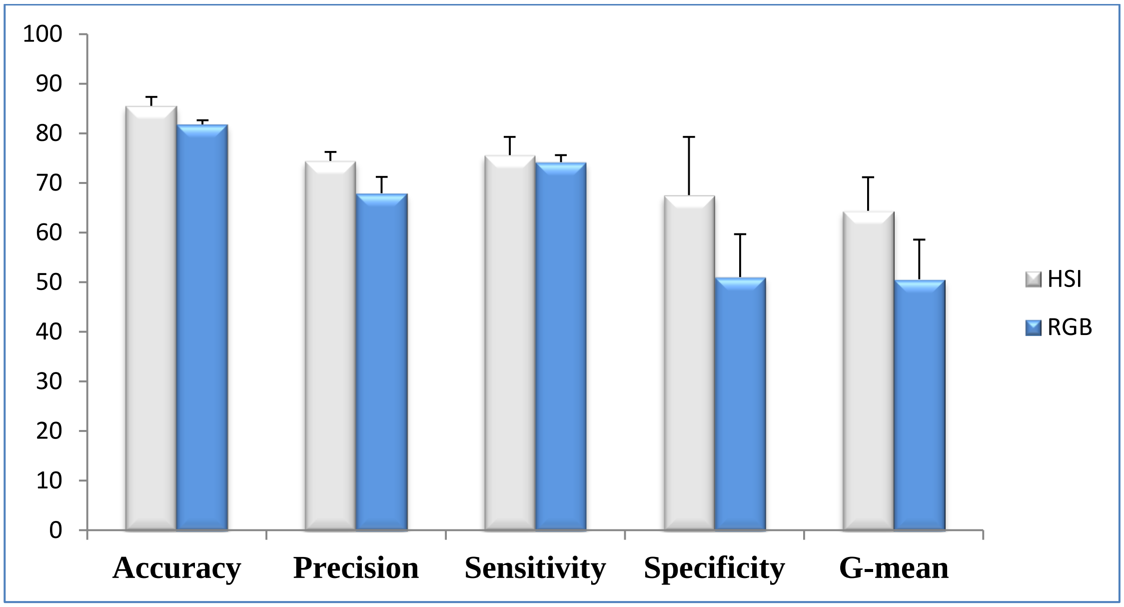

Figure 5-9: LDA Classification parameters comparison between hyperspectral and digital imaging for skin erythema context. HSI displayed a higher average value in the entire six parameters reported, with an outstanding performance in accuracy and precision.

Table 5-3: the difference between HSI and RGB imaging in classification parameters and the corresponding p-values

Parameter	Accuracy	Precision	Sensitivity	Specificity	G-mean
Diff. (%)	3.7	6.49	1.41	16.5	13.84
P-value	0.0003	0.007	0.0012	0.041	0.0037

5.5 Discussion

In this exploratory study, we aimed to investigate the newly developed AOTF-HSI configuration sensitivity to detect skin color change due to an external provocation. This study on healthy volunteers was a checkpoint prior to making use of the developed imaging system in a clinically induced skin erythema. Based on the study results, the newly developed imaging spectrometer performed well in classifying distinct grades of skin erythema supervised by an expert radiotherapist. Although HSI is currently less competitive regarding data processing speed compared to other optical techniques such as diffuse reflectance spectroscopy or digital imaging, it is still distinguishable in other parameters. For instance, HSI has superiority in wide area investigation which may require DRS a great effort and lengthy time to achieve. In contrast, digital imaging might be able to address the same HSI area of interest, but it is poor in terms of resolving narrow spectral changes. Over and above, hyperspectral imaging has been tagged as the gold standard in mapping narrow spectral changes due to the variability of encompassed skin chromophores.

Even though both spectral and color imaging techniques approved the green region as the most sensitive region in erythema sensation; color imaging is unqualified for interpreting the green reflectance change with erythema alteration. In addition to skin reflectance analysis, supervised classification, applying LDA, contributed in clustering distinct level of induced skin erythema. This clustering technique yields a map for distributed changes of skin erythema. Training developed LDA classifier with ground truth created an objective quantitative method of erythema assessment on the test portion of the data sets.

5.6 Conclusion

Ultimately, the exploratory study implemented on artificially induced erythema on volunteers' arm provided a testimony for 1) the feasibility of employing HSI as an objective measure for erythema assessment. 2) HSI and color imaging verified that green spectra are the most sensitive for skin erythema alteration; however, digital color imaging was not able to provide a physiological interpretation for the skin color change. 3) LDA classification method was successful in sorting erythema grades. 4) LDA classification parameters proved the outstanding performance of HSI against digital imaging, in accuracy and precision of detecting erythematous and normal skin regions.

To this end, it is recommended to go through a long-term study for a clinical condition associated with skin erythema. One candidate condition is radiation dermatitis/ skin erythema to evaluate the feasibility of hyperspectral imaging in properly monitoring the modification of skin color on a temporal basis. Based on the exploratory study results, it is expected that HSI could be a well-performing contact-free objective monitoring technique for radiation dermatitis. However, much work needs to be done in order to establish HSI as a bench top system for investigating the skin erythema in dermatological clinics. In the coming chapter, a preliminary study was accomplished using HSI to detect erythema development on skin cancer patients during radiotherapy treatment.

References

[1] N. Kollias and G. N. Stamatas, "Optical non-invasive approaches to diagnosis of skin diseases," J. Investig. Dermatology Symp. Proc., vol. 7, pp. 64–75, 2002.

[2] M. H. Ahmad Fadzil, D. Ihtatho, A. Mohd Affandi, and S. H. Hussein, "Objective

assessment of psoriasis erythema for PASI scoring.," J. Med. Eng. Technol., vol. 33, no. 7, pp. 516–24, 2009.

[3] A. Raina, R. Hennessy, M. Rains, J. Allred, D. Diven, and M. K. Markey, "Objective measurement of erythema in psoriasis using digital color photography with color calibration," Ski. Res. Technol., no. 7, pp. 1–6, 2015.

[4] E. Rizova and A. Kligman, "New photographic techniques for clinical evaluation of acne," J. Eur. Acad. Dermatology Venereol., vol. 15, no. SUPPL. 3, pp. 13–18, 2001.

[5] E. Van Den Kerckhove, K. Stappaerts, S. Fieuws, J. Laperre, P. Massage, M. Flour, and W. Boeckx, "The assessment of erythema and thickness on burn related scars during pressure garment therapy as a preventive measure for hypertrophic scarring," Burns, vol. 31, no. 6, pp. 696–702, 2005.

[6] G. V Oliveira, D. Chinkes, C. Mitchell, G. Oliveras, H. K. Hawkins, and D. N. Herndon, "Objective assessment of burn scar vascularity, erythema, pliability, thickness, and planimetry.," Dermatol. Surg., vol. 31, pp. 48–58, 2005.

[7] Terence S. C. Poon, Johanna M. Kuchel, Aamir Badruddin, Gary M. Halliday, Ross StC. Barneston, Haruhi Iwaki, Masato Hatao, "Objective measurement of minimal erythemal and melanogenic doses using natural and solar simulated light," Photochem. Photobiol., vol. 78, no. 4, pp. 331–336, 2003.

[8] J. Nyström, P. Geladi, B. Lindholm-Sethson, J. Rattfelt, A. C. Svensk, and L. Franzen, "Objective measurements of radiotherapy-induced erythema," Ski. Res. Technol., vol. 10, no. 4, pp. 242–250, 2004.

[9] E. J. Yoshida, H. Chen, M. A. Torres, W. J. Curran, and T. Liu, "Spectrophotometer and ultrasound evaluation of late toxicity following breast-cancer radiotherapy.," Med. Phys., vol. 38, no. 10, pp. 5747–55, 2011.

[10] L. Diana L. Glennie, Joseph E. Hayward, Orest Z. Ostapiak, James Wright and T. J. F. Doerwald-Munoz, "Diffuse reflectance spectroscopy for monitoring erythema in head & neck intensity modulated radiation therapy," J. Radiat. Oncol., 2014.

[11] T. Goerge, B. Ho-Tin-Noe, C. Carbo, C. Benarafa, E. Remold-O'Donnell, B. Q. Zhao, S. M. Cifuni, and D. D. Wagner, "Inflammation induces hemorrhage in thrombocytopenia," Blood, vol. 111, no. 10, pp. 4958–4964, 2008.

[12] N. Konishi, A. Kawada, Y. Morimoto, A. Watake, H. Matsuda, N. Oiso, and S. Kawara, "New approach to the evaluation of skin color of pigmentary lesions using Skin Tone Color Scale.," J. Dermatol., vol. 34, no. 7, pp. 441–446, 2007.

[13] K. Yoshimura, K. Harii, Y. Masuda, M. Takahashi, T. Aoyama, and T. Iga, "Usefulness of a narrow-band reflectance spectrophotometer in evaluating effects

of depigmenting treatment," Aesthetic Plast. Surg., vol. 25, no. 2, pp. 129–133, 2001.

[14] D. L. Glennie, J. E. Hayward, D. E. Mckee, and T. J. Farrell, "Inexpensive diffuse reflectance spectroscopy system for measuring changes in tissue optical properties," J. Biomed. Opt., vol. 19, no. December, pp. 105005–1–105005–6, 2014.

[15] K. S. Cheng, M. W. Huang, and P. Y. Lo, "Objective assessment of sunburn and minimal erythema doses: Comparison of noninvasive in vivo measuring techniques after UVB irradiation," EURASIP J. Adv. Signal Process., vol. 2010, pp. 1–7, 2010.

[16] W. K. Witmer and P. J. Lebovitz, "Clinical Photography in the Dermatology Practice," Semin. Cutan. Med. Surg., vol. 31, no. 3, pp. 191–199, 2012.

[17] S. G. Coelho, S. A. Miller, B. Z. Zmudzka, and J. Z. Beer, "Quantification of UV-Induced Erythema and Pigmentation Using Computer-Assisted Digital Image Evaluation," Photochem. Photobiol., vol. 82, no. 3, pp. 651–655, 2006.

[18] S. Astner, E. Gonzalez, A. Cheung, F. Rius-Diaz, and S. González, "Pilot study on the sensitivity and specificity of in vivo reflectance confocal microscopy in the diagnosis of allergic contact dermatitis," J. Am. Acad. Dermatol., vol. 53, no. 6, pp. 986–992, 2005.

[19] T. Gambichler, G. Moussa, M. Sand, D. Sand, P. Altmeyer, and K. Hoffmann, "Applications of optical coherence tomography in dermatology," J. Dermatol. Sci., vol. 40, no. 2, pp. 85–94, 2005.

[20] X. Wortsman and J. Wortsman, "Clinical usefulness of variable-frequency ultrasound in localized lesions of the skin," J. Am. Acad. Dermatol., vol. 62, no. 2, pp. 247–256, 2010.

[21] B. Querleux, "Magnetic resonance imaging and spectroscopy of skin and subcutis," J Cosmet Dermatol, vol. 3, no. 3, pp. 156–161, 2004.

[22] T. Pramanik, M. T. Sherpa, and R. Shrestha, "Color vision deficiency among medical students: an unnoticed problem.," Nepal Med. Coll. J., vol. 12, no. 2, pp. 81–83, 2010.

[23] T. Pramanik, B. Khatiwada, and R. Pandit, "Color vision deficiency among a group of students of health sciences," Nepal Med. Coll. J., vol. 14, no. 4, pp. 334–336, 2012.

[24] B. Riordan, S. Sprigle, and M. Linden, "Testing the validity of erythema detection algorithms.," J. Rehabil. Res. Dev., vol. 38, no. 1, pp. 13–22, 2001.

[25] J. O'doherty, J. Henricson, C. Anderson, M. J. Leahy, G. E. Nilsson, and F. Sjoberg, "Sub-epidermal imaging using polarized light spectroscopy for assessment of skin microcirculation," Ski. Res. Technol., vol. 13, no. 4, pp. 472–484, 2007.

[26] D. Yohan, A. Kim, E. Korpela, S. Liu, C. Niu, B. C. Wilson, and L. C. Chin, "Quantitative monitoring of radiation induced skin toxicities in nude mice using optical biomarkers measured from diffuse optical reflectance spectroscopy.," Biomed. Opt. Express, vol. 5, no. 5, pp. 1309–20, 2014.

[27] S. B. Phillips, N. Kollias, R. Gillies, J. A. Muccini, and L. A. Drake, "Polarized light photography enhances visualization of inflammatory lesions of acne vulgaris," J. Am. Acad. Dermatol., vol. 37, no. 6, pp. 948–952, 1997.

[28] M. Setaro and A. Sparavigna, "Quantification of erythema using digital camera and computer-based colour image analysis: a multicentre study.," Skin Res. Technol., vol. 8, no. 2, pp. 84–8, 2002.

[29] G. Lu and B. Fei, "Medical hyperspectral imaging: a review.," J. Biomed. Opt., vol. 19, no. 1, p. 10901, Jan. 2014.

[30] C. a Schneider, W. S. Rasband, and K. W. Eliceiri, "NIH Image to ImageJ: 25 years of image analysis," Nat. Methods, vol. 9, no. 7, pp. 671–675, 2012.

[31] A. K. Jain, Fundamentals of digital image processing, vol. 46, no. 3. 1989.

[32] S. Tan, R. Young, D. Budgett, J. Richardson, and C. Chatwin, "A pattern recognition Weiner filter for realistic clutter backgrounds," Opt. Commun., vol. 172, no. 1–6, pp. 193–202, 1999.

[33] Q. Du and H. Ren, "Real-time constrained linear discriminant analysis to target detection and classification in hyperspectral imagery," Pattern Recognit., vol. 36, no. 1, pp. 1–12, 2003.

[34] M. Li and B. Yuan, "2D-LDA: A statistical linear discriminant analysis for image matrix," Pattern Recognit. Lett., vol. 26, no. 5, pp. 527–532, 2005.

[35] T. Bandos, "Classification of hyperspectral images with regularized linear discriminant analysis," Geosci. Remote …, vol. 47, no. 3, pp. 862–873, 2009.

[36] S. Dudoit, J. Fridlyand, T. P. Speed, and P. Terence, "Comparison of Discrimination Methods for the Classification of Tumors Using Gene Expression Data," J. Am. Stat. Assoc., vol. 97, no. 457, pp. 77–87, 2002.

Chapter 6: Radiotherapy Induced Skin-Erythema objective Quantification using Hyperspectral Imaging

6.1 Introduction

Radiotherapy treatment employs ionizing radiation (x-ray photons/ electrons) [1] to preferably kill cancer cells. In general, the prescribed dose of radiation is divided into a number of smaller doses, called "fractions" [2], [3], which allows for optimizing the treatment while minimizing the linked side effects. Larger radiation fractions for treating skin cancer (SC) patients are used for different reasons such as minimizing the inconvenience to elderly people that may discontinue radiotherapy treatment as a result of fatigue [3]. There are upper and lower limitations for the prescribed daily dose (Gy/day) that need to be considered. For instance, 10 Gy fractioned on a daily basis might lead to a mildly delayed tissue complications, while 5-10 Gy could reduce long-term complications, but it may lead to telangiectasia, scarring, and local pigmentation increase [1], [4]. Smaller doses, 3 Gy, are claimed to be optimum in terms of cosmetic effects, where a treatment success rate of 94% in basal cell carcinoma of head and neck patients was reported [5]. In general, significant damages to skin and subcutaneous layers have been reported due to employing ionizing radiation in radiotherapy treatment. Particularly, some studies [6]–[9] reported that at least 85:95% of all radiotherapy patients might have detrimental side effects. These side effects due to radiotherapy treatment vary in severity from mild to severe reactions, since it depends on several parameters [6], [7], [9]–[11]. The parameters correlate with the severity of the skin's adverse reaction have been studied [10], [12]–[14], [19]–[20], [23],[15]. These studies ascertained that age, gender, radiation type, and the treated body part are shown to be the most prominent parameters influencing the intensity of the skin reaction due to radiotherapy, while the dose was found to be less dominant in this aspect [10], [17], [18]. More in depth, the details concerning radiotherapy induced skin toxicities/ reactions can be found elsewhere [15].

In brief, the skin reacts and displays some or all of the following symptoms once the radiation is started: [6], [15]

1- The transient skin redness (skin erythema) might need no longer than a couple of hours to show up as the earliest skin response, or it can linger visibly unseen up to 15 received treatment fractions [16].
2- Skin irritation takes place due to the turbulence-induced death of the epidermal basal cells which generally occurs after approximately receiving 15 fractions. The resultant consequence of moderate skin irritation is either dry or a wet desquamation reaction. This skin reaction can cause major discomfort and adversely affects the patient's quality of life along with a likelihood of lower treatment efficacy [8].

3- A long-term skin response (dermal ischemia and necrosis) may occur 2- 4 months after irradiation advent.

Looking into the more rapid skin reactions, erythema was selected to study the skin temporal response to irradiation. The epidermis and the dermis layers, combined together, thickness are ranging from 0.5 to 2 mm depending on the body location. The visible-near infrared (VIS-NIR) light penetrates the human skin down to a depth of 1.3 mm [19] and thus, imaging in VIS-NIR region will be probing the epidermal layer to capture erythema. Distinct measurement/ imaging based modalities were used to assess induced skin erythema due to distinct causes. See **Chapter 2** for more details.

This preliminary study aimed to investigate the feasibility of HSI, which is objective, for quantitative assessment of radiotherapy induced skin erythema. In a course of six months; eight SC patients were recruited while only five out of them completed the study. Along with HSI, there were two other techniques of erythema evaluation; clinical scoring and digital color imaging. Erythema indices were computed for applicable patients applying Dawson's model [20]. Wilcoxon non-parametric two-tailed test was applied to investigate the significance of the erythema indices temporal variation versus the baseline measurement. A Linear discriminant analysis (LDA) based algorithm was developed to compare HSI and RGB imaging in erythema classification. The study results demonstrated that 1) HSI is a good candidate for contact-free monitoring temporal skin erythema evolution 2) the computed relative erythema index is an excellent factor representing erythema clinical scores 3) fitting the computed absorbance with hemoglobin extinction coefficients provided the opportunity to quantify the relevant induced erythema on daily basis, 4) HSI modality combined with LDA data reasoning technique outperformed the RGB color imaging in supervised erythema classification.

6.2 Methods

6.2.1 Clinical Procedure

The entire clinical work was performed following the McMaster-Hamilton Health Sciences Joint Research Ethics Board approved protocol. The daily protocol for our study includes a sequence of steps as follows:

1- According to our protocol, patients should not wait more than ten minutes once they arrive at the reception room. Therefore one of the research crew is always waiting for meeting them once they arrive at the reception area.

2- The patient is walked by the research crew member to the room specified for the study and seated to begin our clinical procedure.

3- Initially, the patient's ROI is visually assessed by the radiotherapist to evaluate the skin response on a daily basis. Moreover, some questions were introduced to the patient to respond verbally regarding any complaint due to irradiation, sun exposure length, and if any topical agent is applied in the day before the session.

4- The patient is then moved to be seated on a special chair-bed (Ritter couch) in order to be imaged with both the spectral and the photographic video cameras, one at a time, taking into consideration the same field of view, and the orientation.

5- Finally, the patient is sent by our crew's radiotherapist to the room of radiation treatment to receive his daily prescribed radiation dose.

A written consent was given by all the participating patients. Once the consent is signed by the patient, a copy of the study's schedule, including both the study and the treatment sessions, is given to him/ her. Moreover, the patients were instructed not to apply any topical agent or skin dressing except upon recommendation of the oncologist as well as notifying the study's research crew. Clinical assessment, patient recruitment, and experimental measurements commenced in May 2015 and went on for six months. Eight skin cancer patients were consented to participate in the study; however, only five patients completed the study successfully. The other patients' data was not included in our analysis due to the study exclusion criteria. The demographic data of the applicable five patients is summarized in Table 6-1. The average age of the patients is approximately ~75 years, with 2 female and 3 male subjects. The patients were diagnosed with non-melanoma skin cancer (NMSC): be it basal cell carcinoma (BCC) or squamous cell carcinoma (SCC) and receive at least 10 radiation fractions. The treated site varied between the arms, legs and face regions. The prescribed radiation was either electrons or x-rays photons with at least > 4000 cGy dose.

Table 6-1: Demographic data of participating skin cancer patients

Patient	Gender	Age	Histology	Radiation type	Energy	Dose (cGy)	Fractions	Site
1	Female	88	SCC	Electrons	9 MeV	5000	20	Left tibia
2	Female	56	BCC	X-rays	65 KVp	5000	20	Left fore- arm
3	Male	68	BCC	X-rays	65 KVp	4250	10	Left cheek
4	Male	85	BCC	Electrons	12 MeV	4250	10	Right ear
5	Male	75	SCC	X-rays	130 KVp	4250	10	Left temple

The study session was scheduled before the radiation treatment session for each patient. The reason for scheduling the study session before treatment is the interest in monitoring the permanent radiation side-effect rather than the transient one upon the skin. Each day, one of the two radiotherapists, alternatively, scored and documented all the patients' skin erythema score and relevant clinical features. A convertible Ritter couch was used to seat the patients in a pose relatively similar from day to day. An adjustable platform for the imaging instrumentation was designed and built to maintain consistent relative patient-instrumentation displacement. For each individual patient, the region of interest (ROI) outline was marked with a permanent marker to ensure reproducibility. Moreover, a transparent film was used as a backup template for the ROI marks considering permanent landmark features like skin moles and freckles. The purpose of generating this template is to keep tracking of the marks whenever it is washed out after the weekends. In addition to tracking the marks, other information were jotted down such as the ROI orientation at the template edges [16]. An example of the transparent template film placed in coincidence with the patient's ROI marking is shown in Figure 6-1, where the prescribed dose is written on the top-left corner.

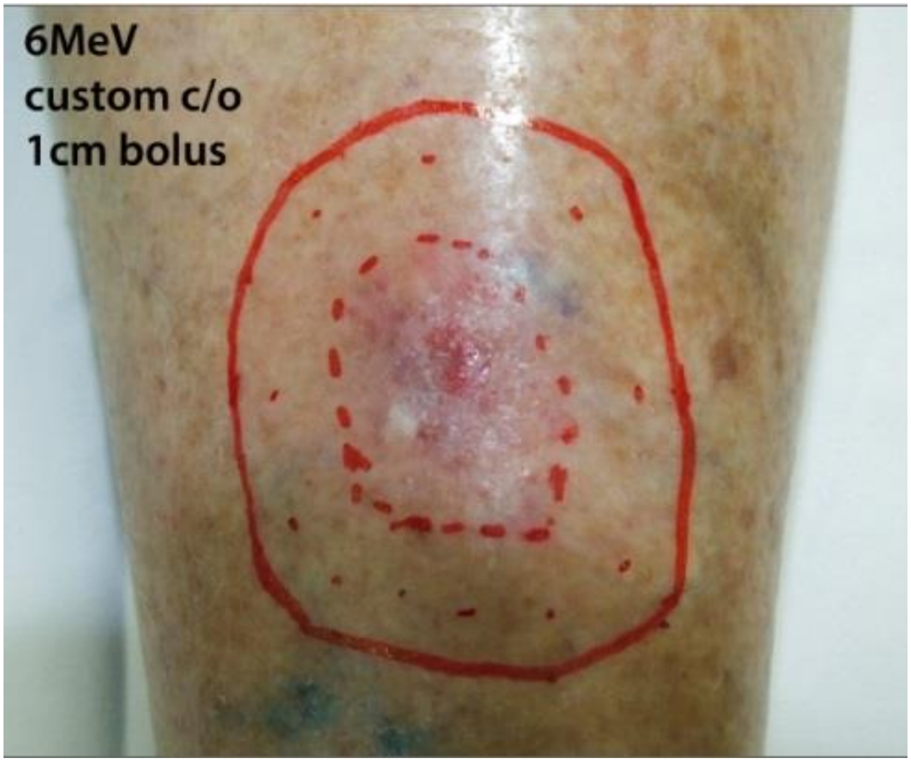

Figure 6-1: A skin cancer patient has ROI in her leg as is marked. The benefit of the marking is being a daily reference during radiotherapy treatment. A transparent film is created with a copy of the patient marks to be used to as a backup in case of the marks washed out to verify the same ROI for clinical and study procedure reproducibility.

6.2.2 Visual Assessment

On a daily basis, the patients responded verbally to a simple questionnaire concerning his/ her previous day activity along with his/ her own observations concerning the temporary skin reaction upon formerly received irradiation. Important information such as whether any topical agents or dressing had been applied to the patient's ROI within the three hours preceding the imaging session was collected. All the patients' answers and erythema scores were securely recorded in an established patient's paper-based and digital record.

Skin-erythema levels were agreed to be graded on a 5-steps scale to express the described skin status mentioned in **Chapter 5**. The qualitative erythema scale is established based on a radiotherapist's 15 years' experience; where each level is assigned to an erythema grade. Frequently, the patient ROI is not developing a homogenous erythematous region, but randomly distinct contoured erythema levels.

6.2.3 RGB color Imaging

Both irradiated, as well as non-irradiated regions, have been imaged by RGB imaging. Taking a photograph for a non-irradiated skin region enabled the individual patient to perform as his/ her own reference. RGB imaging was carried out at least three times repeatedly on every session along the whole study duration. The color photographs were captured with a high definition digital video camera (HYUNDAI-HDMI-768, China) using a 16 megapixels sensor. The video camera is supported by a 3-inch LCD display to adjust the captured FOV. The camera is equipped with an objective lens with an F-number = 3.2, and its focal length f =7.5mm. Moreover, it has small dimensions (110x58x50 mm) and a lightweight (~0.24 kg) which provided maneuverability to accommodate different body parts. The illumination and the perspective view were maintained for individual patients. The digital color images were captured of the size 4608 x 3456 pixels, with a JPEG file format. A digital montage of colored photographs concerning a single recruited patient is shown all over her radiotherapy plan is displayed in Figure 6-2. Color photographs were used to visibly assess alterations of the skin in the treatment field as well as the reference region. Furthermore, it facilitated the cross-validation of the clinical erythema scores with the other radiotherapist.

Figure 6-2: RGB color images montage for a left tibia skin cancer track the development of symptoms on an individual patient's ROI. The images were arranged from left to right and from up to down chronically. The patient had originally a lot of red skin features in her leg before receiving any irradiation. However, she started to develop a visible faint skin erythema at the 8th session of irradiation which had been evolved to dry desquamation in the 4th week after receiving 15th sessions of irradiation.

6.2.4 Hyperspectral Imaging

Hyperspectral data was acquired via a custom-made acousto-optic tunable filter (AOTF)-HSI system, which is described in details in **Chapter 4**. The photographed patient's FOV, comprising both the irradiated and the non-irradiated regions, is re-captured via the hyperspectral camera. In brief, the patient's FOV is illuminated with a halogen filament based light source covering the interesting VIS-NIR spectral region from different directions to reduce the shadow effect. The patient's ROI back-reflected light is collected via a zoom lens and focused at its focal plane. An optical relay is used to convey the captured FOV through the optical configuration using an achromatic lens pair.

A skin region of approximately ~ 11x11cm^2 was considered to involve both irradiated and non-irradiated regions, resulting in a spatial resolution of ~ 50 µm/ pixel. A developed program, in C-language, was used to synchronize the AOTF and the camera operation simultaneously through a user-friendly interface. The spectral imaging data set involves the patient ROI, a white standard surface which has 99% reflectance (SRS-99-010, Labsphere, North Sutton, New Hampshire), and dark datacubes. The white standard datacube is collected right after the patient imaging to maintain the same position and illumination conditions. The dark datacube is collected while the zoom lens cap is on and all lights are off. Eighty-nine narrow band images in the spectral range of 450:850nm were taken in each datacube. The integration time for each image is one second, and thus, each datacube is taking 89 seconds.

Several measures were taken to ensure the patient convenience while hyperspectral imaging is running. Hyperspectral imaging was frequently repeated for at least 2 or 3 times to avoid the patients' unintentional movement. For example, due to using intense light sources, the patients were provided a pair of sunglasses to lessen their eye exposure to the illumination light. To bring the study environment to the brain, an imaging session for a volunteer, simulating cancer patients, is shown in Figure 6-3. All the data were recorded, filed, and labeled with the patient code, session number, date, and repetition number. To give an example, the fourth patient in the 10th session relevant data captured on August 10th in the second spectral imaging repetition will be stored in a file labeled as P04-10-20150810-2. This way of labeling facilitates keep tracking the patients' raw data and its origin.

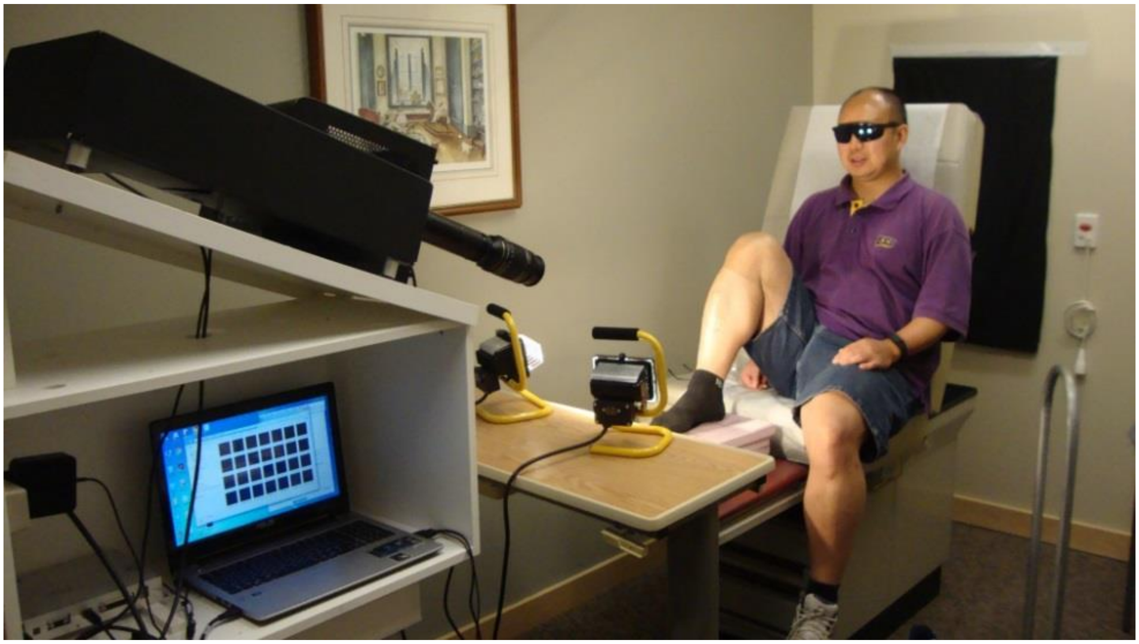

Figure 6-3: A volunteer simulating recruited patient is seated in the position prepared for imaging a treatment field within the right leg. The field of view is illuminated from different directions to avoid the shadow effect. Sunglasses are worn to protect the person eyes from the bright intensity of light sources during imaging time.

6.3 Data Analysis

For each individual patient, day-to-day skin erythema clinical scores were tabulated. In addition, digital color images and spectral datacubes along the entire operating spectral range, were acptued and stored in the patient digital file.

6.3.1 Visual Assessment Score

The erythema total score is determined by multiplying the relatively occupied area within the treatment field by its corresponding visual erythema grade specified by the radiotherapist. The grade of the radiotherapist was transformed numerically to a score value from “zero”, which corresponds to no visible erythema, and an increment of 0.25 with each step higher up to “one” that is relevant to very bright erythema. To give an example, consider a patient, on a certain day, who developed two grades of erythema; one of which is faint erythema, and the other is bright erythema. Supposedly, both grades were spatially distributed equally, 50% of the treatment field for each. The patient’s total visual score will be computed as.

Erythema total score = $\sum A_i * S_i = [0.5 * 0.5] + [0.5*0.75] = 0.625$

The terms A_i and S_i are the relatively occupied area, and the visually transformed score determined earlier by the radiotherapist, respectively. A total score of 1.0 is equivalent to a bright erythema present on the entire treatment field.

6.3.2 Spectral Reflectance Computation

Each patient's ROI captured datacube is normalized in two consecutive steps; the first step is the subtraction of the dark background ($\boldsymbol{I_{dark}}$) from the patient's raw image cube ($\boldsymbol{I_{ROI}}$) as well as from the reference white standard ($\boldsymbol{I_{ws}}$). The second step is the background-free datacubes, regarding the tissue ROI and the white standard, division as shown in (6-1) using the software ImageJ [19].

$$\boldsymbol{R_{ROI}} = \frac{\boldsymbol{I_{ROI}} - \boldsymbol{I_{dark}}}{\boldsymbol{I_{ws}} - \boldsymbol{I_{dark}}} \tag{6-1}$$

The resultant output is the spectral-resolved diffuse reflectance ($\boldsymbol{R_{ROI}}$) datacube for the patient's ROI. Based on the former spectral characterization of the AOTF-HSI equipment, an intermediate band (central wavelength λ = 600 nm) was selected as the reference band for each datacube. This particular band is selected since it has the peak spectral response within the operating range of the newly developed AOTF-HSI spectrometer. The reference band is used for image registration to reduce the patient's unintentional movements during the time lapsed in imaging using ImageJ. A sample of the normalized ROI reflectance datacube for a particular patient in the third week (13th session) of treatment is displayed in Figure 6-4. These sampled frames are picked since they are the most relevant bands to the major skin chromophores regarding our study's spectral range of operation.

The major skin chromophore in erythema context is hemoglobin. This particular chromophore, hemoglobin, is distinguishable with two absorption peaks lying at 560 and 580 nm and thus, the high concentrated hemoglobin regions appear darker [22], [23]. The penetration depth range at the green spectra, involving the formerly mentioned wavelengths, is limited to fractions of a mm [24], which restricts the visibility to the superficial capillaries. However, deeper skin information could be achieved at longer wavelengths since the skin visible chromophores have less absorption preference and thus, light can travel further up to 2 millimeters in the case of using intermediate infrared. Note, the longer wavelength bands might show in the region which has a high hemoglobin concentration, due to erythema, a slight shadow as seen at 650nm, and 700nm bands. At 840nm band majority of the skin, chromophores display absorption minima.

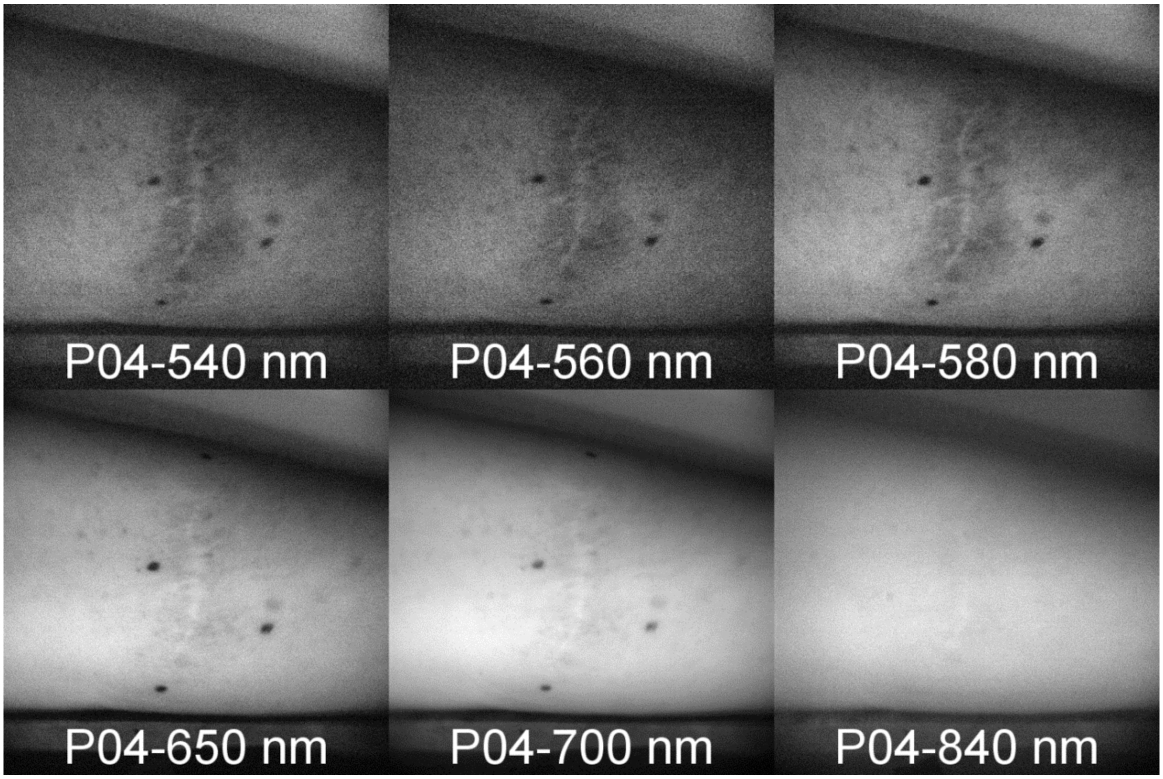

Figure 6-4: Spectral images filtered at wavelength bands (540, 560, 580, 650, 700, and 840nm) manifest the optical properties of one recruited patient ROI were taken at the identical time point (August 13th, 2015) session of radiotherapy treatment are displayed. The bands of central wavelengths 540 nm, 580 nm are highlighting the oxyhemoglobin absorption, the band of central wavelength 560 is relevant to deoxyhemoglobin absorption, the bands of central wavelengths 650 nm, 700 nm are representing the bands used for melanin correction, and finally the band of central wavelength 840 nm, which is NIR band, is showing the low absorption of the majority of skin chromophores (hemoglobin, melanin, and water).

The reason behind visualizing the skin reddening/ erythema due to a sort of inflammation is not a result of more red scattered light, but it is because the green back-reflected portion of light was intensely absorbed. Hence, wherever the concentration of hemoglobin rises up in a skin location, the less green light component is scattered back as shown in Figure 6-5. Hemoglobin is originally residing in the dermis layer of skin, underneath the epidermis. As the melanin concentration of the epidermal layer is undefined, the estimated hemoglobin components concentrations computed via a reflectance measurement technique are considered to be apparent concentrations. This apparent concentration is considered for a single layered tissue model but not exactly the true existing hemoglobin components concentrations. However, the computed apparent concentrations for hemoglobin both parts are still considered as a quantitative measure for skin erythema if a baseline is assigned.

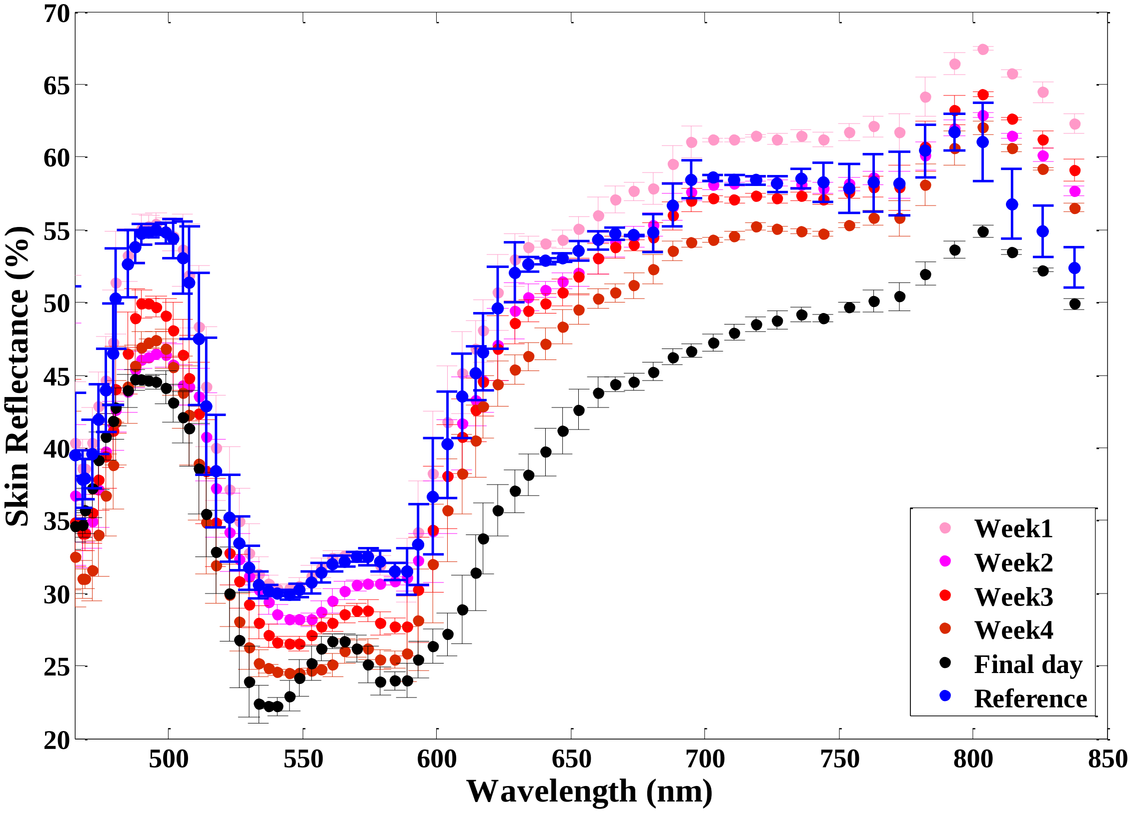

Figure 6-5: Patient diffuse reflectance spectra for the treatment field of skin on treatment days (reddish dots), and at the end of treatment (black dots). A reference diffuse reflectance spectra for non-irradiated skin region is plotted (blue dots).The amount (percent) of reflected light is temporally decreasing in the green region in a gradual style rather than the corresponding arbitrary behavior in the red region.

6.3.3 Erythema Index Computation

The erythema index, computed based on Dawson's model [20], is a common computational method, cited more than 340 times to date, for probing skin pigmentation changes from measured reflectance spectra. The technique is based on computing the area under the curve (AUC) of the logarithm of the reciprocal of the skin diffuse reflectance (LRR) in the visible region (510-620nm). This spectral region comprises two of hemoglobin distinguishable absorption peaks. Dawson's erythema index (DEI) equation is given as follows:

$$\boldsymbol{DEI = 100 * [r + \frac{3}{2}(q + s) - 2(p + t)]} \tag{6-2}$$

Hereby, *p*, *q*, *r*, *s*, and *t* are symbols expressing the LRR values of the measured data at the five wavelengths 510,540,560,580, and 610nm, respectively. Since patients' skin types are typically distinct, we replaced the *p*, *q*, *r*, *s*, and *t* values at the exact formerly mentioned wavelengths by the average of the LRR in the range$(\lambda \pm 5\,nm)$. In order to correct for the effect of melanin in erythema index computation, the tangent to the LRR curve at two wavelengths (650&700nm) is considered. The former two wavelengths were selected since it was estimated that the melanin spectral absorbance is proportional to its concentration at these two spectral points [20]. The reason for selecting this spectral region for melanin investigation is the lower spectral absorbance of the hemoglobin chromophore. There is a more complex approach, which is not applicable here, is to account for the difference between two groups of people, one of which is Caucasian and the other is African. For simplicity purposes, Dawson melanin index (DMI) is computed based on the former two wavelengths, with the same averaging range $(\lambda \pm 5\,nm)$ applying (6-3).

$$\boldsymbol{DMI = 100 * [Log_{10}(\frac{1}{(\bar{R}_{645,650,655}}) \text{-} Log_{10}\left(\frac{1}{(\bar{R}_{695,700,705}}\right) + 0.015]} \quad \textbf{(6-3)}$$

The DEI can now be corrected (DEI$_c$) using the DMI by applying the formula shown in (2-12), where γ=0.04 is an empirically derived balancing constant to avoid negative values as a result of other non-significant skin chromophores [20].

$$\boldsymbol{DEI_c = \left(100 * \left[r + \frac{3}{2}(q + s) - 2(p + t)\right]\right) * (1 + (\gamma * MEI))} \quad \textbf{(6-4)}$$

To compare consecutive measurements of an individual patient skin reflectance, the relative Dawson erythema index (DEI_r) is calculated. DEI_r is simply computed by subtracting the DEI_c either for the treatment field prior to any irradiation or for a control region that receives no irradiation from the index of a later time point. The relative erythema index is a sensitive parameter to skin color changes since it avoids the effect of systemic errors as well as taking the patient's normal skin as a reference. More details about theoretical derivations for Dawson's equation can be found in reference [20].

6.3.4 Estimation of Skin Chromophores

Diffuse reflectance data acquired by spectroscopic based instrumentation need to be interpreted using a model to account for the propagation of the light inside biological tissues. In our case, a broad beam light source was shone onto the object from multiple directions. This setup can be approximated by a perpendicular light source illuminating a semi-infinite, homogeneous slab. Quantitatively estimating the concentrations of the main chromophores can be accomplished with a conditional least-square fitting of the skin-absorbers' extinction coefficients. The logarithmic value of the reciprocal measured diffuse reflectance data $R(\lambda)$ is optimally fitted by a sum of the dominant skin chromophores' extinction coefficients $\varepsilon_n(\lambda)$ in the investigated spectral region, multiplied by their concentrations C_n as shown in (6-5) [25].

$$\boldsymbol{log_{10}\left(\frac{1}{R(\lambda)}\right) = \sum_{n} C_n * \varepsilon_n(\lambda)} \qquad \textbf{(6-5)}$$

Three skin chromophores are dominant in the VIS-NIR spectra 500-840nm are; the oxygenated fraction of hemoglobin (HbO2), the deoxygenated fraction of hemoglobin (Hb), and the melanin. A minor effect might be attributed to other skin chromophores such as water and fats. This effect can be compensated by adding a constant (R_c) as in (6-6):

$$\boldsymbol{-log_{10}\,[R\,(\lambda)] = C_{oxy}.\,\varepsilon_{oxy}(\lambda) + C_{deoxy}.\,\varepsilon_{deoxy}(\lambda) + C_m.\,\varepsilon_m(\lambda) + R_c} \qquad \textbf{(6-6)}$$

Where the terms: C_{oxy}, $\varepsilon_{oxy}(\lambda)$, C_{deoxy}, $\varepsilon_{deoxy}(\lambda)$, C_m, $and\ \varepsilon_m(\lambda)$ are the concentrations and extinction coefficients of HbO2, Hb, and melanin, respectively.

6.3.5 Image Classification

Hyperspectral image classification is the process of allocating data classes from a hyperspectral datacube. The classification in the case of hyperspectral imaging is the result of a multi-step procedure. The primary step is datacube normalization to a standard reference, discussed earlier. Next step is to reduce the embedded datacube noise, and thus, a smoothing technique is applied. For smoothing, few approaches are available to reduce the image noise. However, Wiener filter is considered one of the most efficient noise reduction techniques [26]. It estimates statistically the anonymous information out of the original noisy data. The advantage of Wiener filter is the capability of reducing the noise in the corrupted data with an approximately lossless amount of real information. Wiener filter is based on a statistical approach applying the minimum mean square error (MMSE) method [27]. Wiener has been selected since it enhances the relative signal to noise counts through an appraisal of both signal and noise power spectra applying either parametric or nonparametric techniques [28]. Simply, Wiener filter can be considered as a low-pass imaging filter that is able to be tweaked to the input image's local variance and can be mathematically expressed as follows [26], where the terms $I_w(x, y)$ is the filtered pixel corresponding to the noisy input pixel $I_0(x, y)$, ν expresses the noise variance, and μ and σ^2 are image locally computed mean and standard deviation [29].

$$\boldsymbol{I_w(x,y) = \mu + \frac{\sigma^2+\nu^2}{\sigma^2}(I_0(x,y) - \mu)} \qquad \textbf{(6-7)}$$

Obviously, hyperspectral bands are not equally informative. The reason for certain HSI bands to be less informative is often based on systemic lower performance such as the less spectral emission of illumination at some region of the operating spectra. Not only the illumination but the lower detector's quantum efficiency may be the second reason.

Hence, band/ variable selection (VS) is recommended to exclude the least informative bands in the captured datacubes. VS is not arbitrary but it is accomplished given a threshold of 99% information within datacube should be preserved. VS is originally different from dimensionality elimination based techniques, as the latter methods gather its output from all the captured bands, and has no capability of extracting the significant bands out of the original ones. In our case, matrix low-rank representation (MLRR) [30] was used as a VS criterion. MLRR concept is to sort the variables in terms of band self-contained information. To put it simply, MLRR is clustering data pixels drawn from larger multiple subspaces to delineate outliers. Quantifying the spectral cube bands rank is accomplished using the Frobenius (element-wise) matrix norm, as follows,

$$\|\boldsymbol{X}\| = \sqrt{\sum_{i,j}(\boldsymbol{X}_{i,j})^2}. \qquad \textbf{(6-8)}$$

MLRR clustering starts with calculating the summation for each square matrix, band image, and columns $\|X\|$ and arrange the columns in a descending order. Then, specifying a threshold percentage value P = 0.99 (significance interval), a comparison between each band,$\|X_k\|$ and the average norm $\|\bar{X}\|$ of all the bands will highlight outlier bands among the rest.

$$\frac{\|\boldsymbol{X_k}\|}{\|\bar{\boldsymbol{X}}\|} > \boldsymbol{P}. \qquad \textbf{(6-9)}$$

In summary, VS determines the least informative bands preserving 99% of the contained information in the datacube. The less informative band's removal is a great advantage in the sense of decreasing the computation time in spectral data analysis, however, retaining the most influential information. To give an example, Figure 6-6 displays two rows of images belonging to the same datacube of a single patient. The images in the top row clearly have a very low signal to noise ratio and contribute to less than 1% to the datacubes' information. Elimination of these bands would have a negligible effect on the imperative spectral information. Furthermore, the excluded bands (450-490nm) were found to be in a less interesting spectral region regarding skin erythema, which means it has no distinguishable features relevant to the dominant skin chromophores. For illustration purposes, a sample of the highest informative, spectral bands is shown in the bottom row of Figure 6-6.

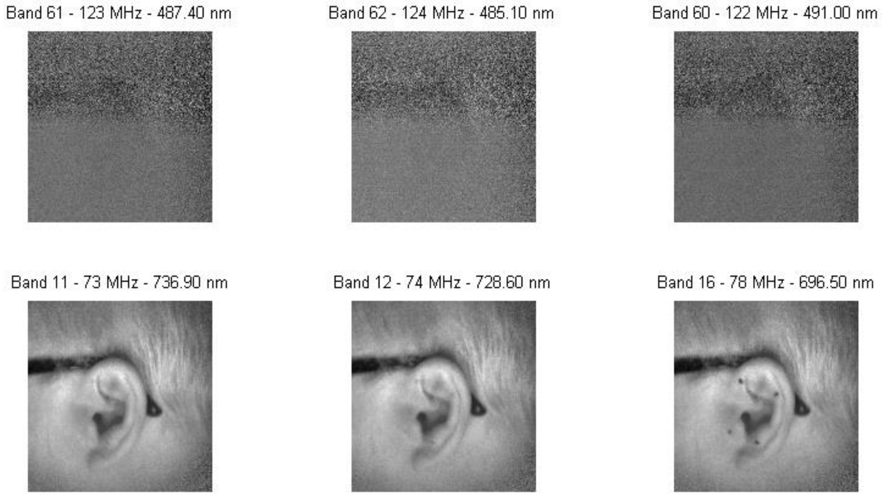

Band 61 - 123 MHz - 487.40 nm

Band 62 - 124 MHz - 485.10 nm

Band 60 - 122 MHz - 491.00 nm

Band 11 - 73 MHz - 736.90 nm

Band 12 - 74 MHz - 728.60 nm

Band 16 - 78 MHz - 696.50 nm

Figure 6-6: A demonstration of the process of variable selection, where three images for the least informative bands (450-490nm) in a patient datacube, determined by matrix low-rank representation, are displayed in the top row, and three corresponding images of the highest informative bands are displayed in the bottom row for the same patient's datacube.

Skin annotations for the distinctly developed skin erythema were generated by an expert radiotherapist through examining the captured digital RGB images for the patient daily with the use of ImageJ. The purpose, of the annotations, is to establish a ground truth data based on the gold standard for erythema assessment, corresponding to the spectral datacube captured at the same time. The ground truth is used in developing the training data sets for the adopted classification method and the cross-validation for the test data sets.

Unfortunately, the skin induced erythematous reactions do not form mutually exclusive contours, and thus, it necessitates corrections. The corrections were made by applying a logic X-OR operation to separate the distinct erythematous reaction regions to end up with contours as shown in Figure 6-7. Furthermore, an extra class for non-erythematous skin was added to express the normal skin spectral signature.

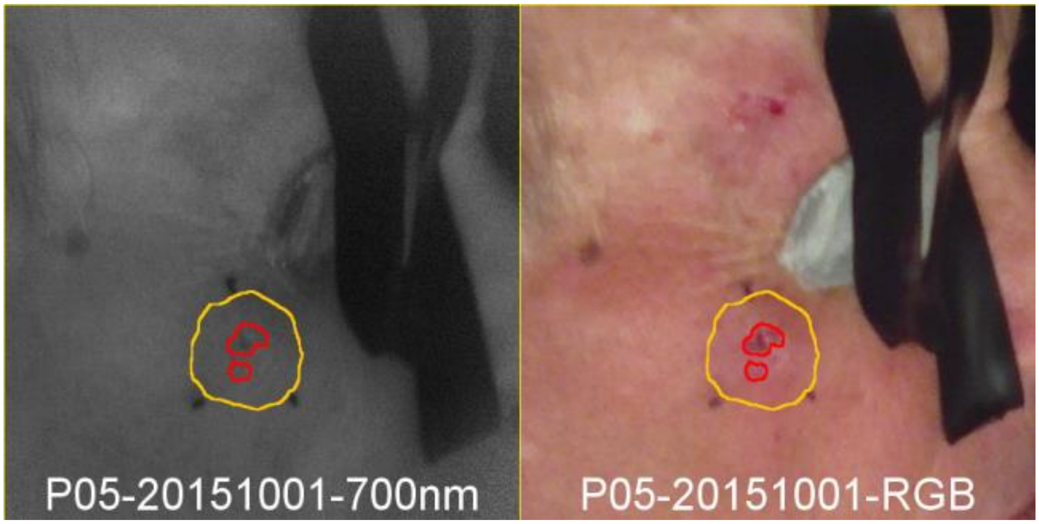

Figure 6-7: A sample of annotations created by the radiotherapist to mark two distinct erythema regions as ground truth data. The annotations are overlaid on both spectral data (left) and digital color image (right). The eye shield appeared in the images was used to protect the eye from the bright light during imaging.

The linear discriminant analysis (LDA) [31] method was selected for classifying both hyperspectral and RGB images. Since LDA is easily implemented once the dependent variable, erythema in our case, is a categorical variable, while the independent variable is an interval in its nature as a time for treatment in our study. In practice, LDA technique looks for a linear transformation matrix H , by which, it is capable of reducing the spectral k-dimensional raw data of vector F to an s-dimensional vector provided that s < k [32].

$$\boldsymbol{a} = \boldsymbol{H}^{\boldsymbol{T}}\boldsymbol{F} \in \mathbb{R}^{s} \qquad \textbf{(6-10)}$$

The spectral datacube dimensional reduction is not implemented on a discretionary basis but it is placed on the concept of achieving the maximum possible separation among data classes dissemination [32]. To make it clear, LDA rule of thumb is to maximize the displacement in between the central mean point (M) of the classes, meanwhile preserving interclass variance (V) to be minimum [33]. The challenge is to find the axis that projects the data cloud into separate clusters with means $M_1, M_2, \dots, M_n$ and small variance $V_1, V_2, \dots, V_n$. For instance, in the case of two classes' mode the term $F(W)$, represents the plane of best separation, should be maximal to achieve superlative separation between each class and the other. An illustration of the basic principle of Fisher LDA in clustering data clouds to separate categories is displayed in Figure 6-8.

$$\boldsymbol{F}(\boldsymbol{W}) = \frac{|\boldsymbol{M_2} - \boldsymbol{M_1}|}{\boldsymbol{V_2} - \boldsymbol{V_1}} \qquad \textbf{(6-11)}$$

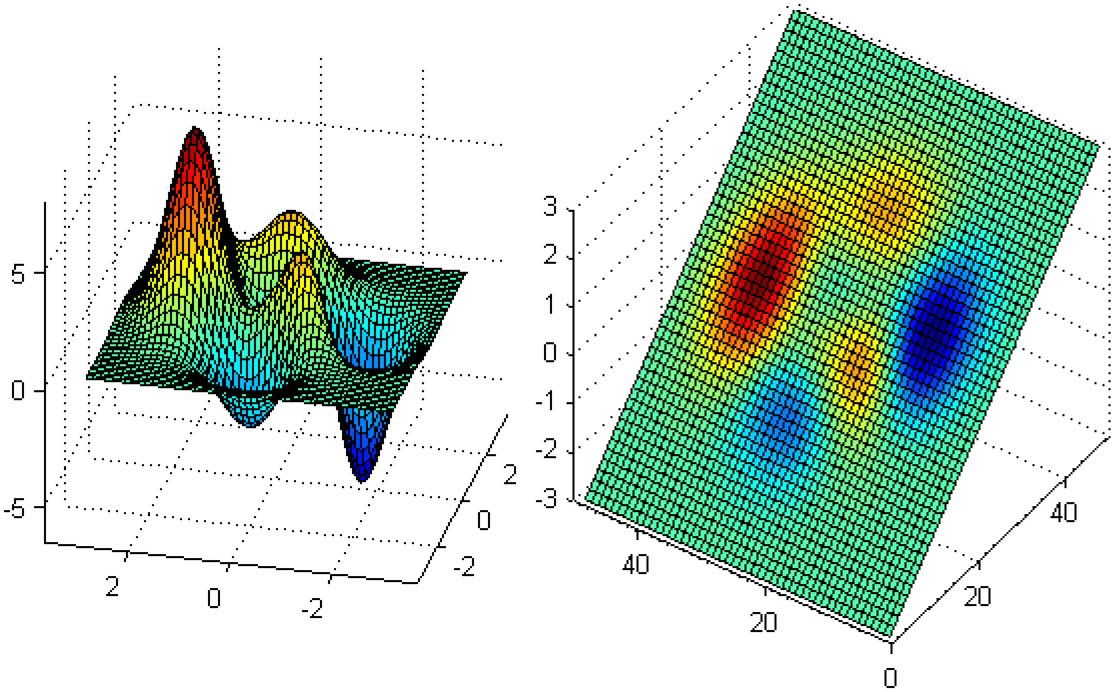

Figure 6-8: Fisher linear discriminant analysis projects data cloud into disconnected clusters by finding the best plane to achieve superlative separation.

It is obvious from the previous figure that the plane of separation was selected, in such a way to achieve the maximum separation between the mean vectors of the distinct data classes while keeping the variability between the interclass members to be minimal. LDA can be used provided that the covariance matrix of the sample population is equal; otherwise quadratic discriminant analysis is used.

6.4 Results and Discussion

6.4.1 Visual Assessment

The total visual erythema score is computed for all the applicable patients in the study along the prescribed radiotherapy plan of treatment, and displayed in Figure 6-9. A baseline is drawn horizontally at the average computed erythema score prior to any irradiation exposure. Notably, the baseline value is not equal to zero where the reason is the presence of skin redness initially in the region of interest in some patients.

Temporal accumulation of the irradiation resulted in a general proportional increase of the skin erythema with almost a linear behavior. However, the standard deviation for the total erythema score is relatively large. At this point, we return the high variability between the patients in developing erythema to the skin type difference and more often to the depth of tumor for individuals. The mechanism of skin response to irradiation exposure is extremely complex since it depends on a vast array of parameters that elucidate the output reaction [10].

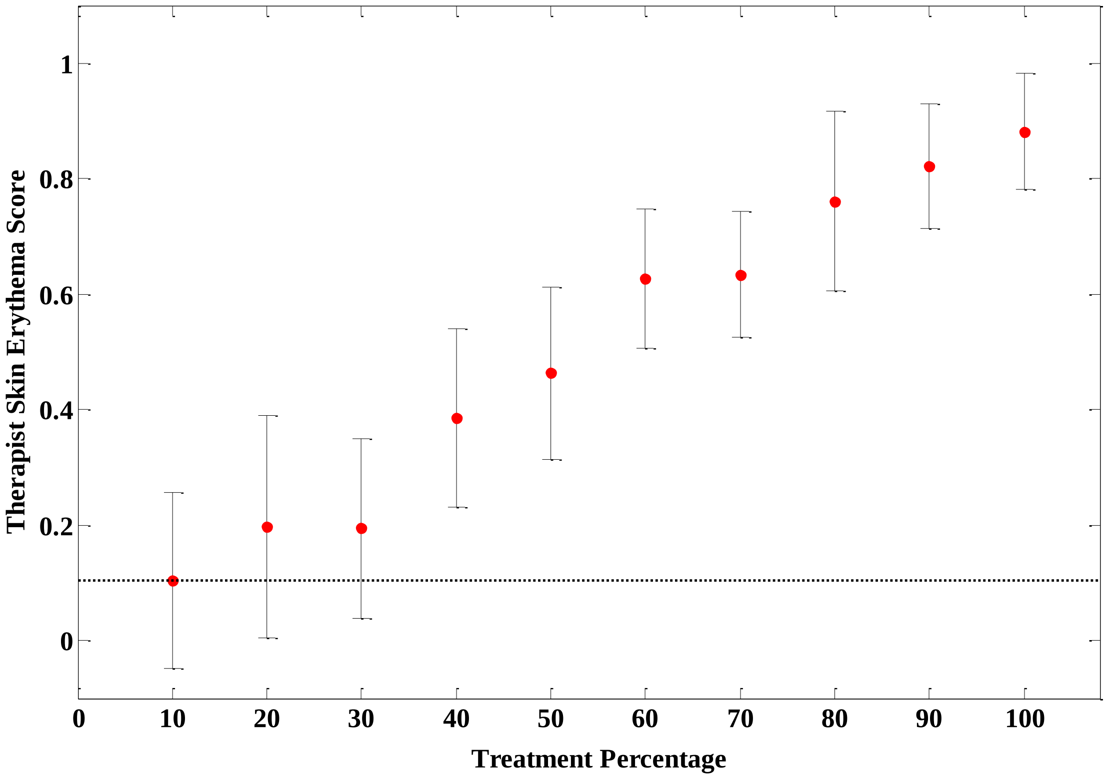

Figure 6-9: Visual assessment total average scores for the study applicable patients during radiotherapy treatment on a daily basis. The scores were presented as treatment percentage due to the difference between the prescribed numbers of sessions among patients. Error bars are the standard deviation among patients.

6.4.2 Skin Melanin and Erythema Indices

Based on the patients' data, it was found that estimated skin melanin content is oscillating through the study time period as shown in Figure 6-10. The existing data points represent the average values of the melanin index, computed by Dawson's model, for the successful patients in our study, while the error bars represent the standard deviation among the patients. Similar to former, a dashed red line is drawn horizontally at the initial level of apparent melanin prior to irradiation beginning to facilitate monitoring the direction of change throughout the days of treatment. The temporal oscillation in melanin index provided a strong evidence for non-consistent alteration in the skin melanin content within the tumor region. For contrast purpose, a healthy volunteer went through the study protocol, except for irradiation, and skin melanin index was computed and results are displayed in blue color in Figure 6-10. The oscillation of melanin index was observed relevant to the first day of data collection.

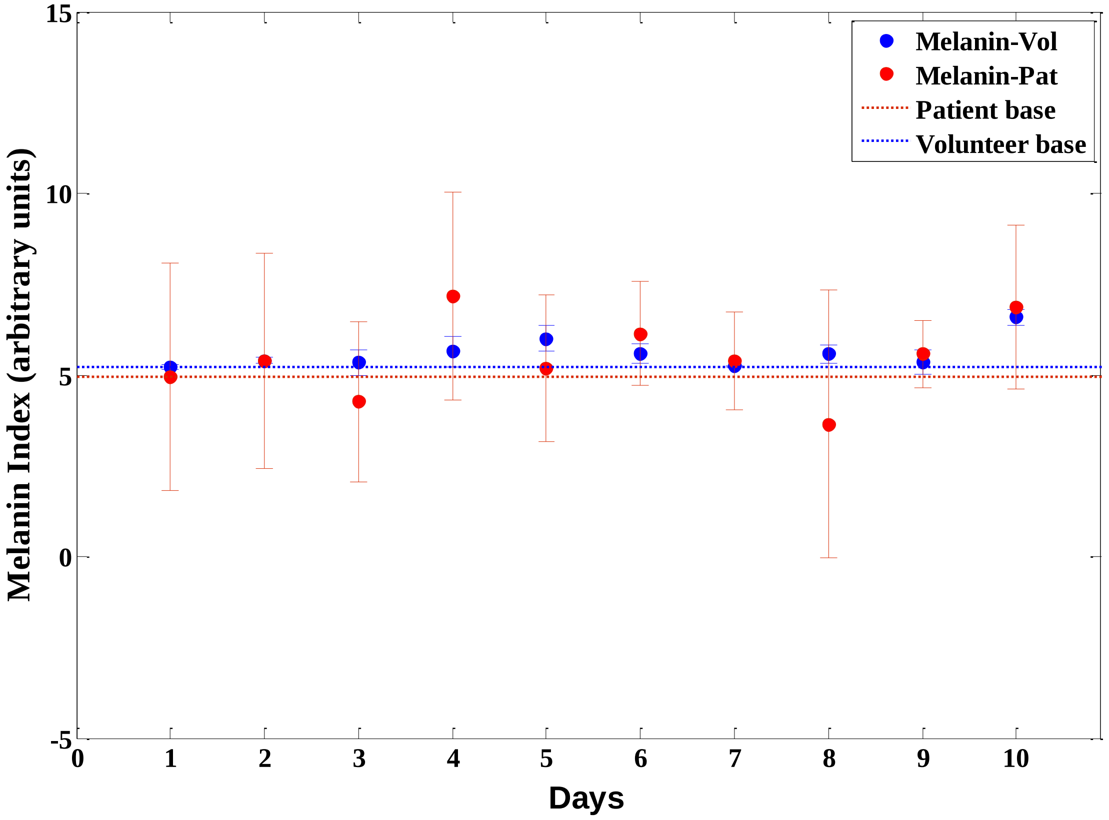

Figure 6-10: (red points) the successful Patients' apparent melanin content was averaged and scattered to evaluate its behavior during the entire radiotherapy treatment plan. The error bars are expressing the variability among patients' skin types, (blue points). A healthy volunteer skin was probed for apparent melanin content for 10 days, similar to patients' plan, and the data was scattered against patients' data for contrast purpose.

Erythema melanin corrected erythema indices, be it absolute or relative, was calculated for the study's applicable patients applying Dawson's model [20]. The outcome of the absolute melanin corrected erythema index is exhibited in Figure 6-11 while the corresponding relative erythema index is displayed in Figure 6-12. To validate the reliability of the used instrumentation and for contrast purposes, a healthy volunteer data was included in both figures. Horizontal baselines were drawn in both cases: patients and volunteer in order to ease monitoring the amount of change with respect to the primary baseline data prior to irradiation.

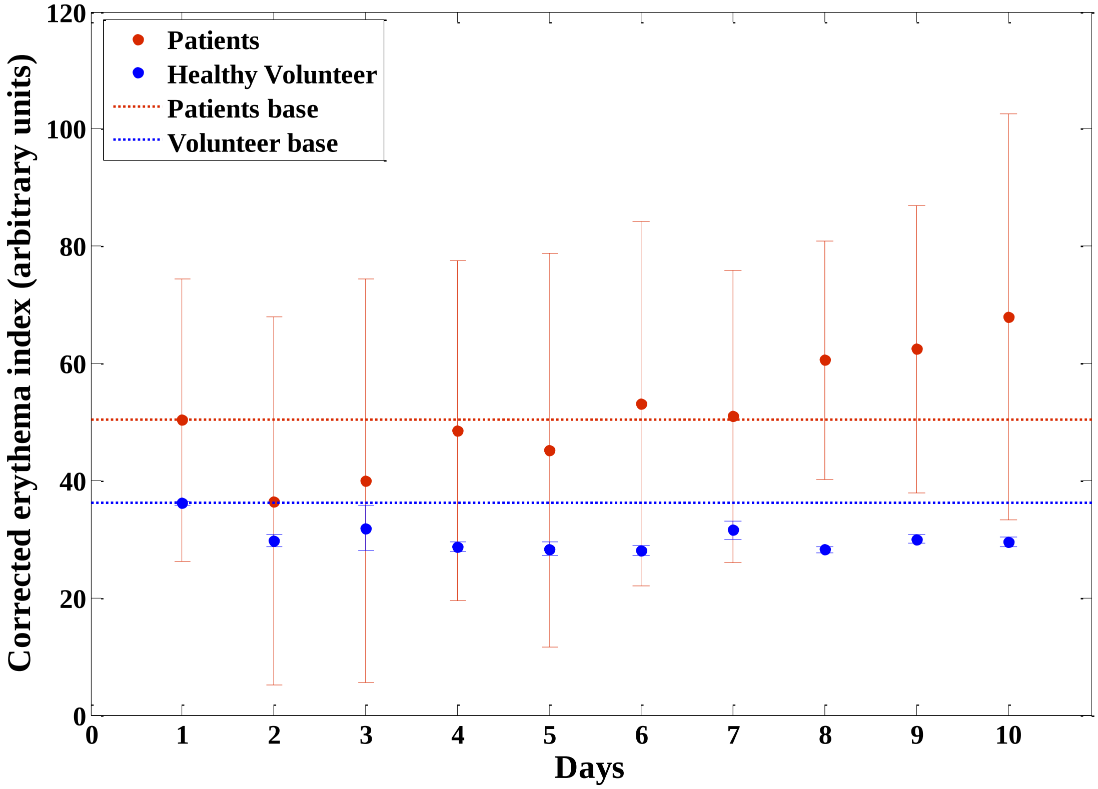

Figure 6-11: (red points) the study successful Patients' average melanin corrected erythema index, calculated by Dawson model, for the entire radiotherapy treatment time are scattered. The error bars are expressing the variability in the computed erythema among patients. Horizontal lines are drawn from the initial points in both patients and volunteer cases.

The corrected erythema index showed a nonlinear style of change during the first half of treatment days while it turned out to increase persistently, with a variable rate, in the second half of the treatment itinerary. We expect that the oscillating behavior of melanin corrected erythema index is due to the fluctuation in the rate of basal cells destruction in the epidermal layer of the skin [15]. Since the inflammatory response of the skin is not absolutely persistent, specifically; if we take into consideration the scheduled stops in treatment due to weekends, or statutory holidays within the treatment plan. These unintentional stops in radiotherapy sessions might be one strong reason in the existing large error bars. On the volunteer side, the index showed an intermittent alteration with respect to the initial base measurement and a small error bar where no stops were allowed in volunteer experiment.

In brief, the comparison between the patients and the volunteer provided imperative observations can be summed as follows; 1) the initial erythema level was higher in patients side rather than the volunteer due to some natural features in some patients' ROI, 2) the maximum variation between the erythema indices in the case of patients is found to be three times higher than in the volunteer case, 3) the volunteer data is showing inconsistent behavior (ups and downs) versus an overall incrementing rate in patients' data.

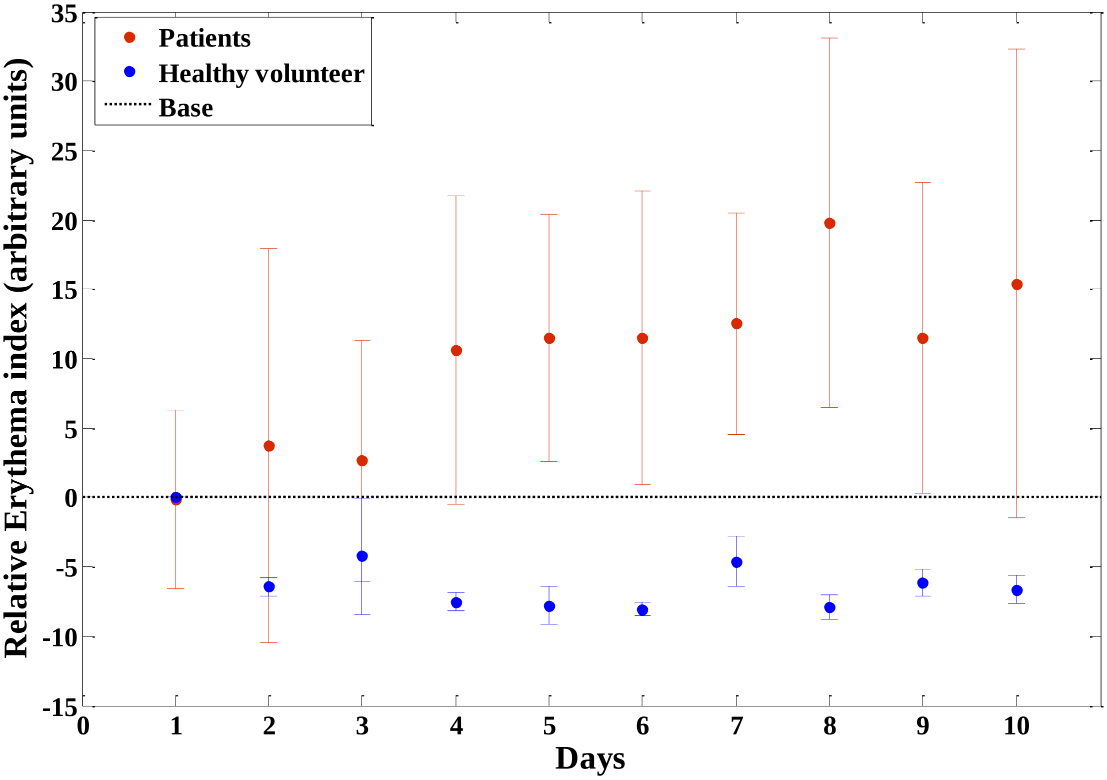

Figure 6-12: Patients' average melanin relative erythema index for the entire radiotherapy treatment time based on a comparison between a reference region and irradiated region (red points) are scattered on the data points while the error bars are expressing the variability in daily erythema change among patients, (blue points) the corresponding volunteer data and base.

Aside from absolute erythema index, the relative erythema index data exhibited a relatively consistent increase proportional to the irradiation dose accumulation. Relative erythema index is dependent on the skin reflectance relative change between the irradiated ROI and a surrounding reference skin region receiving no irradiation. Thereby, the relative erythema index becomes more sensitive to skin color change regardless of illumination effect as shown in Figure 6-12. To give a contrasting example, a volunteer relative erythema data was computed and displayed in Figure 6-12. The volunteer relative erythema index showed approximately a constant behavior upon the whole days of imaging except for the first day which was slightly higher than the rest of the subsequent data points. However, this time, the patients and the volunteer baselines, black dashed lines, are exactly the same. Since the relative erythema at the starting day equals to zero unless the patient already has slight redness at the beginning of the treatment.

Based on previous skin indices behavior, it was interesting to study the change significance for each of them in comparison with the baseline value. For that reason, Wilcoxon nonparametric two-tail paired test was used to examine the hypothesis of a significant difference between the skin's diffuse reflectance at different irradiation time points against the baseline measurement. This statistical test is highly suited to a small number of observations. In brief, Wilcoxon test is analyzing the median difference between two population groups before and after exposure to a certain experiment [34]. The Wilcoxon computed value for each group is compared to a certain tabulated value relevant to the number of observations. Based on the comparison outcome, the null hypothesis is either accepted or rejected. Relative erythema indices, corrected erythema indices, and melanin indices were chosen as dependent parameters on the skin diffuse reflectance at nine-time points along the irradiation treatment. Each data point was examined versus the starting day data point. The test result is compared to the tabulated statistical value for the corresponding number of observations. The tabulated Wilcoxon value, plotted as a black horizontal line as shown in Figure 6-12 (a). This line is the marginal threshold, above which the null hypothesis is rejected. Moreover, the significance of the test results is illustrated in Figure 6-13 (b), respectively. Wilcoxon statistical test showed that the relative erythema, the corrected erythema, and the melanin indices became higher than the null rejection threshold at a certain time point through the study period of time. Notably, the melanin index has only a single time point in the mid-way of treatment period which crossed the threshold. This indicated an inconsistent alteration in apparent melanin concentration with no real physiological interpretation.

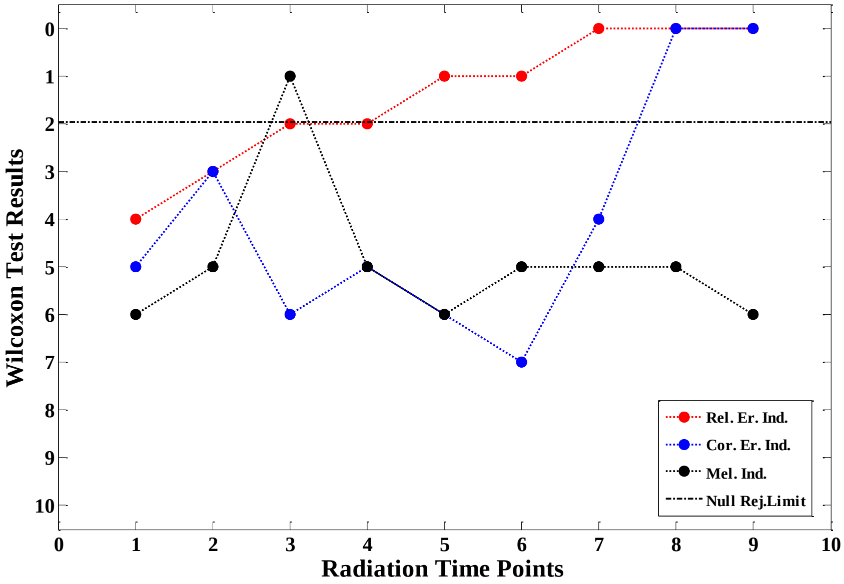

(a)

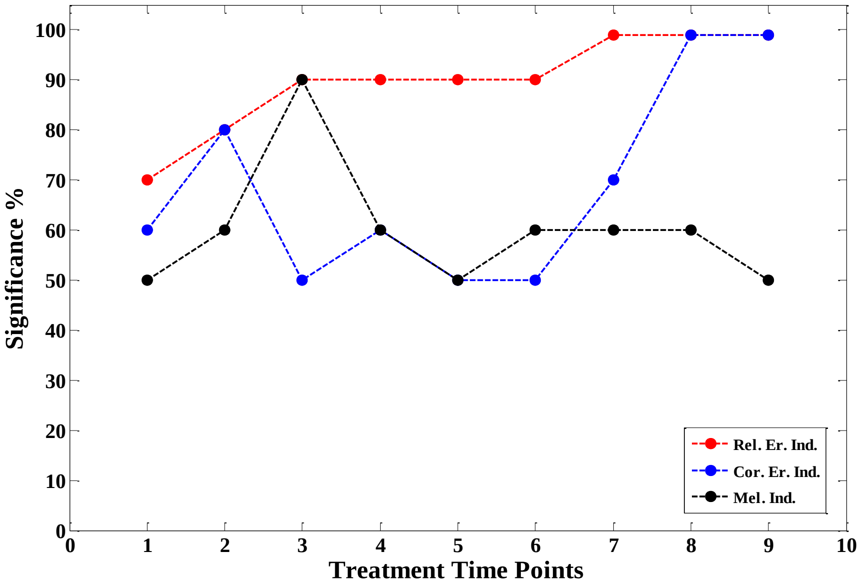

(b)

Figure 6-13: Wilcoxon (a) statistical test results against null hypothesis rejection limit (no change), (b) the corresponding significance for the relative erythema, the corrected erythema, and the melanin indices, all along the radiotherapy treatment.

Relative erythema index was the fastest parameter to achieve a substantial difference in comparison with the baseline with 90% significance. Once more, it is the first parameter to reach a significance of 99% at the seventh time point of measurement. The corrected erythema index is strongly oscillating, but eventually it achieved 99% significance, albeit later than the relative erythema index. This result highlighted the power of the relative erythema index in delineating the skin response to cancer radiation treatment in a consistent sensitive way. Besides, this test presented a second evidence of the inconsistent skin melanin content alteration by irradiation.

In order to confirm the powerfulness of the relative erythema index for monitoring the skin response due to received irradiation, it was interesting to examine its potential relevance to the clinical erythema total score, namely the radiotherapist's visual assessment shown in Figure 6-9. Thereby, the correlation between the erythema indices, and the radiotherapist erythema total score was computed utilizing Pearson correlation coefficient. It was found that a correlation value of 79.1% with respect to visual scores was figured out for the corrected erythema index, however, a much higher value of 97.1% for the relative erythema index. This result emphasized how strongly the relative erythema index is able to assist in judging the skin's reaction upon exposure to irradiation based on an objective measurement technique.

Interpreting skin erythema index in terms of physiology is deeply relevant to the circulatory system oxygenation and perfusion. Particularly, vasodilation and the increase of hemoglobin content in the dermis layer is basically the main cause of inducing skin erythema/ redness. For erythema quantification purpose, the apparent concentration of hemoglobin, both components, needs to be estimated.

6.4.3 Estimation of Hemoglobin chromophores

Since the major responsible chromophore for the skin's redness/ erythema is the hemoglobin with its both parts, oxygenated and non-oxygenated [22]. Probing the hemoglobin dual chromophores apparent concentration is a critical step in the approach to developing a deep understanding of the embedded physiological phenomena standing behind the skin's inflammatory reaction induced due to radiation exposure. Least square fitting for measured data was accomplished using the extinction coefficients for each of the hemoglobin components in a way to quantitatively estimate their apparent concentration during treatment.

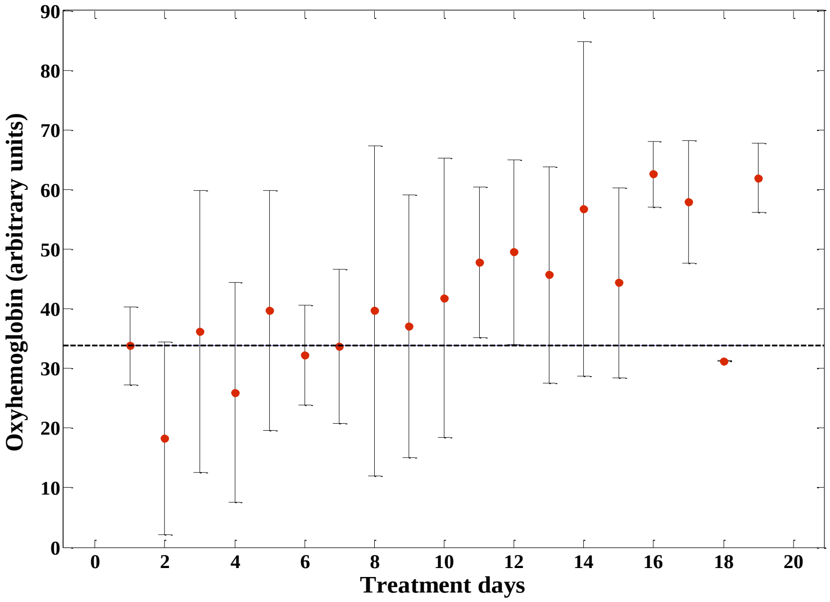

(a)

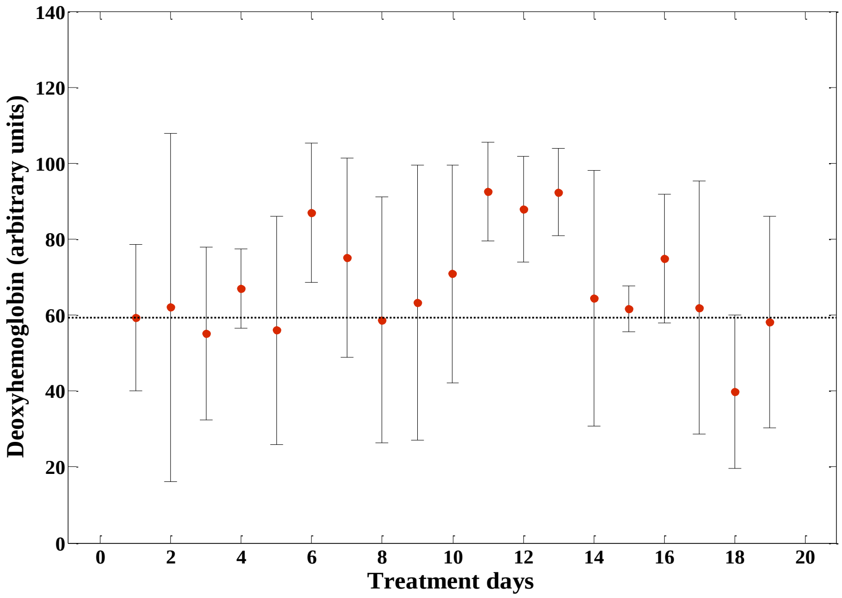

(b)

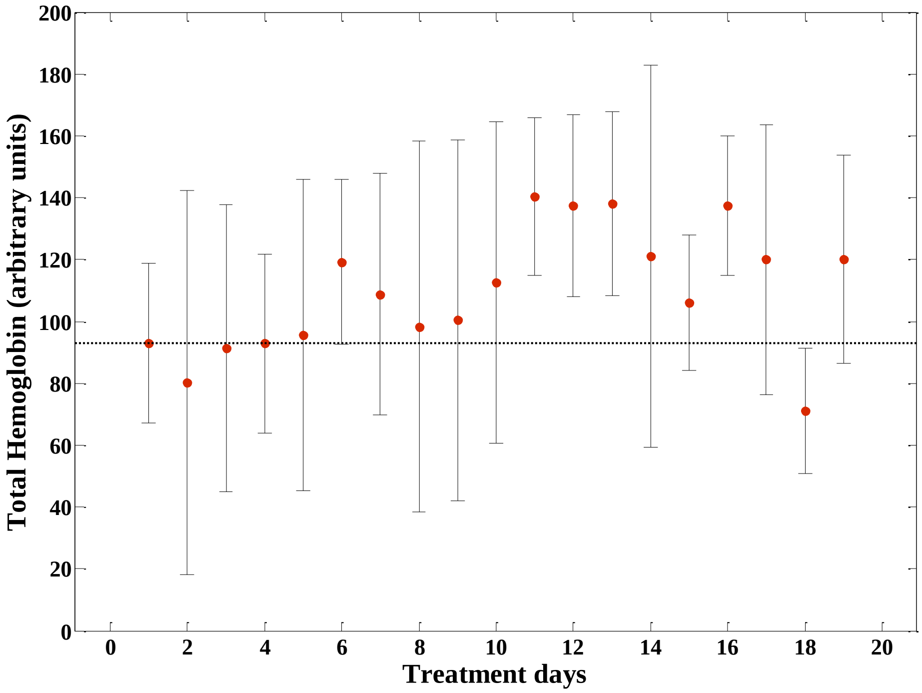

(c)

Figure 6-14: Mean Hb-oxy (a), Hb-deoxy (b), and total hemoglobin (c), as a function of time during irradiation. Error bars are displayed representing standard deviation. Baseline values are drawn in each plot in dashed lines, respectively.

The apparent concentration of hemoglobin both parts for the involved patients were averaged and scattered along the days of treatment as illustrated in Figure 6-14 (a, b). Error bars are representing the standard deviation of hemoglobin concentration among patients. The oxyhemoglobin apparent concentration shows a clear trend of upturn throughout the days of irradiation dose exposure, oppositely, deoxyhemoglobin was interchangeably altering between upturns and downturns. Adding both hemoglobin components was the way to obtain the total hemoglobin apparent concentration displayed in Figure 6-14 (c). The estimated concentration of the total hemoglobin showed a sporadic trend of ups and downs in the treated body part versus the original concentration before irradiation with a general incremental trend. This result is expected due to the unlike temporal apparent concentration behavior acted by both hemoglobin components.

6.4.4 Image Classification

Applying the developed LDA classifier on both digital color photographs and spectral datacubes was the way to contrast both techniques. The contrast was held through a supervised classification for color and spectral data relevant to the ground truth annotations provided by the radiotherapist. I tried distinct ratios between the training sets and the test sets. I found that 50:50 ratios between training and test samples were superior to different other options such as the Pareto principle for 20:80 ratios, as well as other 60:40 ratios. Since the 50:50 ratios produced the most satisfactory results for the entire assessment parameters. The hyperspectral imaging system showed a comparable performance with digital photography in parameters such as accuracy and sensitivity while it outperforms RGB imaging in specificity and the geometrical mean. I report the classification output (mean ± std) for six parameters, for ten repeated times for randomly selected training and test sets within the data population with 50% training to test ratio, displayed in Table 6-2. The displayed values were tested for significance using Wilcoxon statistical test and the p-values are displayed in Table 6-2.

Table 6-2: Classification output parameters comparison for HSI and RGB imaging for skin erythema assessment. P-values out of Wilcoxon test to determine the significance of the classification parameters are included.

Technique	Accuracy	Precision	F-measure	Sensitivity	Specificity	G-mean
HSI-Imaging	91.09 ± 0.83	85.23 ± 0.98	86.65 ± 0.89	88.68 ± 1.01	32.89± 3.39	47.23 ± 2.63
RGB-Imaging	91.28 ± 0.50	83.23 ± 1.99	86.21 ± 0.94	90.10 ± 0.94	16.85 ± 4.63	25.08 ± 6.59
Wilcoxon P-value	0.000266	0.024824	0.024824	0.000138	0.007657	0.007657

6.5 Conclusion

We expect that the preliminary skin erythema study, held within this work, provides a step forward toward objective assessment for skin radiotherapy-induced erythema. In particular, HSI permitted a contactless visualization and a quantitative assessment of relatively wide skin region in terms of oxygenation and perfusion in radiotherapy which saves time in contrast with a skin limited region investigation by diffuse reflectance spectroscopy. Moreover, HSI was able to spectrally resolve the skin color change in contrast with digital color imaging. I identified the power points of this preliminary study as follows:

1- At the time of the 7th day measurement, in average, the relative erythema index reaches 99% significance in differentiating between skin cancer areas treated by high doses of ionizing radiation and the surrounding normal skin. Thus, the relative erythema index, based on the captured skin spectral resolved reflectance, found to be a very sensitive parameter to assess the skin response due to radiotherapy. This was verified since it achieved a value of 0.971 correlations with the gold standard (visual assessment) of erythema evaluation.
2- Oxyhemoglobin chromophore showed a gradual increase with ionizing radiation accumulation time, in the areas surrounding the lesion, which is probably due to skin healing after damage. However, deoxyhemoglobin showed an oscillating behavior upon the same time period. In sum, the total hemoglobin is increasing along the radiotherapy treatment duration. This increase in total hemoglobin interprets the change of the skin color of being more red/ erythematous.
3- The supervised LDA algorithm used for skin erythema classification was very efficient since it has an accuracy of ~90% and precision of ~85%. According to classification results, HSI was not only found to be on par with RGB imaging but actually outperformed the latter tremendously in terms of specificity and geometric mean.

I am convinced that the future progress in producing more even illumination as well as a reduction of the instrumentation noise level will pave the way for a fast, reliable, and, above all, objective quantitative method for erythema classification. Consequently, HSI may serve as a good candidate to the fast recognition of individuals affected by harmful radiation. Further experimental, clinical, and analytical work need to be done to make HSI a real-time clinical instrument.

References

[1] M. Veness and S. Richards, “Role of modern radiotherapy in treating skin cancer.,” *Australas. J. Dermatol.*, vol. 44, no. 3, pp. 159–166; quiz 167–168, 2003.

[2] D. M. Brizel, R. K. Dodge, R. W. Clough, and M. W. Dewhirst, “Oxygenation of head and neck cancer: Changes during radiotherapy and impact on treatment outcome,” *Radiother. Oncol.*, vol. 53, pp. 113–117, 1999.

[3] M. Caccialanza, R. Piccinno, L. Kolesnikova, and L. Gnecchi, “Radiotherapy of skin carcinomas of the pinna: a study of 115 lesions in 108 patients.,” *Int. J. Dermatol.*, vol. 44, no. 6, pp. 513–7, 2005.

[4] N. P. Nguyen, T. Ries, J. Vock, P. Vos, A. Chi, V. Vinh-Hung, S. Thompson, A.

Desai, T. Sroka, R. A. Vo, S. Gelumbauskas, R. Hamilton, U. Karlsson, and A. Mignault, “Effectiveness of radiotherapy for elderly patients with non-melanoma skin cancer of the head,” *Geriatr. Gerontol. Int.*, vol. 15, no. 5, pp. 601–605, 2015.

[5] T. Olschewski, K. Bajor, B. Lang, E. Lang, and M. H. Seegenschmiedt, “[Radiotherapy of basal cell carcinoma of the face and head: Importance of low dose per fraction on long-term outcome].,” *J. Dtsch. Dermatol. Ges.*, vol. 4, no. 2, pp. 124–30, 2006.

[6] W. Maddocks-Jennings, J. M. Wilkinson, and D. Shillington, “Novel approaches to radiotherapy-induced skin reactions: A literature review,” *Complement. Ther. Clin. Pract.*, vol. 11, no. 4, pp. 224–231, 2005.

[7] D. Porock and L. Kristjanson, “Skin reactions during radiotherapy for breast cancer: The use and impact of topical agents and dressings,” *Eur. J. Cancer Care (Engl).*, vol. 8, no. 3, pp. 143–153, 1999.

[8] S. K. MacBride, M. E. Wells, C. Hornsby, L. Sharp, K. Finnila, and L. Downie, “A case study to evaluate a new soft silicone dressing, Mepilex Lite, for patients with radiation skin reactions.,” *Cancer Nurs.*, vol. 31, no. 1, pp. E8–E14, 2008.

[9] S. D’haese, M. Van Roy, T. Bate, P. Bijdekerke, and V. Vinh-Hung, “Management of skin reactions during radiotherapy in Flanders (Belgium): a study of nursing practice before and after the introduction of a skin care protocol.,” *Eur. J. Oncol. Nurs.*, vol. 14, no. 5, pp. 367–372, 2010.

[10] J. W. Denham, C. S. Hamilton, S. A. Simpson, P. M. Ostwald, M. O’Brien, T. Kron, D. J. Joseph, and K. B. G. Dear, “Factors influencing the degree of erythematous skin reactions in humans,” *Radiother. Oncol.*, vol. 36, no. 2, pp. 107–120, 1995.

[11] M. McQuestion, “Evidence-Based Skin Care Management in Radiation Therapy,” *Semin. Oncol. Nurs.*, vol. 22, no. 3, pp. 163–173, 2006.

[12] S. Balter, J. W. Hopewell, D. L. Miller, L. K. Wagner, and M. J. Zelefsky, “Fluoroscopically guided interventional procedures: a review of radiation effects on patients’ skin and hair.,” *Radiology*, vol. 254, no. 2, pp. 326–341, 2010.

[13] M. S. Chin, B. B. Freniere, Y.-C. Lo, J. H. Saleeby, S. P. Baker, H. M. Strom, R. Ignotz, J. F. Lalikos, and T. J. Fitzgerald, “Hyperspectral imaging for early detection of oxygenation and perfusion changes in irradiated skin.,” *J. Biomed. Opt.*, vol. 17, no. 2, p. 026010, Feb. 2012.

[14] N. Lee, C. Chuang, J. M. Quivey, T. L. Phillips, P. Akazawa, L. J. Verhey, and P. Xia, “Skin toxicity due to intensity-modulated radiotherapy for head-and-neck carcinoma,” *Int. J. Radiat. Oncol. Biol. Phys.*, vol. 53, no. 3, pp. 630–637, 2002.

[15] R. I. J . W . HOPEWELL (CRC Normal Tissue Radiobiology Research Group and H. (University of Oxford), The Churchill Hospital, “The skin : its structure and response to ionizing radiation,” *INT. J. RADIAT. BIOL .*, vol. 57, no. 4, pp. 751–773, 1990.

[16] L. Diana L. Glennie, Joseph E. Hayward, Orest Z. Ostapiak, James Wright and T. J. F. Doerwald-Munoz, “Diffuse reflectance spectroscopy for monitoring erythema in head & neck intensity modulated radiation therapy,” *J. Radiat. Oncol.*, 2014.

[17] C. K. Kraemer, D. B. Menegon, and T. F. Cestari, “Determination of the minimal phototoxic dose and colorimetry in psoralen plus ultraviolet A radiation therapy,” *Photodermatol. Photoimmunol. Photomed.*, vol. 21, no. 5, pp. 242–248, 2005.

[18] P. Simonen, C. Hamilton, S. Ferguson, P. Ostwald, M. O’Brien, P. O’Brien, M. Back, and J. Denham, “Do inflammatory processes contribute to radiation induced erythema observed in the skin of humans?,” *Radiother. Oncol.*, vol. 46, no. 1, pp. 73–82, 1998.

[19] K. J. Zuzak, M. T. Gladwin, R. O. C. Iii, I. W. Levin, J. Karel, and R. O. Can-, “Imaging hemoglobin oxygen saturation in sickle cell disease patients using noninvasive visible reflectance hyperspectral techniques : effects of nitric oxide,” vol. 0510, pp. 1183–1189, 2003.

[20] J. B. Dawson, D. J. Barker, D. J. Ellis, E. Grassam, J. a Cotterill, G. W. Fisher, and J. W. Feather, “A theoretical and experimental study of light absorption and scattering by in vivo skin.,” *Phys. Med. Biol.*, vol. 25, no. 4, pp. 695–709, 1980.

[21] C. a Schneider, W. S. Rasband, and K. W. Eliceiri, “NIH Image to ImageJ: 25 years of image analysis,” *Nat. Methods*, vol. 9, no. 7, pp. 671–675, 2012.

[22] G. N. Stamatas and N. Kollias, “In vivo documentation of cutaneous inflammation using spectral imaging.,” *J. Biomed. Opt.*, vol. 12, no. 5, p. 051603, 2007.

[23] T. Lister, P. a Wright, and P. H. Chappell, “Optical properties of human skin.,” *J. Biomed. Opt.*, vol. 17, no. 9, pp. 90901–1, Sep. 2012.

[24] F. H. Mustafa and M. S. Jaafar, “Comparison of wavelength-dependent penetration depths of lasers in different types of skin in photodynamic therapy,” *Indian J. Phys.*, vol. 87, no. 3, pp. 203–209, Nov. 2012.

[25] D. L. Glennie, J. E. Hayward, and T. J. Farrell, “Modeling changes in the hemoglobin concentration of skin with total diffuse reflectance spectroscopy,” *J. Biomed. Opt.*, vol. 20, no. 3, p. 035002, 2015.

[26] S. Tan, R. Young, D. Budgett, J. Richardson, and C. Chatwin, “A pattern recognition Weiner filter for realistic clutter backgrounds,” *Opt. Commun.*, vol. 172, no. 1–6, pp. 193–202, 1999.

[27] M. Isaac N. BANKMAN (Applied Physics Laboratory Johns Hopkins University Laurel, *Handbook of Medical Imaging*. Academic Press, 2000.

[28] T. Wang, Ö. Özdamar, J. Bohórquez, Q. Shen, and M. Cheour, "Wiener filter deconvolution of overlapping evoked potentials," *J. Neurosci. Methods*, vol. 158, no. 2, pp. 260–270, 2006.

[29] *Fundamentals of digital image processing*. Prentice Hall, 1989.

[30] G. Liu, Z. Lin, S. Yan, J. Sun, Y. Yu, and Y. Ma, "Robust Recovery of Subspace Structures by Low-Rank Representation," *Pattern Anal. Mach. Intell. IEEE Trans.*, vol. 35, no. 1, pp. 171–184, 2013.

[31] M. Li and B. Yuan, "2D-LDA: A statistical linear discriminant analysis for image matrix," *Pattern Recognit. Lett.*, vol. 26, no. 5, pp. 527–532, 2005.

[32] T. Bandos, "Classification of hyperspectral images with regularized linear discriminant analysis," *Geosci. Remote …*, vol. 47, no. 3, pp. 862–873, 2009.

[33] U. of T. Welling, Max (Department of Computer Science, "Fisher Linear Discriminant Analysis," 2005.

[34] M. H. Shilts, C. Rosas-Salazar, A. Tovchigrechko, E. K. Larkin, M. Torralba, A. Akopov, R. Halpin, R. S. Peebles, M. L. Moore, L. J. Anderson, K. E. Nelson, T. V Hartert, and S. R. Das, "Minimally Invasive Sampling Method Identifies Differences in Taxonomic Richness of Nasal Microbiomes in Young Infants Associated with Mode of Delivery - Online First - Springer," *Microb. Ecol.*, pp. 233–242, 2016

Chapter 7: Conclusions and Future Work

Hyperspectral imaging combined with precise data analysis, including image processing and data classification, work was employed toward objectively quantifying skin induced erythema post radiation therapy treatment. The entire work done here is to achieve objective quantification for skin induced erythema. This work is presented in the current thesis earlier chapters. This chapter delivers the conclusion of the work introduced earlier. Moreover, it provides the major guidelines for the next continuation phase and the expected endeavor of the research work done here based on the gained experience and the state of the art optical assessment of skin erythema.

7.1 Conclusions

The current clinical gold standard for grading skin erythema is based on subjective qualitative scoring and depends on the experience of the radiotherapist/ clinician. The clinical expertise of a radiotherapist may vary from one to the other. The variability between radiotherapists depends on several factors including; work experience, training, visual acuity, and the operating environment. Consequently, this variability contributes to differences between subjects in erythema assessment. Thereby, many research groups looked into developing quantitative and/ or objective measures to minimize inter-observer subjectivity (Chapter 2). Optical assessment methodologies for skin erythema are the dominant approaches in this challenge including diffuse reflectance spectroscopy (DRS) measurement and digital color (RGB) imaging techniques. However, neither of the used optical methodologies is flawless.

In this thesis, the research question was “Is hyperspectral imaging (HSI) capable of remotely quantifying skin erythema due to radiation therapy?” Skin erythema is a secondary inflammatory response dependent on a vasodilatory process. Thereby, erythema is distinguished by an increase of blood content within the skin dermal microcirculation in the region of inflammation. A key biomarker of blood content is hemoglobin concentration variation. Quantitative measurement of hemoglobin can be achieved via skin back reflectance detection at 540,560, and 580 nm wavelengths. HSI operating in the visible-near infrared (VIS-NIR) is considered to be a feasible approach for measuring the skin reflectance spectra regarding a sizable region of interest. For this reason, I have developed, characterized, and evaluated a high throughput HSI and went through the following milestones:

1- A high throughput acousto-optic tunable filter (AOTF)-based-HSI instrument was designed and implemented while taking clinical compatibility into consideration. The newly developed AOTF-HSI system was fully characterized in spectral and spatial domains. Moreover, it is evaluated against a liquid crystal tunable filter (LCTF)-HSI to demonstrate its capability of measuring spectral signature precisely (Chapter 4).

2- A linear discriminant analysis (LDA) classification method was optimized to cluster the induced skin erythema based on the acquired spectral data with low signal to noise ratio (SNR). Artificially induced skin erythema was induced on the forearm of volunteers and used to check the feasibility of using both the developed AOTF-HSI instrument and LDA method in erythema assessment. The algorithm is designed to be robust, precise and prompt. In addition, HSI was contrasted against digital color imaging in erythema classification (Chapter 5).

3- A preliminary clinical study was run on skin-cancer patients undergoing radiotherapy to quantitatively assess radiation dermatitis/ erythema using the newly developed AOTF-HSI system along with LDA classification. Toward this, melanin and erythema indices were computed using Dawson's model [1]. Following the computation of the skin pigmentation indices, Wilcoxon non-parametric two-tailed test was used to examine the significance of AOTF-HSI sensitivity to detect minute skin color change. Next, the apparent concentration of hemoglobin components was estimated by using the least square fitting to fit the hemoglobin extinction coefficients to the inverse logarithm of the skin reflectance data. Finally, the developed LDA algorithm was used to compare the AOTF-HSI performance against the digital color imaging in terms of classifying the developed radiation dermatitis (Chapter 6).

The newly developed high throughput dual channel AOTF-HSI system was designed and implemented to retrieve in vivo diffuse reflectance data from biological tissues including human skin. The dual channel system throughput was measured and evaluated taking into consideration the existing single channel configurations. The measured transmission throughput of the dual channel AOTF-HSI was proved to be higher, with at least 67% than the closest single channel configuration. Moreover, the system was spectrally characterized to determine its technical parameters. For instance, (1) the RF tuning range used for diffracting the spectral range of operation (450:800 nm), (2) the wavelength-dependent line width (1.5:4.1 nm), (3) the variation between AOTF-HSI both channels in linewidth, and (4) the optimized RF signal amplitude for realizing the highest diffraction intensity. Following the spectral characterization of AOTF-HSI, spatial attributes were also examined. The spatial attributes include (1) localizing the optimal range for the distance between the patient and the instrument, (2) computing the AOTF-HSI instrument depth of focus and finally (3) the spatial resolving power.

For rating purposes, the developed AOTF-HSI configuration was evaluated in contrast with a corresponding LCTF-based spectrometer configuration. The evaluation process addressed four parameters; (1) filter spectral selectivity, (2) resolution, be it spectral or spatial, (3) image quality, and (4) instrument reliability. The evaluation results showed a superior performance of the AOTF-HSI system in the spectral domain. To illustrate more; first, the spectral resolution / line width of AOTF-HSI outperforms its corresponding LCTF along the entire common range. Second, AOTF's selectivity (capability of rejecting the light out of the tuned band) is greatly superior compared with LCTF. In addition to spectral attributes, AOTF is the closer of both designated filters to achieve real-time video monitoring of skin erythema because of its invaluable speed of random wavelength access. Nonetheless, LCTF-HSI is preferable in spatial imaging, where fine spatial details can be resolved well than in AOTF-HSI case. For instance, LCTF advantage of the high spatial resolution would be beneficial in the case of studying the effect of a treatment on skin surface features such as the acne lesions size and count. In conclusion, I advocate AOTF be adopted as a spectral dispersion device in the cases of precise close spectral features while I endorse LCTF to be integrated into spectral imaging systems with more interest in spatial tissue features.

Toward clinical application of the developed AOTF-HSI, a controlled study was planned to prepare for live human imaging and to test the robustness of the developed LDA algorithm. Moreover, it was also a good opportunity to contrast both the spectral and the digital imaging modalities. In this study, 3 volunteers were asked to successfully tackle their forearms using a plastic ruler for 3 minutes. Upon that, erythema with distinct levels of intensity showed up simulating radiation dermatitis. The whole study was clinically supervised; the erythema was scored by an expert radiotherapist. The experiment was promising in the sense that HSI was strongly capable of monitoring the descending severity of skin erythema during the recovery time. Likewise, the study results proved the outstanding performance of HSI versus digital imaging in classifying erythema in 85 % accuracy and 74 % precision.

In clinical work, a preliminary clinical study was performed on a daily basis along 6 months on skin cancer patients. Spectral, digital, and clinical data acquisitions were performed 30-minutes prior each radiation treatment for recruited skin cancer patients. In this study, 8-patients were diagnosed with basal and squamous cell carcinomas consented to participate. However, five out of the eight patients acquired data sets were effectively used. The other three patients' data sets were excluded due to the study exclusion criteria. The onset of the data analysis was computing the skin reflectance and then the erythema indices. Both erythema indices (absolute and relative melanin-corrected indices) were correlated to the visual assessment of the involved radiotherapist in the study. However, the relative index of erythema outperformed the absolute index with a value of 0.97 versus 0.79 positive correlations. Moreover, erythema indices were statistically examined using Wilcoxon non-parametric test. The test results showed, with 99% significance, the difference between the skin reflectance of control and treated regions after receiving 6 radiation treatments using the relative index. In conjunction with prior, the computed absorbance based on the acquired spectral datacubes enabled a quantitative measure for the daily changes in the apparent hemoglobin concentration along the radiotherapy treatment duration. The study results, regarding hemoglobin concentration, showed that the oxygenated part of hemoglobin is consistently increasing during the period of receiving radiation, while the deoxygenated part of hemoglobin may increase or decrease from one radiation session to the next. Based on the total hemoglobin trend, we conclude that in the case of a small number of treatments (10:20 sessions) the inflammation intensity is proportionally increasing with time. This increase in skin inflammation is interpreted physiologically by the incremental accumulation of oxyhemoglobin in the treated region.

7.2 Future Work

The project future work is divided into three paths to move forward. The first is further instrumentation and hardware improvement. The second path will be directed toward the application of the developed AOTF-HSI system in studying other types of cancers, in order to validate the work done but with slightly deeper lesions such as head and neck tumors. Thereby, a correlation between both the tumor and the skin responses due to radiation can be studied. The third and final path will be guided toward finding another application for the developed AOTF-HSI instrument rather being dedicated to skin related symptoms.

7.2.1 Instrumentation optimization

This path will focus on how to improve SNR of the taken spectral images. The expected improvement depends on integrating an advanced detector with higher quantum efficiency, digitization and lower dark current noise. In addition to SNR improvement, this modification is expected to speed up the spectral imaging procedure, provide more image quantization levels. As such, charge-coupled device (CCD) is the closest possible candidate to play this role. Moreover, the forthcoming prototype will be considered carefully to be more compact in size and light in weight in order to increase the maneuverability of the imaging system from a clinic to the other in a shorter time. Illumination of the subject under investigation will be macroscopically considered in order to achieve more even distribution with less inconvenience to patients. For instance, heat protection filters, ring light distribution, and remotely controlling illumination intensity are parameters to be contemplated. In a new study, an LCTF-based spectrometer with a fair spectral resolution is a candidate for implementing a more compact instrument to evaluate radiation dermatitis. The reason to employ this filter is the simplicity of operation and possible comparability with custom-made integrating-sphere based DRS.

7.2.2 Skin to tumor: radiation response correlation

This planned work path will be dedicated to examining the hypothesis of the project which assumes a certain degree of correlation between the skin and the underneath tumor upon exposure to the ionizing radiation. Since the emitted ionizing radiation propagates through the healthy skin in its way to reach tumors in the case of external beam treatment. Consequently, both the skin and tumor cells react to the ionizing radiation. However, the skin reactions are much faster. According to the computed degree of correlation, there could be a chance to tune the prescribed treatment plan for individuals toward achieving better cancer cure. This work requires recruiting a fair number of patients to be examined. These patients need to be examined later to check their tumor size response couple of months post-irradiation to verify or decline the hypothesis.

7.2.3 New clinical study

Parallel to the instrumentation development and skin application, the current imager is germane not only to address skin tissue features but also feasible to scrutinize symptoms pertinent to other body organs. One of the possible organs to be studied using spectral inspection is the eye sclera. This white part of the eye is vulnerable to few diseases that cause a change in color from normal white into red [2], yellow [3], and blue [4]. These diseases are not solely related to the eye health but also to inherent chronic diseases. As such, HSI systems can be effectively an objective technique for differentiating the spectral signatures for the different sclera color symptoms. In addition, the spectral analysis could contribute in correlating each color symptom to the original causing disease, no matter how they look close visually.

As closing remarks, the work presented here in the current thesis has been directed toward the development of a high throughput dual-channel AOTF-HSI system in order to objectively quantify radiotherapy induced skin erythema. The newly developed AOTF-HSI is operating in the VIS-NIR spectral region with nonlinear wavelength dependent linewidth ranges from 1.5:4.1 nm. The dual-channel configuration outperforms the existing single channel configurations by at least 1.5 times transmission ratio. Moreover, the new AOTF imaging spectrometer was evaluated in comparison with a corresponding LCTF instrument and achieved superior performance in the spectral domain. An exploratory study was accomplished on healthy volunteers to examine both the developed AOTF imaging spectrometer and the optimized LDA method to classify the induced erythema, in a way to simulate radiation dermatitis. In addition, the held exploratory study was used to contrast spectral and digital imaging in erythema classification. Finally, hyperspectral imaging was used to monitor the temporal evolution of skin erythema along the radiotherapy duration of treatment for skin cancer patients. Erythema indices were calculated and correlated to the clinical assessment, where the relative index achieved 0.97 positive correlations. Skin hemoglobin chromophore concentration was estimated along the entire irradiation plan of treatment, where oxyhemoglobin showed a temporally increased concentration. LDA supervised classification algorithm output parameters showed the outstanding significant performance of hyperspectral imaging versus digital photography in both specificity and geometrical mean.

To this end, it is recommended to go through long-term studies regarding skin erythema to evaluate the efficacy of hyperspectral imaging in monitoring the alteration of skin pigmentation and color in humans with different backgrounds. As such, it is expected that HSI could be a possible contact-free while being objective, monitoring technique for radiation dermatitis. Much work needs to be done in order to establish HSI as a bench top system for investigating the skin erythema in dermatological clinics.

References

[1] J. B. Dawson, D. J. Barker, D. J. Ellis, E. Grassam, J. a Cotterill, G. W. Fisher, and J. W. Feather, "A theoretical and experimental study of light absorption and scattering by in vivo skin.," Phys. Med. Biol., vol. 25, no. 4, pp. 695–709, 1980.

[2] N. P. Bannister, M. J. Wakefield, a. Tatham, S. L. Bugby, P. M. Molyneux, and J. I. Prydal, "Spectroscopic measurements in scleritis: Bluish-red or deep red?," Br. J. Ophthalmol., vol. 98, no. 12, pp. 1761–1764, 2014.

[3] R. R. Provine, J. Nave-Blodgett, and M. O. Cabrera, "The Emotional Eye: Red Sclera as a Uniquely Human Cue of Emotion," Ethology, vol. 119, no. 11, pp. 993–998, 2013.

[4] C. Evereklioglu, E. Madenci, Y. a. Bayazit, K. Yilmaz, A. Balat, and N. a. Bekir, "Central corneal thickness is lower in osteogenesis imperfecta and negatively correlates with the presence of blue sclera," Ophthalmic Physiol. Opt., vol. 22, no. 6, pp. 511–515, 2002.